Nano Res
DOI 10.1007/s12274-011-0160-7
Review Article

ISSN 1998-0124
CN 11-5974/O4

One-Dimensional ZnO Nanostructures: Solution Growth and Functional Properties

Sheng Xu and Zhong Lin Wang (✉)

School of Materials Science and Engineering, Georgia Institute of Technology, Atlanta, Georgia 30332-0245, USA

Received: 8 May 2011 / Revised: 14 June 2011 / Accepted: 15 June 2011

ABSTRACT

One-dimensional (1D) ZnO nanostructures have been studied intensively and extensively over the last decade not only for their remarkable chemical and physical properties, but also for their current and future diverse technological applications. This article gives a comprehensive overview of the progress that has been made within the context of 1D ZnO nanostructures synthesized via wet chemical methods. We will cover the synthetic methodologies and corresponding growth mechanisms, different structures, doping and alloying, position-controlled growth on substrates, and finally, their functional properties as catalysts, hydrophobic surfaces, sensors, and in nanoelectronic, optical, optoelectronic, and energy harvesting devices.

KEYWORDS

ZnO, one dimensional nanostructures, solution growth, semiconductive, optical, piezoelectric, novel devices

1. Introduction

ZnO is a semiconducting and piezoelectric material with a direct wide band gap of 3.37 eV and a large exciton binding energy of 60 meV at room temperature [1, 2]. It has been demonstrated to have enormous applications in electronic, optoelectronic, electrochemical, and electromechanical devices [3–8], such as ultraviolet (UV) lasers [9, 10], light-emitting diodes [11], field emission devices [12–14], high performance nanosensors [15–17], solar cells [18–21], piezoelectric nanogenerators [22–24], and nanopiezotronics [25–27]. One-dimensional (1D) ZnO nanostructures have been synthesized by a wide range of techniques, such as wet chemical methods [28–30], physical vapor deposition [31–33], metal–organic chemical vapor deposition (MOCVD) [34–36], molecular beam epitaxy (MBE) [37], pulsed laser deposition [38, 39], sputtering [40], flux methods [41], eletrospinning [42–44], and even top-down approaches by etching [45]. Among those techniques, physical vapor deposition and flux methods usually require high temperature, and easily incorporate catalysts or impurities into the ZnO nanostructures. Therefore, they are less likely to be able to integrate with flexible organic substrates for future foldable and portable electronics. MOCVD and MBE can give high quality ZnO nanowire arrays, but are usually limited by the poor sample uniformity, low product yield, and choices of substrate. Also, the experimental cost is usually very high, so they have been less widely adopted. Pulsed laser deposition, sputtering and top down approaches have less controllability and repeatability compared with other techniques. Electrospinning gives polycrystalline fibers. Comparatively speaking, wet chemical methods are attractive for several reasons: they are low cost, less hazardous, and thus capable of

Address correspondence to zhong.wang@mse.gatech.edu

easy scaling up [46, 47]; growth occurs at a relatively low temperature, compatible with flexible organic substrates; there is no need for the use of metal catalysts, and thus it can be integrated with well-developed silicon technologies [48]; in addition, there are a variety of parameters that can tuned to effectively control the morphologies and properties of the final products [49, 50]. Wet chemical methods have been demonstrated as a very powerful and versatile technique for growing 1D ZnO nanostructures.

Here in this review, we focus on the 1D ZnO nanostructures that have been grown by wet chemical methods, although evaluation of ZnO nanostructures is provided in the vast Ref. [1, 5, 6, 51–53]. We cover the following five main aspects. First, we will go over the basic synthetic methodologies and growth mechanisms that have been adopted in the literature. Second, we will display the various kinds of novel nanostructures of ZnO that have been achieved by wet chemical methods. Third, we will summarize ways to manipulate the conductivity of the ZnO nanostructures by doping, such as *n*-type, *p*-type, and transition metal doping, and the ways of engineering the ZnO band gap by alloying with other metal oxides. Fourth, we will show the various techniques that have been implemented to control the spatial distribution of ZnO nanostructures on a substrate, namely patterned growth. Finally we will illustrate the functional properties of 1D ZnO nanostructures and the diverse innovative applications where 1D ZnO nanostructures play an important role.

2. Basic synthetic methodologies and growth mechanisms

ZnO is an amphoteric oxide with an isoelectric point value of about 9.5 [54]. Generally speaking, ZnO is expected to crystallize by the hydrolysis of Zn salts in a basic solution that can be formed using strong or weak alkalis. Zn^{2+} is known to coordinate in tetrahedral complexes. Due to the $3d^{10}$ electron configuration, it is colorless and has zero crystal field stabilization energy. Depending on the given pH and temperature [55], Zn^{2+} is able to exist in a series of intermediates, and ZnO can be formed by the dehydration of these intermediates.

Chemical reactions in aqueous systems are usually considered to be in a reversible equilibrium, and the driving force is the minimization of the free energy of the entire reaction system, which is the intrinsic nature of wet chemical methods [56]. Wurtzite structured ZnO grown along the *c* axis has high energy polar surfaces such as ± (0001) surfaces with alternating Zn^{2+}-terminated and O^{2-}-terminated surfaces [28]. So when a ZnO nucleus is newly formed, owing to the high energy of the polar surfaces, the incoming precursor molecules tend to favorably adsorb on the polar surfaces. However, after adsorption of one layer of precursor molecules, the polar surface transforms into another polar surface with inverted polarity. For instance, a Zn^{2+}-terminated surface changes into an O^{2-}-terminated surface, or vice versa. Such a process is repeated over time, leading to a fast growth along the ± [0001] directions, exposing the non-polar $\{1\bar{1}00\}$ and $\{2\bar{1}\bar{1}0\}$ surfaces to the solution. This is essentially how a 1D nanostructure is formed.

2.1 Growth in general alkaline solutions

An alkaline solution is essential for the formation of ZnO nanostructures because normally divalent metal ions do not hydrolyze in acidic environments [28, 57, 58]. The commonly used alkali compounds are KOH and NaOH. Generally speaking, the solubility of ZnO in an alkali solution increases with the alkali concentration and temperature. Supersaturation allows a growth zone to be attained [58]. KOH is thought to be preferable to NaOH, because K^+ has a larger ion radius and thus a lower probability of incorporation into the ZnO lattice [58, 59]. Furthermore, it has been suggested that Na^+ is attracted by the OH^- around the nanocrystal and forms a virtual capping layer, thus, inhibiting the nanocrystal growth [60].

$$Zn^{2+} + 2OH^- \longleftrightarrow Zn(OH)_2 \quad (1)$$

$$Zn(OH)_2 + 2OH^- \longleftrightarrow [Zn(OH)_4]^{2-} \quad (2)$$

$$[Zn(OH)_4]^{2-} \longleftrightarrow ZnO_2^{2-} + 2H_2O \quad (3)$$

$$ZnO_2^{2-} + H_2O \longleftrightarrow ZnO + 2OH^- \quad (4)$$

$$ZnO + OH^- \longleftrightarrow ZnOOH^- \quad (5)$$

The main reactions involved in the growth are illustrated in the above equations [61, 62]. For the

equation (2), the product is not necessarily $Zn(OH)_4^{2-}$, but could also be in the form of $Zn(OH)^+$, $Zn(OH)_2$, or $Zn(OH)_3^-$, depending on the parameters, such as the concentration of Zn^{2+} and the pH value, as shown in Fig. 1(a). And all of these intermediate forms are actually in equilibrium, with the major forms being different under different reaction conditions. The growth process could be described as follows [63]. At the very beginning, the Zn^{2+} and OH^- ions coordinate with each other, and then they undergo dehydration by proton transfer, forming $Zn^{2+}\cdots O^{2-}\cdots Zn^{2+}$ bonds, and leading to an agglomerate of the form of $[Zn_x(OH)_y]^{(2x-y)+}$, which has an octahedral geometry. The H_2O molecules formed by dehydration migrate into the solution. These aggregates usually contain fewer than 50 ions, and the formation of O^{2-} ions implies dramatic changes within the aggregate. After the aggregates reach around 150 ions, wurtzite type (tetrahedral coordination) ZnO domains are then nucleated in the central region of the aggregates (shown in Fig. 1(b)). The core comprises Zn^{2+} and O^{2-} ions only, while the aggregate surface still mainly consists of Zn^{2+} and OH^- ions. Aggregates of over 200 ions exhibit a nanometer-sized core of the wurtzite structured ZnO which grows as a result of further association and dehydration of Zn^{2+} and OH^- ions [63].

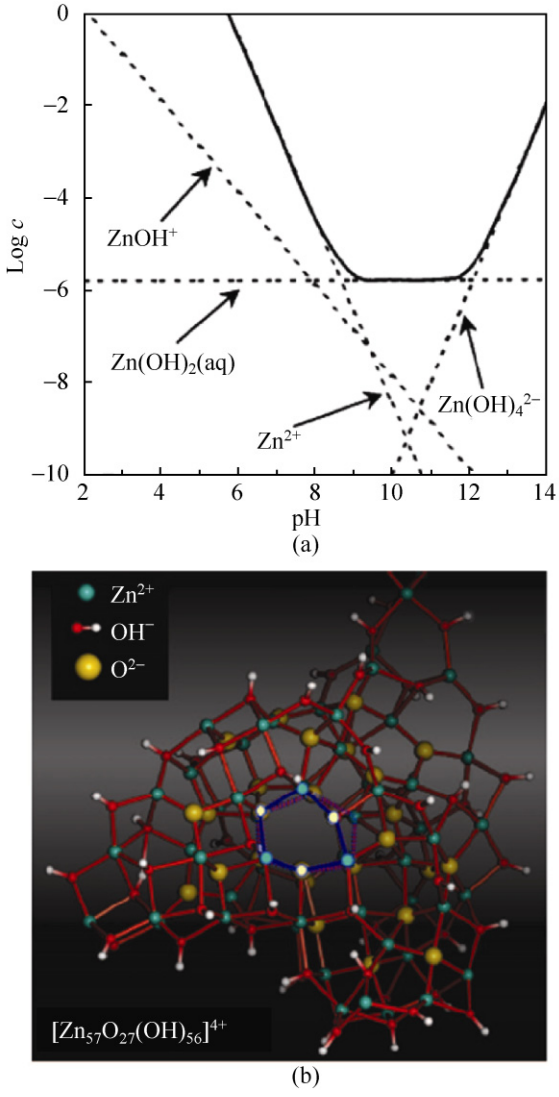

Figure 1 (a) Phase stability diagrams for the ZnO(s)–H_2O system at 25 ˚C as a function of precursor concentration and pH, where the dashed lines denote the thermodynamic equilibrium between the Zn^{2+} soluble species and the corresponding solid phases [64]. (b) Aggregation and nucleation of domains of the wurtzite structured ZnO, where the characteristic six membered rings in the aggregate center are highlighted in blue. The two staggered six-rings form a center of stability and give rise to further ordering in favor of the wurtzite structure [63]. Reproduced with permission

In the above equations, the O^{2-} in ZnO comes from the base, not from the solvent H_2O. Therefore growth of ZnO does not necessarily require the solvent to be H_2O [65]. It could be organic solvents, such as methanol [66], ethanol [67], and butanol [68], or even ionic liquids [69, 70]. Under alkali conditions, the reactions could take place at room temperature by adjusting the ratio of Zn^{2+} and OH^-, giving rise to ZnO nanowires with diameter even below 10 nm. ZnO nanowires with various aspect ratios can be prepared by simply adjusting OH^- concentration and reaction time [68].

The growth of polar inorganic nanocrystals is sensitive to the reaction solvents, and their morphologies could be tuned and controlled by the crystal–solvent interfacial interactions [66]. In such cases, the morphology of ZnO is largely directed by the polarity and saturated vapor pressure of the solvents [65]. As shown in Figs. 2(a)–2(c), the aspect ratio of ZnO nanowires, which is dictated by the relative growth rates of polar and nonpolar surfaces, can be readily tuned by varying the polarity of the solvents. Highly polar solvent molecules have stronger interactions with the polar surfaces of ZnO, and thus hinder the precursor molecules from adsorbing and settling down onto the polar surfaces. The aspect ratio of the ZnO nanostructures increases on going from the more polar solvent methanol to the less polar solvent 1-butanol. All the as-grown ZnO nanowires showed two well-faceted basal planes along the ± c axis as shown in Fig. 2(d) [67].

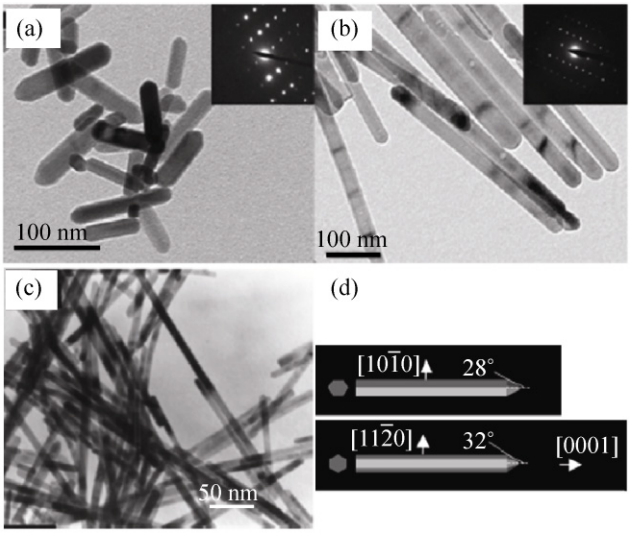

Figure 2 Transmission electron microscopy (TEM) images of ZnO nanowires synthesized in solvents having different polarities: (a) in methanol [66], (b) in ethanol [66], and (c) in 1-butanol [68]. Even though the reaction temperature and the growth time are different, we can still see the effect of the solvent polarity on the nanowire aspect ratio. Insets in (a) and (b) are selected area electron diffraction patterns. (d) Schematic illustration of growing +*c* ends of ZnO with two common interplanar angles [67]. Reproduced with permission

When the solvent contained nonpolar hexane, ultrathin ZnO nanowires of diameters of 2 nm could be synthesized from a simple acetate precursor, as shown in Fig. 3(a) [71]. These ultrathin nanowires also self-assembled into uniform stacks of nanowires aligned parallel to each other with respect to the long axis [71]. Near-UV absorption and photoluminescence measurements were able to determine that quantum confinement effects were present in these ultrathin nanowires, with an excitonic ground state of about 3.55 eV [71]. The ultrathin nanowires were possibly grown by oriented coalescence of quantum dots, as shown in Fig. 3(b). Pacholski et al. suggested that oriented attachment of preformed quasi-spherical ZnO nanoparticles should be a major reaction path during the formation of single crystalline nanowires [72, 73]. The bottlenecks between the attached adjacent nanoparticles were later filled up and the nanowire surfaces were thus, smoothened by Ostwald ripening [72].

The alkaline solution could also be weak bases, such as $NH_3{\cdot}H_2O$ and other amine compounds [74]. For examples, growth kinetics of ZnO nanowires in $NH_3{\cdot}H_2O$ has been well studied in the Ref. [75]. Besides providing a basic environment, $NH_3{\cdot}H_2O$ is also able to mediate heterogeneous nucleation of ZnO nanowires [75–78]. Experiments have shown that due to depletion of Zn^{2+} ions the growth of the ZnO nanowires normally slowed down with time and eventually arrived at growth-dissolution equilibrium for longer reaction times. This limitation can be overcome by adding additional Zn nitrate solution [79], or by replenishing the growth solution [77, 78, 80]. Under the mediation of $NH_3{\cdot}H_2O$, however, Zn^{2+} could be stabilized through the reversible reaction shown in equation (8) below, thus, leading to a relatively low level of supersaturation being maintained in the solution. At the growth temperature (typically 70–95 ˚C), this promoted only heterogeneous growth on the seeded substrate and suppressed the homogeneous nucleation in the bulk solution. That is also the reason that why after growth the bulk solution and reaction container usually remained clear without any precipitation. As the reaction proceeded, Zn^{2+} was gradually

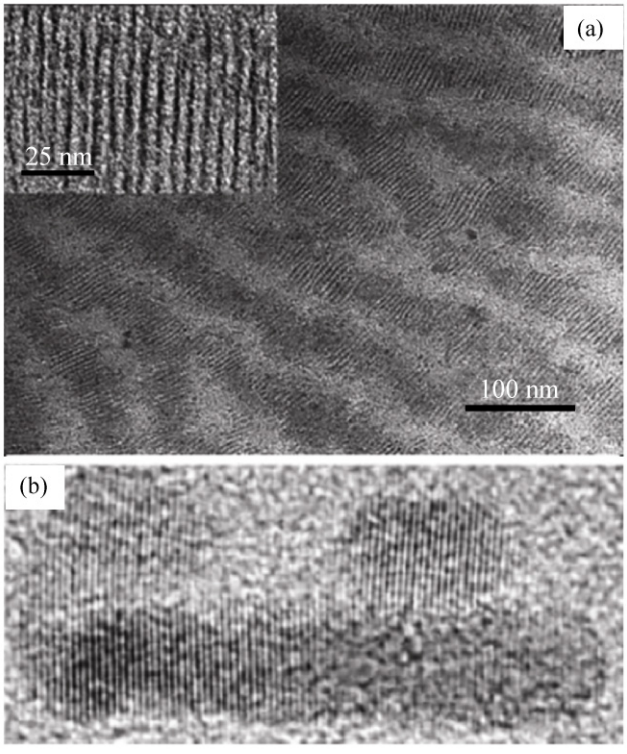

Figure 3 (a) TEM image of self-assembled ZnO nanowires with diameters of about 2 nm (inset: higher resolution image showing the oriented stacking; nanowires are dark contrast) [71]. (b) TEM image of the ultrathin nanowire formed by orientational aggregation of several quantum dots [72]. Reproduced with permission

consumed and the zinc–ammonia complex gradually decomposed, thus, maintaining a stable level of Zn^{2+} in the solution. Therefore, all the reaction nutrient only contributed to the heterogeneous growth of ZnO nanowires on the seeded substrate, so the growth could last for a long time without replenishing the solution.

Equations (1) to (5) only describe a simplified version of the reaction processes. The actual scenario could be much more complicated than what has been discussed above. For example, oxygen molecules have not been considered at all, but in reality, the dissolved O_2 concentration in the solution plays a significant role in the final crystal quality of the ZnO nanowires. There is experimental evidence showing that, if the growth solution was added with extra H_2O_2 that decomposed into H_2O and O_2, high quality ZnO nanowires with sharp top surfaces were grown [81]; if the solution was prepared with boiled de-ionized water to eliminate the dissolved O_2, ZnO nanowires with very ragged surfaces were formed [82].

2.2 Growth mediated by hexamethylenetetramine (HMTA) aqueous solution

Probably the most commonly used chemical agents in the existing literature for the hydrothermal synthesis of ZnO nanowires are $Zn(NO_3)_2$ and HMTA [83, 84]. In this case, $Zn(NO_3)_2$ provides Zn^{2+} ions required for building up ZnO nanowires. H_2O molecules in the solution, unlike for the case of alkali-mediated growth, provide O^{2-} ions.

HMTA is a nonionic cyclic tertiary amine, as shown in Fig. 4. Even though the exact function of HMTA during the ZnO nanowire growth is still unclear, it has been suggested that it acts as a bidentate Lewis base that coordinates and bridges two Zn^{2+} ions [85]. So besides the inherent fast growth along direction of the polar surfaces of wurtzite ZnO, attachment of HMTA to the nonpolar side facets also facilitates the anisotropic growth in the [0001] direction [86]. HMTA also acts as a weak base and pH buffer [49]. As shown in Fig. 4, HMTA is a rigid molecule, and it readily hydrolyzes in water and gradually produces HCHO and NH_3, releasing the strain energy that is associated with its molecular structure, as shown in equations (6) and (7). This is critical in the synthesis process. If the HMTA simply hydrolyzed very quickly and produced a large amount of OH^- in a short period of time, the Zn^{2+} ions in solution would precipitate out quickly owing to the high pH environment, and this eventually would result in fast consumption of the nutrient and prohibit the oriented growth of ZnO nanowires [87]. From reactions (8) and (9), NH_3—the product of the decomposition of HMTA—plays two essential roles. First, it produces a basic environment that is necessary for the formation of $Zn(OH)_2$. Second, it coordinates with Zn^{2+} and thus stabilizes the aqueous Zn^{2+}. $Zn(OH)_2$ dehydrates into ZnO when heated in an oven [84], in a microwave [88], under ultrasonication [89], or even under sunlight [90]. All five reactions (6) to (10) are actually in equilibrium and can be controlled by adjusting the reaction parameters, such as precursor concentration, growth temperature and growth time, pushing the reaction equilibrium forwards or backwards. In general, precursor concentration determines the nanowire density. Growth time and temperature control the ZnO nanowire morphology and aspect ratio [50, 91]. As we can also see from equation (6), seven moles of reactants produce ten moles of products, so there is an increase in entropy during reaction, which means increasing the reaction temperature will push the equilibrium forwards. The rate of HMTA hydrolysis decreases with increasing pH and vice versa [49]. Note that the above five reactions proceed extremely slowly at room temperature. For example, when the precursor concentration is below 10 mmol/L, the reaction solution remains transparent and clear for months at room temperature [82]. The reactions take place very fast if using microwaves as the heating source, and the average growth rate of the nanowires can be as high as 100 nm·min^{-1} [88].

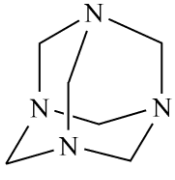

Figure 4 Molecular structure of HMTA

$$HMTA + 6H_2O \longleftrightarrow 4NH_3 + 6HCHO \quad (6)$$

$$NH_3 + H_2O \longleftrightarrow NH_4^+ + OH^- \quad (7)$$

$$Zn^{2+} + 4NH_3 \longleftrightarrow [Z(NH_3)_4]^{2+} \quad (8)$$

$$Zn^{2+} + 2OH^- \longleftrightarrow Zn(OH)_2 \quad (9)$$

$$Zn(OH)_2 \longleftrightarrow ZnO + H_2O \quad (10)$$

Even though the counter-ions are not involved in the growth process according to these reaction equations, they have been shown to have a strong effect on the resulting morphology of ZnO nanowires [49]. Acetate, formate, and chloride mainly result in the formation of rods; nitrate and perchlorate mainly produce wires; and sulfate yields flat hexagonal platelets.

2.3 Seeded growth on general substrates

One main advantage of wet chemical methods is that, using ZnO seeds in the form of thin films or nanoparticles, ZnO nanowires can be grown on arbitrary substrates, such as Si wafers (flat [84], etched [82], and pillar array [92]), polydimethylsiloxane (PDMS) [93], thermoplastic polyurethanes (TPU) [94], paper [95], fibers [96, 97], and carbon fibers [98], as illustrated in Fig. 5. There has been a report of the dependence of nanowire growth rate on the Si substrate orientation, however [99]. The adhesion of the seed layer to the substrate is of critical importance, and can be improved by depositing an intermediate metal layer, such as Cr or Ti, on inorganic substrates [100], and by introducing an interfacial bonding layer, such as tetraethoxysilane molecules, on a polymer substrate [96]. Through the use of seeds, wafer-scale synthesis can be readily achieved [88, 93].

The seed thin film can be coated on the substrate prior to wet chemical growth [83, 84]. The seed layer can be prepared in a number of ways. Sputtering of bulk materials and spin coating of colloidal quantum dots are the two most commonly used methods [100–102]. During the growth, ZnO nanowires preferentially nucleate from the cup tip near the grain boundaries between two adjacent grains in the ZnO seed film [103]. The width of the as-grown nanowires is usually less than 100 nm, which is largely dictated by the grain size of the polycrystalline seeds. The length of the nanowires can be more than 10 μm, so the aspect ratio can be over 100 [104]. The ZnO seed layer has a random in-plane alignment, but generally has the *c* axis perpendicular to the substrate [64], even though there have been occasions when there was non-perfect *c* orientation [105]. The vertical alignment of the nanowire arrays is usually poor due to the polycrystalline nature of the seed [83, 84]. Green et al. demonstrated that ZnO nanocrystal seeds prepared by thermal

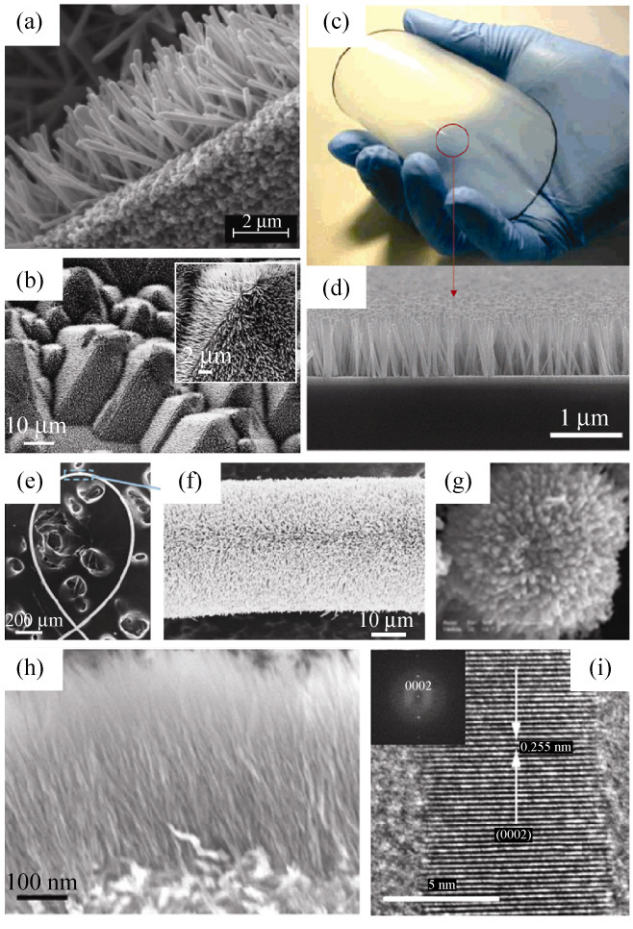

Figure 5 Scanning electron microscope (SEM) images of ZnO nanowire arrays grown on a ZnO seeded (a) flat rigid substrate [84], and (b) etched Si wafer (inset is an enlarged view) [82]. (c) Photograph of a four-inch flexible TPU substrate [94], and (d) SEM image of ZnO nanowire arrays with a uniform length on the TPU substrate [94]. (e) SEM image of a looped Kevlar fiber with ZnO nanowire arrays grown on top, showing the flexibility and strong binding of the nanowires [96], and (f) an enlarged local part of (e), showing a uniform distribution at the bending area [96]. (g) SEM image of ZnO nanowire arrays grown on a polystyrene sphere [107]. (h) Cross-section SEM image of ultrathin ZnO nanofibers grown on a Zn metal substrate [108]. (i) High-resolution transmission electron microscopy (HRTEM) image of a single ZnO nanofiber. Inset is the corresponding fast Fourier transform pattern [108]. Reproduced with permission

decomposition of a zinc acetate precursor could give vertically well-aligned ZnO nanowire arrays [106], and the degree of alignment depended strongly on the ambient humidity level during the seeding step [89].

Zn metal can also be the seed, because it is easily oxidized to ZnO in air and solution [77]. Fang et al. demonstrated an approach to synthesize dense arrays of ultrathin ZnO nanofibers using a Zn metal substrate in an ammonia/alcohol/water mixed solution [108], as shown in Fig. 5. As mentioned above, ZnO can grow in the absence of H_2O using an alkaline medium. Studies by Kar et al. have shown that, in the presence of NaOH using ethanol as the sole solvent, different kinds of morphologies of ZnO could be synthesized on Zn foil, such as nanosheets, nanonails, and well-aligned nanorods [109]. In particular, the degree of alignment of the nanorods improved with the use of NaOH [109].

There is a competition between homogeneous nucleation and heterogeneous nucleation in solution, and heterogeneous nucleation generally has a lower activation energy barrier than homogeneous nucleation. Also, the interfacial energy between crystals and substrates is usually lower than that between crystals and solution [30]. Hence, heterogeneous growth on a seeded substrate occurs at lower levels of supersaturation than nucleation and growth in homogeneous solution [49, 76, 83, 110, 111]. In other words, growth on existing seeds is more favorable than nucleation in homogeneous solution for the reason that the existing seeds bypassed the nucleation step. Therefore, there will be growth of ZnO nanowires wherever there are ZnO seeds, and as a result the density of nanowires is typically quite high [84, 94–96]. Efforts have been made to control the density of the seeded ZnO nanowire arrays for applications such as field emission [112, 113], and direct current nanogenerators [100, 114].

In simple terms, controlling the seed layer thickness can control the nanowire density. The thickness of the seed layer could be small enough that the seeds no longer form a continuous thin film, but form separated islands. Liu et al. found that, when the seed layer thickness was changed from 1.5 nm to 3.5 nm by sputtering, the density of the ZnO arrays changed from 6.8×10^4 to 2.6×10^{10} nanowires/cm^2 [112]. When the seed layer thickness was beyond this range, the nanowire density was less sensitive. If the seed layer was too thin, due to the high surface area and thus the high chemical potential of the polycrystalline seeds, dissolution exceeded deposition in the initial growth stage, and therefore no ZnO nanowires could be formed. If the thickness was larger than a certain value, e.g., 3.5 nm, only the outermost layer of the seed played a role. If the seed layer was prepared by spin coating of colloidal dots, controlling the spin speed enabled control of the density of the colloidal dots on the substrate. By tuning the spin speed from 4000 to 8000 r/min, the dot density changed from $(1.8 \pm 0.03) \times 10^3$ to $(1.8 \pm 0.03) \times 10^2$ dots/μm^2, and consequently the ZnO nanowire array density varied from $(5.6 \pm 0.01) \times 10^2$ to $(1.2 \pm 0.01) \times 10^2$ nanowires/μm^2 [101]. Besides controlling the seed density, diffusion obstacle layers have also been applied to the ZnO seed layer in order to control the nanowire density [113]. For example, a thin blocking polymer film was established on top of the seed layer. In this way, the probability and rate of precursor molecules migrating from solution to the seed layer was adjusted. Therefore, the probability and density of the nucleation and eventual nanowire growth were effectively controlled.

2.4 Electrodeposition

Electrochemical deposition is a very powerful technique for achieving uniform and large area synthesis of ZnO nanostructures [115], because it exerts a strong external driving force to make the reactions take place, even if they are non-spontaneous. In this case, growth of ZnO nanostructures can occur on a general substrate, flat or curved [116], without any seeds, as long as the substrate is conductive. Also, under such an external electric field, better nanowire alignment and stronger adhesion to the substrate have been observed [117]. Generally speaking, ZnO nanowire growth was observed at only the cathode of a d.c. power source [117], and at both electrodes for an a.c. power source. Most importantly, electrodeposition has been shown to be an effective way of doping ZnO nanowires by adding different ingredients into the reaction solution [118–120].

For electrodeposition, a standard three-electrode setup is typically used, with a saturated Ag/AgCl electrode as the reference electrode and Pt as the

counter-electrode. The anode, where growth usually takes place, is placed parallel to the cathode in the deposition solution. The electrical bias throughout the reaction system is controlled by a constant voltage source to maintain a constant driving force to the reaction, or by a constant current source to keep a constant reaction rate. Konenkamp et al. used a $ZnCl_2$ and KCl mixed solution electrolyte to grow vertically aligned ZnO nanowire arrays on a SnO_2 glass substrate, as shown in Fig. 6 [118]. During the growth, O_2 was continuously bubbled through the solution in order to keep a relatively high level of O_2 dissolved in the solution, which was necessary for the growth of high quality ZnO nanowires as discussed above.

From equation (11), reduction of O_2 at the cathode provides a source of OH^- [121], which is required to coordinate with Zn^{2+} and then undergo dehydration to form ZnO, as illustrated by equations (9) and (10). It has also been suggested that when using $Zn(NO_3)_2$ as the precursor, reduction of NO_3^- at the cathode could also provide a possible source of OH^- [122], as indicated by equation (12). In any case, the ratio between the OH^- generation rate at the cathode and the Zn^{2+} diffusion rate to the cathode was proposed to be the major parameter in the electrodeposition of ZnO nanowires [123]. Other than being produced *in situ*, OH^- could also be added to the solution beforehand in the form of alkali precursors [122].

$$O_2 + 2H_2O + 4e^- \longleftrightarrow 4OH^- \quad (11)$$

$$NO_3^- + H_2O + 2e^- \longleftrightarrow NO_2^- + 2OH^- \quad (12)$$

$ZnCl_2$ has commonly been used as the zinc source. It was found that the dimensions of ZnO nanowires could be controlled from 25 to 80 nm by the varying the $ZnCl_2$ concentration [121]. Notably, Cl^- ions became adsorbed preferentially on the Zn-terminated (0001) planes of ZnO, which eventually hindered the growth along the polar axis, giving rise to platelet-like crystals [124], even though the anions are not considered as reactants according to equations (11) and (12). Even when other zinc salts rather than $ZnCl_2$ were used as precursors, the Cl^- could also come from the supporting electrolyte KCl [125]. Interestingly, although the electrolyte KCl was apparently not involved in the reaction, its concentration considerably affected the

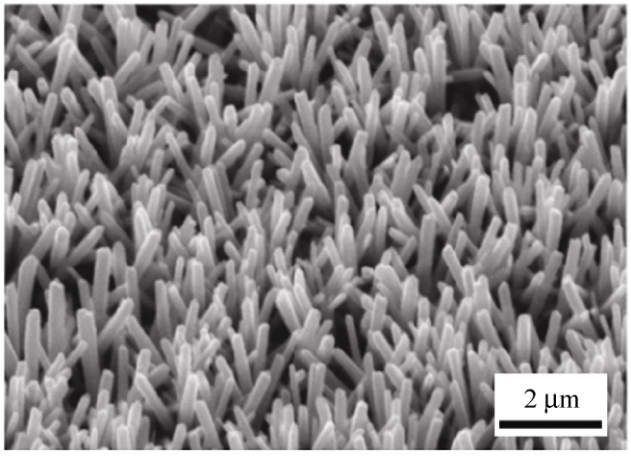

Figure 6 SEM image of free-standing ZnO nanowires formed on a SnO_2 substrate by electrodeposition [118]. Reproduced with permission

reaction process. An increase in KCl concentration led to a decrease in the O_2 reduction rate, and thus led to an augmentation of the growth efficiency of ZnO nanowires, which meant an enhancement of the axial growth rate relative to the radial growth rate. It has also been pointed out, however, that high KCl concentrations (> 1 mol/L) also favored the radial growth of ZnO nanowires [125]. This effect was attributed to Cl^- ion adsorption on the cathode surface, with a preferential adsorption of the Cl^- on the (0001) ZnO surface [125]. In addition, the KCl concentration could also affect the lattice parameters of the as-synthesized ZnO nanostructures, especially for KCl concentrations > 1 mol/L [126], and it was proposed that this was due to the inclusion of zinc interstitials in the lattice.

The effect of counter anions (Cl^-, SO_4^{2-}, and CH_3COO^-) on the reduction of dissolved O_2 in the solution has been systematically investigated [123]. Different counter anions have considerably different coordination capabilities with the different crystal planes of ZnO nanowires. Therefore, the different adsorption behaviors of the anions can result in different morphologies and growth rates of the nanowires. It was also found that varying the counter anions could greatly tune the diameter (65–110 nm) and length (1.0–3.4 μm) of the nanowires. In particular, the presence of Cl^- and CH_3COO^- could produce ZnO nanowires with the lowest and highest aspect ratios, respectively [123].

The ZnO nanowire arrays showed high transmittance

in the visible range due to the large electronic band gap. Interestingly, the band gap of the ZnO nanowire arrays could be tuned by simply changing the zinc precursor concentration during the electrodeposition [127].

2.5 Templated growth

ZnO nanowires can be grown by electrodeposition methods in combination with templates, such as anodic aluminum oxide (AAO), polycarbonate membranes, nano-channel glass, and porous films self-organized from diblock copolymers. In the literature, the most widely used template is probably AAO due to its simplicity and capability of large area fabrication [128]. After nanowire growth, the template can be chemically dissolved and leaving behind the free standing nanowires.

A typical fabrication process is as follows. The template is attached to the surface of a substrate, which can be flat or curved, flexible or rigid. Then the substrate together with the template is set to be the cathode of a d.c. power source. Under the electric field, Zn^{2+} ions or intermediate Zn coordination species diffuse towards the cathode and into the pores of the template. OH^- ions are simultaneously produced at the cathode according to equations (11) and (12). These two ions react and result in the growth of nanowires inside the pores of the template. After the pore is filled, nanowire arrays can be obtained by dissolution of the template membrane. This technique is not limited to ZnO nanowires and applies to the electrodeposition of general semiconductive oxide nanostructures. However, because both ZnO and Al_2O_3 are amphoteric oxides, it is technically difficult to selectively remove the Al_2O_3 membrane in the presence of ZnO nanowires. As an alternative, polycarbonate templates have been shown to be able to produce free standing ZnO nanowire arrays. As shown in Fig. 7, Zhou et al. demonstrated a simple polycarbonate template method to synthesize 1D oxide nanostructures [129], among which, the diameters of the ZnO nanowires could be tuned from 60 to 260 nm, with lengths in the ~μm range, by reliably and reproducibly controlling the template pore channel dimensions [129].

However, the key issue for semiconductor nanowires fabricated by this technique is the crystalline quality, which in most cases is not perfect. The resulting materials are either amorphous or polycrystalline consisting of small crystals with an abundance of defects, which might greatly limit their technical applications, particularly in optoelectronic devices. It is to be anticipated these shortcomings could be overcome by further optimizing the growth conditions.

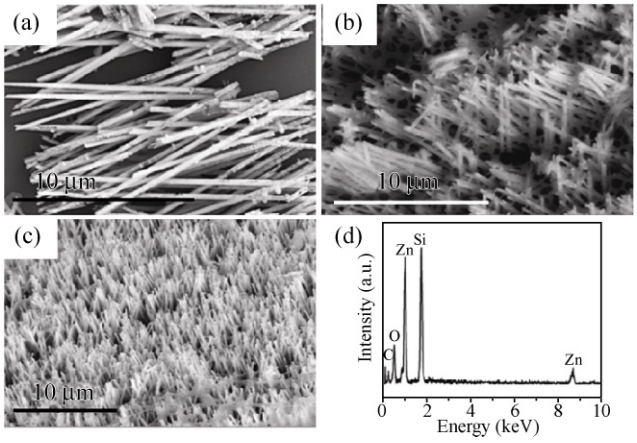

Figure 7 SEM images of (a) isolated ZnO nanowires, (b) ZnO nanowires embedded in a polycarbonate template, (c) free standing ZnO nanowire arrays after removal of the template, and (d) representative energy-dispersive X-ray spectroscopy (EDS) plot of the as prepared ZnO nanowire arrays [129]. Reproduced with permission

Besides porous membranes, the templates could also be formed *in situ* inside the reaction system. Liu et al. showed that metallic Zn particles with their surface oxide coating could be a template for ZnO nanowire growth [130]. The reaction involves a so-called modified Kirkendall process in solution, where the preformed oxide layer serves as a shell template for the initial nucleation and growth [130]. Furthermore, self-assembled ionic polymers can also act a soft template for the growth of ZnO nanowires. Utilizing an Evans blue (EB) dye and a cetyltrimethylammonium bromide (CTAB) system, Cong et al. demonstrated a facile one-step process for the synthesis of a new kind of hybrid ZnO–dye hollow sphere made of aligned ZnO nanowires and dye molecules [131]. During the growth process, CTAB–EB micelles formed by an ionic self-assembly process served as a soft template for the deposition of ZnO [131–134]. In addition, Atanasova et al. demonstrated λ-DNA templated growth of ZnO nanowires, and the electrical resistance of the as-grown nanowires was found to be on the order of Ω [135].

2.6 Epitaxial growth

Just as for seeded growth, epitaxial growth is also considered to involve a heterogeneous nucleation and growth process. Because of the small interfacial lattice mismatch, dangling bonds can be mostly satisfied and are less critical than for general interfaces. The energy benefits from satisfying the interfacial dangling bonds provide the driving force for the epitaxial growth. Different substrates have different isoelectric points—the pH where most sites on the substrate are neutral and the numbers of negative and positive sites are equivalent. So for an epitaxial substrate, positive or negative charge polarities should be considered as appropriate at different reaction pH values [136].

2.6.1 Au coated general substrates

While the formation of well-aligned ZnO nanowires on a pristine Si substrate is difficult because of a large mismatch (~40%) between ZnO and Si, it is appealing to take advantage of the relatively small lattice mismatch between ZnO and other materials, such as Au [10, 137, 138], Pd [139], and Cu [140]. Figure 8(a) shows a crystal geometry diagram illustrating the epitaxial relationship of ZnO(0001)[11$\bar{2}$0]//Au(111)[$\bar{1}$10], which have a lattice mismatch of 12.7% [141].

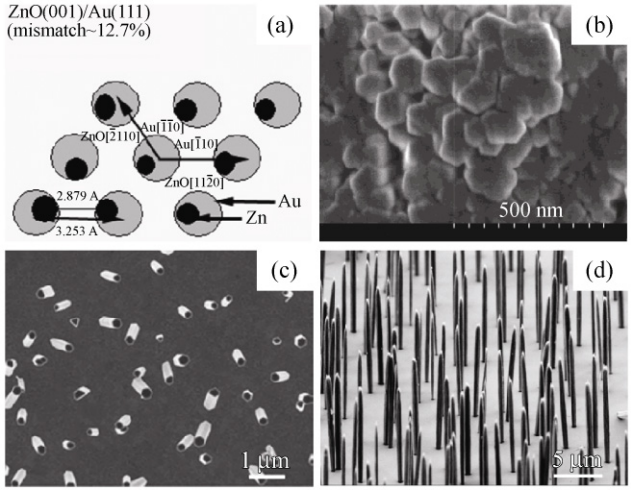

Figure 8 (a) Schematic illustration of the epitaxial relationship between ZnO(0001) and Au(111) [141]. SEM images of (b) 500-nm-thick ZnO on single crystal Au(111) substrate [142], (c) density controlled ZnO nanowire arrays on polycrystalline Au(111) substrate [91], and (d) aspect ratio enhanced ZnO nanowire arrays guided by a statistical design of experiments [50]. Reproduced with permission

In the physical vapor deposition, Au was utilized as a catalyst in a vapor–liquid–solid process [32]. In wet chemical methods, Au is believed to be a mere epitaxial substrate [91]. ZnO nanowires have been electrodeposited epitaxially onto Au(111), Au(110), and Au(100) single crystal substrates as shown in Fig. 8(b) [142]. The ZnO nanowire arrays were *c*-axis oriented, and had in-plane alignment, which was probed by X-ray pole analysis [142]. As can be seen from Fig. 8(b), the nanowires were very dense, almost continuous as a thin film. To replace the expensive single crystalline Au, polycrystalline Au thin films coated on substrates such as Si wafers and flexible polymers were employed. As long as the substrate surface is locally flat to promote the vertical alignment of the ZnO nanowires [91], as shown in Fig. 8(c) [91, 143]. X-ray diffraction studies showed the as-deposited polycrystalline Au thin films were <111> oriented normal to the substrate, even though they had random in-plane orientations [82]. The <111> oriented Au film resulted in the growth of [0001] oriented ZnO nuclei due to the small lattice mismatch between them [141]. The density of the ZnO nanowires could be readily tuned and was found to be controlled by the concentration of the reactants, such as HMTA and $Zn(NO_3)_2$ [91]. The nanowire density increased with $[Zn^{2+}]$ at low concentrations and decreased with $[Zn^{2+}]$ at high concentration levels. The nanowire morphology was very sensitive to the growth temperature. When the temperature was increased from 70 °C to 95 °C, the nanowires transformed to nanopyramids, exposing the higher energy {01$\bar{1}$1} surfaces [91]. This was probably due to the electrostatic interaction between the ions in the solution and the polar surfaces, and as a result higher Miller index surfaces became preferred [144]. One thing worth noting is that, by virtue of the surface tension, the substrate was put face-down floating on the nutrient solution [91], as shown in Fig. 9, to keep any precipitates from falling from the bulk solution onto the substrate, which would otherwise inhibit the growth of the desired nanostructures and possibly initiate secondary growth [91]. When the substrate was floating, it was suggested that the nuclei of ZnO were actually formed at the air–solution–substrate three-phase boundaries and then migrated and settled down on the substrate [82].

Figure 9 A digital photograph of the reaction container showing the substrate floating on the solution surface by surface tension

The aspect ratio is typically around 10 for ZnO nanowires grown on a polycrystalline Au thin film. A novel way of optimizing the nanowire aspect ratio by utilizing the statistical pick-the-winner rule and one-pair-at-a-time main effect analysis to sequentially design the experiments and identify optimal reaction settings has been demonstrated [50]. By controlling the hydrothermal reaction parameters, such as reaction temperature, time, precursor concentration, and possibly capping agent, the aspect ratio of ZnO nanowires was increased from around 10 to nearly 23, as shown in Fig. 8(d). These statistical design and analysis methods were very effective in reducing the number of experiments needed to be performed to identify the optimal experimental settings [50].

2.6.2 n-GaN/p-GaN

Due to a small lattice mismatch, almost perfectly vertically aligned ZnO nanowire arrays can be grown on GaN (*n*-type [48] and *p*-type [145–149]), AlN, SiC, Al_2O_3, and $MgAl_2O_4$ substrates [150], either by hydrothermal decomposition [151] or electrodeposition. In particular, ZnO and GaN have the same wurtzite-type structure with a low lattice mismatch of 1.8% [152], which is much smaller than that (12.7%) with Au(111). This is reflected by the much better vertical alignment of the ZnO nanowire arrays grown on *n*-type GaN(0001) (Figs. 10(a) and 10(b)) than on Au(111) (Figs. 8(c) and 8(d)). Nevertheless, the nanowires grown on both substrates have uniform length and width, and are well distributed on the substrates with one nanowire growing on one spot.

The epitaxial relationship between the as-grown ZnO nanowires and the GaN substrate is evidenced by X-ray diffraction (XRD) [136, 153]. Figure 10(c) shows a six-fold rotational symmetry in the azimuthal scan. The results clearly showed that the epitaxial nanowires had uniform vertical as well as in-plane alignment. If some of the nanowires have a different in-plane orientation, then the ϕ-scan will be characterized by more than six peaks. The ϕ-scan of the ZnO nanowires could be superimposed on the ϕ-scan for the GaN substrate, which indicated a good epitaxial relationship between the as-grown ZnO nanowires and the GaN substrate. Furthermore, the small full width at half maximum of the diffraction peaks also showed a good crystalline quality [153].

2.7 Capping agent-assisted growth

Capping agents can be included in the solution to modify the growth habits of the ZnO nanostructures [154]. Commonly used capping agents for hydrothermal growth of ZnO nanostructures may be placed in two categories: those that adsorb onto the

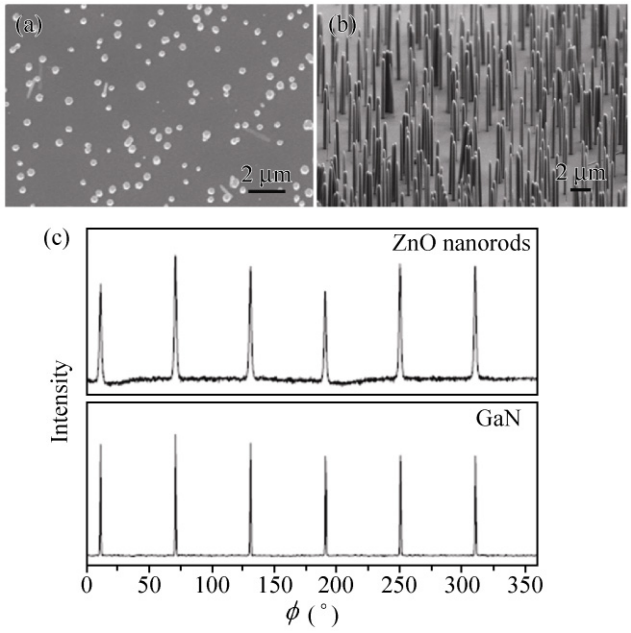

Figure 10 SEM images of ZnO nanowires on a *n*-type GaN wafer: (a) top view and (b) oblique view [82]. (c) ϕ-scan profiles of the ZnO nanowires/GaN/*c*-sapphire structure with the family of planes of ZnO nanowires on the top, and the GaN film at the bottom [153]. Reproduced with permission

side surfaces and enhance the vertical growth, such as amines like polyethylenimine (PEI) [18, 155, 156] and ethylenediamine [67, 137]; those that cap onto the basal plane of the ZnO nanostructures and promote lateral growth, such as Cl^- [124] and $C_3H_5O(COO)_3^{3-}$ (citrate ions) [150, 157, 158].

The isoelectric point of ZnO powder is at around pH = 9.5 [54]. The sign of the ZnO surface sites is predominately positive or negative for pH values below or above the isoelectric point, respectively [136]. PEI is a nonpolar polymer with a large amount of amino side-groups ($–NH_2$), which can be protonated over a wide range of pH values (3–11) and therefore become positively charged. The pH value of the growth solution could be adjusted to fall in the range that leads to the protonation of PEI, and therefore the linear PEI with its high positive charge density adsorbs strongly on the negatively charged surfaces due to electrostatic attraction [155], as shown in Fig. 11(a). Thus, the lateral growth of the nanowires will be largely hindered [156].

Other than their capping behavior, PEI additives also help to grow longer nanowires by extending the growth time [156], as shown in Fig. 11(b). This is similar to the effect of adding $NH_3{\cdot}H_2O$ to increase the solubility of the nutrient precursor, and can be attributed to the decrease of the free $[Zn^{2+}]$ that usually combines with OH^- and precipitates in the form of $Zn(OH)_2$, due to the coordination of PEI to Zn^{2+}. Also after the growth, less precipitate was expected to form in the bulk solution in the presence of PEI coordination than without PEI. Thus, longer nanowire arrays could be produced through prolonging the growth time without refreshing the growth solution, because the Zn^{2+} depleted during the growth would be replenished through the decomposition of PEI-Zn^{2+} complexes [156].

Citrate ions are characterized by three negative charges under the normal growth environment. Experimental results in the literature as well as theoretical calculations suggest that citrate ions strongly and specifically adsorb to the Zn^{2+} ions on the (0001) surface, and thus inhibit the growth along [0001] and forced to grow along the $\langle 01\bar{1}0\rangle$ or $\langle 2\bar{1}\bar{1}0\rangle$ directions [150, 157, 160]. With citrate ions, rather than long hexagonal nanowires, flat hexagonal nanoplates were produced, as shown in Fig. 11(c) [150, 157]. Due to the high roughness factor and/or the large areas of exposed polar basal planes, the ZnO nanoplates showed enhanced photocatalytic properties for decomposition of volatile organic compounds in comparison with common 1D ZnO nanowire arrays [161]. Also, it was suggested that due to the presence of the citrate ions, the surface tension of the growth solution was reduced, which lowered the energy needed to form a new

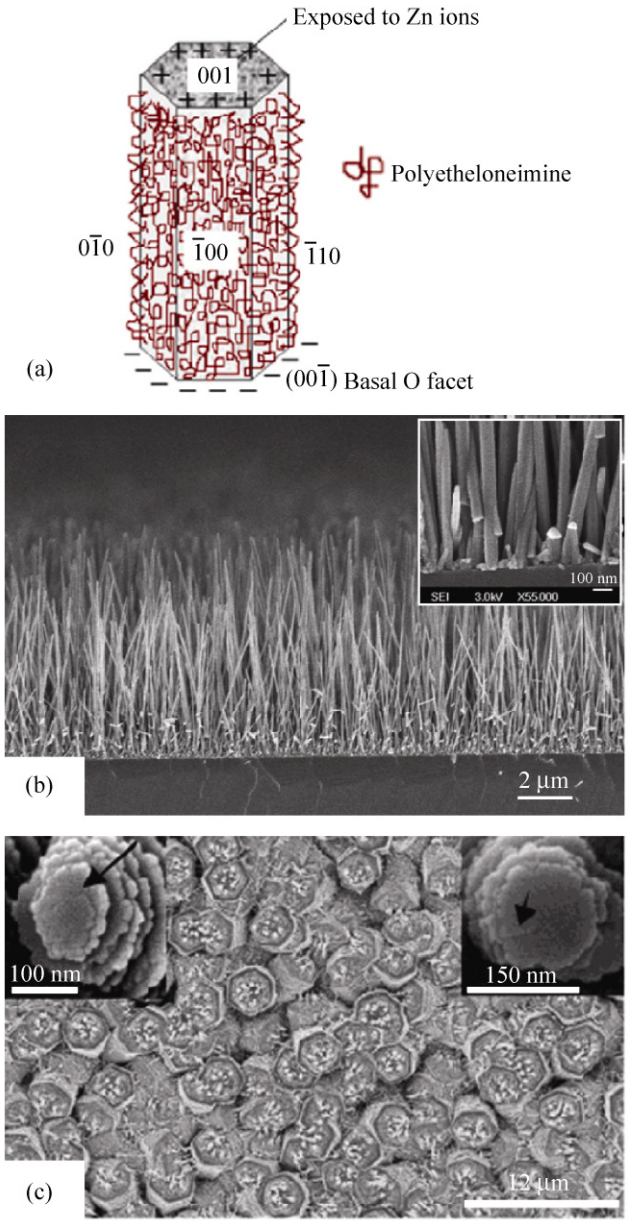

Figure 11 (a) Schematic illustration of the adsorption of PEI molecules on the ZnO nanowire side surfaces [159]. (b) SEM image of the ZnO nanowires formed with the addition of PEI [155]. (c) Large arrays of well-aligned helical ZnO whiskers on top of ZnO rod base [150, 157]. Reproduced with permission

phase, and thus ZnO nanostructures could therefore nucleate at a lower supersaturation [158]. In addition to ZnO, this synthetic approach can also be employed to modify and control the growth of other nanostructures such as conductive polymer nanowires [162] and TiO_2 nanotubes [163].

3. Different structures

ZnO can be manipulated into a variety of forms and morphologies, including nanowires, nanobelts, tubes/rings, twinning structures, hierarchical structures, and heterostructures with other materials, showing the great versatility of wet chemical methods.

3.1 Belts

ZnO can grow along non-polar directions, such as $\langle 01\bar{1}0\rangle$ and $\langle 2\bar{1}\bar{1}0\rangle$, and form 1D nanobelts [31], which have high energy polar ± (0001) side surfaces. This configuration has normally been observed using gas phase synthesis approaches [14, 31, 164–166], and is not favorable using aqueous approaches because—as discussed previously—wet chemical methods are usually considered to be under thermodynamic equilibrium, and the driving force is the minimization of the free energy of the entire reaction system [56]. However, there have been several reports of the synthesis of rectangular cross-sectional ZnO nanobelts by wet chemical methods, even though they were not necessarily growing along the non-polar directions. The nanobelts were free floating in the bulk solution [73] or standing on a substrate [167, 168].

Figure 12(a) shows a an SEM image of ZnO nanobelts synthesized in a microemulsion-mediated solution method [73]. The reverse micelles formed microreactors to confine the ZnO nanoparticles. Owing to the anisotropic growth property of wurtzite ZnO, the nanoparticles undergo an oriented attachment process to lower the overall system energy by piling up and then fusing with the adjacent nanoplates. This eventually led to the formation of unique 1D rectangular cross-sectional ZnO nanobelts. This oriented attachment-based growth mechanism dominated when the concentration of the precursors was high. The subsequent Ostwald ripening process smoothened out the resulting nanobelts when the precursor concentration was lowered [73]. Rectangular cross-section ZnO nanobelts, growing along the [0001] direction, have also been synthesized by a regular alkaline hydrothermal method with the help of ethylenediamine (Fig. 12(b)) [167]. Other than that, vertically aligned ZnO nanobelts on metallic Zn substrate have been fabrication by an *in situ* electrochemical method, as shown in Fig. 12(c). For the formation of ZnO nanowire or nanobelt arrays, it was suggested that the critical step is whether the nucleation is slow or fast, which leads to the formation of nanowires or nanobelts, respectively [168]. Porous ZnO nanobelts, shown in Fig. 12(d), were prepared from the thermal decomposition of synthetic bilayered basic zinc acetate nanobelts obtained by a simple synthetic route under mild conditions. During calcination in air, organic ligands and intercalated water molecules were removed from the synthetic bilayered basic zinc acetate nanobelts, leaving behind the inorganic porous ZnO nanobelts and nanoparticle chains. In essence, the synthetic bilayered basic zinc acetate nanobelts serve as templates [169].

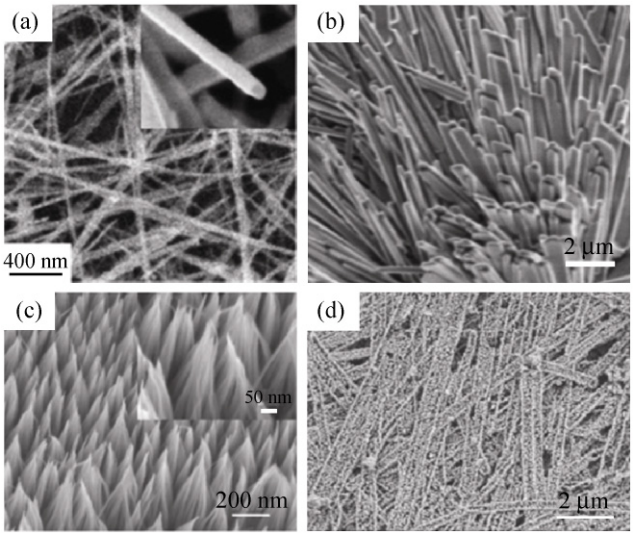

Figure 12 (a) SEM image of ZnO nanobelts synthesized by a microemulsion-mediated wet chemical method. Inset shows a typical rectangular cross-section feature of the nanobelts [73]. (b) SEM image of free standing nanobelt arrays [167]. (c) SEM image of ZnO nanobelt arrays grown on a metallic Zn substrate [168]. (d) SEM image of porous polycrystalline ZnO nanobelts and nanoparticle chains formed by the thermal decomposition of synthetic bilayered basic zinc acetate nanobelts [169]. Reproduced with permission

3.2 Tubes/rings

Tubular structures are of particular interest for many potential applications, such as in high efficiency solar cells due to the high internal surface area relative to nanowires, and in novel bimolecular or gas sensors due to the well-defined adsorption microcavities [170]. ZnO nanotubes have been fabricated using a variety of approaches [170–172], such as optimizing the seed layer thickness [173], utilizing appropriate solvent composition [174], ultrasonic pretreatment of the reaction solution [175], and post pH adjustment [176]. The ZnO nanotubes can be made by one-step growth methods [117, 174], or two-step growth and etching processes [177, 178], as shown in Fig. 13. The nanotube wall thickness can be precisely controlled by controlling the electrodeposition time [179]. The nanotube could also be grown on large scale on seeded general substrates [180], with a yield approaching 100% [181].

Different formation mechanisms have been proposed in the literature. For example, She et al. proposed that the tubular morphology was formed via the defect selective etching of ZnO nanowires on the polar surface by protons generated from anodic water splitting [172]. The high energy (0001) basal plane of ZnO nanowire results in preferential etching in the (0001) direction [104]. The distribution of point defects on the basal plane of the ZnO nanowire was rather non-uniform with the center higher than the peripheral part. Therefore, the center part was etched away faster than the peripheral part, which led to tubular morphology. This hypothesis was indirectly supported by a control experiment in which annealed ZnO nanowires could not be etched to give nanotubes [172]. Also, it is suggested that different termination atoms—zinc or oxygen—on the (0001) basal plane play a decisive role in the formation of nanotubes or nanowires [182]. Yu et al. proposed that the formation of ZnO nanotubes arose from the low concentration of precursor molecules during electrodeposition [117]. The electric field around the edge was stronger than that right above the hexagonal basal plane, so the limited precursor molecules would preferentially drift to the edge where as a result growth was faster than at the center. However, Li et al. ascribed the formation

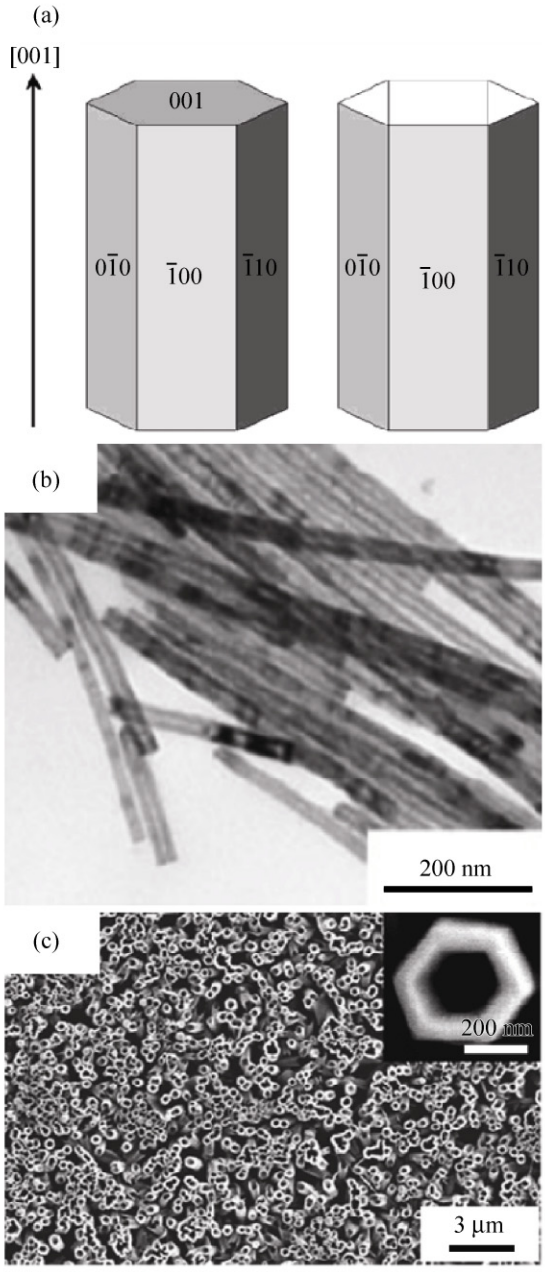

Figure 13 (a) Crystal growth habit of wurtzite ZnO hexagonal nanowires and nanotubes [170]. (b) TEM image of high aspect ratio ultrathin single crystalline ZnO nanotubes [173]. (c) SEM image of arrayed ZnO nanotubes [172]. Reproduced with permission

of nanotubes to the incorporation during the initial growth, and subsequent dissolution, of nitrogen-containing organic compounds at the core of the ZnO nanowires [183]. Yang et al. also suggested a scrolling of layer structures as the mechanism of formation of the nanotubes [178].

Nevertheless, it is accepted that the formation of

ZnO nanotubes is a kinetically controlled process. The final morphology and dimension of the nanostructures are determined by a competition between adsorption and desorption of the precursor molecules, or in other words crystal growth and dissolution processes [56, 184]. At the initial stage, the growth rate is relatively high because of the high supersaturation degree of growth nutrient. With prolonged hydrothermal treatment, the reaction reaches a certain equilibrium, and the solution composition is no longer thermodynamically favorable for formation of $Zn(OH)_2$ that can subsequently dehydrate into ZnO [87], and the rate of ZnO dissolution is faster than the rate of formation [174]. As discussed previously, the polar surfaces will be dissolved preferentially since this decreases the system energy during the subsequent aging process, and that gradually leads to the formation of ZnO nanotubes [183, 185], as illustrated in Fig. 14 [186].

In a further step, ZnO rings could also be synthesized by the growth of plates and a subsequent etching process [187]. Li et al. used sodium bis(2-ethylhexyl)sulfosuccinate (NaAOT) as surfactant/template to fabricate ZnO rings and disks at low temperature on a large scale, as shown in Fig. 5(a) [187]. The anionic surfactant NaAOT can form micelles/microreactors with diverse shapes from spheres to rods, ellipsoids, and disks by adjusting the experimental parameters [188]. ZnO nanostructures can grow in the resulting microreactors. The self-assembled AOT ions at the water/oil interface can attract Zn^{2+} ions and thus direct the nucleation of the ZnO. By controlling the growth parameters, such as the growth temperature and molar ratio of reactants, the nanodisks can be converted into rings due to the electrostatic interaction between the anionic AOT ions and the Zn^{2+} ions on the (0001) surface of ZnO, which therefore inhibits the growth along the [0001] direction, and promotes growth along $\langle 2\bar{1}\bar{1}0\rangle$, forming hexagonal nanodisks enclosed by $\{10\bar{1}0\}$ side surfaces. A subsequent etching leads to the formation of hexagonal nanorings [187].

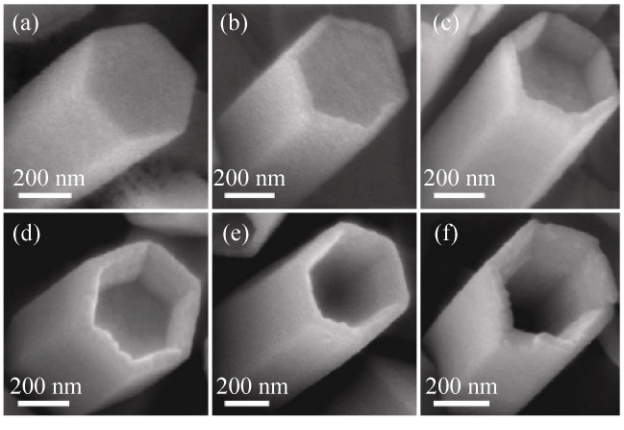

Figure 14 SEM images illustrating the formation of ZnO nanotubes at different etching stages: (a) 0 min, (b) 5 min, (c) 10 min, (d) 15 min, (e) 60 min, and (f) 120 min [186]. Reproduced with permission

In addition to the growth and etching processes, a self-template directed growth process was shown to lead to fabrication of ZnO rings, as shown in Fig. 15(b) [189]. By a simple solvothermal method, the atypically shaped coordination polymer particles were formed by the cooperation of two different organic ligands, namely *N*,*N*′-phenylenebis(salicylideneimine)dicarboxylic acid (A) and 1,4-benzenedicarboxylic acid (B). The growth mechanism is shown in Fig. 15(c) [190]. These two ligands formed coordination polymer disks, which later served as templates for the formation of the Zn^{2+} precursor shell, followed by dissolution of the coordination polymer disks. Calcination of the disks together with the Zn^{2+} precursor shell gave rise to ZnO rings, which was polycrystalline in nature [190].

3.3 Twinning

Twinned structures are very commonly formed by wet chemical methods [83, 111, 191–193]. Typical twinned ZnO structures [174] are shown in Fig. 16. Two joined hexagonal prisms connected by a common basal plane forming a twinning growth relationship. TEM studies showed that the ZnO is a single crystal with the oriented growth direction along the [0001] direction. A growth mechanism was proposed based on the linkage/incorporation of the growth units. Wang et al. suggested that the twinning relationship of the two branches should be altered in different growth solutions [194]. In pure water or weakly basic solutions, the twinned species are bipyramidal and take $(000\bar{1})$ as the common connection plane. In contrast, when the growth solution contained KBr or $NaNO_2$ as mineralizers, the twinning morphologies were dumbbell-like

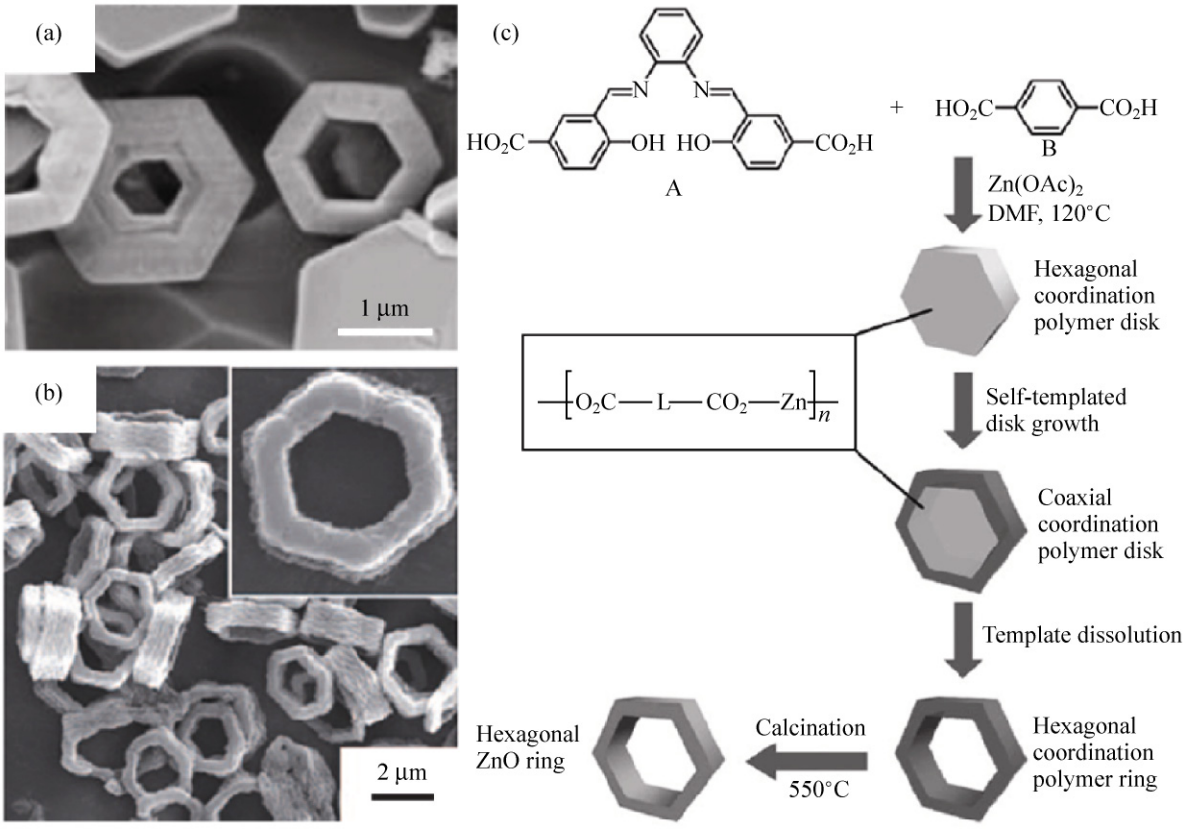

Figure 15 (a) SEM image of the as synthesized ZnO rings prepared by the growth and etching process [187]. (b) SEM image of the templated growth and calcination of ZnO rings [189], and (c) the proposed growth mechanism, where $^{-}O_2C–L–CO_2^{-}$ represents deprotonated acid A or B [190]. Reproduced with permission

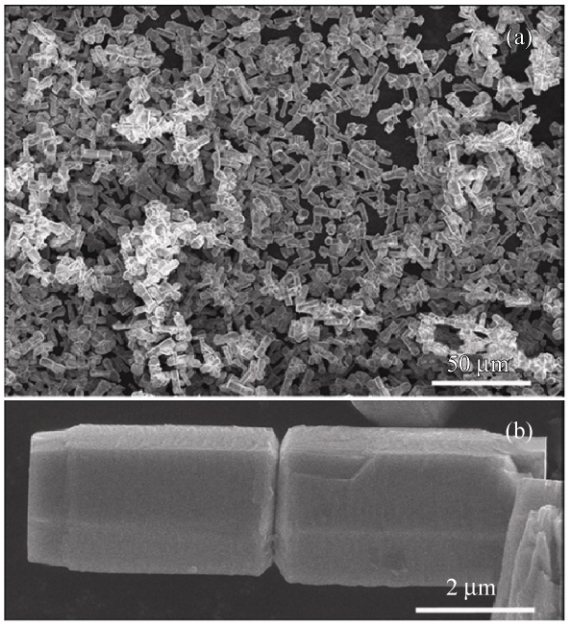

Figure 16 (a) A general view of the as-grown twinned ZnO structures, and (b) a magnified view of a symmetric twinned structure [174]. Reproduced with permission

and took (0001) as the common connection plane. For the latter case, the K^+ or Na^+ ions might act as a bridge between the ZnO_4^{6-} tetrahedral growth units, similar to the structure of mica [194]. In any case, the twinned structure is clearly favorable under specific reaction conditions [174].

3.4 Hierarchical structures

It is attractive to fabricate complex three-dimensional nanostructures with controlled morphology and orientation. Tian et al. demonstrated a strategic facial wet chemical method to synthesize well-controlled complex and oriented ZnO nanostructures [161]. Based on the conventional seeded growth of ZnO nanowires, they used citrate anion as capping agent, which has three negative charges and preferentially adsorbs onto the ZnO basal planes [160], which greatly inhibits the growth along the [0001] direction, resulting in the formation of thin nanoplatelets, as shown in Figs. 17(a)

and 17(b). The as-grown ZnO columnar nanoplatelets were remarkably similar to the nacreous plate structures in red abalone fish shown in Figs. 17(c) and 17(d).

In conjunction with citrate anions, diamines–such as ethylene diamine, diaminobutane, and diaminopropane —have also been used to direct the growth, leading to initiation of secondary nucleation on the ZnO nanowire side surfaces [195–198]. The growth mechanism was proposed to involve their effect on the solution pH and coordination with Zn^{2+} [198]. Similar secondary nucleation on the ZnO nanowire side surfaces has also recently been demonstrated by coating with another round of seed nanoparticles [199]. Since the diaminopropane molecules combine with water molecules and release hydroxide ions, the preferred adsorption of the diaminopropane molecules on the nanowire side surfaces is expected to raise the local pH value, which assists the formation of the first a few layers of ZnO clusters near the side surfaces. These nucleated clusters perform as seeds to initiate the following vertical growth of the secondary branches on the side surfaces of the primary nanowires. When a small amount of diaminopropane was used, sparse and tapered ZnO nanotips grew randomly. As the amount of diaminopropane was increased, dense and more organized tapered ZnO nanotips resulted, almost covering the entire side surfaces [195].

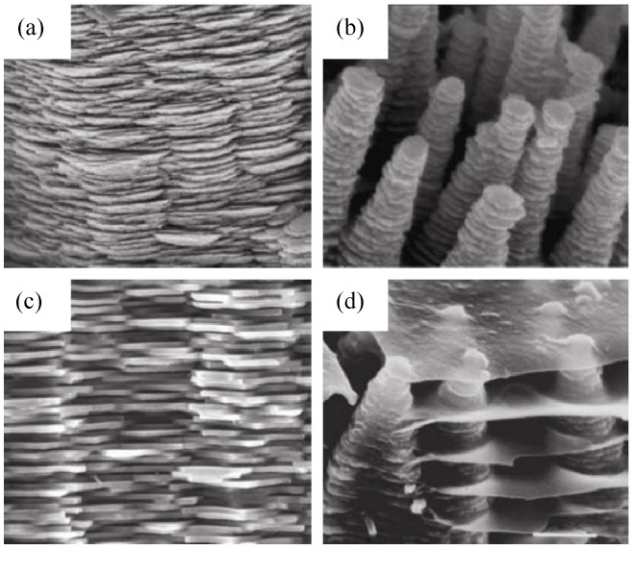

Figure 17 (a) Side view and (b) oblique view of oriented biomimetic ZnO columnar nanoplates, which resemble the (c) side view and (d) oblique view of the nacreous plate structures in red abalone fish [161]. Reproduced with permission

By rationally alternating the order of addition of the citrate and the diaminopropane, Zhang et al. have demonstrated a full capability to fabricate hierarchically oriented and ordered complex ZnO nanostructures step by step by wet chemical methods, as shown in Fig. 18 [195]. They conducted a series of systematic growth procedures to reveal the roles and the growth kinetics of these two organic structure-directing agents in the formation of secondary and tertiary ZnO nanoplates and nanobranches on selected facets of ZnO nanowires. As shown in Fig. 18(a), using the as-grown common vertical ZnO nanowires as the platform, when diaminopropane was added to initiate the secondary growth, side branches were nucleated all over the side surfaces of the hexagonal prism. Subsequently, using the as-grown secondary nanostructures, with citrate added to initiate tertiary growth, nanoplates formed on both the primary prism and the side branches. They also switched the sequence of addition of the two structure-directing agents, and the results were just as expected, as shown in Figs. 18(d)–18(f) [195].

Other hierarchical structures, such as microspheres composed of radial ZnO nanowire arrays, have also been made by thermolysis of zinc and ethylenediamine complex precursors in the presence of poly(sodium 4-styrenesulfonate) (PSS), as shown in Fig. 19(a) [200]. It was suggested that the growth process starts with the PSS stabilized colloidal nanoclusters. The nanoclusters later aggregate into larger secondary spherical particles in order to minimize their surface energy. Then these secondary spherical particles further collide and merge with each other to form multimers (e.g., dimers, trimers, etc) by random Brownian motion. By Ostwald ripening, the hollow hemispheres made of ZnO nanowire arrays were formed by dissolving small multimers. Liu et al. reported a different approach towards hollow spherical ZnO aggregates, as shown in Figs. 19(b) and 19(c) [201]. The self-assembly of ZnO hollow spherical structures was made by the coordination of CTAB, $Zn(NO_3)_2{\cdot}6H_2O$, and ethylenediamine. The initial oriented attachment of the nanorods to the central stems [202] was followed by the formation of complex multi-pod units, and finally the construction of spheres from the multi-pod units. In other words, this hierarchical organization process

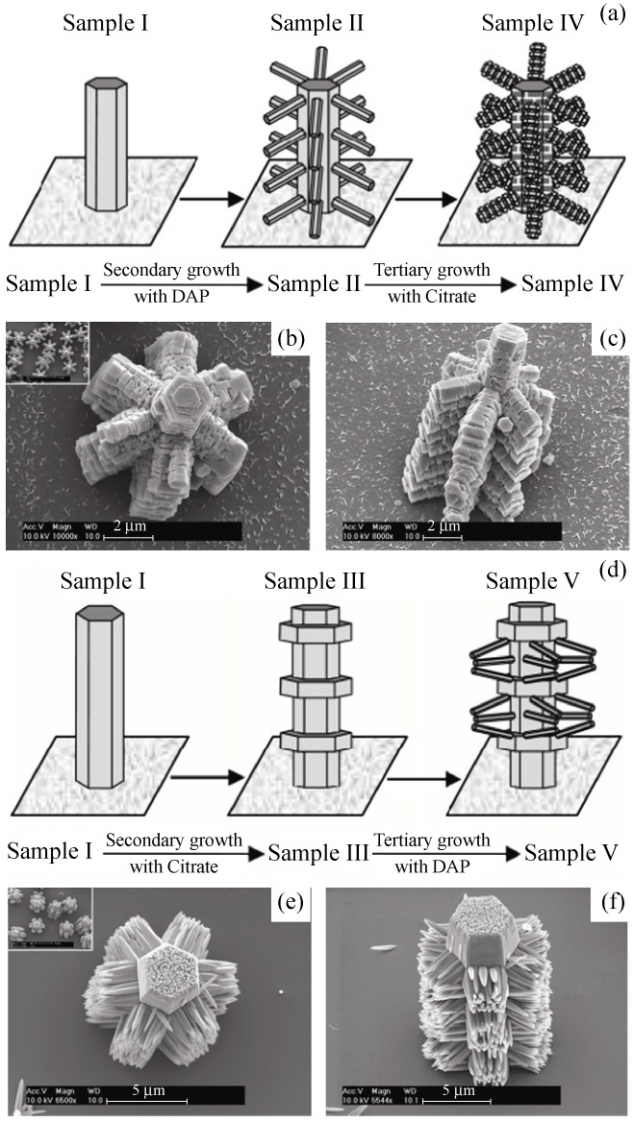

Figure 18 (a) Schematic illustration of the effect of consecutive addition of diaminopropane and citrate on the growth of hierarchical ZnO nanostructures, and (b) and (c) the corresponding SEM images of the as-grown nanostructures. (d) Schematic illustration of consecutive addition of citrate and diaminopropane on the growth of hierarchical ZnO nanostructures, and (e) and (f) the corresponding SEM images of the as-grown nanostructures [195]. Reproduced with permission

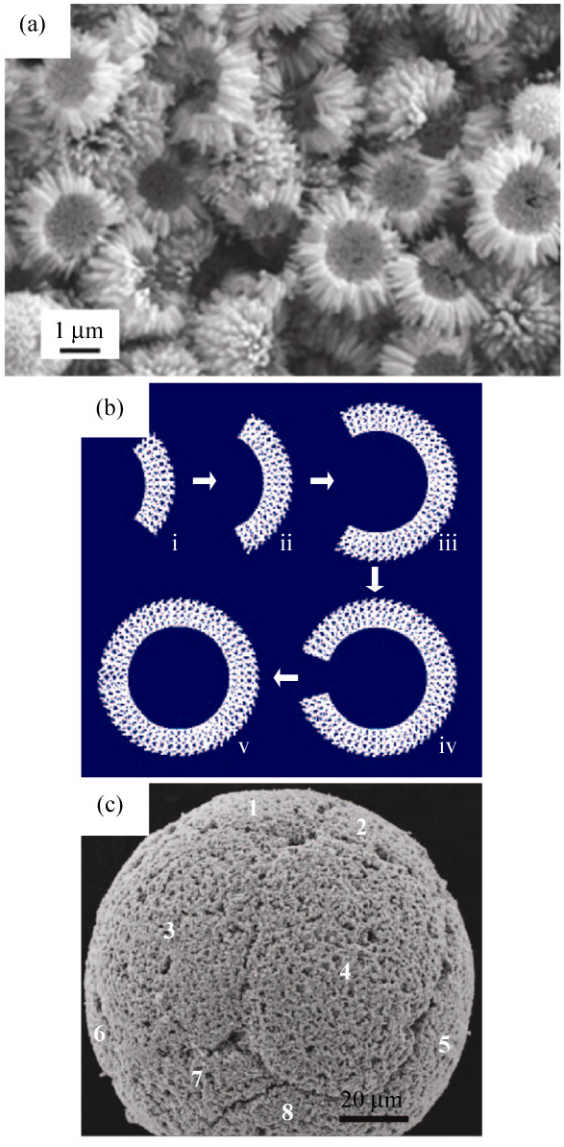

Figure 19 (a) SEM image of the hollow hemispheres self-assembled from ZnO nanowire arrays [200]. (b) Schematic illustration of the self-assembly process of the hollow microspheres, and (c) SEM image of a self-assembled hollow microsphere [201]. Reproduced with permission

started from the generation of ZnO nanorods, then the nanorods became aggregated into multipod units, and finally the multipod units aggregated into the hollow microspheres [201].

Besides microspheres, layered ZnO nanowire arrays have been formed by wet chemical methods. Chow et al. and Koh et al. presented a template-free self-assembly of densely packed bilayered ZnO nanowire arrays, as shown in Fig. 20(a) [203, 204]. In an alkaline environment, a thin layer of hydrotalcite-like zincowoodwardite plates was first formed as a result of the reaction between zinc and aluminum ions [203, 205, 206]. Zincowoodwardite belongs to a family of layered compounds with positively charged layers of Zn^{2+} and Al^{3+} with hydroxide anions, and interlayer charge-balancing anions SO_4^{2-}. It has a lattice constant of 3.076 Å in the basal plane which has about 5% lattice mismatch with the basal plane of the wurtzite

ZnO (3.249 Å). Therefore the hydrotalcite-like plates can provide an epitaxial substrate for the oriented growth of well-aligned ZnO nanowire arrays on both the top and the bottom surfaces. The size of the nanowires could be controlled by changing the pH value of the solution [203]. Heterogeneous nucleation on the hydrotalcite-like plates requires a low interfacial energy, and is more favorable than the homogeneous nucleation of ZnO nanowires in the bulk solution [203, 204]. Furthermore, delamination of the thin hydrotalcite-like plate at high temperatures produced free standing sheets of ZnO nanowire bundles [203]. Bilayer structured ZnO nanowire arrays were also formed by a ZnO thin film seeded growth method, as shown in Fig. 20(b) [207]. As the growth proceeded, growth nutrient was consumed, and the precursor concentration became dilute, which induced secondary growth and a decrease in the nanowire diameter and eventually the formation of bilayered structures [207].

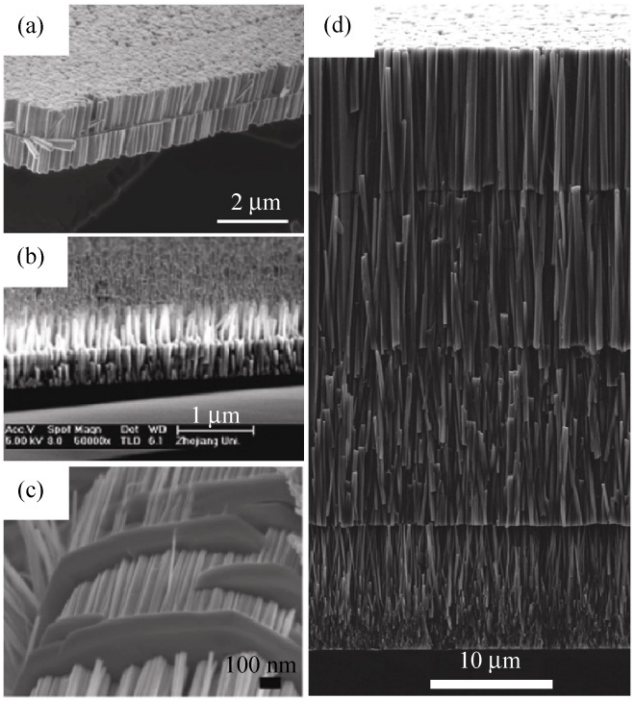

Figure 20 (a) SEM image of bilayered densely packed ZnO nanowire arrays on both sides of hydrotalcite-like zincowoodwardite plates [204]. (b) SEM image of bilayered ZnO nanowire arrays induced by secondary growth [207]. (c) SEM image of multilayered ZnO nanowire arrays sandwiched between parallel disks [208]. (d) SEM image of four-layered ZnO nanowire arrays [209]. Reproduced with permission

Li et al. demonstrated multilayered ZnO nanowire hierarchical structures, as shown in Fig. 20(c) [208]. The ZnO nanowire arrays were connected between parallel ZnO hexagonal disks. The reaction was conducted through a temperature-dependent multistep process. The precursor $[Zn(NH_3)_4]^{2+}$ underwent hydrolysis and dehydration to form nuclei for brucite-type polynuclear lamellar zinc hydroxide hexagonal disks, which later served as an intermediate substrate for the growth of ZnO nanowires. At the same time, as the temperature increased, the metastable zinc hydroxide disks dehydrated and transformed into ZnO disks. During dehydration, many regular nanosized ZnO islands were left on the disk surface, which seeded the secondary growth of ZnO nanowires, resulting in multicell sandwiches or nanowire–disk–nanowire–disk superlattices, as shown in Fig. 20(c) [208]. Most recently, Xu et al. demonstrated a novel technique for multilayer ZnO nanowire assemblies [209]. They coated a hydrophobic self-assembled monolayer (SAM) on the primary ZnO nanowires. Then by ultraviolet ozone treatment, the nanowire top surfaces were selectively exposed to refreshed solution resulting in additional growth, while the nanowire side surfaces were protected by the SAM from widening and fusing together. This process could be repeated multiple times, and a four-layer ZnO nanowire assembly was achieved as shown in Fig. 20(d). Finally, for device applications, all of the SAM coating could be removed by calcination.

Liu et al. demonstrated a templateless approach to grow hierarchical ZnO nanowire arrays with step-like heights on a common metallic zinc substrate [210] using equimolar $Zn(ClO_4)_2$ and *L*-cysteine solutions with a pH value of 10. The metallic zinc substrate was vertically immersed into the solution without sealing. The reaction took place at room temperature over 3 days. The solution gradually evaporated, and therefore the vertical Zn substrate was gradually exposed to the air from positions I to V, as illustrated in Fig. 21. The growth time of the ZnO nanowires in the solution increased from positions I to V, and therefore the nanowires had different lengths. The length of the ZnO nanowires showed a nearly linear relationship with the position on the Zn substrate. However, the reason for stepwise growth rather than a gradual increase of the nanowire length is not clear.

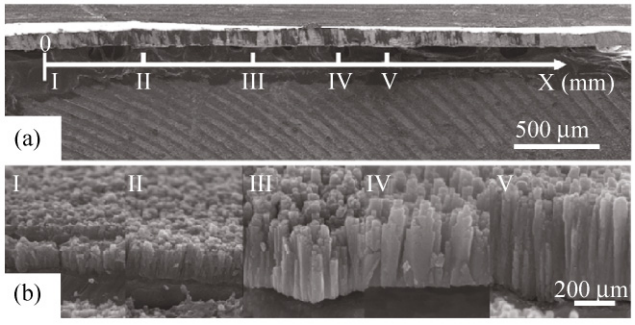

Figure 21 (a) Gradational growth of 1D ZnO nanowire arrays on a common zinc substrate from left to right, and (b) cross-sectional SEM images of the 1D ZnO nanowire arrays at five different locations [210]. Reproduced with permission

3.5 Heterostructures

Each single component material has its own functions and also limitations. For future multifunctional nanosystems, it is necessary to integrate many different materials in a rational manner. Heterostructures of nanomaterials are a preliminary step towards this application.

3.5.1 ZnO compound semiconductors

It is possible to passivate the surface dangling bonds of ZnO nanowires by coating with other compound semiconductors, such as CdSe [19, 211, 212] and CdTe [213] by electrodeposition, CdS [214], SnO_2 [215], MgO [216, 217], and ZrO [217] by hydrothermal reaction, Co_3O_4 [218] by photochemical reaction, ZnS [219, 220] by sulfidation, and Al_2O_3 [221] and TiO_2 [222] by atomic layer deposition (ALD). In most cases, the as-formed shell layers are polycrystalline or amorphous in nature.

CdSe was electrodeposited onto ZnO nanowires from an aqueous solution of $N(CH_2COOK)_3$, $CdSO_4$ and Na_2SeSO_3 at room temperature [211]. The $N(CH_2COOK)_3$ acted as a complexing agent whilst $CdSO_4$ and Na_2SeSO_3 were the sources of Cd and Se, respectively. During the electrodeposition, the ZnO nanowire sample was set to be the cathode, and Pt was the counter electrode. As shown in Fig. 22(a), the as-deposited CdSe layer uniformly covered the ZnO nanowires. The CdSe layer thickness could be increased by increasing the deposition current density and prolonging the deposition time [212]. X-ray diffraction studies showed the CdSe was polycrystalline in the cubic sphalerite phase [19]. Annealing should eliminate the organic components and also improve the shell crystallinity for further photovoltaic applications [19].

CdTe has a high optical absorption coefficient, a narrow band gap, and forms a typical type II band alignment with ZnO, which renders it an excellent inorganic semiconductor sensitizer for photovoltaic

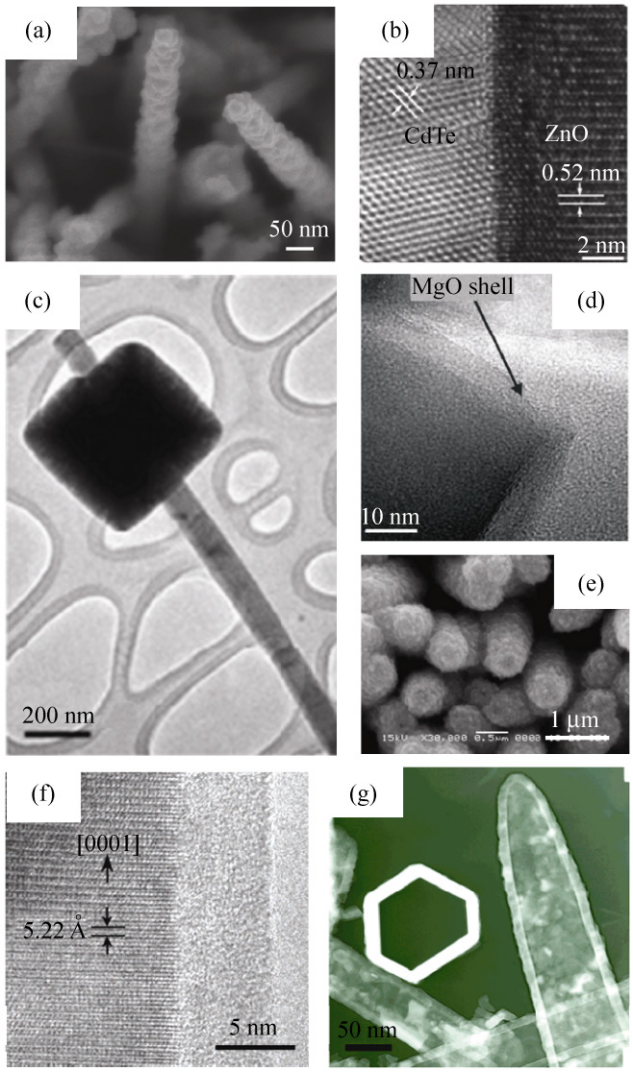

Figure 22 (a) Top view of ZnO nanowires covered with a CdSe thin film [211]. (b) HRTEM image taken from the ZnO/CdTe interface region, showing the well-crystallized structure of the CdTe layer [213]. (c) Low magnification TEM image showing SnO_2 capping a ZnO nanowire with the nanowire tip exposed [215]. (d) TEM image of a ZnO–MgO core–shell nanowire [216]. (e) SEM image of cable-like ZnS–ZnO nanowire structures [219]. (f) HRTEM image of the interface of a ZnO/Al_2O_3 core–shell nanowire [221]. (g) Negative TEM image of an anatase TiO_2 nanotube formed by etching away the ZnO nanowire core in 1 mol/L aqueous HCl [222]. Reproduced with permission

applications. The traditional reaction conditions for fabricating CdTe are too stringent to allow the presence of ZnO nanowires [223–226]. Wang et al. demonstrated the deposition of large-scale ZnO–CdTe core–shell nanowire arrays on indium-tin-oxide (ITO) substrates through a benign electrodeposition method (pH 8.3), which was compatible with the ZnO nanowires [213]. The electrodeposition was carried out with a three-electrode system, with the ZnO nanowire array as the working electrode, a standard calomel electrode (SCE) as the reference electrode, and a Pt foil as the counter electrode. The as-deposited CdTe shell was uniform in thickness, and could be tuned from several tens to hundreds of nanometers by changing the deposition time and the current density. As shown in Fig. 22(b), after deposition, an intact interface was formed between the single crystal ZnO nanowire core and the high crystallinity CdTe shell. XRD results showed that the CdTe shell had a zinc-blende structure, and the crystallinity could be further increased by annealing [213].

SnO_2 has a wide band gap of 3.6 eV. Indium or fluorine doped SnO_2 have been widely explored and used in industry as transparent electrodes. Shi et al. reported the capping of ZnO nanowires with doped SnO_2, which could act as the top electrode of the ZnO nanowires [215]. The wet chemical growth of the SnO_2 cap was conducted in a solution of $SnCl_4{\cdot}5H_2O$, ethanol, and distilled water with a pH of 12. Under such a high pH environment, the as-grown ZnO nanowires in the first step may have dissolved, and later reformed on the Zn substrate on which SnO_2 caps were formed, as shown in Fig. 22(c). The similar photoluminescence spectra of the ZnO nanowire arrays before and after the SnO_2 capping indicate that the electronic and optical qualities of the inner ZnO nanowire were not degraded after the secondary solution growth. From the cathode luminescence spectrum, the near-band-edge emission was enhanced and the defective deep level emission was suppressed after the capping. SnO_2 has a larger band gap than ZnO, which confines the electrons/holes in the ZnO nanowires more efficiently and thus leads to high internal quantum efficiency. In addition, the surface states of the ZnO nanowires (dangling bonds and/or surface defects) could be partially reduced via the capping surface passivation. The cap/nanowire configuration also allowed a direct measurement on the single nanowire junction (Zn/ZnO/SnO_2). The *I*–*V* curve indicated there was a small barrier between the Zn substrate and the ZnO nanowire, and the SnO_2/ZnO interface did not introduce any barrier [215]. In contrast, using SnO_2 nanowires prepared by vapor phase deposition, Cheng et al. reported the seeded growth of ZnO/SnO_2 nanowires and, interestingly, random lasing behavior was observed from the heterostructures [227].

Plank et al. demonstrated a low temperature wet chemical method to coat a MgO shell layer onto ZnO nanowires that did not require a subsequent high temperature annealing [216]. In their process, the ZnO–MgO core–shell nanowire structures were fabricated by submerging the ZnO nanowires in a mixed solution of $Mg(NO_3)_2$ and NaOH. The thickness of the as-coated MgO layer could be controlled up to 8 nm, as shown by the TEM image in Fig. 22(d) [216]. Electrons could efficiently tunnel through the "insulating" MgO shell. The ZnO–MgO core–shell nanowires showed an enhanced efficiency in hybrid photovoltaic devices by enhancing the photoinduced charge generation [217] and the photocurrent and open circuit voltage [216]. Similarly, a ZrO_2 shell could also be deposited on the ZnO nanowires by replacing the magnesium nitrate with zirconium acetate as precursor [217].

The synthesis of sulfide compounds is usually challenging, and a strongly reducing environment is required, because sulfides are easily oxidized into oxides. Wang et al. demonstrated a wet chemical approach to fabricate ZnO–ZnS core–shell nanowire arrays by secondary sulfidation of ZnO nanowires [219]. In their method, they simply immersed the as-grown ZnO nanowire arrays in a Teflon autoclave containing an aqueous solution of thioacetamide. By controlling the reaction time, the product could be controlled to be pure ZnS nanotube arrays or ZnO–ZnS nanocables with various ZnO-to-ZnS ratios. The growth mechanism was suggested to be non-epitaxial, and involve ion exchange processes [228, 229]. The as-coated ZnS shell had a cubic structure and, as can be seen from Fig. 22(e), the substantial surface roughness of the ZnS indicated it was polycrystalline. This method could be modified and extended to the preparation of other semiconductor compounds that are also sensitive to oxygen, such as ZnSe and CdS [219].

In addition, wet chemically grown ZnO nanowires could also be used as a sacrificial template for the growth of other nanostructures, such as ZnS by vapor phase sulfidation via an ion exchange reaction [229], an Al_2O_3 thin layer by thermal annealing of an $AlCl_3$ solution [221] or ALD [222], a TiO_2 thin layer by sol–gel methods [222, 230, 231], and ZnS and ZnSe nanoparticles by wet chemical synthesis [232]. The ZnO core can subsequently be removed, and a tubular structure of such deposited layers can be prepared, as shown in Figs. 22(f) and 22(g).

3.5.2 ZnO–metals

Semiconductor–metal heterostructures exhibit many interesting chemical, optical, and electronic properties that have found various applications in catalysis, biomedicine, photonics, and optoelectronics [233]. In particular, noble metal nanoparticle-decorated semiconductor nanowires possess several merits. First is the surface enhanced Raman scattering effect due to a high density of hot spots on the surface of the semiconductor nanowires [234, 235]. Also, the decoration of Ag, Au, Pt, or Co onto the ZnO nanowire surfaces changes the Fermi level equilibrium and band structure of the ZnO through storing and shuttling photogenerated electrons from the ZnO to acceptors in photocatalytic processes [137, 236, 237]. In addition, the photocatalytic efficiency is generally limited by the fast recombination of the photogenerated electron–hole pairs. But in the semiconductor–metal heterostructures, the photogenerated carriers will be trapped by the noble metal, which promotes interfacial charge-transfer processes and increases the carrier lifetime [238].

Pacholski et al. reported site-specific deposition of Ag nanoparticles onto ZnO nanorods by a photocatalytic wet chemical method, as shown in Fig. 23(a) [238]. The growth solution was composed of $AgNO_3$ solution and well-dispersed ZnO nanorods. Under illumination by ultraviolet light, electrons and holes were separated in the ZnO nanorods. The electrons reacted with the absorbed Ag^+ ions reduced them to Ag, and the holes concomitantly oxidized the alcohol molecules in the solution. The Ag nanoparticles grown by photoreduction were preferentially located at one end of the ZnO nanorods probably because of a preferentially small lattice mismatch between Ag and ZnO in the particular crystallographic planes as evidenced by HRTEM studies. Once an Ag nucleus was formed on the ZnO nanorod, it acts as a seed for the further photocatalytic reduction of Ag, and thus more nuclei were prevented from forming on one ZnO nanorod. An inbuilt Schottky barrier was suggested at the ZnO/Ag interface. Raman enhancement was observed in the Ag nanoparticles on ZnO nanowire arrays [92].

As the opposite process to the secondary growth of Ag nanoparticles on ZnO nanorods, Fan et al. demonstrated the secondary growth of ZnO nanorods onto the {111} facets of Ag truncated nanocubes by a wet chemical method, as shown in Fig. 23(b) [239]. Using Ag nanocubes as the nano-substrate, ZnO selectively nucleated and grew on the eight {111} facets. Due to spatial confinement, only seven branches of ZnO nanorods at most were observed. This growth mechanism was suggested to result from two factors. First is a low lattice and symmetry mismatch (2.68%) between the ZnO $(2\bar{1}\bar{1}0)$ spacing (d = 0.1625 nm) and the Ag $(\bar{1}12)$ spacing (d = 0.16697 nm). The other is the direct interface of the Zn layer with Ag that initiates the formation of the ZnO lattice. Convergent beam electron diffraction studies showed that Zn atoms were the first layer bonded to the surface of the Ag seeds and the growth front of the nanorod was an oxygen layer [239].

In addition to Ag, Au nanoparticles have also been decorated onto ZnO nanowires by wet chemical methods. Au has excellent chemical stability, biocompatibility, and capability of near infrared excitation [240]. Liu et al. used a mixture of sodium citrate, ascorbic acid, and $HAuCl_4$ reacted at room temperature for 5 min [130]. The as-synthesized Au nanoparticles were about 5–25 nm in diameter, and were well dispersed on the surface of the ZnO nanowires, as shown in Fig. 23(c). The Au-modified ZnO nanowires showed a distinct color change from the bare ones, which is consistent with a surface plasma resonance peak of Au at about 530 nm. In addition to wet chemical syntheses, He et al. have described a novel approach to decorate ZnO nanowires with Au nanoparticles by electrophoretic deposition [241]. The basic working principle of electrophoretic deposition is that charged nanoparticles (in a colloidal solution) will be

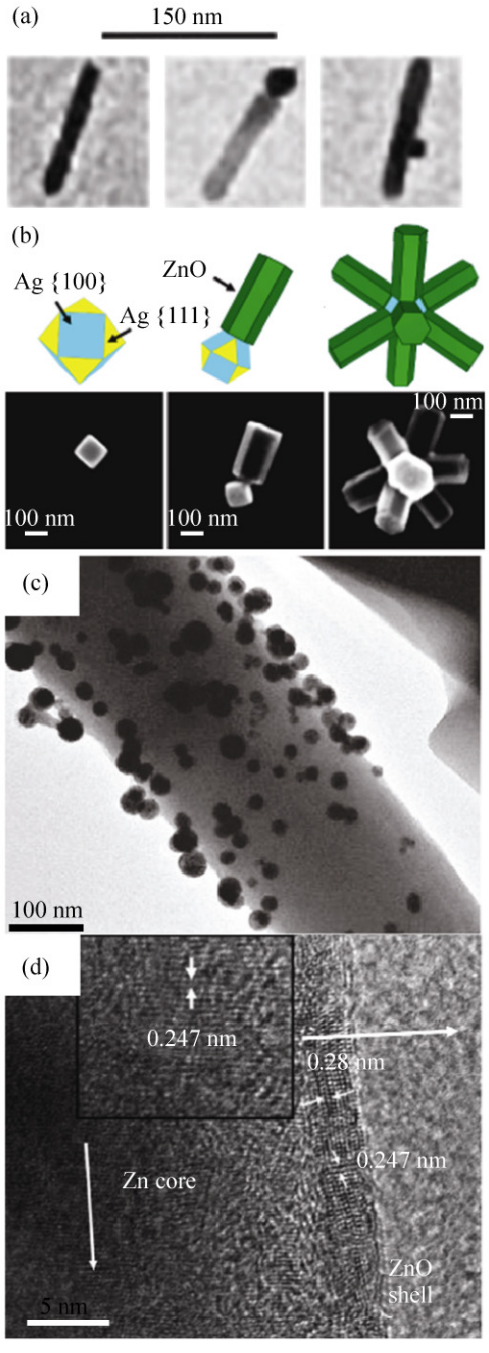

Figure 23 (a) TEM images showing ZnO nanorods with deposited Ag nanoparticles at different locations of the nanorod [238]. (b) SEM images showing the selective growth of ZnO nanowire branches on the {111} facets of Ag truncated nanocubes, where the yellow and cyan planes represent the {111} and {100} facets of Ag, respectively; the green planes represent the facets of the ZnO nanowires [239]. (c) Low magnification TEM image of a Au-decorated ZnO nanowire [241]. (d) HRTEM image of a coaxial Zn–ZnO core–shell nanorod [244]. Reproduced with permission

driven to deposit on the target substrate under an external electric field. In their experiment, the gold colloidal solution was made by laser ablation of a gold target in water, which produced Au nanoparticles with fresh surfaces [242]. Then the ZnO nanorod array was immersed into the Au colloidal solution and used as the anode for the electrophoretic deposition. HRTEM studies revealed that the Au nanoparticles had good interfacial connection with the ZnO nanorods which is probably due to the strong van der Waals forces. Also, Au nanoparticles preferentially attach to the basal planes of ZnO since the interfacial energy between metal and polar surfaces is lower than that between metal and nonpolar surfaces [243]. Such Au-decorated ZnO nanowire arrays demonstrated very strong surface enhanced Raman spectroscopy activity due to the coupling effect between the Au nanoparticles and the ZnO nanowires [241]. In addition to post-treatment techniques, Shen et al. have reported a simple and mild solvothermal approach to co-precipitate a ZnO–Au heterostructure by virtue of the low lattice mismatch between the ZnO (0001) planes and the Au {111} planes [137].

Besides ZnO–noble metal heterostructures, 1D Zn–ZnO core–shell heterostructures have been obtained by a low temperature solvothermal approach [244]. As shown in Fig. 23(d), well-crystallized wurtzite ZnO was epitaxially grown along the [0100] direction, which is perpendicular to the [0002] direction along which the single crystalline Zn core was grown. The epitaxial relationship followed [0002]Zn/[0100]ZnO, and there were defects at the interface to accommodate the lattice mismatch [244].

3.5.3 *ZnO–carbon nanotubes*

Zhang et al. have demonstrated the fabrication of a ZnO nanowire/carbon nanotube heterostructure by hydrothermal synthesis, as shown in Fig. 24 [245]. In their method, a thin film of ZnO seed layer was pre-coated on vertically aligned carbon nanotubes by radio frequency (r.f.) sputtering or ALD [246]. After sputtering, the carbon nanotubes preserved their vertical alignment. The growth solution was made up of saturated $Zn(OH)_4^{2-}$ formed by dissolving ZnO in NaOH aqueous solution. The as-grown high density of ZnO nanowires on the carbon nanotube arrays

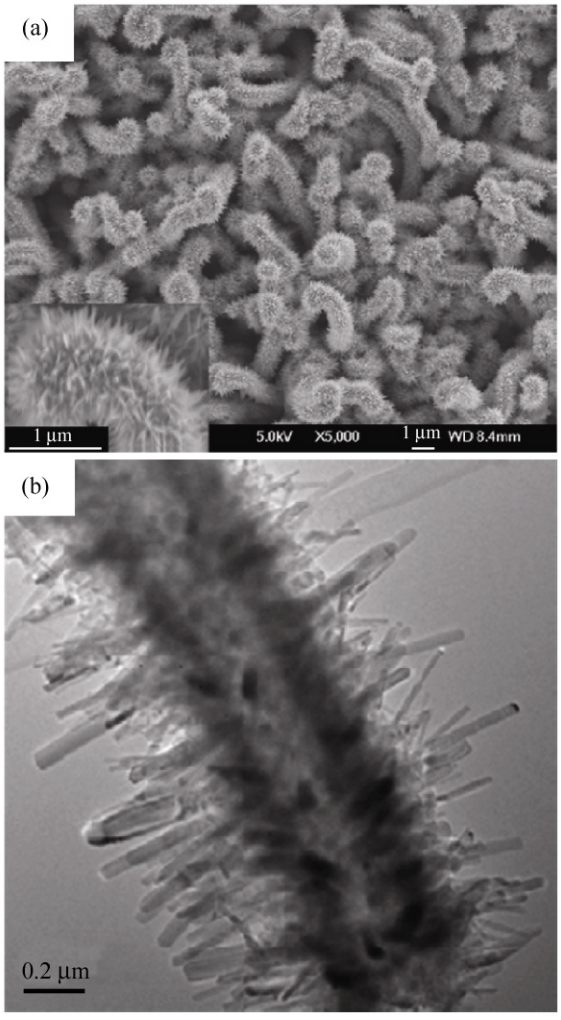

Figure 24 (a) Top view SEM image of ZnO nanowire–carbon nanotube heterostructures, and (b) TEM image showing the morphology of the radial ZnO nanowires on carbon nanotubes [245]. Reproduced with permission

showed greater surface to volume ratio than the ZnO nanowires grown on flat substrates. Moreover, the thin ZnO seed layer provided a continuous pathway for carrier transport for electronic applications [245, 247]. In another report [203], a thin layer of Al was coated onto carbon nanotube so that a hydrotalcite-like zinc aluminum hydroxide interfacial compound formed [205, 206], which was very effective in promoting the growth of ZnO nanorods.

4 Rational doping and alloying

Doping and alloying are the primary techniques to control the physical properties of semiconductor nanomaterials, such as electrical conductivity, conductivity type, band gap, and ferromagnetism [86].

4.1 *n*-type doping

ZnO nanowires are intrinsically *n*-type due to the inevitable point defects, such as oxygen vacancies and zinc interstitials. It is possible to substitute and thus reduce these defects by doping elements with similar electronegativities. Cui et al. used ammonium chloride to alter the growth properties of ZnO nanowires by electrochemical deposition [119]. They used an aqueous solution of $Zn(NO_3)_2{\cdot}6H_2O$, HMTA, and NH_4Cl as the precursor. The successful doping of chloride into the ZnO nanowires was confirmed by compositional and structural analysis. The chloride-doped ZnO nanowires had larger diameters with reduced lengths. Photoluminescence studies demonstrated that the chlorine doping had two main effects. First was the reduced number of oxygen-related defects during ZnO growth. As shown in Fig. 25, the intensity of the visible broad band at around 530 nm, originating from the emission of point defects, was gradually reduced as the concentration of the chloride ions in the precursor was increased, which indicates chloride helped to reduce the number of oxygen vacancies in ZnO nanowires. This phenomenon might be interpreted by considering the saturation of the growth surface by chloride, which limited the evolution of oxygen

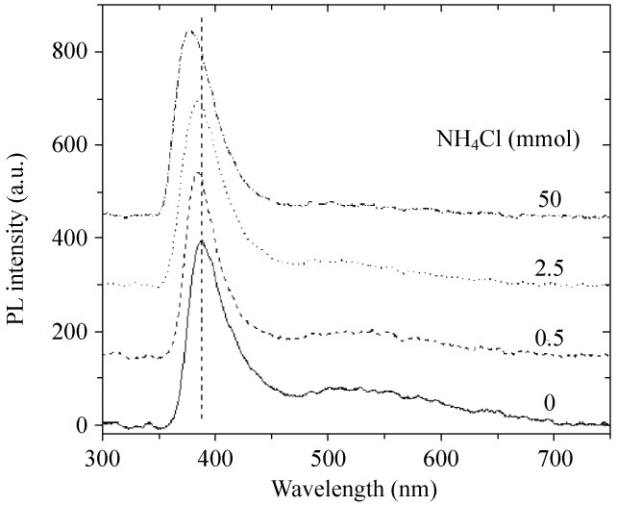

Figure 25 Photoluminescence spectra excited by a 248 nm laser of ZnO nanowires with different amount of chloride doping [119]. Reproduced with permission

vacancies in ZnO. Second, a blue-shift of ~10 nm of the band-edge emission peak at 385 nm was observed as the amount of chloride was raised from 0 to 50 mmol in the growth solution, which indicates a widening of the band gap in ZnO nanowires, which was attributed to the blocking of the lowest states in the conduction band [119, 248].

Electrochemical deposition has been shown to be a powerful technique to dope ZnO nanowires. Beside chloride, Al-doped ZnO nanowire arrays have been fabricated by introducing $AlCl_3$ [249], $Al(NO_3)_3{\cdot}9H_2O$ [250], or $Al_2O_{12}S_3$ [118] into the electrolyte. Microprobe analysis confirmed the incorporation of Al into the ZnO nanowires. The size of the ZnO nanowires could also be changed by tuning the Al^{3+} ion concentration in the electrolyte. After Al doping, it was found that the ZnO nanowires had higher electron mobilities and better conductivity in comparison with common undoped ZnO nanowires [118, 249], even though there was also a band gap widening after Al doping [119]. In addition, Al doping was also shown to have a effect on the mechanical and piezoelectric properties of ZnO nanowires as characterized by scanning probe microscopy [250].

4.2 *p*-type doping

It is highly desirable to make stable and reproducible *p*-type ZnO for fabricating ZnO homojunction optoelectronic devices, and this area still remains challenging and controversial [251]. Basically, to make *p*-type ZnO nanowires, group-V or group-I element atoms are needed to react and then diffuse through the defects of ZnO to replace oxygen or zinc atoms in ZnO. There have been many efforts using both vapor phase [252, 253] and solution phase growth approaches [254]. For example, *p*-type doping of ZnO nanowire arrays has been reported by post-treatment of as-grown *n*-type ZnO nanowires, such as using NH_3 plasma treatment [255], and thermal deposition and diffusion of As from GaAs wafers [256].

Utilizing a wet chemical method, Hsu et al. demonstrated intrinsic *p*-type ZnO nanowires [254]. In their report, *p*-type or *n*-type ZnO nanowires could be grown from the same growth solution at 90 ℃, and the key to controlling the conductivity type was found to be the preparation of the seed layer. ZnO nanowires fabricated on an electrodeposition seed layer exhibited *n*-type behavior, whilst those on zinc acetate derived seed layers showed *p*-type behavior. The difference in the conductivity type were attributed to several factors, such as the dependency of native defect concentrations, the different concentrations of zinc vacancies, and the different incorporation of compensating donor defects, like hydrogen and indium atoms. In their study, the as-grown *p*-type ZnO nanowires on the *n*-type seed layer homojunctions were characterized by many different techniques, such as measuring the current an capacitance dependence on the voltage and electrochemical impedance spectroscopy (EIS) measurements, as shown in Fig. 26. The presence of zinc vacancy related defects was confirmed by positron annihilation spectroscopy measurements.

The estimated hole concentration was on the order of 10^{17} cm^{-3} and was stable over a period of six weeks. More importantly, room temperature electroluminescence has been demonstrated based on homojunction and heterojunction light emitting diodes (LEDs) containing the as-grown *p*-type ZnO nanowires [254].

4.3 Transition metal doping

Transition metal doped dilute magnetic semiconductors are of particular research interest for potential applications in spintronic devices and visible light photocatalysis. A few studies have been reported of the synthesis and characterization of ZnO nanowires doped with different transition metal ions, like Co, Ni, Mn, Cu, Fe, and Ag [86, 257, 258].

Simple addition of transition metal precursors into the ZnO nanowire growth solution does not necessary result in incorporation of transition metal atoms in ZnO nanowires. Cui et al. demonstrated a low temperature electrochemical deposition of Co and Ni doped ZnO nanowire arrays [120, 259]. In their recipe, cobalt or nickel nitrate was added to the conventional ZnO nanowire growth solution, under a negative potential of 0.8 V relative to a gold reference electrode. Quantitative energy-dispersive X-ray (EDX) spectral analysis showed concentrations of 1.7% Co and 2.2% Ni in the nanowires. In contrast, when no potential was applied, there was no measurable doping by Co

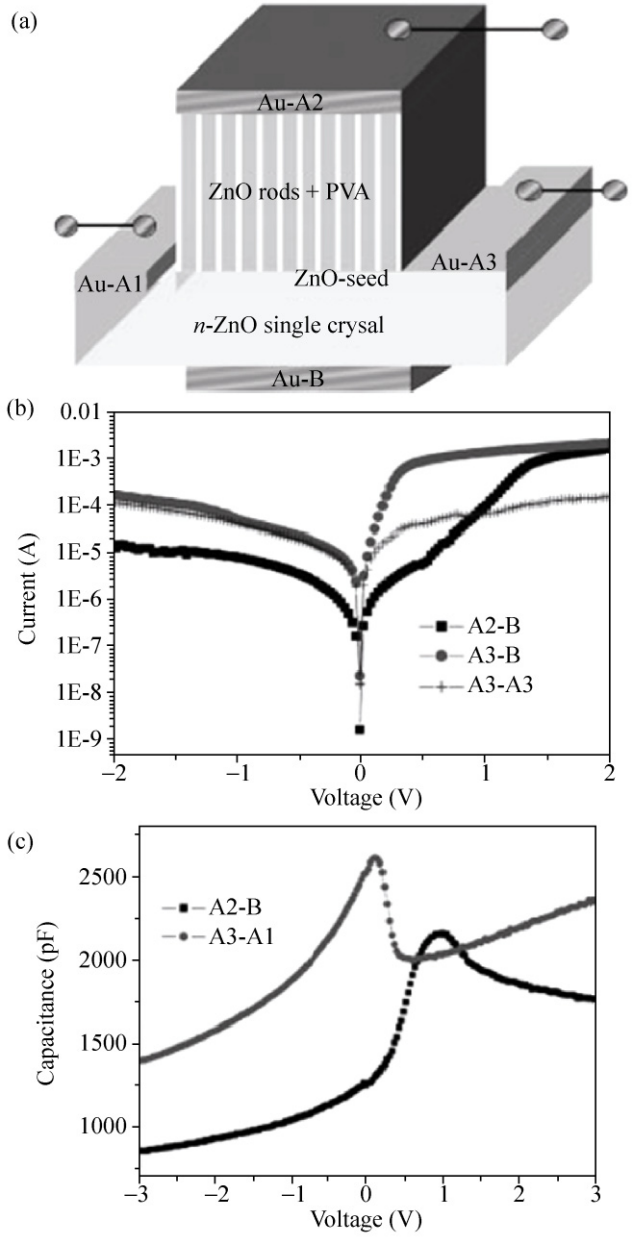

Figure 26 Capacitance-voltage measurements for ZnO nanowires grown with different seed layers. (a) Schematic device structure. (b) *I–V* curves. (c) *C–V* curves for the seed and rods [254]. Reproduced with permission

or Ni. Thus, the applied potential is critical, and it was suggested to adjust the interfacial energy and reduce the energy barrier for the incorporation of Co and Ni into the ZnO nanowires. XRD studies showed that after Co or Ni doping, the wurtzite structure of ZnO did not change, but the lattice expanded as evidenced from the shift in the (002) diffraction peak position. Room temperature anisotropic ferromagnetism was observed in both Co and Ni-doped ZnO nanowire arrays, whereas undoped ZnO nanowires have paramagnetic behavior. As shown in Fig. 27, there was a hysteresis loop for the Ni-doped ZnO nanowires when the magnetic field was applied parallel or perpendicular to the nanowire *c* axis. The orientation of the easy magnetization axis could be parallel or perpendicular to the nanowire *c* axis, and it was suggested to be dependent on the aspect ratio and density of the nanowires [120]. Annealing of the doped nanowires would help rearrange the dopants and enhance the magnetization. But when the annealing temperature was too high, it led to precipitation and clustering of the dopant atoms [260].

The Co-doped ZnO nanowires had interesting optical properties. When excited with ultraviolet light, both the near-band-edge emission and the defect emission peaks diminished in intensity after cobalt inclusion in the pristine ZnO nanowires. In addition, the peak centered at 680 nm in the photoluminescence spectrum corresponds to the transition from $^4T_1(P)$ to $^4A_2(F)$ of tetrahedrally coordinated Co^{2+} ions in the ZnO lattice, which indicates the substitution of Zn^{2+} by Co^{2+} [258]. The local dopant coordination environments were studied by X-ray diffraction and absorption spectroscopy [261]. The results showed that the transition metal doped ZnO nanowires were single crystal, single domain, and single phase in nature. The dopant ions were in a uniform environment which

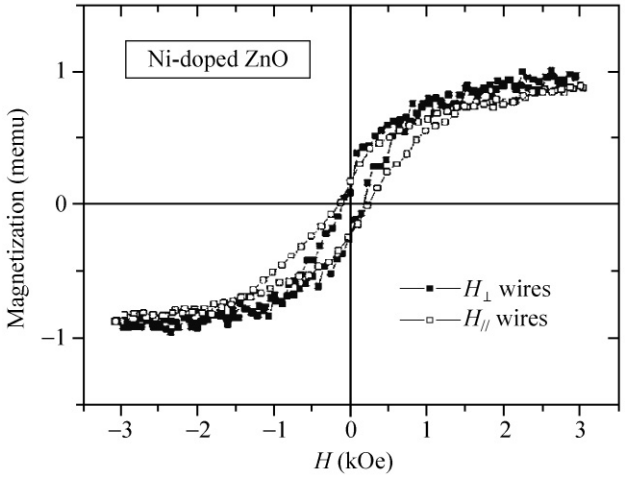

Figure 27 Magnetization hysteresis loop of Ni-doped ZnO nanowires with the applied magnetic field perpendicular and parallel to the nanowire *c* axis [120]. Reproduced with permission

did not induce a large degree of disorder in the nanowires. This homogeneous and uniform doping of the transition metal ions correlated with the weak ferromagnetic behavior of the nanowires [261]. Electron transport measurements on single Co-doped ZnO nanowires showed that the electron mobility could be as high as 75 $cm^2/(V \cdot s)$ [262]. Magnetotransport measurements showed that the magnetoresistivity was positive at low magnetic field due to the *s–d* exchange induced spin splitting of the conduction band, and was negative at high magnetic field due to suppression of weak localization of impurity centers [262].

4.4 Alloying

Band gap engineering of ZnO by alloying ZnO (E_g = 3.37 eV) with MgO (E_g = 7.7 eV) to form $Zn_{1-x}Mg_xO$ alloys is an attractive approach for electronic and optoelectronic applications. Usually ZnO has a wurtzite hexagonal structure with a lattice parameter of a = 0.32 and c = 0.52 nm (cubic ZnO is very rare), while MgO has a cubic structure (a = 0.42 nm). Thus, alloying wurtzite ZnO with cubic MgO results in metastable wurtzite ($x > 0.49$) or zinc blende ($x < 0.5$) structures. Traditionally, $Zn_{1-x}Mg_xO$ nanostructures are made using vapor phase approaches, such as metallorganic vapour phase epitaxy (MOVPE), metal oxide chemical vapor deposition (MOCVD), and PLD. Gayen et al. reported the growth of aligned $Zn_{1-x}Mg_xO$ ($0 < x < 0.2$) nanowires by a wet chemical route on seeded glass substrates [263]. The aqueous solution was composed of $Zn(NO_3)_2$, $Mg(NO_3)_2$, and NaOH. By assuming the percentage of Mg in the as-grown $Zn_{1-x}Mg_xO$ nanowires was proportional to the percentage of Mg in the precursor [264], the results showed that changing the amount of $Mg(NO_3)_2$ relative to $Zn(NO_3)_2$ readily changed the value of x in the $Zn_{1-x}Mg_xO$ alloy. As shown in Fig. 28, on increasing the amount of Mg in the precursor solution, the aspect ratio of the alloyed nanowires increased significantly. XRD studies showed that the as-synthesized $Zn_{1-x}Mg_xO$ nanowires were of single phase without phase separation. The value of E_g changed from 3.14 to 3.75 eV as the Mg content was varied between 0.05 and 0.20 [263].

Shimpi et al. reported a two-step method for fabrication of uniform and large scale ZnO:MgO nanowire arrays without post-annealing. In their method, common ZnO nanowire arrays were immersed into an aqueous solution of $Zn(NO_3)_2 \cdot 6H_2O$, HMTA, and $Mg(NO_3)_2 \cdot 6H_2O$ in a 1:1:2 ratio, at a growth temperature of 155 °C for 4 h. In the photoluminescence spectra, ZnO:MgO nanowires showed a blue-shifted near-band-edge UV emission at both room temperature and low temperature, relative to the pristine ZnO nanowires [265].

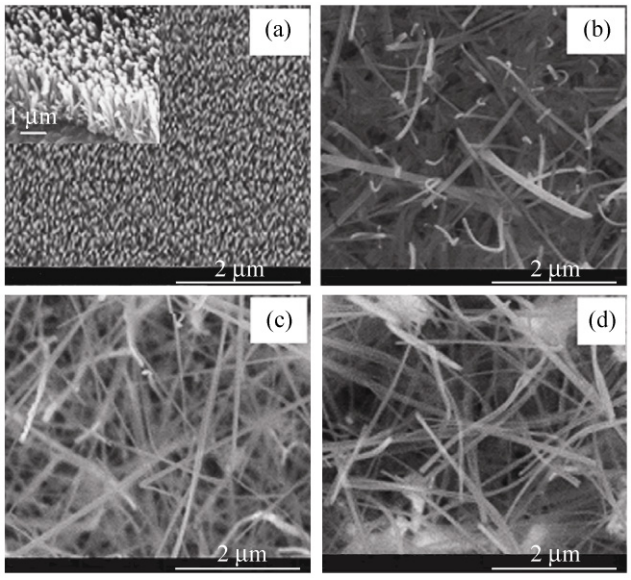

Figure 28 SEM images of $Zn_{1-x}Mg_xO$ ($0 < x < 0.2$) nanowire arrays grown on seeded glass substrates with (a) x = 0, (b) x = 0.05, (c) x = 0.1, and (d) x = 0.2 [263]. Reproduced with permission

5. Patterned growth

It is interesting and essential to manipulate the building blocks into a regular form for future advanced nanodevices. Here we will discuss various strategies for defining the spatial distribution of ZnO nanowires on a substrate, including photolithography, electron beam lithography, interference lithography, nanosphere lithography, nanoimprint lithography, micro-contact printing, and inkjet printing. Finally we will also discuss the feasibility of pattern transfer.

5.1 Photolithography

Photolithography basically employs UV light to transfer a geometric pattern from a mask to photosensitive materials on the substrate [266]. In a typical process, first the substrate is spin-coated with a layer of

photosensitive material (e.g., photoresist), and then is exposed to UV light under a patterned photomask. The pattern on the photomask is usually generated by electron beam lithography, and the opaque area on the mask is covered by a metal, such as Cr. The subsequent step is to develop the exposed photoresist, which could be positive tone or negative tone. For a positive tone photoresist, high energy UV photons break up the chemical bonds and scissor the long polymer chains of the photoresist into short pieces. Therefore the area which has been exposed to UV light has a higher solubility in the developer than the area which has not. In contrast, for a negative tone photoresist, UV photons provide energy to overcome the energy barrier of forming new chemical bonds crosslinking the side chains of the small monomer molecules producing larger molecules that have a lower solubility in the developer than the original monomer molecules. In either case, the photoresist is selectively dissolved away and the local substrate underneath is exposed. In this way, a pattern is copied onto the substrate from a photomask that is reusable.

Tak et al. combined a photolithography procedure and a wet chemical method to grow patterned ZnO nanowire arrays [77]. The advantage of this technique is that the patterns can be made on a square inch scale in one batch, which results in high throughput and low cost. The wavelength of the UV light, however, is normally hundreds of nanometers, and therefore the feature size of the pattern is limited to the micrometer range, which gives rise to very dense nanowire arrays growing out of one spot on seeded substrates [77, 99]. On a patterned substrate, the growth rate of the nanowires was shown to be inversely proportional to the nanowire density [267, 268], simply because the growth nutrient was shared between the competing nanowires. Also, the as-grown nanowires were not straight or uniformly oriented on seeded substrate [77], even though well-controlled ZnO nanowire arrays were grown on GaN substrates using photolithography with one or two nanowires growing out of one spot [269].

Photolithography could also be realized without a photoresist by using photosurface functionalization [270, 271]. Morin et al. demonstrated patterned growth of ZnO nanowire arrays on photosensitive polymers, such as commercial polycarbonate and polyester [271]. As shown in Fig. 29(a), the polycarbonate surface could be oxidized and grafted with carboxylic acid groups [272] or sulfate anion groups [273] where it was exposed to UV light in air, which was confirmed by fluorescence microscopy imaging [271]. The acidic groups could be further converted into hydroxyl groups by a simple hydrolysis [273]. The carboxylic acid groups generate a local acidic environment and thus suppress the nucleation and growth of ZnO nanowires. Without developing, the patterned polymer surface can directly be used to grow ZnO nanowire arrays by a wet chemical method. As shown in Fig. 29(b), well-organized ZnO nanowire arrays were grown on the unexposed polymer surfaces [271].

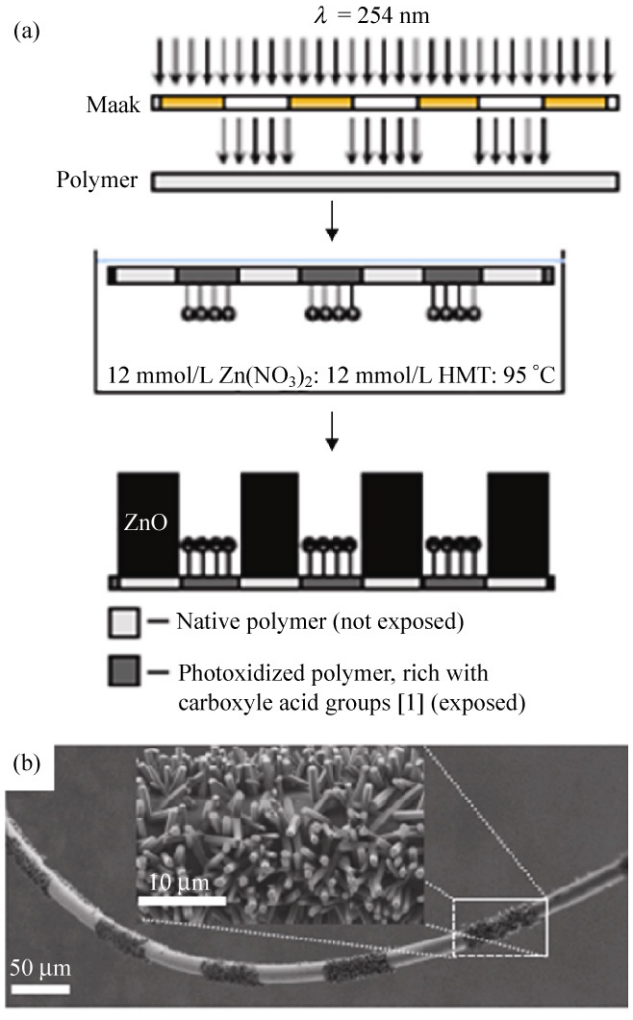

Figure 29 (a) Schematic flow chart of the use of UV oxidation to pattern a polycarbonate surface by photolithography, and (b) a SEM image of the as-grown ZnO nanowire arrays on the patterned polyester filament surface [271]. Reproduced with permission

5.2 Electron beam lithography

Since photolithography has a bottleneck arising from the diffraction limit of UV light, a combination of electron beam lithography and a wet chemical growth method has been developed [48]. Electrons are accelerated by tens of kilovolts and have a wavelength on the order of Ångstroms, which gives a much higher resolution than conventional photolithography [274]. The growth mask can be a polymer resist, e.g., polymethyl methacrylate (PMMA), or any inert material, e.g., SiO_2 [146].

The non-epitaxial growth of ZnO nanowire arrays on Si wafers (or any other inorganic/polymer substrates) can be assisted by a thin film of ZnO seed [48, 275]. Even though it had been annealed, the seed film was still composed of many tiny crystals several nanometers to tens of nanometers in size with random in-plane orientations. The opening size patterned by electron beam lithography was around 100 nm, in which there were a number of seed grains exposed [48]. Each seed grain can give rise to one nanowire. Consequently in most cases, multiple nanowires grow out of one single patterned opening, as shown in Fig. 30(a). Interesting, by increasing the growth temperature from 70 ˚C to 95 ˚C, the multiple nanowires from one single opening merge together and form a thicker nanowire (Fig. 30(b)), probably due to the fact that ZnO nanowires in close proximity are inclined to coalesce with each other [67, 72, 276].

Employing the epitaxial relation between ZnO and GaN, well-aligned ZnO nanowire arrays have been realized, as shown in Figs. 30(c)–30(f) [48]. Single crystal ZnO wafers with or without metallic Ru thin film coating have also been used to grow well-aligned ZnO nanowire arrays [277]. The as-grown nanowires exhibited a remarkable vertical alignment and uniformity in diameter and length. By X-ray diffraction rocking curve measurements, θ–2θ scanning showed a full width at half maximum value of only 0.15° [48]. It should be noted, that because the as-grown nanowires have a small diameter, a large aspect ratio, and possibly a weak connection to the substrate, the sample had to be dried in supercritical fluid to preserve the ordered alignment [278]. Otherwise, the residue solution droplets on the nanowires gradually evaporated away and shrank in size, and the surface tension of the droplet bundled the nanowires together or swept them all down onto the substrate [279].

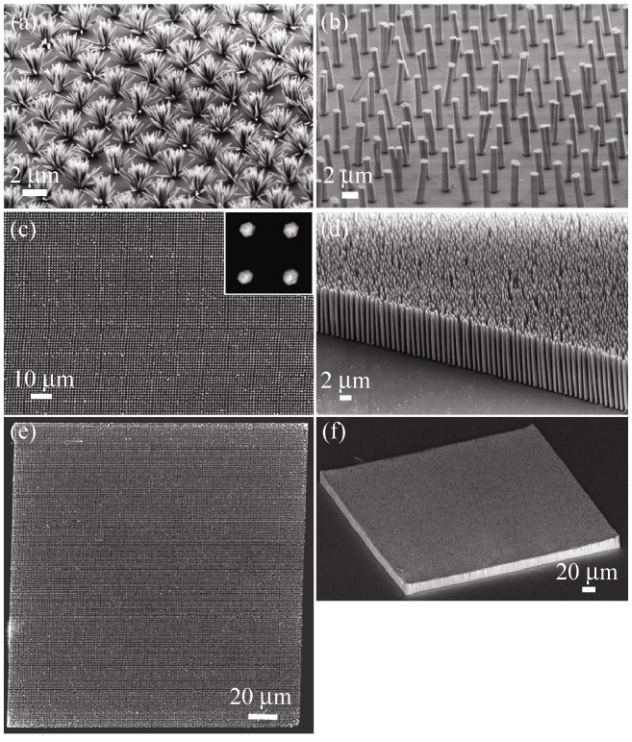

Figure 30 SEM images of the ZnO nanowire arrays on a seeded Si wafer grown at (a) 70 ˚C and (b) 95 ˚C. (c) Top view and (d) 60° tilt view of the ZnO nanowire arrays on a GaN substrate grown at 95 ˚C. The inset in (c) is the enlarged view with a pitch of 1 μm. (e) Top view and (f) 60° tilt view of a 200 μm × 200 μm patterned ZnO nanowire array [48]. Reproduced with permission

In physical vapor deposition, the width of the nanowire is often dictated by the size of the catalyst particles and normally does not change with growth time, simply because the incoming molecular species are preferentially adsorbed on the catalyst particles and the growth occurs at the interface between the catalyst particle and the solid nanowire. But in the wet chemical method, size expansion is always observed in both vertical and lateral directions when the nanowires are grown on pre-patterned substrates [48, 280]. The width of the as-grown nanowires was found to be almost three times the size of the patterned openings. Accordingly, a two-step growth process was proposed [48]. Firstly, the nanowire grew inside the patterned opening with the same lateral dimensions, as confined by the opening. As the nanowire grew out of the

opening, there was no lateral confinement for the nanowire, and it can grow in both vertical and lateral directions, because incoming precursor molecules from the surrounding solution can adsorb on both top and side surfaces. But growth was apparently faster in the vertical direction than in the lateral direction as discussed previously. The growth in the lateral direction rendered the nanowire width greater than the opening size. Even though there was lateral expansion, the nanowire width could still be tuned by defining different opening sizes [48].

The main advantage of electron beam lithography is its high resolution. As can be seen from Figs. 30(e) and 30(f), a large array (200 μm by 200 μm) of well-defined ZnO nanowires, with a patterned opening diameter of 100 nm and 1 μm in pitch, could readily be achieved [48]. Its major drawback, however, is the high cost and low throughput due to the long beam-writing time. In addition, the electron beam lithography system may not be stable, especially over large areas.

Horizontally aligned ZnO nanowire arrays have as many important applications as vertical ones [281]. But there has been only limited research and progress in this area. For example, a seed layer was put on the side wall instead of the top surface of the substrate to grow horizontal ZnO nanowires [282, 283]. There has also been a report of the epitaxial growth of horizontal nanowires by physical vapor deposition [284]. However, the uniformity and spatial control was rather poor. Horizontal alignment of the ZnO nanowires after growth was also achieved by dispersing the nanowires into solvents and then applying a high frequency alternating electrical field [285].

An unprecedented strategy for patterned horizontal ZnO nanowire arrays was demonstrated by combing electron beam lithography and a solution growth method [280]. The basic principle is illustrated in Fig. 31(a). For horizontal growth, $[2\bar{1}\bar{1}0]$ or $[01\bar{1}0]$ oriented single crystal ZnO substrates are required. Also, because of the anisotropic growth habits of the ZnO nanowires, the strip shape openings had to be along the [0001] direction of the substrate to grow individually separated nanowires. As shown in Fig. 31(b), the horizontal nanowires were epitaxially grown on the substrate with uniform length and width. Although the nanowires suffered from lateral expansion once they grew out of the mask confinement as discussed previously [286], the dimensions of the nanowires could still be adjusted by controlling the opening sizes. Also, to make use of the lateral expansion, multi-segment monolithic ZnO superstructures were demonstrated, as shown in Fig. 31(c) [56].

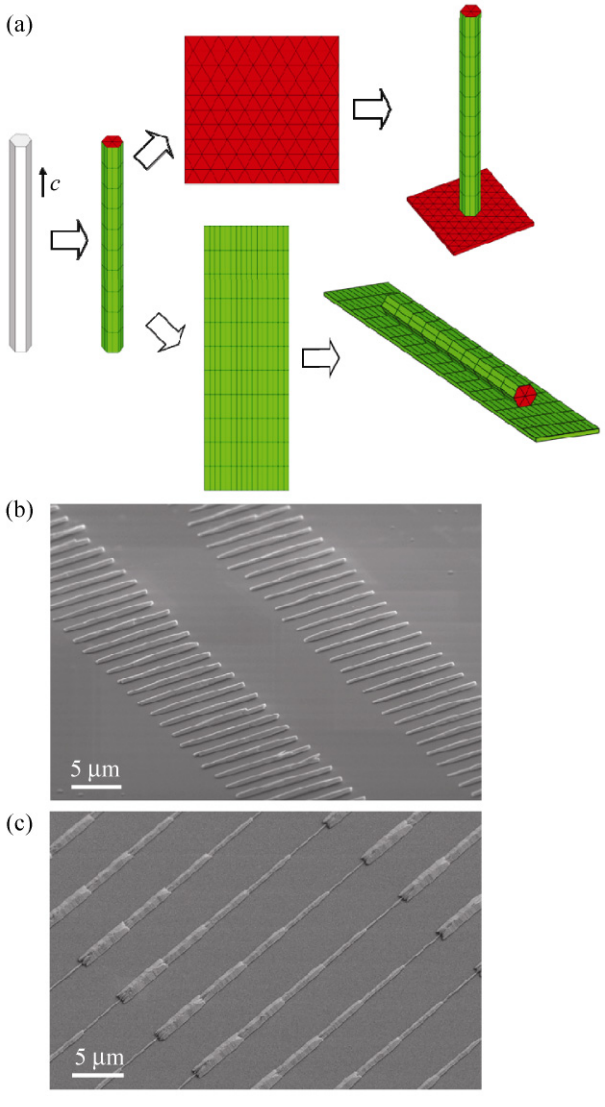

Figure 31 (a) From a crystal structure point of view, wurtzite structure ZnO has a six-fold symmetry at its basal surfaces and a two-fold symmetry at its side surfaces. On a six-fold symmetry epitaxial substrate, ZnO will grow vertically on the substrate. On a two-fold symmetry substrate, it will grow horizontally on the substrate. (b) A 60° tilt view of thick (top row) and thin (bottom row) ZnO nanowire arrays growing out of 2 μm by 400 nm and 2 μm by 200 nm openings, respectively [280]. (c) A 30° tilted view of the horizontal nanowire-array-based five-segment monolithic superstructures [56]. Reproduced with permission

An electron beam could also be used to directly generate ZnO nanowires by writing on a zinc naphthenate resist [287]. The resist became insoluble in toluene after exposure to a high energy electron beam, giving rise to negative patterns. The as-fabricated polycrystalline ZnO nanowires could be reduced to sub-10 nm dimensions after calcination [287].

5.3 Interference lithography

Laser ablation was originally used to generate patterned ZnO seeds for the growth of ZnO nanowire arrays [288]. The laser is primarily used as a heating source to melt the precursor materials, which are later ejected through a mask. In addition to being a heating source, it was also found that a femtosecond laser was able to generate patterns on a single crystal ZnO wafer by virtue of the second harmonic generation excited in the ZnO wafer [289]. By changing the experimental conditions, different patterns such as dot arrays, ripples or regular gratings can be obtained. Other than that, based on laser interference, two-dimensional (2D) [290] or 3D [291] periodic structures could be generated by so-called laser interference lithography. The periodically distributed high intensity of light physically burned off the polymer mask layer [292, 293] or the substrate itself [294], which was used to pattern the growth of ZnO nanowire arrays. For example, in a study by Wei et al. [293], the nanowire growth method followed what had been previously reported [48, 91]. The benefits of laser interference lithography were claimed to be high throughput and low cost on a wafer scale, as shown in Fig. 32 [293].

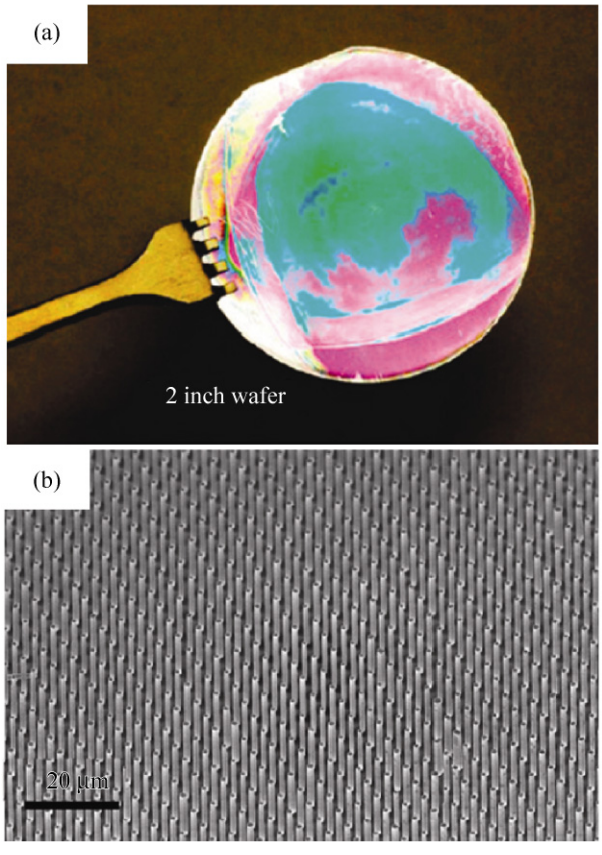

Figure 32 (a) Large scale growth of patterned ZnO nanowire arrays on a two-inch wafer by laser interference lithography, and (b) the corresponding SEM image [293]. Reproduced with permission

5.4 Nanosphere lithography

Sub-micrometer sized spheres, such as polystyrene and silica spheres, will self-assemble on a water surface into a hexagonally close-packed structure driven by the water surface tension. A honeycomb pattern is formed [295], called nanosphere lithography. These spheres are commercially available with well-controlled monodisperse sizes. The hexagonally close-packed structure can be used as a mask, and the feature size is tunable by using spheres of different sizes and also by post-heat treatment [296]. When heated, the spheres deform and therefore the gaps between them shrink in size. Li et al. differentiated the connected pattern and the inverted pattern of the hexagonally close-packed spheres by introducing a secondary complementary replication process [297]. In Li's study, the growth of a single nanowire out of one gap was achieved by a wet chemical method, and the distribution of the nanowires had very good fidelity to the original sphere patterns. The aspect ratio of the nanowires was fairly small. Also, there were many defects in the self-assembled spheres. Nevertheless, nanosphere lithography offers a simple, cost-effective, and high throughput lithographical approach.

5.5 Nanoimprint lithography

Nanoimprint lithography is an embossing technique, which describes the transfer of a sub-micron scale pattern from the mold to the target substrate or device [298]. It is known for achieving sub-100 nm resolution on a large scale in a time-efficient and cost-effective

manner. Basically, it employs a relatively hard mold template that is used to carve into a relatively soft surface. The hard molds are generally made of wearable and durable materials, such as silicon and flexible PDMS, which can be used repeatedly. The pattern in the mold is typically written by electron beam lithography. The mold surface properties can be tuned to be hydrophilic or hydrophobic [299]. An anti-stick coating is often applied on the mold to prevent any residues that will introduce defects into the pattern. Figure 33 shows a flow chart of the nanoimprint lithography process. The pattern is recorded on a piece of mold by electron beam lithography and chemical etching. On the substrate is a sol-gel derived ZnO seed layer. A mold is then embossed intimately into the seed layer. After drying, a complementary replica of the mold is made in the seed layer [300].

5.6 Micro-contact printing

With a similar methodology, micro-contact printing (μCP) utilizes a mold inked with functional molecules [301]. When the mold is in contact with a substrate, the functional molecules are transferred and self-assemble on the substrate following the patterns of the mold, as shown in the Fig. 34(a). The self-assembled functional molecules can inhibit or promote the growth of ZnO nanowires locally. Hsu and coworkers developed an approach that combines μCP and self-assembled monolayers on a Ag surface to direct the

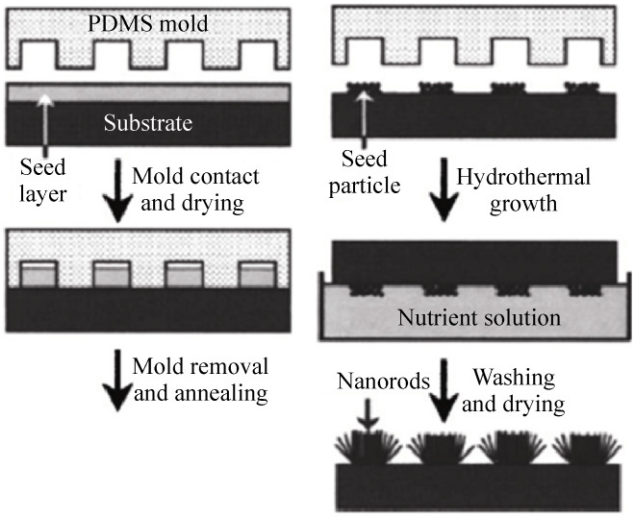

Figure 33 Schematic illustration of nanoimprint lithography [300]. Reproduced with permission

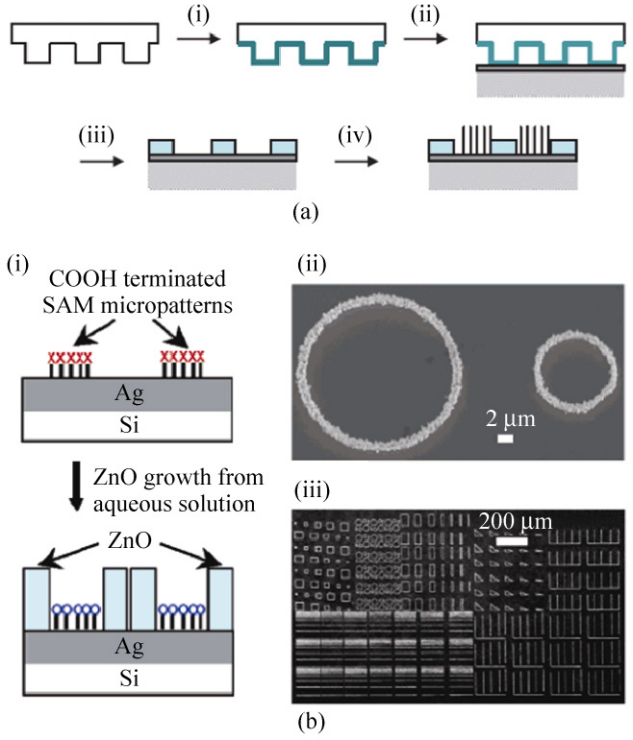

Figure 34 (a) Schematic illustration of micro-contact printing. (i) Inking the mold with octadecyltrichlorosilane (OTS) solution, (ii) μCP of the substrate, (iii) transferring the OTS pattern to the substrate, and (iv) ZnO growth on regions where there is no OTS [304]. (b) Patterned growth of ZnO nanowires on Ag with SAM patterns. (i) μCP patterned SAM on Ag surfaces (top) and the resulting ZnO nanowires on the bare Ag regions (bottom). X in the top panel denotes the –COOH end group; O in the bottom panel denotes COO^-–HMTA–H^+ complexes. SEM images of (ii) ZnO nanowires organized in two rings. The surrounding regions are covered by the SAM molecules, where no ZnO nanowires are grown, and (iii) large area patterns where ZnO nanowires appear white [302]. Reproduced with permission

spatial distribution of ZnO nanowire arrays [302]. In their particular case, they used a functional molecule that had a thiol group and a carboxyl group at its two ends. The thiol groups self-assembled and anchored themselves on the Ag surface; the acidic carboxyl group bound the HMTA molecules forming COO^-–HMTA–H^+ complexes which inhibited the local nucleation and growth of ZnO nanowires due to the electrostatic charge interactions between the charged species in solution and the surface-bound charged complexes. ZnO nanowires were observed to grow only on bare Ag surfaces, with more than one nanowire growing on each spot because the pattern feature size was much larger than the width of a single nanowire. Additives

could be added to modify the growth behavior, and a thicker nanowire disk was formed on one spot [302]. The authors also found that the COO^-–HMTA–H^+ complexes played the major role in suppressing the nucleation of ZnO. In their control experiment, when Zn^{2+} was first introduced to the carboxyl groups, the nucleation selectivity was much less obvious. Also, restricting regions of nucleation resulted in an increase in nucleation density in the unrestricted regions [303].

5.7 Inkjet printing

The basic structure of an inkjet printer is composed of a stage where the substrate is placed, at a distance away a nozzle from which ink is injected onto the substrate [305]. For the growth of ZnO nanowire arrays, a sol–gel derived zinc acetate precursor ejected from the nozzle can be dropped on a substrate that was heated to decompose the zinc acetate into ZnO seed crystals [306]. The typical resolution of an inkjet printed pattern is on the order of micrometers, and depends on many factors, such as the droplet size ejected from the nozzle, the accuracy of the droplet landing on the substrate, the wettability and spreading of the droplet on the substrate, and possibly convolution/interactions between the neighboring droplets. Of these factors, the size of the droplets is currently the bottleneck to narrowing down the feature size of this technique, and much effort is nowadays devoted to this topic [307], such as controlling the viscosity, evaporation rate, and surface tension of the precursor ink. Sekitani et al. have recently demonstrated an inkjet technology with micrometer line resolution [308]. In any case, inkjet printing provides a direct writing technique that is simple, versatile, and inexpensive and can potentially be scaled up.

5.8 Pattern transfer

The as-grown ZnO nanowire arrays can be transferred intact onto flexible substrates [56, 149]. Due to the lateral expansion of the ZnO nanowires from the patterned areas [48, 280], the actual contact area between the nanowire and the substrate is usually a fraction of the overall size of the nanowire, which enables easy cleavage at the interface without breaking the nanowires apart. In a typical pattern transfer process, a thin conformal layer of polymer was coated on the nanowires. In this process, selective adhesion of the coating polymer layer to the nanowires rather than to the underlying substrate is desirable, and possible interfacial bonds can be introduced between the coating polymer layer and the ZnO nanowires [56]. After that, another thicker layer of polymer was coated, which provided the flexible substrate with the mechanical strength to hold the nanowires. Then a straightforward peeling off or delamination was applied to the as-coated polymer layers. Rapid heating/cooling can also be used to separate the inorganic substrate and the polymer coating layers due to their different thermal expansion coefficients. Therefore, the patterned ZnO nanowire arrays can be transferred onto the as-coated polymer substrate, as shown in Fig. 35, which was later used to grow second generation of ZnO nanowire arrays, replicating the original pattern [193]. This technique has great potential for future flexible and foldable electronic applications [309].

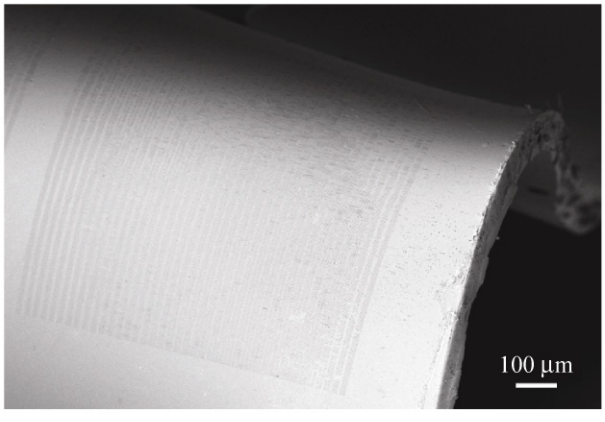

Figure 35 Low magnification SEM image of patterned nanowire arrays transferred onto a flexible substrate [56]. Reproduced with permission

6. Properties and applications

ZnO nanowire arrays have found innovative applications in a variety of areas due to their unique chemical and physical properties, as discussed specifically in the following sections.

6.1 Catalytic properties

ZnO has received great attention as a photocatalyst for the degradation and mineralization of environmental

pollutants due to its large band gap and low fabrication cost [310]. Under UV illumination, ZnO will generate electron and hole pairs able to generate hydrogen by water splitting [311], synthesize H_2O_2 [312], and reduce graphene oxides to graphene [313]. In particular, the generated holes can be used to oxidize/decompose organic pollutants, such as rhodamine 6G [210], methyl orange [314], methylene blue [159], and formaldehyde [315]. Because of the presence of active defect sites—such as oxygen vacancies—on the surface, ZnO has also been used in industry as a catalyst for the synthesis of methanol from CO and H_2 [316], or as a supporting scaffold for other catalysts, such as Cu [317], Cu/Fe composites [318], CuO [319], Au [320], for oxidative steam reforming of methanol.

ZnO nanowires are an efficient photocatalyst due to their high surface to volume ratio in comparison with ZnO bulk materials. Zhou and Wong showed that ZnO nanowires had an even higher catalytic activity than nanoparticles and bulk forms due to their high purity and crystallinity [129]. In addition, if the size of the nanowire is smaller than a critical value of approximately 50 nm, the effective band gap of ZnO will increase, the redox potentials will increase, and therefore the photogenerated electrons and holes will have a higher reducing/oxidizing power. In addition, with a larger band gap energy, the photogenerated electron and hole pairs will be less likely to recombine, which in turn enhances the charge transfer efficiency between the catalyst and the pollutants [310]. There are also other approaches to hinder the recombination of the photogenerated electron and hole pairs, such as using CdS nanoparticle–ZnO nanowire heterostructure arrays [321], and SnO_2 and ZnO composites to improve the charge separation efficiency [322].

Figure 36(a) shows the absorption spectra of methyl orange solution with catalytic amounts of ZnO and different UV illumination times. The Beer–Lambert law states that the absorption is proportional to the concentration of the absorbing species. The intensity of the characteristic absorption peak at 464 nm for methyl orange decreases with increasing exposure time, and the peak completely fades away after about 80 min; as shown in the inset images of Fig. 36(a), the sample is also completely decolorized.

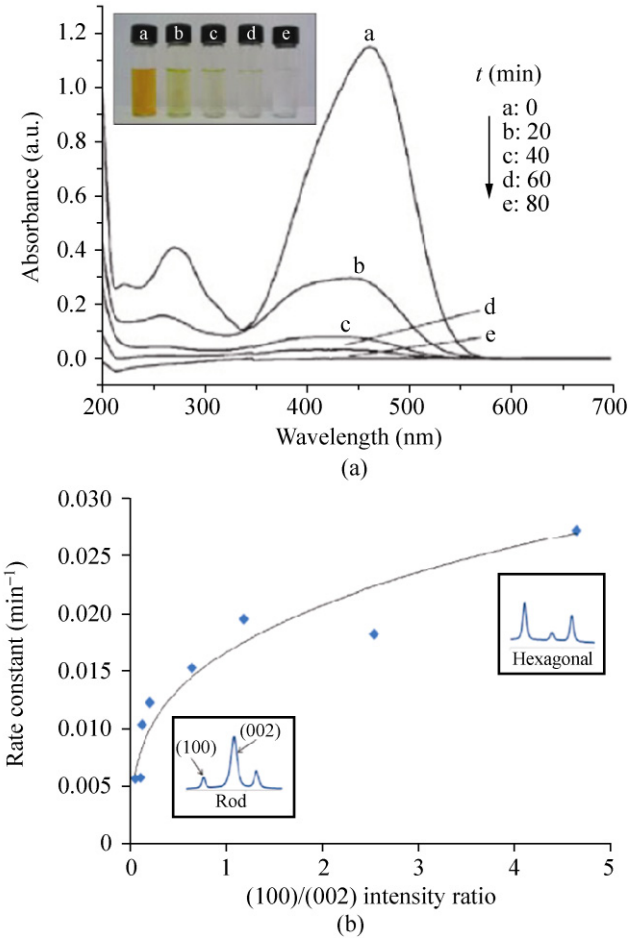

Figure 36 (a) Time-dependent color change (inset photo in the upper left) and corresponding optical absorbance spectra for methyl orange solution in the presence of micro/ nanoarchitectured ZnO after exposure to UV light [314]. (b) Plot of the photocatalytic decomposition rate constant as a function of the dominant facets (characterized by the XRD (100)/(002) intensity ratio) of the ZnO nanoparticles [159]. Reproduced with permission

It is widely accepted that catalytic properties are dependent on specific crystal facets, since different crystal facets have different dangling bond configurations [323]. Mclaren et al. carried out an interesting study showing that the polar (0001) or (000$\bar{1}$) basal planes of ZnO have a stronger catalytic effect than the nonpolar {01$\bar{1}$0} or {2$\bar{1}\bar{1}$0} side planes for the photocatalytic decomposition of methylene blue [159]. In their study, they used hexagonal nanoplates and rod-shaped nanowires synthesized by controlling the oleic acid to zinc acetate ratio. As shown in Fig. 37(b), they found that on going from nanowires to nanorods and then to nanoplates, the ratio of the exposed basal

planes to the side facets increased, and the photocatalytic decomposition rate constant of methylene blue increased accordingly. The activity of the nanoplates was more than five times higher than that of the nanowires. The higher activity of the polar basal planes was attributed to the intrinsically high surface energy of {0001}, which favors adsorption of the reactant molecules [159]. Li et al. attributed this high activity, however, to the correlation between the proportion of exposed polar surfaces and the surface oxygen vacancy density, since oxygen vacancies help to trap the photogenerated electrons and thus assist the charge separation [324].

The main disadvantage with ZnO photocatalysts is their stability and durability. ZnO is unstable in acidic and basic media, so photocorrosion under UV illumination is considered to be one of the main reasons for the decrease in ZnO photocatalytic activity over time. Therefore ZnO is only suitable for photocatalytic applications in neutral environments [314].

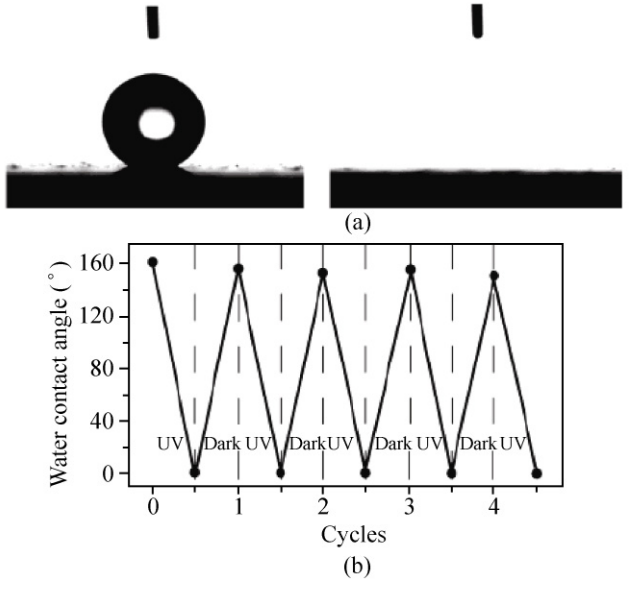

Figure 37 (a) Photographs of a spherical water droplet on aligned ZnO nanowire thin films before (left) and after (right) UV illumination. (b) Reversible superhydrophobic to superhydrophilic transitions of the as-prepared thin films under alternating UV irradiation and storage in the dark [325]. Reproduced with permission

6.2 Hydrophobic properties

Wettability of a solid surface is of critical importance for many industrial applications [326]. Feng et al. reported reversible switching between superhydrophobicity (contact angle > 150°) and superhydrophilicity (contact angle ~0°) of ZnO nanowire arrays by alternating UV irradiation and storage in the dark [325]. Figure 37(a) shows a water droplet on the ZnO nanowire array before (left image) and after UV illumination by a Hg lamp for 2 h (right image). The superhydrophobicity can be restored by putting the nanowires in dark for 7 days. This process can be repeated several times without obvious deterioration as shown in Fig. 37(b). This phenomenon was attributed to the correlation of the surface photosensitivity with the porous structure of the vertical ZnO nanowire arrays [327]. Wettability is governed by the material surface chemistry and also the geometrical structure of the surface [304, 328]. An as-grown ZnO nanowire array with appropriate density is a rather porous structure and exposes mostly the low energy non-polar side surfaces [101], which greatly enhances the hydrophobic behavior. Under UV irradiation, ZnO nanowires generate electron and hole pairs, and the holes can free the negatively charged oxygen molecules chemisorbed on the nanowire surfaces [329], leaving behind empty binding sites on the surface that are later occupied by hydroxyl groups, which therefore increases the hydrophilicity of the nanowire surfaces. Water droplets are sucked into the porous nanowire arrays by a capillary effect. In the dark, the hydroxyl groups on the ZnO nanowire surfaces are gradually replaced by oxygen molecules since their adsorption is actually thermodynamically more favorable [325].

As an alternative to UV irradiation, Badre and coworkers demonstrated an approach to reverse the surface wettability by controlling the electrochemical potential [330]. It has been shown that coating a monolayer of hydrophobic molecules on ZnO nanowire surfaces can considerably increase their hydrophobicity [331]. In Badre's study, they utilized a ferrocene silane molecule, N(3-trimethoxysilyl)propylferrocenecarboxamide, which has an anchoring group to ZnO nanowire surfaces on one end, and a redox change group on the other end. These two functional groups are separated by an alkyl chain. Under an electrochemical potential, the molecules can undergo ferrocene to ferrocenium redox changes, with ferrocene being the

low free energy state and ferrocenium being the high free energy state. This change can be used to reversibly adjust the surface from hydrophobic to superhydrophilic. These smart surfaces could find applications in drug delivery and biosensors [331].

6.3 Field emission properties

Field emission finds applications in photoelectric panel display, X-ray sources, and microwave devices [332]. ZnO, with the advantage of low manufacturing cost on a large scale and also allowing relatively high oxygen partial pressure during its operation, has become a good candidate for use in field emission cathodes.

It is desirable to have relatively high density and vertically aligned fine tips for enhanced local electric field around the tips [207, 333]. Hung et al. reported ZnO nanotip array-based field emitters [334]. The ZnO nanotip arrays (Fig. 38(a)) were grown by a hydrothermal method on a sputtered ZnO thin film or existing ZnO microrods, with a 1:2 ratio of zinc nitrate and HMTA as the nutrient. Field emission tests are usually carried out in vacuum at room temperature. The ZnO nanotip arrays are placed as the cold cathode, and a counter anode with known size is placed at a defined distance away from the cathode. An electric field is built up between the two electrodes when a voltage is applied [207]. The turn-on field and the threshold field are defined as the macroscopic fields required to produce a current density of 10 μA/cm^2 and 10 mA/cm^2, respectively [112]. Figure 38(b) shows a plot of field emission current density as a function of the applied field [304]. The turn-on field can be effectively lowered by modifying the ZnO tips with metal nanoparticles [335]. Stability of the emission current density is usually a big concern in field emission technology [336].

The field emission behavior is governed by the so called Fowler–Nordheim (F–N) theory [337]: $J = (AE^2\beta^2/\Phi)\exp(-B\Phi^{3/2}/\beta E)$, where J is the emission current density in A/cm^2; E is the macroscopically applied electric field in V/cm, and β is the field enhancement factor, defined by $E_{local} = \beta E = \beta V/d$, where E_{local} is the local electric field around the emitter tips. β reflects the degree of the field emission enhancement of a tip over a flat surface. β is affected by many factors, such as the emitter geometry, crystal structure quality, vertical alignment, and emitter density. It is desirable to have high β values. Density of emitters plays an important role. If it is too low, then the emission current density will be low; if it is too high, then

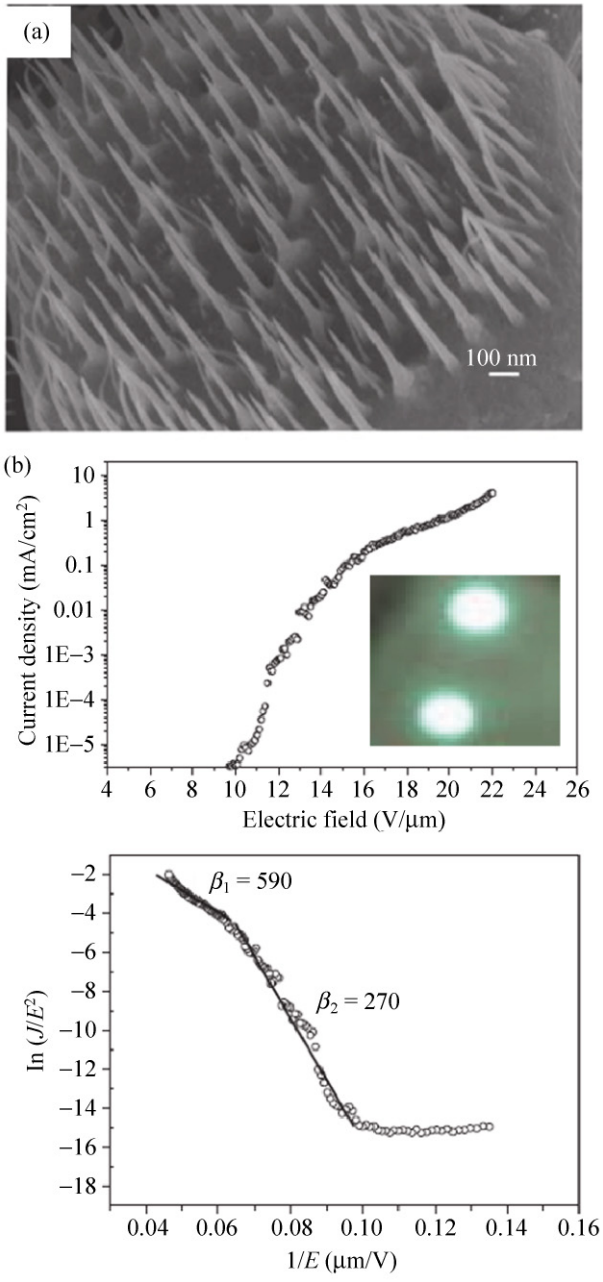

Figure 38 (a) As-grown ZnO nanotip arrays on existing ZnO microrods [334]. (b) Field emission current density as a function of applied electric field [334]. Inset is an uniform fluorescent field emission image on atypical green phosphor coated glass [339]. (c) The corresponding *F–N* plot with different β values indicated [334]. Reproduced with permission

the local electric field around the emitter tips will have an electrostatic screening effect induced by the neighboring nanowires, which generally lowers the β value [112, 338]. Φ is the emitter work function, which is about 5.4 eV for ZnO [337]. A and B are two constants with values of 1.56×10^{10} (A·V^{-2}·eV) and 6.83×10^3 (V·eV$^{-3/2}$·μm^{-1}), respectively. By plotting ln (J/E^2) versus $1/E$ as shown in Fig. 38(c) [334], the curve shows more than one slope, which may result from the variation in the tip local fields, or absorbate induced emission saturation [141]. When the applied field is high, the curve is roughly linear, which indicates the field emission current comes from barrier tunneling extracted by the applied electric field [75]. The β values could be derived from fitting the experimental curve to F–N theory according to $\beta = 6.83 \times 10^9\ d\Phi^{3/2}/k$, where d is the gap distance between the two electrodes and k is the slope of the F–N curve.

6.4 Photonic crystals

Periodically aligned vertical ZnO nanowire arrays give rise to a periodic modulation of dielectric constants for photons traveling inside, resulting in a refractive index contrast; this is called a photonic crystal [340]. Just as the periodic arrangement of atoms in crystals gives rise to a periodic distribution of electrical potential for electrons traveling inside, resulting in an electronic band gap, a photonic crystal has a photonic band gap for photons. Propagation of photons with frequencies within the photonic band gap is suppressed. Defects in the photonic crystal can also introduce localized states in the photonic band gap, allowing the propagation of photons with frequencies at the localized states. These properties of photonic crystals can be used to control the emission and propagation of photons for developing future integrated optical communications [341–345]. Inverted photonic crystals can also be made by infiltrating the empty spaces between the ZnO nanowires with polymers followed by dissolving the nanowires away with acids or bases.

Using an effective numerical method, as shown in Fig. 39(a), Kee et al. calculated the photonic band structures of a periodic array of vertically aligned ZnO nanowires with a frequency dispersion for the transverse magnetic (TM) mode (where the electric field is parallel to the c axis of the nanowires) [340]. In their calculation, the periodic array of well-aligned nanowires can be treated as a 2D photonic crystal provided that the nanowire height is much larger than the nanowire width. Otherwise, if the nanowire height is too small, the 2D photonic crystal is too thin. In this case, its optical confinement is rather weak and it is not suitable for use as a waveguide. The calculation results showed that the center position and width of the band gap were dependent on the nanowire width and also the array pitch. By tuning the ratio between the two factors, a photonic band gap in the visible range could be obtained, as shown in Fig. 39(b) [340]. The crystal quality of the building blocks for the photonic crystals is very important, because defects such as voids and grain boundaries scatter electromagnetic waves leading to propagation loss. Figure 39(c) shows a typical transmission spectrum of a photonic crystal. The large full width at half maximum of the transmission peak indicates that it is a non-perfect photonic crystal [341, 342]. Figure 39(d) shows a six-fold optical diffraction pattern of white light passing through a hexagonally patterned ZnO nanowire array. Dispersion along the radial directions is clearly seen [343, 344].

6.5 Light emitters

ZnO-based light emitters have been considered as a potential candidate for the next generation of high efficiency blue/near-UV light sources, due to the direct wide band gap energy of 3.37 eV, a large exciton binding energy of 60 meV at room temperature, and several other manufacturing advantages of ZnO [346], including its availability on a large scale at a relatively low cost, amenability to wet chemical etching, great tolerance to high energy radiation, and long-term stability. They can be used for a variety of technological purposes, such as solid state lighting, optical interconnects, and high density information storage.

6.5.1 Optically excited light emission

Using optical excitement of ZnO nanowires, researchers have studied their photoluminescence properties, realized lasing behavior from the Fabry–Perot cavity formed by the two basal planes, and also studied nonlinear effects.

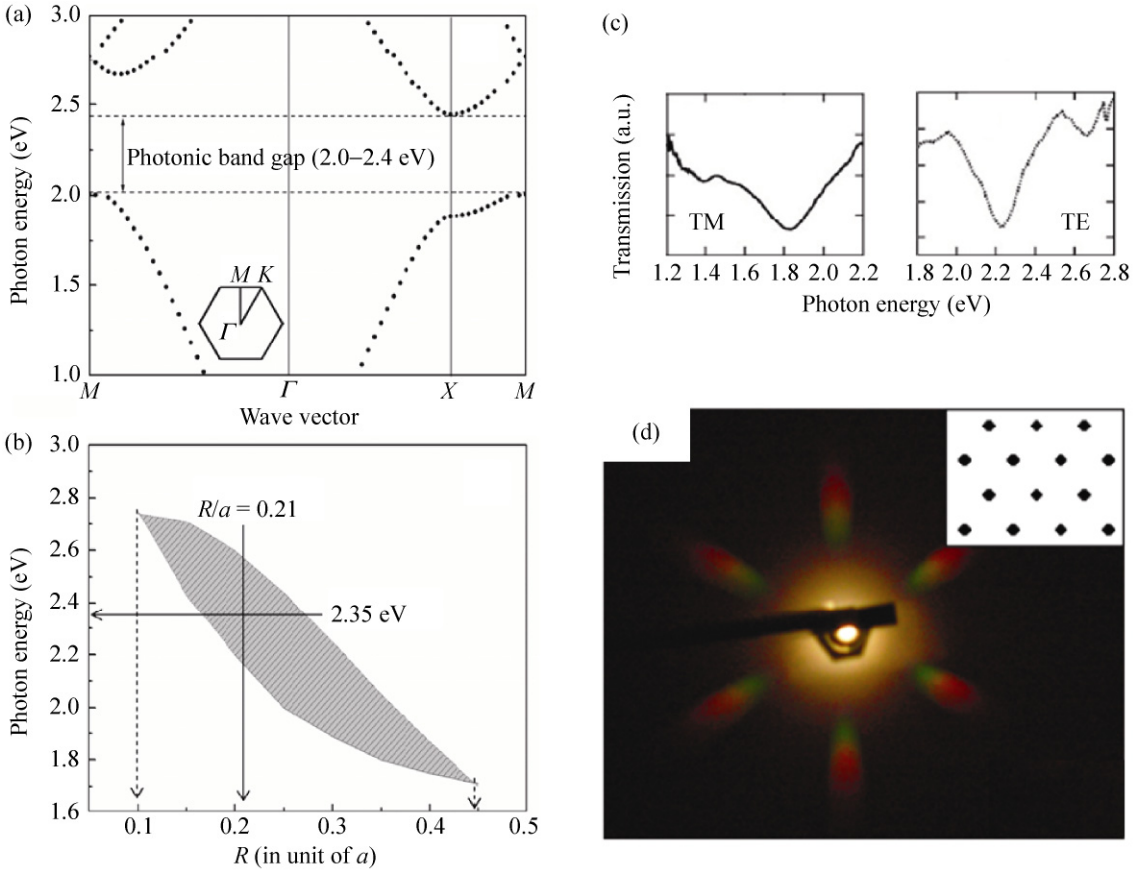

Figure 39 (a) The lowest three photonic bands for TM modes in a triangular lattice of ZnO nanowires when the array pitch a is 240 nm and the nanowire width $2R$ is 120 nm, where R is the nanowire radius. There is a photonic band gap in the range 2.0–2.4 eV. The inset denotes the first Brillouin zone of a 2D triangular lattice [340]. (b) The dependence of the band gap on R/a when a = 240 nm. The hatched area denotes the band gap. Note that when R/a = 0.21, the photonic band gap center is located at around 2.35 eV, which is the spectral maximum frequency of the green luminescence band of ZnO nanowires due to oxygen vacancies or zinc interstitials [340]. (c) The measured transmission spectra of the ZnO nanowire hexagonal array in the Γ–M direction for both TM and TE polarizations. The array has a photonic lattice constant of 250 nm and a height of about 500 nm [341, 342]. (d) Diffraction pattern using a white light source from a hexagonal array of ZnO nanowires [343, 344]. Reproduced with permission

6.5.1.1 Photoluminescence

The photoluminescence spectrum of ZnO, excited by a UV laser at room temperature, usually has two emission bands. One is in the UV range, which is attributed to the near-band-edge emission through exciton–exciton collision processes [347]. The other is in the visible range, and presumably comes from the electron–hole recombination at a deep level in the band gap caused by intrinsic point defects and surface defects, e.g., oxygen vacancies, zinc interstitials, and the incorporation of hydroxyl groups in the crystal lattice during solution growth [124, 348–350]. These two emission bands have been used to enhance the photoluminescence intensity of rare earth compounds [351].

Figure 40(a) shows a typical photoluminescence spectrum of ZnO nanowires at room temperature [352]. The dominant UV emission peak is observed at around 380 nm, together with a rather weak visible emission at about 500 nm. Emission in the near-IR at around 760 nm for the ZnO nanowires grown on Au-coated ITO substrates is attributed to the second order feature of UV band-edge emission [353, 354]. The blue-shift in the peak position of the near-band-edge exciton emission as the size of the nanowire decreases to below 10 nm is possibly due to a confinement effect [355]. The defect-derived green emission usually results in

a decrease in exciton lifetime and quantum efficiency of UV light devices, and therefore an increase in lasing emission threshold. To reduce the defect emission and to enhance the near-band-edge UV emission, post-plasma treatment, or annealing at different temperatures and in different atmospheres has been performed [356, 357]. Studies have shown that annealing at 200 °C can largely reduce the defect concentration as evidenced by positron annihilation spectroscopy [349]. A polymer coating on the ZnO nanowires was also demonstrated to effectively depress the defect emission and enhance the near-band-edge emission [358]. A photoluminescence spectrum of ZnO nanowires at 4.2 K is shown in Fig. 40(b) [338]. Generally as the temperature was decreased from room temperature to 4.2 K, the photoluminescence intensity increased [104], and its temperature dependence

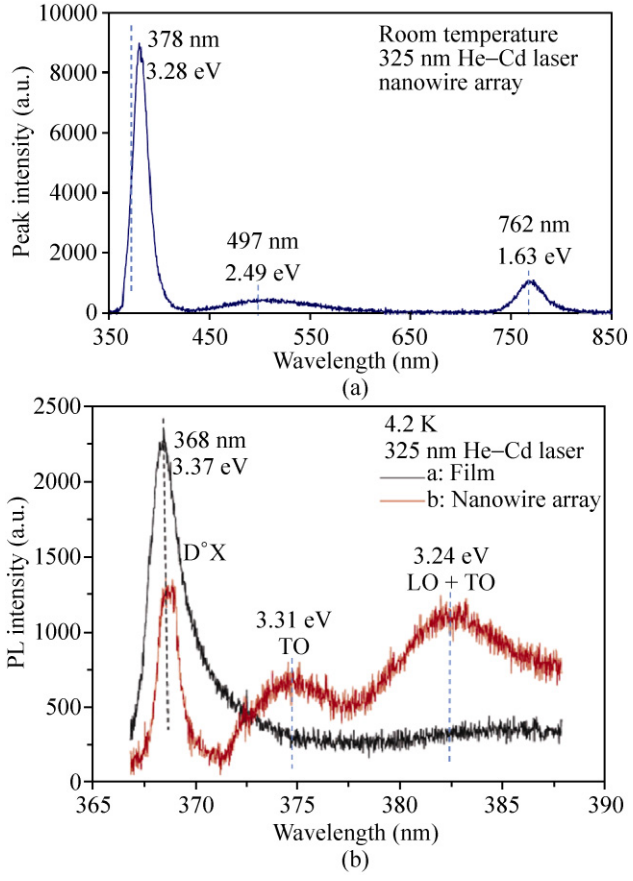

Figure 40 (a) Room temperature photoluminescence spectrum of ZnO nanowires grown on Au-coated ITO substrates at room temperature [352]. (b) Photoluminescence spectrum of ZnO nanowires and ZnO thin film at 4.2 K [338]. Reproduced with permission

satisfied the Arrhenius relationship [184]. The main UV emission peak, assigned as the shallow bound exciton [338], was blue-shifted from 378 nm to 368 nm, because the band gap of ZnO increases as temperature decreases following the Varshni relationship [359]. In addition, the longitudinal and transversal optical (LO and TO) phonon replicas were also apparent [338]. The energy separation between these phonon replicas, as labeled in Fig. 40(b), matched well with the reported phonon energies in ZnO crystals [1, 360–362].

6.5.1.2 Optically pumped lasers

ZnO nanowire arrays are good materials for the fabrication of room temperature lasers for two reasons [10]. First, ZnO is a wide band gap semiconductor with a large exciton binding energy (60 meV) that is greater than the thermal energy at room temperature (25 meV). So the excitons can be stable at room temperature, and efficient excitonic recombination is prerequisite for lasing. Second, the nanowire structure with two highly reflective top and bottom end facets forms a Fabry–Perot cavity, as shown in Fig. 41(a) [363]. Each nanowire has a Fabry–Perot cavity. Furthermore, the high refractive index of ZnO (n = 2.45) can laterally confine the light traveling inside as a sub-wavelength waveguide for low order modes with an appreciable effective gain length.

Govender et al. demonstrated an optically pumped broadband visible laser based on ZnO nanowire arrays grown by a wet chemical method [10]. The nanowire arrays were optically pumped by a nitrogen laser, with the wavelength (337 nm) and pulse (800 ps) matched to the band gap (365 nm) and excitonic lifetime (~350 ps) of ZnO nanowires. The pumping source was either in the vertical direction [10, 363], or at a grazing angle to the substrate [152]. The detector was placed at the substrate normal. The threshold pumping power density (I_{th}) was determined by the slope change of the photoluminescence intensity (I_{PL}) as a function of the excitation laser intensity (I_{ex}). The I_{th} is thought to be sensitive to the density of states at the band edge of the material and the size of the cavity [9], and typically ranges from 40 kW/cm² to 7 MW/cm² [152].

When the value of I_{ex} is less than I_{th}, the emission is dominated by spontaneous emission; when I_{ex} is similar to I_{th}, amplified spontaneous emission takes place;

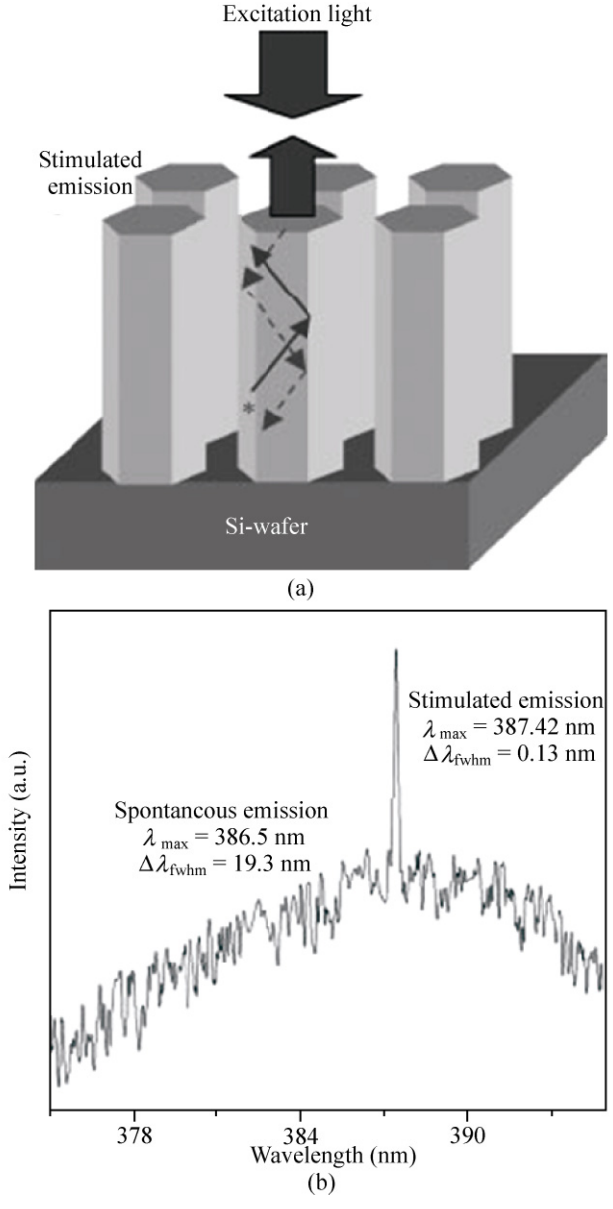

Figure 41 (a) Schematic illustration of the working principle of a nanowire Fabry–Perot cavity, in which the photons are bouncing back and forth between the two mirrors. (b) Emission spectrum of EHP lasing from ZnO nanowire arrays [363]. Reproduced with permission

when the value of I_{ex} is greater than I_{th}, lasing shows up with a much narrower full width at half maximum (FWHM) than spontaneous emission, based on exciton and exciton scattering process; when the value of I_{ex} is further increased, a second stimulated emission due to the electron and hole plasma (EHP) can be observed. The EHP lasing peak is usually red-shifted in comparison with the exciton-based lasing, probably because of the band gap renormalization from the Coulomb interactions between the free electrons and holes at the band edge. The exciton lifetime generally decreases from spontaneous emission to EHP lasing [364].

The emitted photons oscillate between the two basal facets, and a series of emissions at the modal frequencies of the cavity can be detected. The wavelength spacing between these modes can be calculated by $\Delta\lambda = \lambda^2/2L(1/n\text{-}\lambda(\partial n/\partial\lambda))$, where n is the refractive index of the cavity, L is the cavity length, and $\partial n/\partial\lambda$ is the frequency dispersion of the material [364]. The lasing modes covered almost the entire visible spectrum [10], and so can serve as a white light source. Choy et al. reported a second stimulated emission (EHP) peak at a wavelength of 387.42 nm, as shown in Fig. 41(b) [363]. The FWHM was about 0.13 nm, which was rather small. Because ZnO nanowires can serve as waveguides, random lasing through the side facets of the nanowires is not likely to happen [10]. Secondly, random lasing has a higher threshold than the lasing from the nanowire cavity [10, 364]. Thirdly, random lasing is highly chaotic, while the lasing from the nanowire resonant cavity had a strong polarization in the horizontal substrate plane [364].

6.5.1.3 Nonlinear optics

Nonlinear optical properties of semiconductor nanowires have potential applications in frequency converters and logic/routing elements in optoelectronic nanocircuits [366]. In particular, ZnO with its polar surfaces can be used for frequency doubling of intense ultrashort laser pulses.

Voss et al. studied the resonant second harmonic generation (SHG) from ZnO nanowire arrays under excitation with intense femtosecond pulses [365]. In their experiment, they used a wavelength-tunable near-infrared (700–900 nm) femtosecond oscillator to excite the nanowires. The light pulses had an energy of 12 nJ with 50 fs duration. Figure 42 shows the emission curves for different excitation times. In the spectra, three different sets of peaks, in order of increasing wavelength, can be assigned as follows: the resonant SHG at a wavelength of 360 nm for femtosecond oscillator excitation of 720 nm, the near-band-edge photoluminescence, and the emission from deep defect

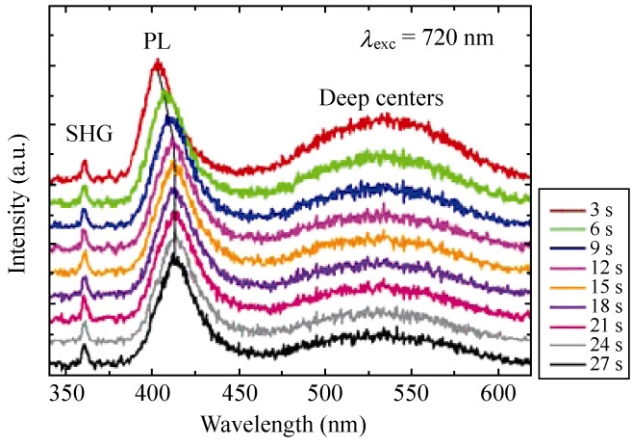

Figure 42 Emission spectra of ZnO nanowire arrays at different time delays after the excitation laser was unblocked. The integration time was 100 ms for all curves [365]. Reproduced with permission

centers. The photoluminescence peaks exhibited a red-shift during the first 27 s after the intense laser excitation, because of the band gap shrinkage induced by the temperature rise in the nanowires. Both *s*- (TE) and *p*- (TM) polarized excitation pulses were used to selectively detect the *p*-polarization component of the nonlinear optical output. A phenomenological four-layer model was used to simulate the angular dependence of the polarization curve. The ratio between the two relevant components of the $\chi^{(2)}{}_{311}/\chi^{(2)}{}_{333}$ was found to be –0.1. The effective length of the nanowires was calculated to be 2.3 μm, compared with 3.2 μm obtained from SEM images [365].

6.5.2 *Electrically driven light emission*

Light emission driven by electricity is more attractive than that driven by optical pumping, in the sense that the device is capable of being integrated with chip circuits. At present, electrically driven light emission from wet chemically grown ZnO nanowires is limited to LEDs. Electrically pumped lasers are difficult to realize due to the low crystal quality of the ZnO nanowires which leads to a low internal quantum efficiency and thus a high threshold voltage. The device usually fails before reaching the lasing threshold voltage due to Joule heating at high bias voltages.

6.5.2.1 *ZnO homojunction LEDs*

The most efficient solid state light emitters are based on *p*–*n* junctions [251]. Hsu et al. demonstrated the hydrothermal synthesis of undoped *p*-ZnO nanowire arrays, and used as-grown *p*-type ZnO nanowire arrays to fabricate homojunction LEDs [254]. Figure 43 shows the photoluminescence and electroluminescence spectra of the *p*-ZnO nanowires on A *n*-ZnO single crystal substrate. When under bias, a blue peak and a broad red/near infrared emission band could be observed. Inset is a camera image of the LED when under bias. The blue peak arises from the exciton recombination of electrons from substrate and holes from the nanowire, and the broad red/near infrared emission is likely to be due to electroplex emission since this band was absent in the photoluminescence spectra [254].

6.5.2.2 *Inorganic heterojunction LEDs*

More often in LEDs, instead of ZnO homojunctions, heterojunctions of *n*-ZnO and other *p*-type materials have been used, of which *p*-GaN is of particular interest considering it has similar crystallographic and electronic properties to ZnO [11, 367–369]. In addition, it has been suggested that the ZnO nanowire/GaN substrate heterojunction has a higher carrier injection efficiency and a higher recombination rate than other junctions [370].

In all of the previous cases, the *n*-ZnO nanowires were randomly distributed on the substrate. However, Xu et al. have demonstrated the possibility of controlling the spatial distribution of blue/near-UV LEDs

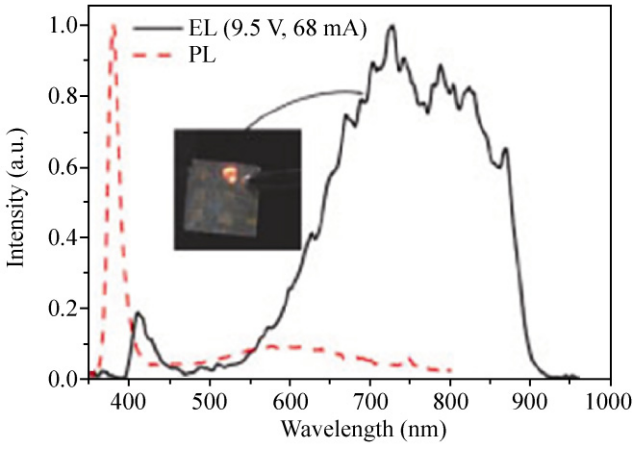

Figure 43 Photoluminescence (red dashed curve) and electroluminescence (black solid curve) spectra for a *p*-ZnO nanowire array grown on a *n*-ZnO single crystal substrate. Spin-on-glass was used as an insulating layer to fill up the space between the nanowires. The inset image shows the LED when lit up [254]. Reproduced with permission

based on position-controlled arrays of *n*-ZnO nanowires on a *p*-GaN thin film substrate [371]. The device was fabricated by combining a low temperature wet chemical method and electron beam lithography [48]. Ohmic contacts to the bottom *p*-GaN and top *n*-ZnO nanowires were made by Ni/Au and ITO films, respectively. The need for deposition of an ohmic electrode on the GaN substrate could be avoided by employing a ZnO nanowire/GaN substrate/ZnO nanowire heterostructure [370]. The turn-on voltage of the diode was about 3.5 V, which is relatively low, probably due to the presence of interfacial defects [372] owing to the low growth temperature (< 100 °C) of the chemical method. Figure 44 shows an optical image (exposed for 9 s with a gain value of 1) of the lit-up LED at a forward bias voltage of 10 V. In the device, all of the nanowires were connected in parallel and each single nanowire is a light emitter. The difference in brightness of the individual nanowires probably arises from the different serial contact resistances with the bottom GaN substrate and top ITO electrode, which leads to different injection currents.

The physical origin of the electroluminescence has been extensively studied but is still under debate [373–375]. There has also been a controversy about whether the emission is from the *n*-ZnO side [147, 376] or the *p*-GaN side [372, 377]. In reality, the hole concentration in the Mg doped *p*-GaN substrate (~10^{18} cm^{-3}) is higher than the electron concentration in the *n*-ZnO nanowire (~10^{17} cm^{-3}), but the carrier mobility in the *p*-GaN is smaller than in the *n*-ZnO. Also the barrier heights at the interface for the holes (0.57 eV) and for the electrons (0.59 eV) are comparable. In this case, the charge injection by electrons and holes should be comparable from both sides. Of course, the energy band offset at the ZnO/GaN interface is largely determined by the fabrication process [378], and any possible interfacial absorbates incorporated during the wet chemical growth [379].

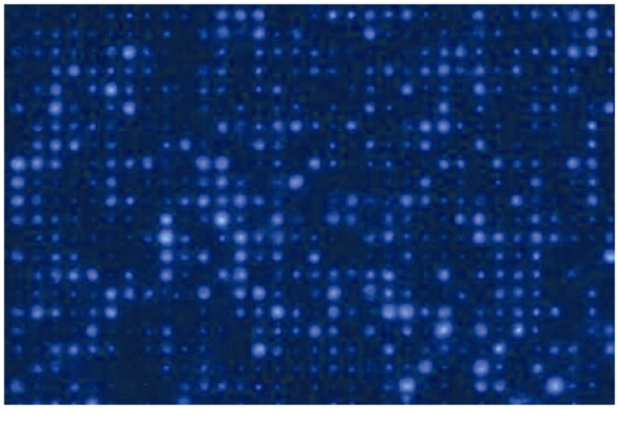

Figure 44 Optical image with artificial bluish color of a turned-on LED from ordered ZnO nanowire arrays grown on *p*-GaN thin film. The pitch is 4 μm and the resolution is 6350 dpi. [371]. Reproduced with permission

As shown in Fig. 45(a), the emission spectra of the *n*-ZnO nanowire/*p*-GaN thin film LED were monitored at different bias voltages at room temperature. From 4 V to 10 V, the dominant emission peak was slightly blue-shifted in the range 400–420 nm with a FWHM of about 60 nm. Peak deconvolution of the blue/near-UV emission with Gaussian functions (shown in the inset in Fig. 45(a)) showed that the broad blue/near-UV emission spectra consisted of three distinct bands (Fig. 45(b)) centered at 395–415 nm, 420–440 nm, and 450–510 nm. Each emission band corresponded to a particular recombination process [374]. The near-UV emission band centered at around 400 nm was attributed to the near-band-edge emission in ZnO nanowires originating from the recombination of ZnO free and bound excitons [377, 380]. Whereas the red-shifted violet emission band centered at about 430 nm was ascribed to the transitions from the conduction band or shallow donors to deep Mg acceptor levels in the *p*-GaN thin film substrate [372, 377, 380]. The blue emission at around 460 nm was assigned to the radiative interfacial recombination of the electrons from *n*-ZnO and holes from *p*-GaN [380–382]. The interface states generally act as nonradiative centers that annihilate free electrons and holes. Therefore, a high quality interface is required in order to obtain high efficiency LEDs. The weak red emission at around 790 nm comes from the native deep level point defects (oxygen vacancies and zinc interstitials) in ZnO nanowires [377]. It should be noted that the emission spectra could be changed by thermal annealing [380].

As the bias voltage was increased, the intensities of the main peak and of all of the four sub-bands increased exponentially and the bands were blue-shifted. The blue-shift has been attributed to several different factors, such as band renormalization and band filling [383], and the screening effect of the built-in

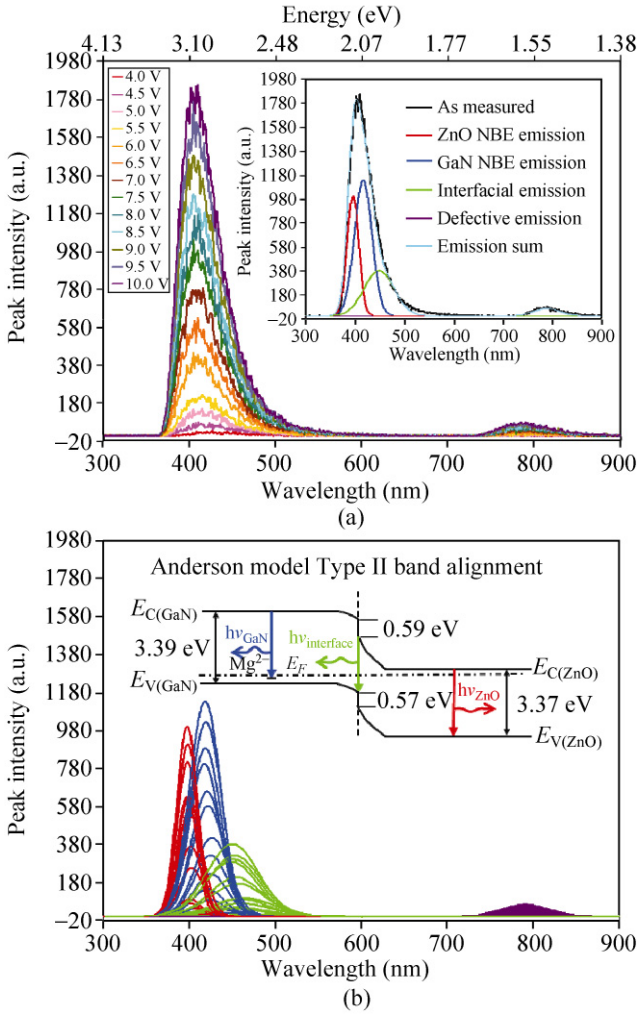

Figure 45 (a) Electroluminescence spectra as a function of the forward bias voltage. Inset shows how by Gaussian deconvolution analysis the blue/near-UV emission can be decomposed into three distinct bands that correspond to three different optoelectronic processes. (b) All of the four emission bands evolve as a function of the bias voltage. Inset schematics show the band diagram of the *n*-ZnO/*p*-GaN heterojunction under no or small bias voltage, where the three emission bands making up the blue/near UV band are indicated in different colors [371]. Reproduced with permission

piezoelectric field [384]. As shown in Fig. 46, the blue-shift of the emission peak came has two origins: the blue-shift in emission band positions, and the change in relative intensities of the luminescence at different injection currents [380]. The blue-shift of the ZnO and GaN near-band-edge emission positions (Fig. 46(a) i and ii) might be caused by the increasing kinetic energies of the electrons and holes as the bias voltage was increased. As the bias voltage was gradually increased, the kinetic energy of the free carriers going across the barrier was accordingly increased (assuming the mobility of the carriers did not change too much when the bias voltage was increased), which could contribute to the energy of the emitted photons. The most obvious blue-shift of the peak position came from the interfacial recombination process (Fig. 46(a) iii), which was simply because the increases in kinetic energies from both electrons and holes contributed to the interfacial recombination.

The blue-shift of the electroluminescence spectrum also resulted from the change in the relative intensity of the four bands, as shown in Fig. 46(b). The intensity of the GaN near-band-edge emission increased fastest among the four sub-bands. As the bias voltage was increased, the band bending of the *p*-GaN and *n*-ZnO was reduced, therefore the kinetic energies of the

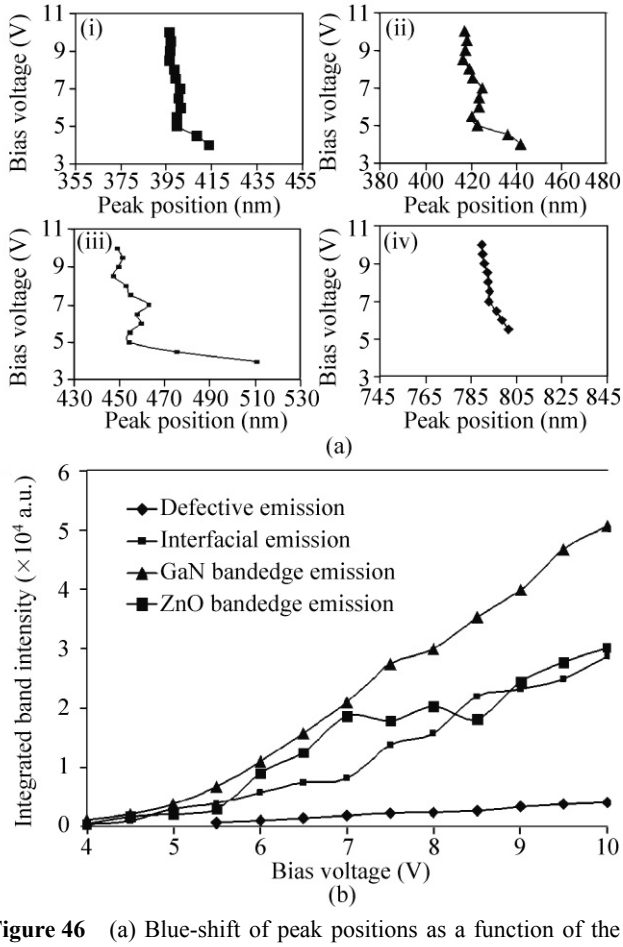

Figure 46 (a) Blue-shift of peak positions as a function of the bias voltage for (i) ZnO near-band-edge emission, (ii) GaN near-band-edge emission, (iii) interfacial emission, and (iv) defect emission. (b) The integrated emission band intensities as a function of the bias voltage. When the bias voltage is below 5.5 V, the defect emission can hardly be distinguished from the noise level [371]. Reproduced with permission

electrons and holes were increased giving them a much higher probability of going across the interface barrier and recombining at the other side. Comparison of the curve for ZnO near-band-edge emission and that for GaN near-band-edge emission (Fig. 46(b)) shows that, at low bias voltages (< 7.0 V), the ZnO near-band-edge emission had a competitive increase in intensity relative to GaN. As the bias voltage was increased, the ZnO near-band-edge emission fell behind that of GaN. In comparison with a high quality GaN thin film fabricated by MOCVD, the relatively high level of native defects in the hydrothermally grown ZnO nanowires undermines its internal quantum efficiency, especially when the bias voltage is relatively high. These point defects in the ZnO nanowires act like trapping centers and give rise to nonradiative recombinations.

6.5.2.3 *Inorganic–organic hybrid LEDs*

ZnO nanowire arrays can be grown on flexible polymer substrates at low temperature and low cost on a large scale by electrochemical deposition [385, 386] or seeded growth [95]. When filled with insulating polymers as a supporting matrix, these ZnO nanowires can hybridize with *p*-type organic polymers to give flexible and foldable LEDs or materials for photovoltaic applications [249]. This provides an interesting alternative to all-organic counterparts. In fact, they are probably superior to their all-organic counterparts in the sense that the active optical component in such hybrid structures is the inorganic material, which usually has a higher carrier mobility and lifetime than organic materials [386]. Also, stability in air may be better than for all-organic devices [385, 387].

Konenkamp et al. demonstrated a ZnO nanowire/polymer hybrid LED [385]. The device structure is illustrated schematically in Fig. 47(a). ZnO nanowire arrays were grown on fluorine doped tin oxide (FTO) glass by electrochemical deposition. Similar arrays can also be achieved on flexible polymer substrates [249, 386, 388]. Annealing at around 300 ℃ helps to increase crystallinity and surface roughness of the nanowires, which leads to an increase in the excitonic emission of the electroluminescence. Addition of $AlCl_3$ to the deposition electrolyte was found to improve the conductivity of the nanowires, resulting in an increased emission intensity [249]. During the electrodeposition

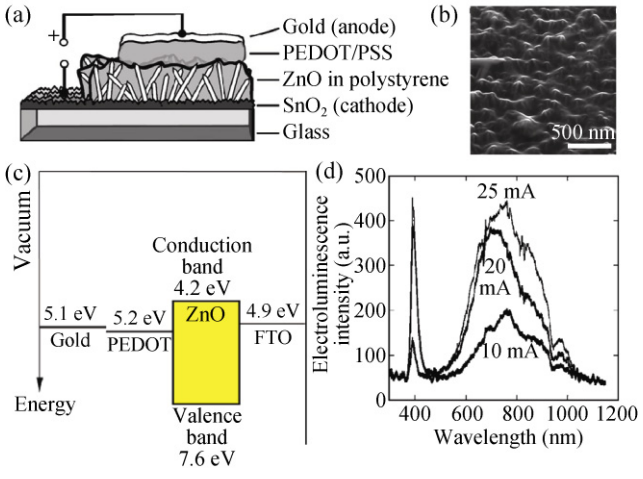

Figure 47 (a) Schematic diagram of a hybrid LED structure [385]. (b) SEM image of the ZnO nanowires embedded in an insulating polymer matrix [385]. (c) Energy levels of the components in the hybrid LED [386]. (d) Electroluminescence spectra at different injection currents obtained at room temperature in air. The labeled current values are for a device area of 0.3 cm^2, and the ZnO nanowires have been annealed [386]. Reproduced with permission

process, electrons flowed continuously from the FTO substrate to the ZnO nanowires, so good contact was formed between the nanowires and the underlying substrate. The nanowires were then encapsulated with a thin layer of insulating polymer as shown in Fig. 47(b), which is often the case when making top electrodes of nanowire arrays. Polymers adhere well to the oxide surfaces, and by adjusting the spin speed, the polymer molecular mass, and the polymer concentration, the thickness of the polymer on the nanowire tip can be varied from 10–50 nm, which is sufficiently thin that electric transport through the layer can occur via electronic and structural defects [385, 388]. Oxygen plasma can also be used to etch away the polymer on the nanowire tip and expose fresh ZnO nanowire tips [386].

A diode was fabricated by spin/spray coating a layer of strongly *p*-doped poly(3,4-ethylene-dioxythiophene)/poly (styrenesulfonate) (PEDOT:PSS) on top of the nanowire tips. Typically the *p*-type polymer layer was about 1 μm in thickness. Top contact to the *p*-type polymer was made by depositing a semitransparent layer of Au that needs to be thin enough to allow light transmission yet thick enough to maintain its conductance integrity. The similarity between the

photoluminescence and the electroluminescence spectra of the annealed ZnO nanowire indicated that the ZnO nanowires were the active material where radiative electron and hole recombination took place. The energy level diagram is shown in Fig. 47(c). There was a 2.4 eV barrier for hole injection from the PEDOT:PSS to the ZnO valence band edge. Multiple layers of *p*-type polymers were used between PEDOT:PSS and ZnO as band offset stepping layers to ensure effective hole transport and electron blocking [389, 390]. There was a 0.7 eV barrier for electron injection from the FTO to the ZnO conduction band edge, so a minimum forward bias voltage of 3.1 V was required to drive the device. Luminescence was observed experimentally at around 5 to 7 V. In the operational voltage regime, the injection current was found to be proportional to the square of the bias voltage, which can be explained by the space-charge-limited injection [249]. Fitting the experimental data with the Mott–Gurney law suggested that the ZnO nanowires are trap-free [249]. High voltage (~40 V) scanning has been shown to be beneficial for electrical conductance by virtue of its effect at the interfaces of the different layers [385]. The emission spectra of the hybrid LED after the ZnO nanowires were annealed are shown in Fig. 47(d) [386]. The emission covers most of the visible range, giving rise to a white color. In addition, there was a narrow UV band centered at 393 nm with a FWHM of about 24 nm. Even without further encapsulation, the device was shown to be stable over 1 h under ambient conditions [385].

Beside PEDOT:PSS, other *p*-type polymers have also been used as the hole injection layer, such as poly(3-methylthiophene) [391] and many others [392]. Sun et al. used *N*,*N*′-di(naphth-2-yl)-*N*,*N*′-diphenylbenzidine (NPB), for which the lowest unoccupied molecular orbital is at a higher level than that of PEDOT:PSS, and enhances hole transport as well as electron blocking. Electrons cannot flow from ZnO to NPB and are accumulated on the ZnO side near the ZnO/NPB interface, and gradually fill up the conduction band of ZnO, which eventually results in a blue-shifted and broadened excitonic emission at 342 nm [393].

6.5.2.4 Schottky diode-based LEDs

Like *p*–*n* junctions, Schottky diodes can also produce electroluminescence under bias, which was first experimentally observed for SiC [394]. Since then, Schottky diode-based LEDs have been reported for various materials under either forward or reverse biases, including ZnSe [395, 396], porous Si [397], GaN [398], as well as ZnO nanowires and nanotubes [399–401].

The working principle of Schottky type LEDs is illustrated in Fig. 48. To take a *n*-type ZnO nanowire/Au electrode as an example, a Schottky diode is formed under equilibrium. When under forward bias above the threshold voltage, electrons will diffuse from the ZnO into the Au. When the forward bias is further increased, of course more electrons will diffuse across the interface. It is also possible that holes will be injected from the Au into the ZnO valence band when the ZnO valence band is above the Au Fermi level under high forward bias voltage. To put it in a different way, electrons are injected from the ZnO valence band to the Au, leaving holes in the ZnO valence band. These holes will then recombine with electrons giving rise to near-band-edge emission. When the Schottky diode is strongly reverse biased, electrons can tunnel through the Schottky barrier and inject into the ZnO conduction band. These energetic electrons will cause impact ionization which generates more electron and hole pairs by an avalanche effect. Electron and hole radiative recombination enables near-band-edge emission in ZnO.

In the study by Wang et al., the Schottky diode was formed between ZnO nanowire arrays and a semi-transparent Au top electrode [399]. Electroluminescence was observed at a forward bias voltage of 6 V at room temperature. The electroluminescence spectrum consisted of two peaks: one centered at 392 nm and the other at 525 nm, corresponding to excitonic near-band-edge and defect emission, respectively [399]. The electroluminescence near-band-edge emission (392 nm in this case) was red-shifted in comparison with the photoluminescence peak (378 nm in Fig. 40(a)). This was because structural defects, such as point defects and surface dangling bonds in nanowires, can form band-tail states near the band edge. The amount of excess carriers injected by the electric current is far less than that excited by the laser. As a result, the low density of electrically injected carriers mainly fill the band-tail states, leading to the red-shift of near-band-edge emission [402].

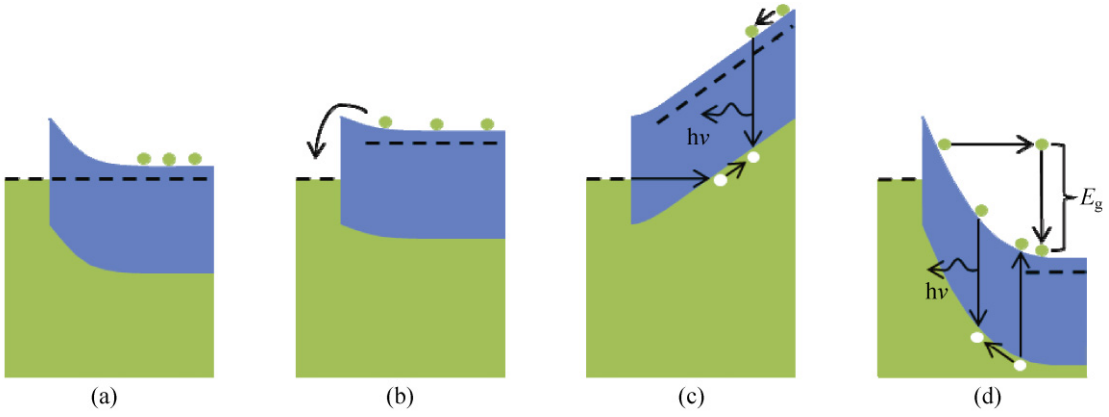

Figure 48 Schematic band diagrams showing the working principle of Schottky diode-based LEDs. (a) Under equilibrium, (b) under forward bias above the threshold, (c) under strong forward bias, and (d) under strong reverse bias

6.5.2.5 *Light extraction*

Due to the high refractive index of the active materials, flat thin film-based LEDs suffer from low light extraction efficiency limited by the total internal reflection [403]. Extensive efforts have been made to tackle this problem, such as roughening the emitting surface of the thin film [404, 405], reshaping the geometry of the LED architecture [406, 407], utilizing a resonant cavity [408], coupling with surface plasmons [409], fabricating photonic crystal structures [410, 411], and using corrugated Bragg gratings [412]. Nanowire/thin film heterostructures have been proposed to be a promising solution, considering the waveguiding properties of the nanowires that should enhance light extraction efficiency of the LED's [9, 413–418].

For the case of a ZnO nanowire/GaN substrate configuration, under single mode waveguide cavity conditions [419, 420], 86.5% of the light can be confined within a nanowire of diameter of 223 nm:

$$V = 2\pi \frac{a}{\lambda_o}\left(n_1^2 - n_2^2\right)^{\frac{1}{2}} = 2.405$$

where V is the single mode cut-off value, a is the diameter of the nanowire, λ_o is the wavelength of the propagating light (~400 nm), and n_1 and n_2 are the effective refractive index of the ZnO nanowire and the cladding PMMA thin film, respectively [371]. The facets of the nanowire were assumed to be perfectly flat under the single mode conditions. In reality, the nanowires which were grown by wet chemical methods usually had rounded tips and rough surfaces, large surface to volume ratio, and thus a high density of surface states near the band edge, which allowed a large reduction in the back reflections at the ZnO nanowire surfaces, known as the omnidirectional reflector effect [421]. The refractive indices of GaN, ZnO, PMMA, and air are 2.49, 2.10, 1.59, and 1.00, respectively. Based on the effective medium theory, graded refractive indices can largely reduce the Fresnel reflection between GaN/ZnO, ZnO/PMMA, and PMMA/air interfaces, which should benefit optical transmission. By virtue of such advantages provided by the nanowires, the light can easily be extracted by multiple scattering. ZnO had a transmittance of over 90% in the visible range [414], so self-absorption by the nanowires should not be a major concern.

Figure 49 shows the room temperature external quantum efficiency (calculated by from the ratio of the output light power to the input electrical power) versus d.c. injection current for the nanowire/thin film heterostructure LED [371]. The external quantum efficiency of the LED was about 2.5%, which is very high for a single *p*–*n* junction-based LED. As the bias voltage/injection current was gradually increased, the external quantum efficiency became steady, indicating that the serial resistance or the nonradiative recombination through the defects, e.g., Auger recombination, did not increase in proportion with the increasing injection current.

The patterned ZnO nanowire arrays formed a quasi 2D photonic crystal, which potentially have a photonic band gap for light traveling parallel to the surface of

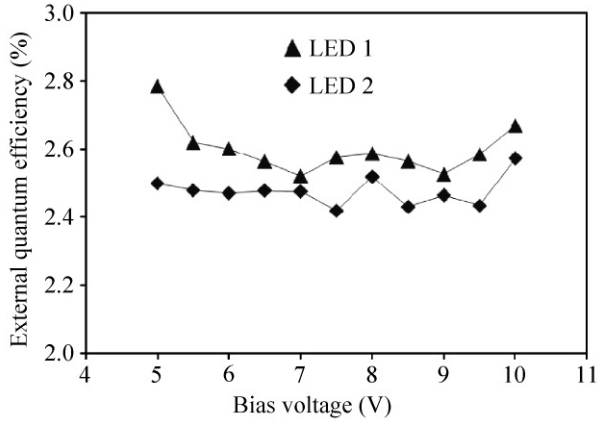

Figure 49 External quantum efficiencies of two ZnO nanowire/GaN thin film heterostructural LEDs as a function of the bias voltage/injection current [371]. Reproduced with permission

the substrate. Therefore by controlling the pitch of the nanowire array, it might be possible to match the wavelength of the electroluminescence to the band gap of the photonic crystal. Kee et al. used finite difference time domain simulations to show the light propagation behavior within the photonic crystal [340]. Figure 50 shows the spatial distribution of a TM mode electric field in a quasi-2D triangular ZnO nanowire photonic crystal, when the photon frequency is inside and outside the photonic band gap. When the photon frequency was outside the photonic band gap, the photon propagated freely in any in-plane direction. When the photon frequency was inside the photonic band gap, however, the photon did not propagate, all in-plane guiding modes were decayed to zero, and the photons were coupled entirely to the free space modes. This resulted in an enhanced extraction efficiency, and also light emission in a normal direction [340].

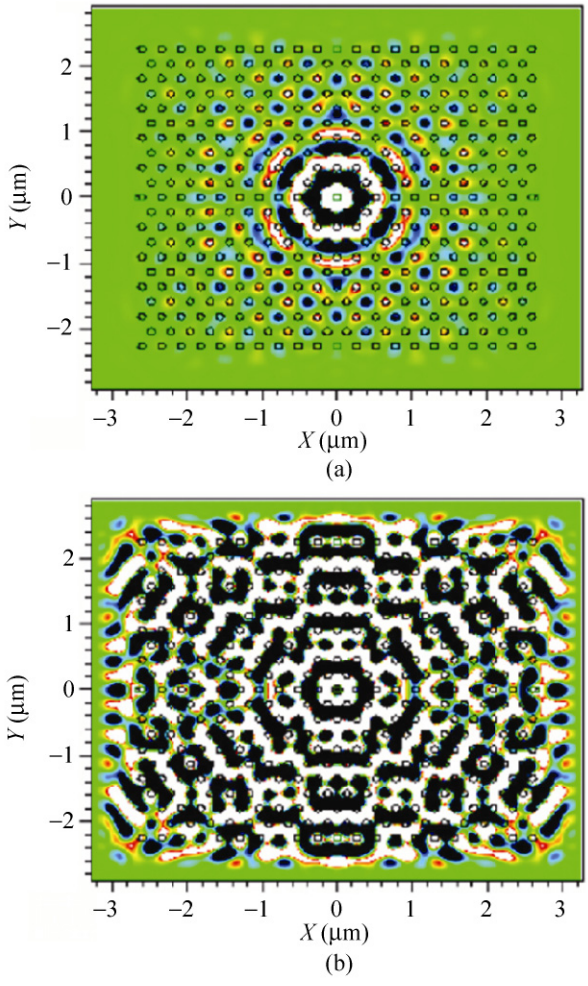

Figure 50 Spatial distribution of the electric field radiated from a point source at the center of a 2D triangular ZnO nanowire photonic crystal, when the frequency of the photon is (a) inside and (b) outside the photonic band gap [340]. Reproduced with permission

6.6 Electrochromic displays

Electrochromic devices undergo color change on charge injection or extraction driven by an external voltage [423]. They have low cost and low power consumption, high coloration efficiency, and memory effects under open circuit states. There are generally four categories of electrochromic devices [424]. Sun et al. demonstrated a fast-switching electrochromic device based on a viologen-decorated ZnO nanowire array electrode [422]. The schematic structure of the device is shown in Fig. 51. The ZnO nanowires were grown on a

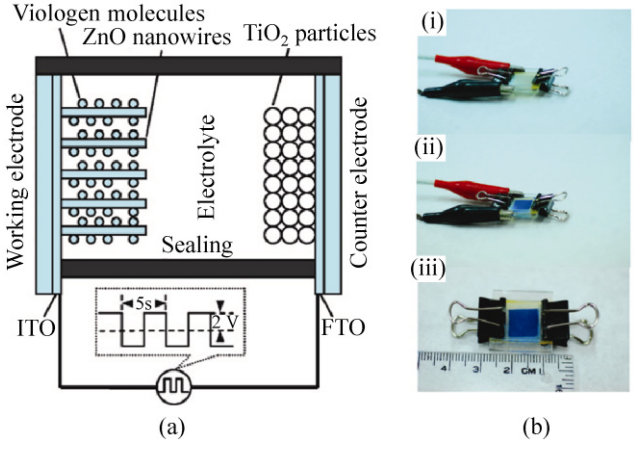

Figure 51 (a) Schematic structure of the electrochromic device, and (b) photographs of the electrochromic device (i) before and (ii) after applying an external voltage, and (iii) at the open circuit state [422]. Reproduced with permission

transparent conductive substrate by a wet chemical method. Then the organic chromophore—methyl viologen molecules in this case—were loaded onto the nanowires by immersing them in a methyl viologen solution. Unattached viologen molecules were rinsed away, and only those that were physically/chemically adsorbed on the nanowire surface were left to ensure a direct charge transport between the nanowire and the viologen molecule. Therefore the switching speed of the device was very fast, and the nanowire itself provided a direct charge transport path. The electrolyte was made of $LiClO_4$ in γ-butyrolactone. The nanowires decorated with viologen molecules were used as the working electrode, which was sealed together with a reference electrode since the redox reaction of the viologen molecules is sensitive to oxygen. When under negative bias, the viologen molecules were reduced and become deep blue within about 170 ms, and the color was retained for over 1 h after the bias was removed. When under positive bias, the bluish color was bleached within about 142 ms. The switching time became shorter for larger bias voltage and smaller device size. The device performance was also dependent on the nanowire density [425].

6.7 Field effect transistors

Field effect transistors (FETs) based on a single ZnO nanowire [426] or ZnO nanowire thin films [427] have been fabricated for use in optically transparent mechanically flexible electronics [428, 429]. The fact that ZnO nanowires can grow *in situ* between the source and drain electrodes is one of the merits of low temperature wet chemical methods [283, 430, 431]. Ko et al. demonstrated an all-solution fabrication process for a ZnO nanowire transistor on polymer substrates, as shown in Fig. 52(a) [430]. The source and drain electrodes were fabricated by nanoimprint lithography of Au nanoparticles followed by low temperature soft annealing. ZnO nanoparticles were applied to the patterned Au electrodes, and later seeded the growth of ZnO nanowires. Depending on the channel width between the source and drain electrodes, the ZnO nanowires could grow and connect the two electrodes through forming complex nanowire networks, as shown in Fig. 52(b). Even though there is a work function mismatch between Au (5.1 eV) and ZnO (4.5 eV), the

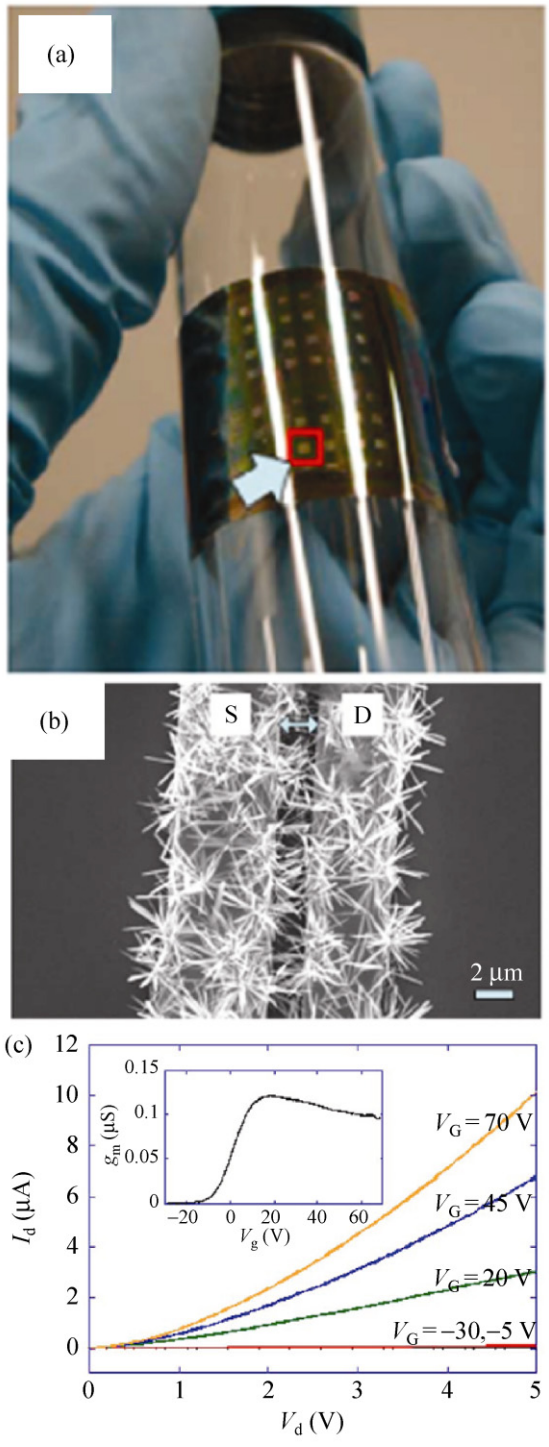

Figure 52 (a) A digital photograph of ZnO nanowire transistor arrays on a flexible substrate. The red square includes an array of thirty-six transistors. (b) SEM image of the ZnO nanowires grown *in situ* between the source and drain electrodes. (c) Output characteristics of eighteen ZnO nanowire transistors with 10 μm channel length. The inset shows a plot of transconductance as a function of gate voltage [430]. Reproduced with permission

contact between them should be ohmic because during the wet chemical growth process, the interface is not perfect. Therefore the transport properties are not determined by the intrinsic work function difference, but rather by the interfacial defect states [432]. The output characteristics and averaged transconductance g_m are shown in Fig. 52(c), which shows an *n*-type channel with an on/off current ratio of 10^4–10^5. The maximum value of g_m was about 100 nS. The mobility μ_e of the electrons in the nanowire was calculated to be 0.2 $cm^2/V{\cdot}s$, according to $\mu_e = g_m^2 L/2I_d C_{ox} W$, where C_{ox} is the gate capacitance, and L and W are the channel length and width, respectively. Konenkamp et al. reported that the carrier mobility in the undoped ZnO thin film was as high as 23 $cm^2/V{\cdot}s$ [118], but that was probably due to the nanowire surface state scattering-induced decrease in electron mobility. The ZnO nanowire transistor did not show a saturation regime as the drain voltage was increased, probably because of the dominant phonon scattering and the impurity-derived grain boundaries in the bridged ZnO nanowires [431]. Of course, the FET characteristics were dependent on the alignment of the ZnO nanowires [427].

6.8 Sensors

ZnO nanowires have been used as active components in gas sensors [167, 168, 433], visible light sensors [434], visible-blind UV sensors [95, 280, 435], biosensors [94, 436], and strain sensors [437]. These depend on the resistance or piezoresistance change of the nanowires [438], or the barrier height change at the contact [15–17, 437, 439], or are based on the heterostructured *p*–*n* diodes [434].

ZnO is amphoteric, with a isoelectric point of about 9.5 [54]. The ZnO surface will be functionalized with protons H_3O^+ or hydroxyl OH^- groups with different ζ potentials, when the pH value is lower or higher than the isoelectric point, respectively. By utilizing ZnO nanowires as an electrochemical probe, Al-Hilli et al. reported an intracellular pH sensor [440]. The benefits of using ZnO nanowire arrays are that they have high surface to volume ratio and offer high sensitivity and real-time detection. In Al-Hilli's experiment, ZnO nanowire arrays were grown on a sharp borosilicate glass tip as the working electrode, and Ag/AgCl was used as the reference electrode. The basic working principle is that a pH change in the surroundings leads to a surface potential change in the nanowire, which is detected as a voltage change between the working and reference electrodes. The two electrodes were first calibrated with standard pH buffer solutions at room temperature. As shown in Fig. 53(a), the electrochemical potential between the two electrodes was almost linearly proportional to the buffer electrolyte pH within the pH range 4–11, with a sensitivity of about 52 mV/pH. The authors noted that the ZnO nanowires were thermodynamically stable over the tested pH range at room temperature [440]. For the measurement of intracellular pH value, both electrodes were then pushed to penetrate the membrane of a human fat cell. As shown in Fig. 53(b), the two electrodes were in direct contact with the cell cytoplasm, and the intracellular pH value was read to be 6.81. ZnO is

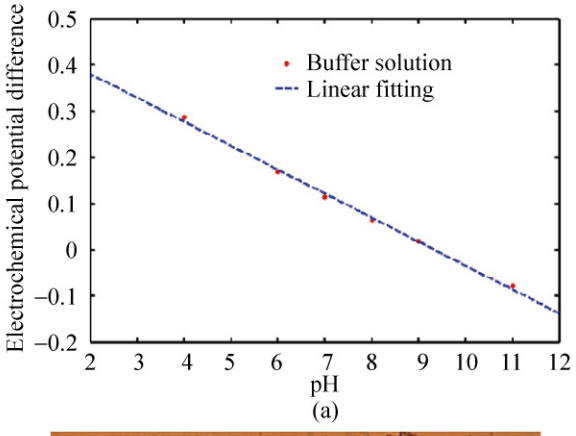

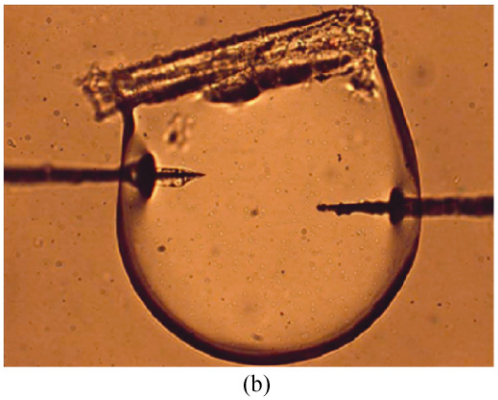

Figure 53 (a) Calibration curve of the two electrodes in standard buffer solution. (b) Optical image showing the intracellular pH measurements in a single human fat cell [440]. Reproduced with permission

nontoxic and biocompatible [441, 442]. The intracellular measurement did not visibly affect the cellular viability so this technique could be a good way of *in situ* pH measurement in single living cell.

6.9 Energy harvesting devices

ZnO nanowire arrays are playing a very active role in energy harvesting technologies nowadays. Preliminary proof-of-concept devices include solar cells, piezoelectric nanogenerators, and water splitting devices, as shown in the following sections.

6.9.1 Solar cells

Silicon-based conventional solar cells have low defect densities and high carrier mobilities, and currently dominate the solar energy industry due to the relatively high energy conversion efficiency and well-developed fabrication technologies [443]. Extensive studies of other inorganic and organic materials have been carried out with the aim of further reducing the cost per unit energy output. ZnO nanowire arrays are good candidates in particular for solar cell applications for three straightforward reasons: they have low reflectivity that enhances the light absorption, relatively high surface to volume ratio that enables interfacial charge separation, and fast electron transport along the crystalline nanowires that improves the charge collection efficiency. ZnO nanowire arrays have been implemented for both conventional *p*–*n* junction solar cells and excitonic solar cells (including organic, hybrid organic–inorganic, dye-sensitized, and nanoparticle-sensitized solar cells), as discussed individually in the following sections.

6.9.1.1 Enhancement of light absorption

Antireflection coating layers play an important role in enhancing the device efficiency by increasing the light coupled with the active region of the solar cell [50, 118, 138, 444]. ZnO is attractive for this purpose because of its good transparency, appropriate refractive index ($n \approx 2$), and controllable textured growth [444].

Lee et al. reported that highly textured ZnO nanorod arrays synthesized by a low temperature solution growth method could be used as an efficient antireflective coating [444]. The fundamental principle is that the intricate distribution and the textured surface of the nanorods ensures a gradual reduction of refractive index from the surface to air, and leads to impedance matching between the substrate and air, which results in photon trapping and reflection suppression over a broad wavelength range. In Lee's study, by changing the growth conditions in the presence of 1,3-diaminopropane, the shape of ZnO nanorod tips could be modified and slight changes in the tip morphology gave rise to significant changes in antireflection properties. The experimental result was in agreement with simulations by rigorous coupled wave analysis. The reflectance spectra in Fig. 54 show the significant effect on the reflectance of five different samples: sol–gel thin film, an optimized SiN antireflection coating on a Si solar cell, a flat top nanorod array, tapered nanorod array, and a highly tapered nanorod array [444]. To quantify these reflectance curves, weighted reflectance was used. As can be seen from the spectra, the highly tapered nanorod resulted in the strongest broadband suppression of reflectance, with a weighted reflectance value of 6.6% (black curve). Compared with the flat top nanorod array (red curve), the less tapered nanorod array (orange curve) eliminated the optical interference fringes due to a variation in nanorod length and the ragged ZnO–air

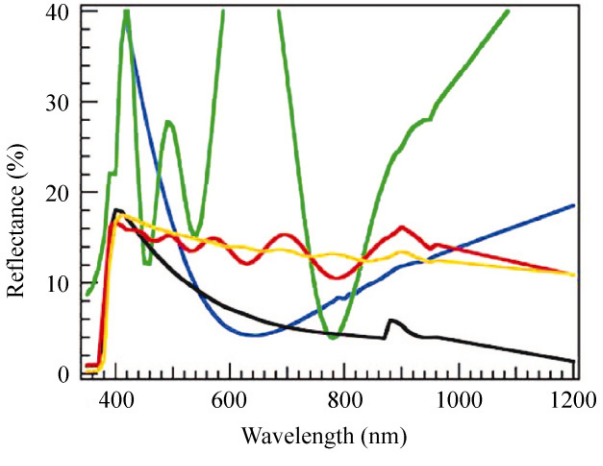

Figure 54 Reflectance spectra of five different samples: sol–gel thin film (green), optimized SiN antireflection coating on Si solar cell (blue), flat top nanorod array (red), tapered nanorod array (orange), and highly tapered nanorod array (black). The little bumps at around 900 nm on the curves arise from the detector change of the equipment during the date collection [444]. Reproduced with permission

interface. The optimized SiN antireflection coating on the Si solar cell (blue curve) exhibited a highly wavelength-dependent reflectance response with a minimum at around 640 nm due to destructive interferences. The sol–gel thin film had a stepwise change of refractive index from the substrate to air, and has the highest weighted reflectance (green curve) [444].

6.9.1.2 *Dye sensitized solar cells*

High efficiency dye sensitized solar cell (DSSC) have been reported based on TiO_2 nanoparticle thin film [445]. In conventional *p*–*n* junction solar cells, the semiconductor has the dual functions of light absorption and free carrier transport, whereas in DSSCs the two functions are decoupled. The working principle of a DSSC is shown in Fig. 55. The dye molecules, typically ruthenium complexes [445], or indolene dyes [217], absorb incident photons, go from ground state to excited state, and inject electrons into the conduction band of the semiconductor. The oxidized dye molecules are then quickly neutralized by the redox couples in the electrolyte (typically I^-/I_3^-), driven by the energy difference between the oxidized dye and the redox couple, which prevents the recapture of electrons from the excited state to the ground state of the dye molecules [446]. The electrons are collected by the semiconductor, flow through the external circuit doing useful work, and return to the counter electrode where the redox couples are reduced and replenished.

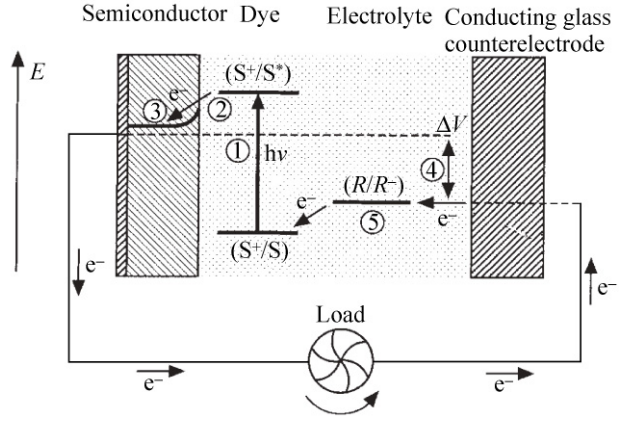

Figure 55 Schematic working principle of a DSSC [445]. Reproduced with permission

Electrons percolate in the sintered TiO_2 nanoparticle networks via a series of trap-limited interparticle hopping steps, which greatly decreases the lifetime and diffusion length of the free electrons. Drift transport is prevented to a certain degree in a DSSC because the macroscopic electric field is screened by ions in the electrolyte. In such a case, the electrons must cross an estimated 10^3–10^6 TiO_2 nanoparticles to reach the substrate electrode [447]. A typical ambipolar diffusion length for the electrons is about 7–30 μm, so it is disadvantageous to increase the thickness of the active region in the hope of increasing the light absorption.

Electron transport in oriented crystalline nanowires is expected to be several orders of magnitude faster [448, 449]. The transportation time is on the order of tens of microseconds as revealed by intensity-modulated photocurrent studies [450], by virtue of the high nanowire crystallinity and in particular an internal electric field that assists the exciton separation and charge collection [18, 447]. Based on this idea, Law et al. demonstrated a DSSC based on dense vertically aligned ZnO nanowires, and the efficiency was boosted up to 1.5% at a full sun intensity, as shown in Fig. 56(a) [18]. It was shown that nanowires of aspect ratio less than 70 have similar internal quantum efficiencies, indicating that electron transport in the nanowires is not a limiting factor [451]. In spite of their inferior optical properties, hydrothermally grown nanowires exhibited even higher power conversion efficiency than vapor phase grown nanowires due to higher dye adsorption [452]. Other than that, the benefits of nanowires over nanoparticle thin film also include the efficient kinetic electron injection into the nanowires due to the surface fields [222]. Femtosecond transient absorption spectroscopy studies have shown that electron injection from photoexcited ruthenium dyes into nanowires with mainly nonpolar side facets has a much smaller time constant than that for nanoparticles with an ensemble of random surfaces [18]. Also, the nanowires were directly grown on top of the substrate, which ensured an intimate contact for electron transport between the nanowires and the substrate. In addition, a nanowire morphology has a higher resistance to crack formation and propagation than nanoparticle thin films, due to the efficient release of bending stress, which is promising for applications in stable flexible solar cells [453].

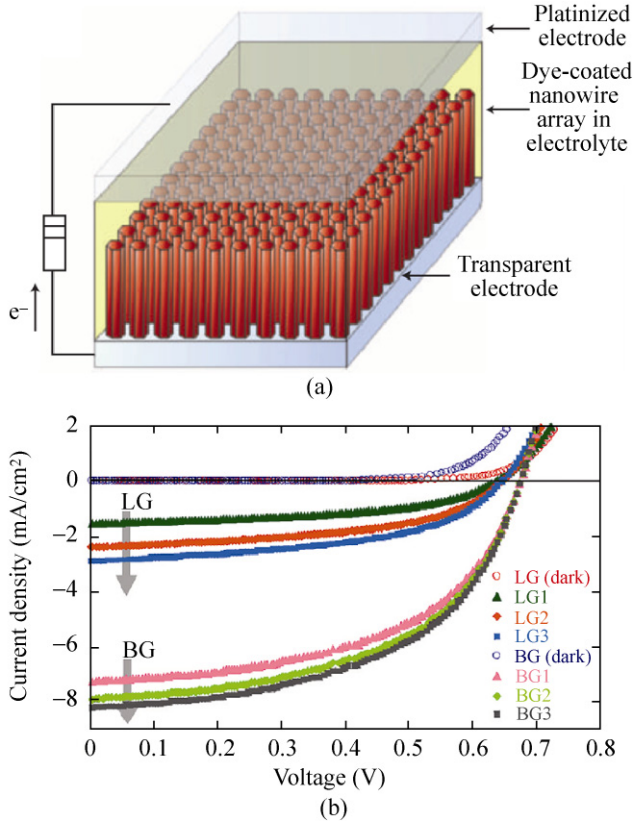

Figure 56 (a) Schematic diagram of a ZnO nanowire array DSSC [18]. (b) *J*–*V* curves of a DSSC based on hierarchical ZnO nanowire "nano-forest" with increasing lengthwise growth (LG) and branched growth (BG) [199]. Reproduced with permission

One downside with nanowire array DSSCs is that their internal surface area was found to be only one fifth of that of the nanoparticle thin film [18], which largely limits the cell efficiency [454], so it is helpful to make thinner, longer, and denser nanowires in order to increase the dye loading and the light absorption, and eventually to boost the efficiency. In this regard, studies on nanotubes [455, 456], nanoparticle/nanowire composites [453, 457–460], hierarchical [199, 461] structures [209, 462–464], and different growth parameters [465] have been shown to give several-fold increases in efficiency (Fig. 56(b)).

Conventional solar cells are 2D. The limited surface area significantly constrains the light absorption efficiency. Adopting a different approach, Weintraub et al. demonstrated a three dimensional (3D) DSSC [20]. As shown in Fig. 57(a), the ZnO nanowires were grown surrounding an optical fiber surface. The light was shone onto the fiber from one end along the axial direction, and underwent multiple interactions with the active materials due to internal reflection within the fiber (Fig. 57(b)), which greatly increase the effective propagation distance and absorption efficiency of the photons. At the same time, the distance electrons had to travel to reach the collecting electrode remained the same. The energy conversion efficiency of the 3D DSSC was enhanced by a factor of up to six compared with the same device when illuminated normal to the optical fiber axial direction. Also, the 3D DSSC could be concealed and located away from the surface, therefore allowing applications at remote locations such as underground or in deep water. Wei et al. extended this strategy one step further by integrating multiple stacks of planar optical waveguides with nanowires [21].

DSSCs offer several manufacturing advantages, including their simple production process, low cost, non-toxicity, and a variety of material resources to choose from [466]. Compared with other solar cells, DSSCs have relatively high efficiency under weak light illumination, so they can be used for internal applications, such as in laptops and mobile phones [466]. The low efficiency of ZnO-based DSSCs probably arises for four reasons: the accumulation of stable Zn^{2+}/dye complexes instead of chemisorption of the

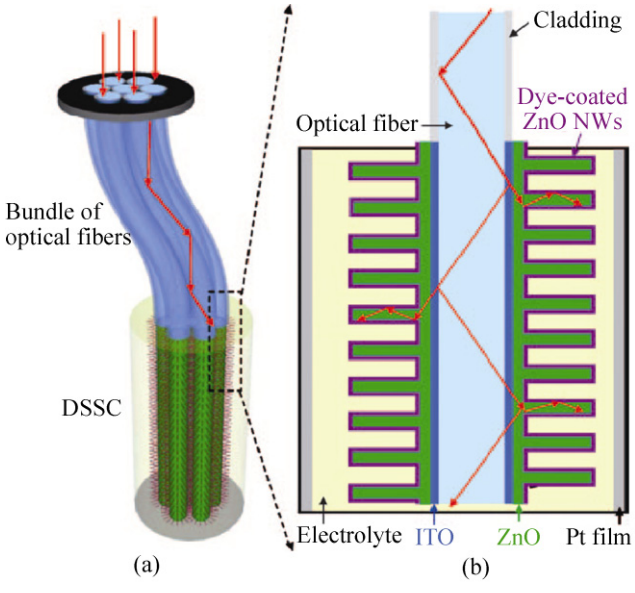

Figure 57 (a) Schematic design and working principle of a 3D DSSC, and (b) illustration of the multiple interactions with the active materials along the optical fiber [20]. Reproduced with permission

dye molecule on ZnO [463]; the low electron injection efficiency induced by the energy level mismatch between the lowest unoccupied molecular orbital (LUMO) of the dye and the photoanode conduction band minimum; the dye regeneration efficiency induced by energy level mismatch between the highest occupied molecular orbital (HOMO) of the dye and the redox mediator potential in the electrolyte [458, 463]; the high carrier recombination rate due to the defect surface trap states of ZnO nanowires [467], which can be decreased by coating with TiO_2, Al_2O_3, or ZrO_2 passivating shells [222, 468].

6.9.1.3 Quantum dot-sensitized solar cells

Instead of photosensitive dyes, narrow band gap semiconductor quantum dots, such as CdS [469], CdSe [454], and CdTe [470] have also been used to sensitize ZnO nanowires for use in solar cells. ZnO has a large direct band gap of 3.37 eV and is transparent in the visible region. Narrow band gap semiconductor materials can absorb visible light in a complementary fashion, and enable the solar cell to cover a wider spectral range. In comparison with organic dyes, quantum dots have several advantages. First, the band gap and thus the absorption spectrum of quantum dots can be tailored by varying the semiconductor material, dot size, or annealing temperature [471], and can be tuned to match the solar spectrum and maximize the light absorption, as shown in Fig. 58(a) [472]. Second, quantum dots have been demonstrated to be able to produce multiple electron–hole pairs per incident photon, which improves the internal quantum efficiency of the device [473, 474]. Third, semiconductors, such as CdS [469] and CdSe [454], typically form a type II heterojunction with ZnO, and the presence of numerous interfaces between the quantum dots and the ZnO nanowires is greatly beneficial to both light absorption and charge separation. As shown in Fig. 58(a), the surface photovoltage increased with increasing loading of CdS quantum dots on ZnO nanowires [472]. Following this strategy, quantum dots sporadically dispersed on the nanowire were replaced with core–shell structures of different materials, such as CdS [475], CdSe [211, 212], and CdTe [213, 476], to further enhance the device efficiency.

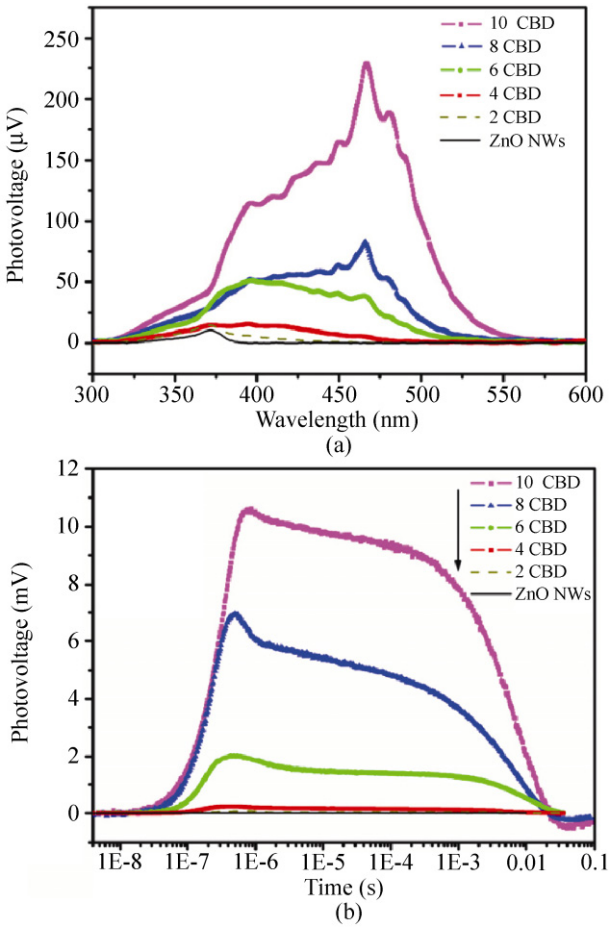

Figure 58 (a) Surface photovoltage spectra and (b) transient photovoltage spectra of ZnO nanowire arrays before and after different numbers of chemical bath deposition (CBD) cycles with CdS quantum dots [472]. Reproduced with permission

Electron–hole pairs are generated when incident photons are absorbed by the quantum dots. The electron–hole pairs are confined inside the quantum dots and then separated at the interface, which prevents their recombination. For a typical type II band alignment, electrons are injected from the quantum dot excited state to the ZnO conduction band, gaining the energy benefits of the difference in electron affinity. Holes are left in the quantum dot which are neutralized by hole conductors or redox couples in the electrolyte, provided that the quantum dot valence band edge is below the hole conductor HOMO or the reductant level of the redox couple. A similar analysis applies when the electron–hole pairs are generated inside the ZnO nanowires. The charge separation at the quantum dot/nanowire interface is facilitated by the overlap between the quantum dot electronic states

and the ZnO electronic bands [454], and normally occurs on a subnanosecond time scale [454], which is shorter than the exciton lifetime. As shown in Fig. 58(b) [472], transient photovoltage studies indicated that the carrier lifetime increased dramatically from microseconds for bare ZnO nanowires to milliseconds for ZnO nanowires coated with a CdS sensitizer. Furthermore, as the amount of CdS sensitizer increased, the carrier lifetime increased accordingly [472]. The quantum dots are usually capped with ligands that can form chemical bonds with the ZnO nanowire surfaces. Therefore the ligand molecule length influences the charge transfer rate at the interface, with short chain lengths having faster transfer rates [477].

6.9.1.4 *Inorganic p–n junction solar cells*

The built-in electric field at the interface of *p–n* junctions divorces the photon-excited electron–hole pairs, and provides the basis for conventional inorganic *p–n* junction solar cells. This is also one of the fundamental differences between conventional *p–n* junction solar cells and excitonic solar cells: free electrons and holes in conventional solar cells, and excitons (an electron–hole pair tightly bound via coulombic forces) in excitonic solar cells. Another fundamental difference is that the open circuit voltage in conventional cells is limited to less than the magnitude of the band bending, while in excitonic solar cells the open circuit voltage is commonly greater than the band bending.

While ZnO *p–n* homojunction solar cells have rarely been reported due to the lack of stable *p*-ZnO materials, heterojunctions have been employed as an alternative. Cui et al. demonstrated solar cells based on *n*-ZnO/*p*-Cu_2O nanopillar arrays fabricated by a low cost electrodeposition method [478]. The device structure is shown in Fig. 59(a). The top *p*-Cu_2O layer is the absorber due to its narrow band gap of 2.1 eV. This configuration maximizes the interface area while maintaining the direct fast transport of electrons along the nanowires, which is reflected by the relatively high short circuit current density in comparison with their thin film counterparts, as shown in Fig. 59(b). The small open circuit voltage was attributed to the dominance of differently exposed crystal facets of the nanowires [478], as also evidenced by surface photovoltage studies [479]. The energy conversion efficiency

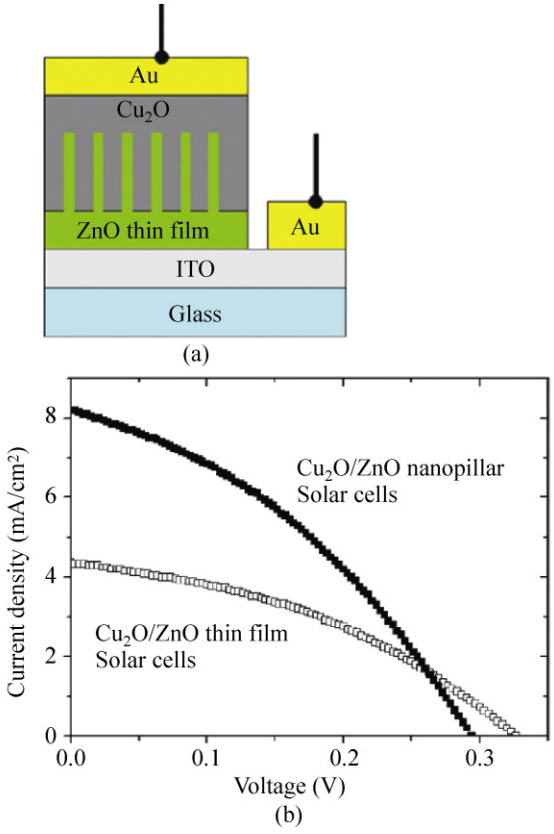

Figure 59 (a) Schematic structure of a *n*-ZnO/*p*-Cu_2O solar cell. (b) Typical *I–V* characteristics of *n*-ZnO/*p*-Cu_2O nanopillar and thin film solar cells [478]. Reproduced with permission

was found to be 0.88%, which might potentially be increased by many parameters, such as replacing the top Au contact layer that significantly attenuated the incident light intensity.

Combining the working principle of *p–n* junction solar cells and the advantage of excitonic solar cell, Levy–Clement and coworkers demonstrated the concept of extra thin absorption (ETA) solar cells based on ZnO/CdSe/CuSCN composites [19, 480]. The structure is illustrated in Fig. 60(a). In addition to the conventional *p*-CuSCN/*n*-ZnO junction, there is a conformal layer of CdSe sandwiched in between. The band gap of CdSe (1.7 eV) is much smaller than that of either ZnO (3.3 eV) or CuSCN (3.4 eV), so CdSe acts as the absorber. The band diagram of the device is shown in Fig. 60(b). At equilibrium, an electric field was built up across the entire CdSe layer. When the device was illuminated, electrons and holes were generated, separated, and rapidly migrate across the absorber layer. Furthermore, the highly structured

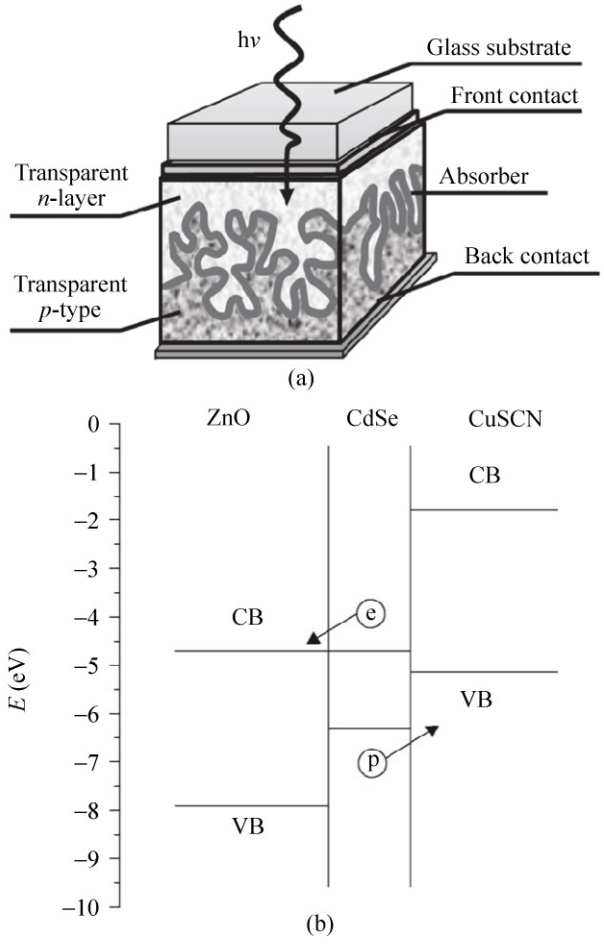

Figure 60 (a) Schematic structure of the ETA solar cell [19]. (b) Band diagram of the ZnO/CdSe/CuSCN heterostructure [480]. Reproduced with permission

interface substantially reduces the transport distance for the free carriers, and also significantly increases the optical path for the incident photons. In the range 400–800 nm of the AM1.5 solar spectrum, the averaged absorption and reflectance of this structure were about 89% and 8%, respectively. Other than that, the all-inorganic composition of the device ensured relatively larger carrier mobility and wider operating temperature than for organic solar cells.

6.9.1.5 Hybrid solar cells

Organic solar cells have reasonably high efficiency, and are great for manufacturing large-scale low-cost flexible solar cells. Due to the very limited carrier mobility of organic semiconductors, the thickness of organic solar cells is typically less than 200 nm, which significantly constrains the incident photon absorption. Organic–inorganic hybrid solar cells have attracted great attention in this regard, since they combine the manufacturing advantages of polymers and the high carrier mobility of inorganic semiconductors. A distinct difference between hybrid solar cells and DSSCs is that there is no liquid electrolyte in the former but there is in the latter [443].

Olson et al. introduced vertically aligned ZnO nanowire arrays into organic solar cells [481]. The basic structure is shown in Fig. 61(a) [482]. In this hybrid structure, ZnO nanowire arrays were grown by a low temperature wet chemical method that was compatible with general flexible substrates [483]. The active components were a P3HT:PCBM polymer blend ([6,6]-Phenyl C71 butyric acid methyl (PCBM) ester). ZnO nanowires performed as "electric fingers" that penetrated into the polymer blend and provided an electron conductance highway with small series resistance [484]. Thus, longer ZnO nanowires allowed the fabrication of thicker active polymer layers, and resulted in higher efficiency [485]. The polymers could be functionalized to give chemical bonds with the ZnO nanowire surface [486]. The band diagram of this hybrid structure is illustrated in Fig. 61(b) [482]. Upon light radiation, excitons were generated and dissociated at the interface between the electron donor P3HT and acceptor PCBM. The interface area between ZnO nanowires and P3HT is much smaller than that between the two polymers, so exciton dissociation by the ZnO nanowires is less likely to happen in this case. The VO_x layer performed as an electron-blocking layer that obstructed the electron transport from P3HT to the Ag electrode, which was found to be crucial for high device efficiency, as illustrated in Fig. 61(c) [482].

The reported efficiency was about 2%, which is probably restricted by the following factors [481]: first was the low open circuit voltage that is defined by the difference between the donor HOMO level and the acceptor LUMO level, which was suggested to be due to the blocking effect of the ZnO layers on hole transport from the polymer to the ITO electrode [485]; Second was the ZnO nanowire spacing (~100 nm), which is larger than the typical carrier diffusion length in P3HT (< 10 nm), and this markedly decreased the short circuit current [481]. Control experiments were carried out without PCBM, and the short circuit

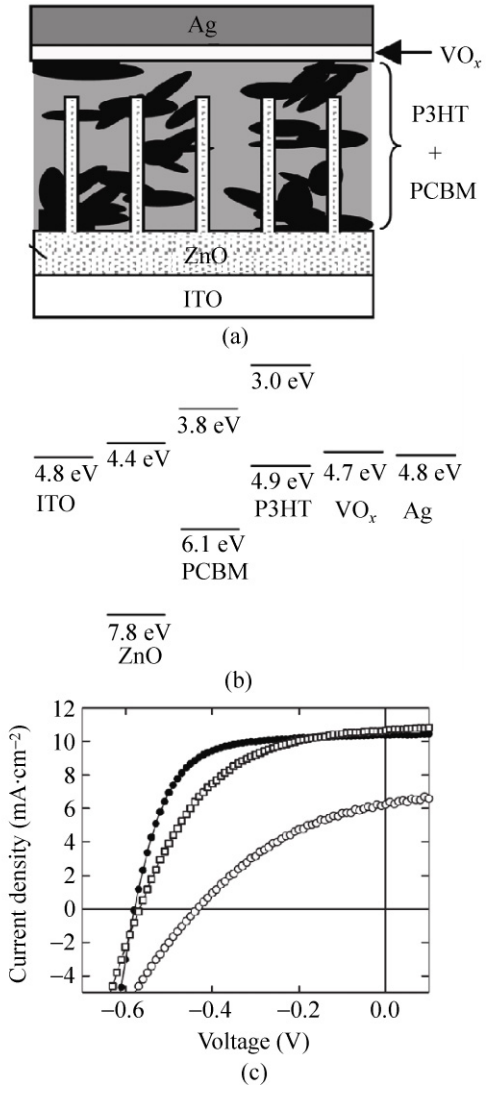

Figure 61 (a) Schematic structure and (b) corresponding energy diagram of a hybrid solar cell. (c) Current density–voltage characteristics of three differently configured solar cells. The open circles indicate the device with a ZnO thin film without a VO_x buffer layer, the open squares denote the device with a VO_x buffer layer, and the closed circles denote the device with ZnO nanowire arrays and a VO_x buffer layer [482]. Reproduced with permission

current of the ZnO/P3HT solar cell decreased to only one fifth of that of the solar cell with PCBM. This is probably due to the large band offset between P3HT and ZnO, which leads to inefficient exciton dissociation at the ZnO/P3HT interface. The PCBM probably serves as an offset stepping layer that enhances effective carrier transport. Similar studies have also been reported on an amphiphilic grafted dye molecule that not only bridged between hydrophilic ZnO nanowires and hydrophobic polymers, but also assisted interfacial electron cascade transportation by enhancing the electronic coupling between the polymer LUMO and the ZnO conduction band [487, 488]; Third is that the processing parameters such as the polymer infiltration, the solvent used, and the annealing temperature/atmosphere were not optimized [489–491]. In an attempt to further enhance the efficiency, ZnO/TiO_2 heterojunctions have also been used in hybrid solar cells to facilitate the charge separation and transport [492, 493].

Finally, we note that since hybrid solar cells and hybrid LEDs share a similar structure, dual-functionality could be realized in a single device [494].

6.9.2 *Piezoelectric nanogenerators*

The search for sustainable micro/nano-power sources for driving wireless and mobile electronics is an emerging field in today's energy research, and could offer a fundamental solution to the energy needs of nanodevices/nanosystems [495–498]. A piezoelectric nanogenerator that converts mechanical energy into electricity was first demonstrated using ZnO nanowire arrays [22]. Following this initial discovery, both direct current [23, 499, 500] and alternating current [24] ZnO nanogenerators have been developed. In addition, nanogenerators based on other materials, such as GaN nanowires [501–503], InN nanowires [504], AlGaN nanocones [505], CdS nanowires [506], ZnO/ZnS heterojunction nanowires [507], lead zircornia titanates (PZT) nanofibers [508], nanoribbons [509–513], nanotubes [514], and single crystalline nanowires [515], $BaTiO_3$ nanowires [516], $NaNbO_3$ nanowires [517], and poly(vinylidene fluoride) (PVDF) nanofibers [518, 519], have shown promising potential for enhancing nanogenerator performance. Consequently, a worldwide effort has been launched in this regard, forming a new research field in nanotechnology and energy science [520].

6.9.2.1 *Fundamentals*

The non-centrosymmetry of the wurtzite ZnO crystal structure leads to piezoelectricity which arises from atomic scale polarization [25, 26, 521]. As shown in Fig. 62(a), the ZnO unit cell has a Zn^{2+} cation situated inside a tetrahedral cage formed by O^{2-} anions. Under non-stress conditions, the positive and negative centers of mass coincide with each other so there are no

dipoles (Fig. 62(b)). When the crystal is subjected to a mechanical force, however, the positive and negative centers of mass become displaced with respect to each other, leading to an electric dipole (Fig. 62(c)). In single crystal ZnO, electric dipoles in all the unit cells are lined up in the same direction, resulting in a macroscopic dipole with positive and negative charges built up on opposite crystal faces. This provides the basis for the nanogenerators.

Piezoelectric ZnO converts mechanical signals into electric signals, and vice versa. The polarization/surface charge density and applied stress are linearly related as shown by the equation: $P_i = d_{ij} \cdot T_j$, where T_j is the mechanical stress exerted along direction j, P_i is the induced polarization along direction i, and d_{ij} is the piezoelectric coefficient. The strongest piezoelectric coefficient d_{33} in ZnO arises from stress applied along the [0001] direction resulting in polarization in the [0001] direction as well. The effective piezoelectric coefficient d_{33} of a ZnO nanowire/nanobelt grown by a vapor phase method was experimentally measured by piezoresponse force microscopy, and ranged from 14.3 pm/V to 26.7 pm/V depending on the frequency, which is higher than the value for bulk ZnO of 9.93 pm/V [522, 523], due to surface relaxation-induced volume reduction in nanowires/nanobelts—as shown by first principles calculations [523–526]. The converse piezoelectric effect also exists according to the equation: $S_j = d_{ij} \cdot E_i$, where E_i is the applied electric field along direction i, and S_j is the induced strain along direction j.

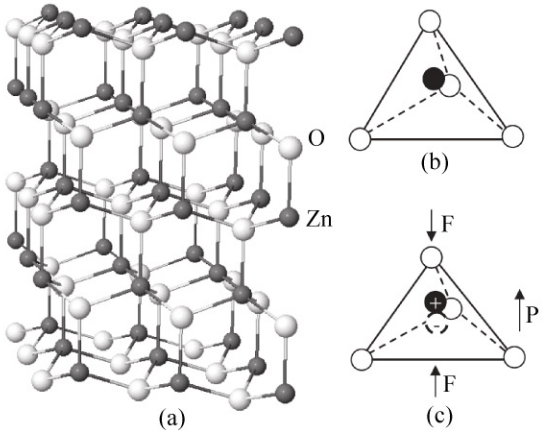

Figure 62 (a) Wurtzite ZnO showing the alternating polar surfaces along the [0001] direction. (b) Tetrahedral coordination between Zn (filled circles) and oxygen (open circles). (c) Distortion of the tetrahedral unit under compressive strain, showing the displacement of the positive charge center from the negative charge center [26]. Reproduced with permission

The advantage of using ZnO nanowires for mechanical energy harvesting is their robustness under high stress and responsiveness to tiny random disturbances/stimuli. Under elastic deformation, the nanowire builds up a piezoelectric potential field inside itself. The static ionic charges cannot freely move around. But in practice there are free electrons in intrinsic n-type ZnO nanowires due to the oxygen vacancies $\left(O_O^x \longleftrightarrow \frac{1}{2}O_2(g) + V_O^{\bullet\bullet} + 2e'\right)$ and zinc interstitials ($Zn_i^x \longleftrightarrow Zn_i^{\bullet\bullet} + 2e'$). The free electrons may screen the positive piezoelectric charges to a certain degree. Within an elastic linear mechanics regime, a ZnO nanowire 50 nm in diameter and 500 nm in length is calculated to produce a piezoelectric potential of about 0.6 V if the free electrons inside are ignored [527]. The piezoelectric potential drops to ~0.3 V due to the screening of the Madelung constant [528] if a moderate carrier concentration of ~10^{16}–10^{17} cm^{-3} is taken into consideration [529]. The free carrier concentration in the nanowire is highly dependent on the synthesis and post-annealing conditions [126, 530], and may vary from one nanowire to another even from the same synthesis batch [528]. The finite piezoelectric potential indicates that the free electrons cannot completely neutralize or screen the piezoelectric ionic charge, even though it is reduced in magnitude. A potential of 0.3 V is sufficient to drive a nanogenerator and give useful work.

6.9.2.2 *Atomic force microscopy-based nanogenerators*

Nanogenerators are based on the coupling of piezoelectric and semiconducting properties. The first nanogenerator based on vertical ZnO nanowire arrays was demonstrated by Wang et al. using atomic force microscopy (AFM) [22]. ZnO nanowire arrays were grown by vapor phase transportation. As shown in Fig. 63(a), when a nanowire with its c axis pointing up was scanned by a Pt-coated AFM tip in contact mode, a constant normal force of ~5 nN was maintained between the tip and the sample surface. The nanowire underwent deformation, and as a result created a strain field and charge separation across the

nanowire with the tensile side positive and compressive side negative, as calculated by the strain and polarization relationship [531]. The central axis of the nanowire remained neutral. In addition to Pt, ZnO has been reported to form Schottky diodes with a variety of metals, such as Ag [532], Au [533], Pd [534], and Ni [534]. Surface treatment can effectively improve the diode performance [535, 536]. The Pt coated tip was grounded and had a zero potential. When the tip was in contact with the tensile side of the nanowire, the tip potential was lower than that of the ZnO nanowire. The Schottky diode was revered biased, and there was little current flowing through the tip/nanowire interface. When tip was scanned over the nanowire, there was a moment when it touched the compressive side of the nanowire. The Schottky barrier was then forward biased, and there was a relatively large amount of current flowing though the interface from the tip to the nanowire, which is detected as an electric pulse. The surface potential of a bent ZnO nanowire was measured to be in the range of 50 mV to 80 mV by Kelvin probe force microscopy [250]. Tip abrasion after scanning for long times reduced the magnitude of the output signals [537, 538], and this could be mitigated by diamond coating [539].

Following this working principle, Gao et al. demonstrated a flexible nanogenerator based on ZnO nanowire arrays on a conductive plastic substrate prepared by a wet chemical method [114]. The voltage generated from a single nanowire was as high as 45 mV. The AFM topography image and the corresponding output voltage profile from the ZnO nanowire array are shown in Figs. 63(b) and 63(c), respectively. By comparing the number of topographic peaks and electric pulses, the percentage of discharge events of the nanowires captured by the AFM tip was found to be about 60%. By virtue of the flexibility of the device, very large deformations could be applied to both the nanowires and the substrate, indicating the potential of the device to act as a power source for flexible and foldable electronics.

Similarly, a nanotube-based nanogenerator has also been demonstrated [177]. It was shown that ZnO nanotubes were approximately five times more flexible than the corresponding nanowires, which leads to enhanced output voltage in nanogenerators [540].

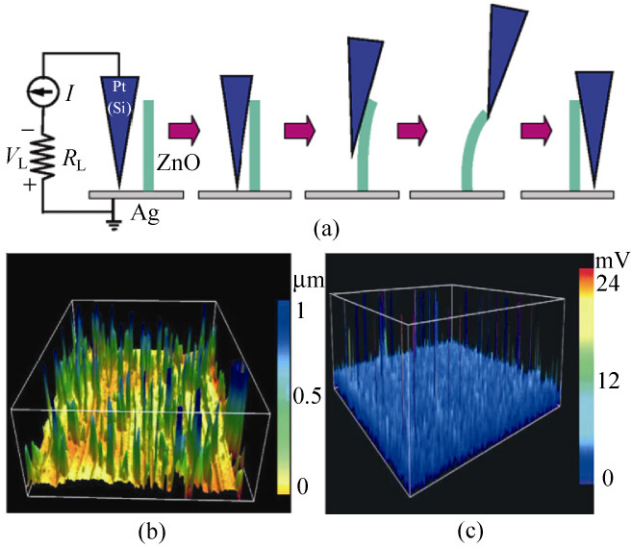

Figure 63 (a) Experimental setup and working procedure of the nanogenerator based on AFM [22]. (b) The AFM topography image and (c) the corresponding voltage output profile obtained over a 40 μm × 40 μm area of vertically aligned ZnO nanowires [114]. Reproduced with permission

6.9.2.3 *Direct current nanogenerators*

To improve the power generation capabilities of a nanogenerator, it is necessary to replace the AFM tip with a simpler source of mechanical energy that can actuate an array of nanowires simultaneously and continuously. Wang et al. designed direct current nanogenerators [23]. Basically, they replaced the AFM tip with an array of zigzag shaped teeth as the top electrode. By covering the zigzag top electrode over an array of ZnO nanowires, encapsulating the entire structure with flexible polymers, and then exciting the device with ultrasonic waves, a constant and steady d.c. output was observed. In this design, the zigzag top electrode mimicked an array of AFM tips. When excited by ultrasonic waves, there is a relative movement between the top electrode and the free standing ZnO nanowires. The ultrasonic waves can also vibrate the nanowires. Each and every zigzag tooth on the top electrode performed as an AFM tip to bend and collect the electrical discharges from the nanowires underneath. Due to the rectification of the Schottky diode, the discharge current of each pair of tooth and nanowire was in the same direction, going from the tip to the nanowire. The resulting millions of electric pulses added together, give rise to a continuous direct current output [23].

The weakness with this design, however, is that only a small fraction of the nanowires are actually active in the current generating process, because most of them are either too short to reach the zigzag electrode, or not at the right position to be bent by the zigzag top electrode. Due to the non-uniform heights and random distribution of the nanowires, it was estimated that only 5% of the nanowires were actually active in the current generation process, while the other nanowires performed as parasitic capacitors bringing down the overall output voltage [541].

In order to improve the device performance, there are two straightforward approaches to increase the number of active nanowires. First, the distribution of the ZnO nanowires on the substrate needs to be controlled [48], so that it matches the shape and morphology of the zigzag top electrode. This will eventually enlarge the portion of active nanowires which can generate electricity. The other approach is to design a nanogenerator that is composed of paired nanotip-to-nanowire nanobrushes as illustrated in Fig. 64(a) [100]. This configuration can be achieved on flat substrates [100], or on curved fibers [96, 542]. Both the ZnO nanotip and nanowire arrays could be synthesized by wet chemical methods at < 100 ℃ on the two surfaces of a common substrate (Figs. 64(b) and 64(c)). The densities of the ZnO nanowires and nanotips play a critical role in the current generating process. If they are too high, when the nanowire is bent, the nanowire will probably touch the adjacent nanowires, which will result in charge leakage and decrease the voltage output of the nanogenerator. If the density is too low, then the output power density will be rather small. The Au-coated nanotip array acted like the AFM tip array, partially interpenetrating into the spacing between the nanowires underneath, just like two face-to-face brushes with a small degree of interdigitated overlap at the two ends. In the same way, a multilayered nanogenerator was integrated by stacking multiple pieces of such structures together with each layer having two terminals. As shown in Fig. 64(d), four layers of nanogenerators, L1, L2, L3, and L4, had output voltage of 11 mV, 14 mV, 16 mV, and 20 mV, respectively. When they were connected in series, the resultant total output voltage was ~62 mV, which is approximately their numerical sum. The output power density reached about 0.11 μW/cm².

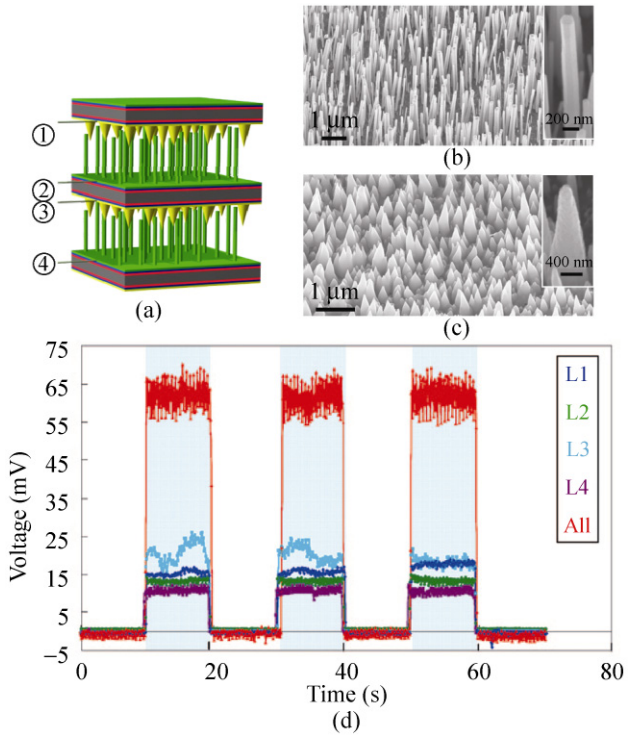

Figure 64 (a) Basic design of a two-layered nanogenerator. SEM images of the rational growth of (b) ZnO nanowire and (c) ZnO nanotip arrays by wet chemical methods. (d) Nanogenerator output voltages measured from four individual layers and the four-layer device connected in series. The stimulating ultrasonic wave was turned on and off periodically with an interval of 10 s [100]. Reproduced with permission

This nanotip-to-nanowire approach has four major advantages. First, both the nanotip and the nanowire arrays are randomly distributed on the substrate. Therefore, it is not necessary to pay extra effort to define the nanostructure positions on the substrate, which simplifies the fabrication process and will bring down the cost when scaling up. Second, the heights of both nanotips and nanowires are not uniform so that long nanowires can be covered by short nanotips, and short nanowires can be reached by long nanotips. Third, the nanotip and nanowire arrays can be grown on both sides of a substrate, which affords a layer-by-layer stacking of multiple electrodes. The output voltage and current can therefore be greatly enhanced by simply connecting these electrodes in series or in parallel. Fourth, the operation of the nanogenerator relies on mechanical deflection/bending of the nanowires, and resonance of nanowires is not required. This significantly expands the applications of the nanogenerator from low frequencies (approximately

the hertz range) to relatively high frequencies (approximately the megahertz range), and allows effective harvesting of mechanical energies in our everyday life [100, 543].

ZnO nanowire arrays are optically transparent [89]. Therefore, by replacing the Si wafers with flexible and transparent conducting electrodes, such as ITO deposited on plastic substrates [499, 544], carbon nanotube networks [545], and graphene [546–548], rollable and transparent nanogenerators can be fabricated as power sources for touch sensors, artificial skins, and wearable personal electronics.

6.9.2.4 *Alternating current nanogenerators*

Yang et al. reported a flexible alternating current generator based on cyclic stretching/releasing of a ZnO fine wire that was firmly attached to metal electrodes at both ends [24, 549]. Low frequency cyclic stretching and releasing of a single ZnO wire with a strain of 0.05%–0.1% created an alternating output voltage of up to ~50 mV and an output current of a fraction of a nanoampere, with an energy conversion efficiency of about 6.8%. The working principle from the energy band diagram point of view is illustrated in Fig. 65. There is a Schottky diode on one side of the wire. The Fermi levels of both sides are lined up when the wire is free (Fig. 65(a)). When the wire is subjected to tensile strain, a piezoelectric field is created in the wire with the left side positive and right side negative if the *c* axis of the wire is to the left (Fig. 65(b)). Then the Fermi

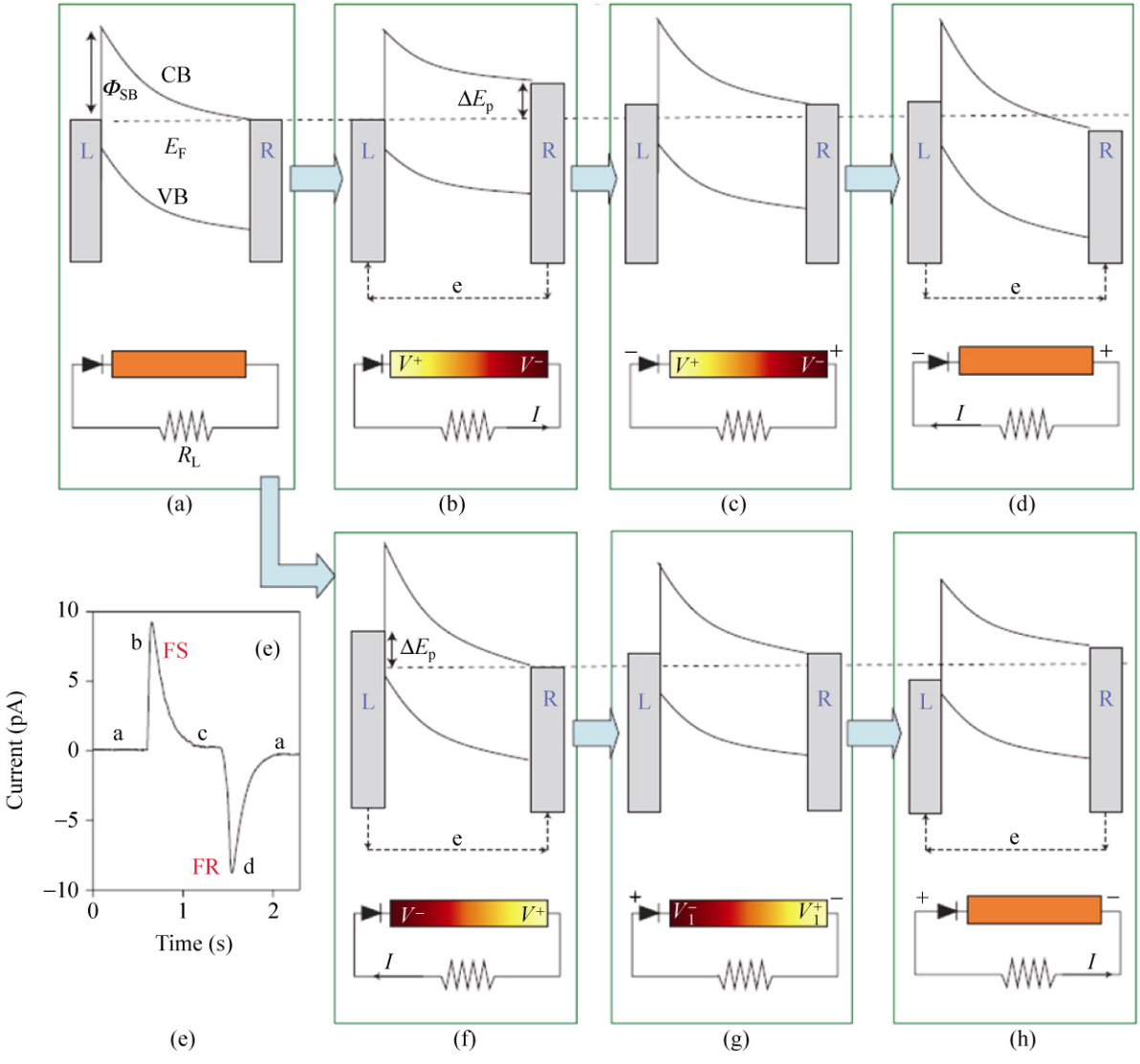

Figure 65 Proposed working mechanism for a single ZnO wire alternating current generator [24]. Reproduced with permission

level of the right electrode is raised up with respect to the left electrode, which drives the electrons flow from the right electrode to the left electrode through an external load. The electrons do not pass through but rather accumulate at the wire/electrode interface because there is a Schottky barrier there (Fig. 65(c)). These accumulated electrons gradually rise up to the Fermi level of the left electrode until the Fermi levels of two electrodes reach a new equilibrium (Fig. 65(c)). When the tensile strain in the wire is released, the piezoelectric potential disappears, which lowers the Fermi level of the right electrode. Then the electrons accumulated at the wire/left electrode interface flow back through the external circuit to the right electrode (Fig. 65(d)), resetting the system to its original state. The output electric signals corresponding to this process are shown in Fig. 65(e). The same analysis applies when the wire is under compressive strain, or the *c* axis of the wire is to the right (Fig. 65(f) and 65(g)) [24]. This design can effectively harvest low frequency mechanical energy in the environment [550, 551].

The voltage and power produced by a single wire are insufficient for real devices. The integration of large numbers of nanowire energy harvesters into a single power source is therefore necessary [432, 552]. Using the same principle, an integration of 700 rows of ZnO nanowires on a flexible substrate has been demonstrated, with each row containing ~20,000 nanowires, as shown in Fig. 66 [432]. When the substrate was stretched, all the nanowires on a substrate were subject to a pure tensile strain because the diameter of a nanowire is much smaller than the thickness of the substrate. Each active nanowire works as a "charging pump", and is independent of the other nanowires as the substrate is bent and released. The integrated nanogenerator was capable of producing a peak voltage of 1.26 V at a low strain of 0.19%, which is sufficient to recharge an AA battery. Integration of so many nanowires has two key requirements. First, all the nanowires should have the same crystallographic orientation to ensure the polarities of the generated piezoelectric potentials are aligned. The nanowires therefore need to be rationally grown, directly on the substrate, rather than by chemical assembly, which usually gives orientational alignment but not alignment of crystallographic polarity. Second, the charging and

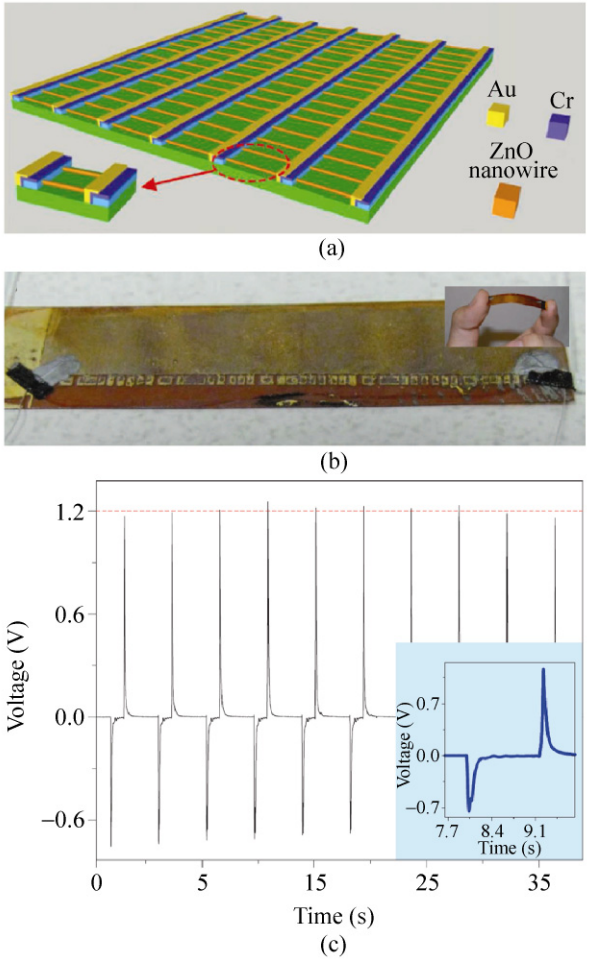

Figure 66 (a) Schematic design of a laterally integrated nanowire array nanogenerator, in which gold and chromium are used to create Schottky and ohmic contacts at the two ends of the lateral nanowires, respectively. (b) Low-magnification optical image of the laterally integrated nanogenerator. Inset in (b) is a demonstration of the nanogenerator flexibility. (c) Open circuit output voltage measured for a laterally integrated nanogenerator composed of 700 rows of nanowire arrays. The inset in (c) is the output voltage for one cycle of mechanical deformation. The laterally integrated nanogenerator was periodically deformed at a straining rate of 2.13% s^{-1} to a maximum strain of 0.19% [432]. Reproduced with permission

discharging processes of the nanowires should be synchronized so that the output alternating voltages can be added constructively, resulting in a high output voltage. It is interesting that the output voltage was greatly enhanced by lateral integration, but the output current was rather limited (~26 nA), which is probably attributable to the following factors. First, the orientational alignment of the as-grown lateral nanowires was not perfect and only a fraction of them were in reality in contact with the gold electrode. Of

the nanowires that were in contact, only a fraction of these were actually actively outputting electricity, and the inactive nanowires acted as a capacitance to reduce the output current and voltage. Second, the binding between the gold and ZnO was not very strong, and could become loosened during repeated mechanical stretching cycles. According to theoretical calculations, within the elastic linear mechanics regime, the output voltage of a single nanowire is linearly proportional to the magnitude of its deformation [527]. A maximum strain of only 0.19% was applied in this study, which is much smaller than the 6% maximum tensile strain predicted theoretically for a ZnO nanowire before fracture [553]. Finally, the inner resistance of the entire integrated sheet was 1–10 MΩ, which significantly reduced the total output current.

As an alternative to the lateral configuration, vertically aligned ZnO nanowire arrays can also be utilized to fabricate alternating current nanogenerators based on the same working principle. All of the nanowires are connected in parallel, and every nanowire works as a charge pump, independent from one another, as shown in Fig. 67(a) and 67(b) [432]. The nanowires were grown on a flat gold-coated Si wafer by a wet chemical method. The crystallographic alignment of the nanowires indicates their piezoelectric alignment in response to the external stress. Thus, the piezoelectric potentials created along each nanowire had the same tendency of distribution, leading to an enhanced macroscopic behavior. The presence of a Schottky contact at least at one end of the nanowires is essential for the operation of the vertically integrated alternating nanogenerator. The output voltage could be greatly enhanced by linearly integrating a number of layers of vertically integrated alternating nanogenerators [432, 554]. As shown in Fig. 67(c), three vertically integrated alternating nanogenerators with individual output voltages of 80, 90, and 96 mV, respectively, were connected in series, leading to an output voltage of 0.243 V. The output current could also be enhanced by parallel stacking several layers of vertically integrated alternating nanogenerators [432].

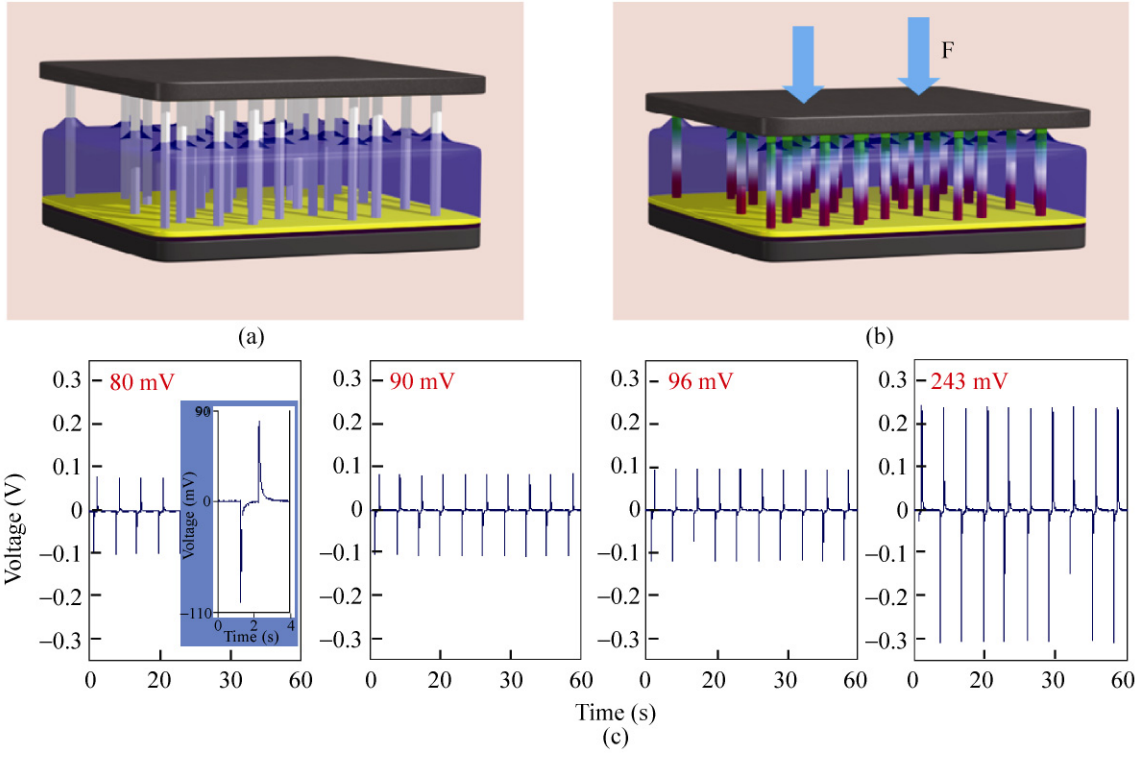

Figure 67 (a) Schematic structure of a vertically integrated alternating current nanogenerator, and (b) the nanogenerator under uniaxial strain. (c) Enhancing the output voltage of the nanogenerator by integrating them in series. Inset in the left panel is the an enlarged view of a single pulse [432]. Reproduced with permission

6.9.2.5 *Self-powered nanosystems*

Building self-powered nanosystems is a future direction of nanotechnology [495]. A nanosystem is an integration of nanodevices, functional components, and a power source. Energy harvesting from the environment for powering a nanosystem is vitally important for its independent, wireless, and sustainable operation [495–497, 555]. A piezoelectric nanogenerator is a promising approach for this application [22].

A "self-powered" nanosystem has been demonstrated based on a vertical ZnO nanowire array nanogenerator and a single nanowire-based nanosensor. The two separate components were connected in series to form a loop. As shown in the inset in Fig. 68, a vertical nanowire array nanogenerator was connected to a ZnO nanowire-based pH sensor, and the voltage across the nanosensor was monitored by a voltmeter. The pH sensor was coated with a 10 nm Si_3N_4 layer, which was thin enough to allow electrostatic interaction between the surface adsorbed charges and the carriers in the nanowire. By powering the pH sensor using a vertical nanowire array nanogenerator that generated an output voltage of ~40 mV, a clear sensitivity to local pH change was observed. When the buffer solution was basic, the surface of the nanosensor was dominated by $-O^-$ groups. These negatively charged groups resulted in depletion regions at the surface of the *n*-type ZnO nanowire, which

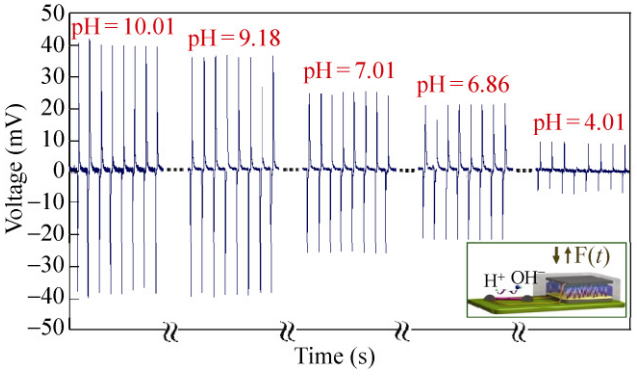

Figure 68 Voltage drop across a single ZnO nanowire-based pH sensor powered by a vertical nanogenerator with an output voltage of 40 mV, showing a stepwise drop of the voltage across the nanosensor as a function of its local pH value. The ZnO nanowire was covered with a thin layer of Si_3N_4 and the testing was carried out within 1 h so that the etching effect from the solution was negligible [432]. Reproduced with permission

increased the resistance of the ZnO nanowire. Thus, the voltage drop on the ZnO nanowire was relatively high. As the buffer solution was changed from basic to acidic, the surface of the nanosensor was gradually changed from $-O^-$ to $-OH_2^+$ groups. Therefore, the depletion regions at the ZnO nanowire surface diminished, which lowered the resistance of the ZnO nanowire. As the pH value of the testing buffer solution was changed from 10.01, 9.18, 7.01, 6.86, then to 4.01, the voltage drop on the pH sensor changed accordingly.

This unambiguously indicated that the vertical nanowire array 20–40 mV nanogenerator could power a nanosensor. When using a variable resistor, the voltage across the resistor was found to be sensitive to the magnitude of its resistance and the result fits well with linear circuit theory [432]. The powering of a nanosensor was a pivotal step towards building self-powered, solely nanowire-based nanosystems. Recently, nanogenerators based on a ZnO nanowire-textured thin film were shown to produce an alternating output voltage of 10 V, and after full wave charge rectification [515], wireless data transmission was realized [556].

6.9.3 *Water splitting*

Hydrogen has one of the highest energy density values. It combines with oxygen to produce electricity and water without generating pollutants. Semiconductor metal oxides, e.g., ZnO and TiO_2 nanostructures, have been recognized for their potential as high performance photoanodes (*n*-type) or photocathodes (*p*-type) for water splitting in photoelectrochemical cells (PEC) [557]. In particular, ZnO nanowire arrays have been used for this purpose because of their large surface to volume ratio, appropriate direct band gap and flat band potential, low series resistance, and high electron transfer efficiency when compared with TiO_2.

Yang et al. reported the implementation of *n*-type ZnO nanowire arrays as photoanodes in PEC cells for water splitting [311]. The nanowire arrays were grown by a hydrothermal method and were later annealed in ammonia to incorporate a controllable concentration of nitrogen atoms by varying the annealing time. The incorporation of nitrogen atoms into ZnO introduces intermediate energy levels in the ZnO band gap,

which push the absorption spectrum of ZnO from the ultraviolet into the visible region, as evidenced by the enhanced incident photon to current efficiency in comparison with undoped ZnO nanowires. However, after nitrogen incorporation the nanowires were still *n*-type. CdTe-sensitized [558], CdS and CdSe quantum dot-cosensitized [559], and ZnO–CdS core–shell [560] nanowires have also been utilized to enhance the absorption in the visible region. It is believed that CdTe has a more favorable conduction band energy than CdSe and thus can inject electrons into ZnO more efficiently [558]. Also, quantum dots afford multiple excitons from a single absorbed photon, which can greatly increase the overall efficiency [473, 474]. From Mott–Schottky measurements, the flat band potential, electron density, and depletion region thickness were determined to be –0.58 V, 4.6×10^{18} cm^{-3}, and 22 nm, respectively. Under illumination, electron and hole pairs were generated in the nanowire, and were separated in the depletion region at the nanowire surface, with holes drifting to the nanowire/electrolyte interface to oxidize the OH^- groups and give rise to O_2, while electrons flowed to the cathode and reduced the H^+ groups producing H_2. The overall reaction for this water splitting process is:

$$2\,H_2O + \text{light} \longrightarrow 2\,H_2 + O_2$$

The nitrogen-doped ZnO nanowires showed a photo-to-hydrogen conversion efficiency of 0.15% under an external potential of + 0.5 V [311]. To improve the efficiency, ZnO nanowire/multi-wall carbon nanotube heterostructures were employed to increase the overall active surface area of the PEC device [247].

Non-ideal factors with PEC devices include the photodecomposition and dissolution of the anode itself—that is, oxidation of the anode by holes in the depletion region if the photopotential is higher than the redox potential of the anode material. Another major source of non-ideality is the presence of energy states associated with the electrode surface that are different from those in the interior of the electrode. These surface states can act as efficient channels for electron transfer, if they are at an appropriate level.

In addition to the PEC devices, Hong et al. showed that a piezoelectric potential could also be implemented to drive the nonspontaneous water splitting reaction [561]. The working principle is shown in Fig. 69. Under mechanical agitation by ultrasonic waves, ZnO nanowires, or any other piezoelectric materials, undergo physical deformation and generate surface charges on the tensile and compressive sides. When the piezopotential was greater than the standard redox potential of H_2O (1.23 eV), then H_2O can be split into H_2 and O_2 in the molar ratio of 2:1. This indicates that these piezoelectric nanostructures can scavenge mechanical energy waste from the environment, such as noise vibrations, to produce H_2 for green energy applications.

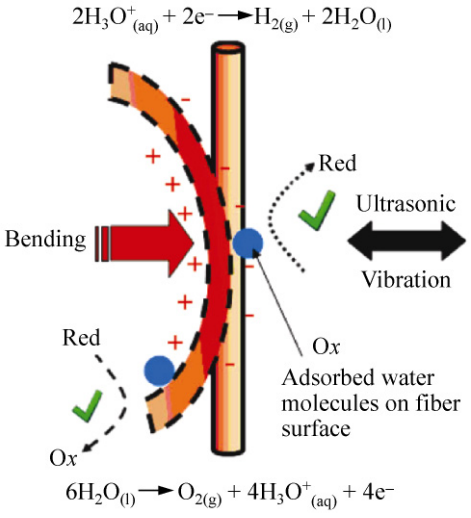

Figure 69 Schematic diagram showing that by bending under ultrasonic vibration, the charges and piezopotential developed on a piezoelectric material, such as a ZnO fiber, can drive the splitting of water into oxygen and hydrogen [561]. Reproduced with permission

7. Concluding remarks

Before reaching a conclusion, we would like to share our perspectives on some critical issues in the field and possible solutions to potentially address these issues.

There are three main challenges. The first is to control the crystal quality. ZnO nanostructures grown by wet chemical methods are usually of low crystal quality with abundant defects, such as point defects and voids, which can sometimes be seen from their very rough surfaces. These defects result in low fracture toughness, low carrier mobility, short carrier

lifetime, and high threshold pump power, greatly undermining the mechanical, electrical, and optical properties of the nanostructures. The high defect level is due to the nature of solution growth at low temperature in a rather complex environment composed of many kinds of ions and molecules. To improve the crystal quality, it is of critical importance to start from an appropriate precursor, choose well-controlled reaction parameters, and possibly introduce appropriate capping agents and/or even control some seemingly trivial species, such as the counter ions in the Zn^{2+} salt precursor and the dissolved oxygen concentration. The second is to minimize the surface conductivity for piezoelectric applications. ZnO naturally exhibits *n*-type surface conductivity due to the loss of oxygen atoms to the ambient environment $\left(O_O^x \longleftrightarrow \frac{1}{2}O_2(g) + V_O^{\bullet\bullet} + 2e'\right)$. The thickness of the surface conductive region is calculated to be on the order of tens of nanometers. This finite concentration of electrons will partially screen the piezoelectric potential, which significantly weakens the performance of ZnO-based piezoelectric devices. To reduce the oxygen deficiency, it is possible to push the defect equation to the left by providing an oxygen-rich environment, such as annealing under high oxygen partial pressure or implanting energetic oxygen atoms under oxygen plasma. Finally, based on the reduced intrinsic *n*-type conductivity, it is feasible but still challenging to dope ZnO with group V and/or group I element atoms to achieve *p*-type conductivity. The doping reaction of ZnO nanostructures with foreign atoms is typically entropically favorable but enthalpically unfavorable. So it is desirable to choose appropriate elements with similar ionic radii and electronegativities under well-controlled reaction conditions (pressure, temperature, and precursor concentration) to minimize the enthalpy change. Although there are debates about *p*-type doping in ZnO thin films, *p*-doping in 1D ZnO nanostructures appears quite promising due to the absence of dislocations.

Nevertheless, this article has given a comprehensive review of the growth control and functional applications of 1D ZnO nanostructures prepared by wet chemical approaches. The resulting 1D ZnO nanostructures are biologically compatible and environmentally safe. They have multi-functional materials with semiconducting, optical, piezoelectric and other properties. More importantly and most distinctly, they can be grown using low temperature wet chemical approaches, so that they can be easily integrated with a wide range of materials and technologies. All of these advantages combine to make 1D ZnO nanostructures unique building blocks for fabricating diverse novel devices.

Acknowledgements

We thank NSF, DARPA, and BES DOE for support. We also thank those authors and many of our collaborators who made contributions to the published data reviewed in the text here.

References

[1] Ozgur, U.; Alivov, Y. I.; Liu, C.; Teke, A.; Reshchikov, M. A.; Dogan, S.; Avrutin, V.; Cho, S. J.; Morkoc, H. A comprehensive review of ZnO materials and devices. *J. Appl. Phys.* **2005**, *98*, 041301.

[2] Look, D. C. Recent advances in ZnO materials and devices. *Mat. Sci. Eng. B-.Adv.* **2001**, *80*, 383–387.

[3] Heo, Y. W.; Norton, D. P.; Tien, L. C.; Kwon, Y.; Kang, B. S.; Ren, F.; Pearton, S. J.; LaRoche, J. R. ZnO nanowire growth and devices. *Mat. Sci. Eng. R* **2004**, *47*, 147.

[4] Yi, G. C.; Wang, C. R.; Park, W. I. ZnO nanorods: Synthesis, characterization and applications. *Semicond. Sci. Technol.* **2005**, *20*, S22–S34.

[5] Wang, Z. L. Oxide nanobelts and nanowires—growth, properties and applications. *J. Nanosci. Nanotechno* **2008**, *8*, 27–55.

[6] Wang, Z. L. Splendid one-dimensional nanostructures of zinc oxide: A new nanomaterial family for nanotechnology. *ACS Nano* **2008**, *2*, 1987–1992.

[7] Wang, Z. L. ZnO nanowire and nanobelt platform for nanotechnology. *Mat. Sci. Eng. R* **2009**, *64*, 33–71.

[8] Wang, Z. L. Ten years' venturing in ZnO nanostructures: From discovery to scientific understanding and to technology applications. *Chinese Sci. Bull.* **2009**, *54*, 4021–4034.

[9] Huang, M. H.; Mao, S.; Feick, H.; Yan, H. Q.; Wu, Y. Y.; Kind, H.; Weber, E.; Russo, R.; Yang, P. D. Room-temperature ultraviolet nanowire nanolasers. *Science* **2001**, *292*, 1897–1899.

[10] Govender, K.; Boyle, D. S.; O'Brien, P.; Binks, D.; West, D.; Coleman, D. Room-temperature lasing observed from ZnO nanocolumns grown by aqueous solution deposition. *Adv. Mater.* **2002**, *14*, 1221–1224.

[11] Park, W. I.; Yi, G. C. Electroluminescence in *n*-ZnO nanorod arrays vertically grown on *p*-GaN. *Adv. Mater.* **2004**, *16,* 87–90.

[12] Mao, D. S.; Wang, X.; Li, W.; Liu, X. H.; Li, Q.; Xu, J. F. Electron field emission from hydrogen-free amorphous carbon-coated ZnO tip array. *J. Vac. Sci. Technol. B* **2002**, *20*, 278–281.

[13] Zhu, Y. W.; Zhang, H. Z.; Sun, X. C.; Feng, S. Q.; Xu, J.; Zhao, Q.; Xiang, B.; Wang, R. M.; Yu, D. P. Efficient field emission from ZnO nanoneedle arrays. *Appl. Phys. Lett.* **2003**, *83*, 144–146.

[14] Wang, W. Z.; Zeng, B. Q.; Yang, J.; Poudel, B.; Huang, J. Y.; Naughton, M. J.; Ren, Z. F. Aligned ultralong ZnO nanobelts and their enhanced field emission. *Adv. Mater.* **2006**, *18*, 3275–3278.

[15] Wei, T. Y.; Yeh, P. H.; Lu, S. Y.; Wang, Z. L. Gigantic enhancement in sensitivity using Schottky contacted nanowire nanosensor. *J. Am. Chem. Soc.* **2009**, *131*, 17690–17695.

[16] Yeh, P. H.; Li, Z.; Wang, Z. L. Schottky-gated probe-free ZnO nanowire biosensor. *Adv. Mater.* **2009**, *21*, 4975–4978.

[17] Zhou, J.; Gu, Y. D.; Hu, Y. F.; Mai, W. J.; Yeh, P. H.; Bao, G.; Sood, A. K.; Polla, D. L.; Wang, Z. L. Gigantic enhancement in response and reset time of ZnO UV nanosensor by utilizing Schottky contact and surface functionalization. *Appl. Phys. Lett.* **2009**, *94*, 191103.

[18] Law, M.; Greene, L. E.; Johnson, J. C.; Saykally, R.; Yang, P. D. Nanowire dye-sensitized solar cells. *Nat. Mater.* **2005**, *4*, 455–459.

[19] Levy-Clement, C.; Tena-Zaera, R.; Ryan, M. A.; Katty, A.; Hodes, G. CdSe-sensitized *p*-CuSCN/nanowire *n*-ZnO heterojunctions. *Adv. Mater.* **2005**, *17*, 1512–1515.

[20] Weintraub, B.; Wei, Y. G.; Wang, Z. L. Optical fiber/ nanowire hybrid structures for efficient three-dimensional dye-sensitized solar cells. *Angew. Chem. Int. Ed.* **2009**, *48*, 8981–8985.

[21] Wei, Y. G.; Xu, C.; Xu, S.; Li, C.; Wu, W. Z.; Wang, Z. L. Planar waveguide-nanowire integrated three-dimensional dye-sensitized solar cells. *Nano Lett.* **2010**, *10*, 2092–2096.

[22] Wang, Z. L.; Song, J. H. Piezoelectric nanogenerators based on zinc oxide nanowire arrays. *Science* **2006**, *312*, 242–246.

[23] Wang, X. D.; Song, J. H.; Liu, J.; Wang, Z. L. Direct-current nanogenerator driven by ultrasonic waves. *Science* **2007**, *316*, 102–105.

[24] Yang, R. S.; Qin, Y.; Dai, L. M.; Wang, Z. L. Power generation with laterally packaged piezoelectric fine wires. *Nat. Nanotechnol.* **2009**, *4*, 34–39.

[25] Wang, Z. L. The new field of nanopiezotronics. *Mater. Today* **2007**, *10*, 20–28.

[26] Wang, Z. L. Nanopiezotronics. *Adv. Mater.* **2007**, *19*, 889–892.

[27] Wang, Z. L. Towards self-powered nanosystems: From nanogenerators to nanopiezotronics. *Adv. Funct. Mater.* **2008**, *18*, 3553–3567.

[28] Laudise, R. A.; Ballman, A. A. Hydrothermal synthesis of zinc oxide and zinc sulfide. *J. Phys. Chem.* **1960**, *64*, 688–691.

[29] Verges, M. A.; Mifsud, A.; Serna, C. J. Formation of rod-like zinc-oxide microcrystals in homogeneous solutions. *J. Chem. Soc., Faraday Trans.* **1990**, *86*, 959–963.

[30] Vayssieres, L.; Keis, K.; Lindquist, S. E.; Hagfeldt, A. Purpose-built anisotropic metal oxide material: 3D highly oriented microrod array of ZnO. *J. Phys. Chem. B* **2001**, *105*, 3350–3352.

[31] Pan, Z. W.; Dai, Z. R.; Wang, Z. L. Nanobelts of semiconducting oxides. *Science* **2001**, *291*, 1947–1949.

[32] Huang, M. H.; Wu, Y. Y.; Feick, H.; Tran, N.; Weber, E.; Yang, P. D. Catalytic growth of zinc oxide nanowires by vapor transport. *Adv. Mater.* **2001**, *13*, 113–116.

[33] Yao, B. D.; Chan, Y. F.; Wang, N. Formation of ZnO nanostructures by a simple way of thermal evaporation. *Appl. Phys. Lett.* **2002**, *81*, 757–759.

[34] Park, W. I.; Yi, G. C.; Kim, M. Y.; Pennycook, S. J. ZnO Nanoneedles grown vertically on Si substrates by non-catalytic vapor-phase epitaxy. *Adv. Mater.* **2002**, *14*, 1841–1843.

[35] Park, W. I.; Kim, D. H.; Jung, S. W.; Yi, G. C. Metalorganic vapor-phase epitaxial growth of vertically well-aligned ZnO nanorods. *Appl. Phys. Lett.* **2002**, *80*, 4232–4234.

[36] Yuan, H.; Zhang, Y. Preparation of well-aligned ZnO whiskers on glass substrate by atmospheric MOCVD. *J. Cryst. Growth* **2004**, *263*, 119–124.

[37] Heo, Y. W.; Varadarajan, V.; Kaufman, M.; Kim, K.; Norton, D. P.; Ren, F.; Fleming, P. H. Site-specific growth of ZnO nanorods using catalysis-driven molecular-beam epitaxy. *Appl. Phys. Lett.* **2002**, *81*, 3046–3048.

[38] Sun, Y.; Fuge, G. M.; Ashfold, M. N. R. Growth of aligned ZnO nanorod arrays by catalyst-free pulsed laser deposition methods. *Chem. Phys. Lett.* **2004**, *396*, 21–26.

[39] Hong, J. I.; Bae, J.; Wang, Z. L.; Snyder, R. L. Room-temperature, texture-controlled growth of ZnO thin films and their application for growing aligned ZnO nanowire arrays. *Nanotechnology* **2009**, *20*, 085609.

[40] Chiou, W. T.; Wu, W. Y.; Ting, J. M. Growth of single crystal ZnO nanowires using sputter deposition. *Diam. Relat. Mater.* **2003**, *12*, 1841–1844.

[41] Xu, C. K.; Xu, G. D.; Liu, Y. K.; Wang, G. H. A simple and novel route for the preparation of ZnO nanorods. *Solid State Commun.* **2002**, *122*, 175–179.

[42] Lin, D. D.; Pan, W.; Wu, H. Morphological control of centimeter long aluminum-doped zinc oxide nanofibers prepared by electrospinning. *J. Am. Ceram. Soc.* **2007**, *90*,

71–76.

[43] Lin, D.; Wu, H.; Pan, W. Photoswitches and memories assembled by electrospinning aluminum-doped zinc oxide single nanowires. *Adv. Mater.* **2007**, *19*, 3968–3972.

[44] Sui, X. M.; Shao, C. L.; Liu, Y. C. White-light emission of polyvinyl alcohol/ZnO hybrid nanofibers prepared by electrospinning. *Appl. Phys. Lett.* **2005**, *87*, 113115.

[45] Wu, J. J.; Wen, H. I.; Tseng, C. H.; Liu, S. C. Well-aligned ZnO nanorods via hydrogen treatment of ZnO films. *Adv. Funct. Mater.* **2004**, *14*, 806–810.

[46] Zhang, H.; Yang, D. R.; Ma, X. Y.; Du, N.; Wu, J. B.; Que, D. L. Straight and thin ZnO nanorods: Hectogram-scale synthesis at low temperature and cathodoluminescence. *J. Phys. Chem. B* **2006**, *110*, 827–830.

[47] Chang, P. C.; Lu, J. G. ZnO nanowire field-effect transistors. *IEEE T. Electron Dev.* **2008**, *55*, 2977–2987.

[48] Xu, S.; Wei, Y.; Kirkham, M.; Liu, J.; Mai, W.; Davidovic, D.; Snyder, R. L.; Wang, Z. L. Patterned growth of vertically aligned ZnO nanowire arrays on inorganic substrates at low temperature without catalyst. *J. Am. Chem. Soc.* **2008**, *130*, 14958–14959.

[49] Govender, K.; Boyle, D. S.; Kenway, P. B.; O'Brien, P. Understanding the factors that govern the deposition and morphology of thin films of ZnO from aqueous solution. *J. Mater. Chem.* **2004**, *14*, 2575–2591.

[50] Xu, S.; Adiga, N.; Ba, S.; Dasgupta, T.; Wu, C. F. J.; Wang, Z. L. Optimizing and improving the growth quality of ZnO nanowire arrays guided by statistical design of experiments. *ACS Nano* **2009**, *3*, 1803–1812.

[51] Pearton, S. J.; Norton, D. P.; Ip, K.; Heo, Y. W.; Steiner, T. Recent progress in processing and properties of ZnO. *Prog. Mater. Sci.* **2005**, *50*, 293–340.

[52] Klingshirn, C. ZnO: From basics towards applications. *Phys. Status Solidi B* **2007**, *244*, 3027–3073.

[53] Schmidt-Mende, L.; MacManus-Driscoll, J. L. ZnO—nanostructures, defects, and devices. *Mater. Today* **2007**, *10*, 40–48.

[54] Zang, J. F.; Li, C. M.; Cui, X. Q.; Wang, J. X.; Sun, X. W.; Dong, H.; Sun, C. Q. Tailoring zinc oxide nanowires for high performance amperometric glucose sensor. *Electroanal.* **2007**, *19*, 1008–1014.

[55] Baruah, S.; Dutta, J. pH-dependent growth of zinc oxide nanorods. *J. Cryst. Growth* **2009**, *311*, 2549–2554.

[56] Xu, S.; Shen, Y.; Ding, Y.; Wang, Z. L. Growth and transfer of monolithic horizontal ZnO nanowire superstructures onto flexible substrates. *Adv. Funct. Mater.* **2010**, *20*, 1493–1495.

[57] Li, W. J.; Shi, E. W.; Zhong, W. Z.; Yin, Z. W. Growth mechanism and growth habit of oxide crystals. *J. Cryst. Growth* **1999**, *203*, 186–196.

[58] Demianets, L. N.; Kostomarov, D. V.; Kuz'mina, I. P.; Pushko, S. V. Mechanism of growth of ZnO single crystals from hydrothermal alkali solutions. *Crystallogr. Rep.* **2002**, *47*, S86–S98.

[59] Liu, B.; Zeng, H. C. Room temperature solution synthesis of monodispersed single-crystalline ZnO nanorods and derived hierarchical nanostructures. *Langmuir* **2004**, *20*, 4196–4204.

[60] Viswanatha, R.; Amenitsch, H.; Sarma, D. D. Growth kinetics of ZnO nanocrystals: A few surprises. *J. Am. Chem. Soc.* **2007**, *129*, 4470–4475.

[61] Demianets, L. N.; Kostomarov, D. V. Mechanism of zinc oxide single crystal growth under hydrothermal conditions. *Ann. Chim. Sci. Mat.* **2001**, *26*, 193–198.

[62] Dem'yanets, L. N.; Kostomarov, D. V.; Kuz-mina, I. P. Chemistry and kinetics of ZnO growth from alkaline hydrothermal solutions. *Inorg. Mater.* **2002**, *38*, 124–131.

[63] Kawska, A.; Duchstein, P.; Hochrein, O.; Zahn, D. Atomistic mechanisms of ZnO aggregation from ethanolic solution: Ion association, proton transfer, and self-organization. *Nano Lett.* **2008**, *8*, 2336–2340.

[64] Yamabi, S.; Imai, H. Growth conditions for wurtzite zinc oxide films in aqueous solutions. *J. Mater. Chem.* **2002**, *12*, 3773–3778.

[65] Zhang, J.; Sun, L. D.; Yin, J. L.; Su, H. L.; Liao, C. S.; Yan, C. H. Control of ZnO morphology via a simple solution route. *Chem. Mater.* **2002**, *14*, 4172–4177.

[66] Cheng, B.; Samulski, E. T. Hydrothermal synthesis of one-dimensional ZnO nanostructures with different aspect ratios. *Chem. Commun.* **2004**, 986–987.

[67] Liu, B.; Zeng, H. C. Hydrothermal synthesis of ZnO nanorods in the diameter regime of 50 nm. *J. Am. Chem. Soc.* **2003**, *125*, 4430–4431.

[68] Cao, H. L.; Qian, X. F.; Gong, Q.; Du, W. M.; Ma, X. D.; Zhu, Z. K. Shape- and size-controlled synthesis of nanometre ZnO from a simple solution route at room temperature. *Nanotechnology* **2006**, *17*, 3632–3636.

[69] Hou, X. M.; Zhou, F.; Sun, Y. B.; Liu, W. M. Ultrasound-assisted synthesis of dentritic ZnO nanostructure in ionic liquid. *Mater. Lett.* **2007**, *61*, 1789–1792.

[70] Alammar, T.; Mudring, A. V. Facile ultrasound-assisted synthesis of ZnO nanorods in an ionic liquid. *Mater. Lett.* **2009**, *63*, 732–735.

[71] Yin, M.; Gu, Y.; Kuskovsky, I. L.; Andelman, T.; Zhu, Y.; Neumark, G. F.; O'Brien, S. Zinc oxide quantum rods. *J. Am. Chem. Soc.* **2004**, *126*, 6206–6207.

[72] Pacholski, C.; Kornowski, A.; Weller, H. Self-assembly of ZnO: From nanodots to nanorods. *Angew. Chem. Int. Ed.* **2002**, *41*, 1188–1191.

[73] Zhang, D. F.; Sun, L. D.; Yin, J. L.; Yan, C. H.; Wang, R. M.

Attachment-driven morphology evolvement of rectangular ZnO nanowires. *J. Phys. Chem. B* **2005**, *109*, 8786–8790.

[74] Guo, L.; Ji, Y. L.; Xu, H. B.; Simon, P.; Wu, Z. Y. Regularly shaped, single-crystalline ZnO nanorods with wurtzite structure. *J. Am. Chem. Soc.* **2002**, *124*, 14864–14865.

[75] Liu, J. P.; Huang, X. T.; Li, Y. Y.; Ji, X. X.; Li, Z. K.; He, X.; Sun, F. L. Vertically aligned 1D ZnO nanostructures on bulk alloy substrates: Direct solution synthesis, photoluminescence, and field emission. *J. Phys. Chem. C* **2007**, *111*, 4990–4997.

[76] Gao, Y. F.; Nagai, M.; Chang, T. C.; Shyue, J. J. Solution-derived ZnO nanowire array film as photoelectrode in dye-sensitized solar cells. *Cryst. Growth Des.* **2007**, *7*, 2467–2471.

[77] Tak, Y.; Yong, K. J. Controlled growth of well-aligned ZnO nanorod array using a novel solution method. *J. Phys. Chem. B* **2005**, *109*, 19263–19269.

[78] Xu, C. K.; Shin, P.; Cao, L. L.; Gao, D. Preferential growth of long ZnO nanowire array and its application in dye-sensitized solar cells. *J. Phys. Chem. C* **2010**, *114*, 125–129.

[79] Postels, B.; Wehmann, H. H.; Bakin, A.; Kreye, M.; Fuhrmann, D.; Blaesing, J.; Hangleiter, A.; Krost, A.; Waag, A. Controlled low-temperature fabrication of ZnO nanopillars with a wet-chemical approach. *Nanotechnology* **2007**, *18*, 195602.

[80] Hua, G. M.; Zhang, Y.; Zhang, J. X.; Cao, X. L.; Xu, W.; Zhang, L. D. Fabrication of ZnO nanowire arrays by cycle growth in surfactantless aqueous solution and their applications on dye-sensitized solar cells. *Mater. Lett.* **2008**, *62*, 4109–4111.

[81] Tang, Q.; Zhou, W. J.; Shen, J. M.; Zhang, W.; Kong, L. F.; Qian, Y. T. A template-free aqueous route to ZnO nanorod arrays with high optical property. *Chem. Commun.* **2004**, 712–713.

[82] Xu, S.; Wang, Z. L. Unpublished results.

[83] Boyle, D. S.; Govender, K.; O'Brien, P. Novel low temperature solution deposition of perpendicularly orientated rods of ZnO: Substrate effects and evidence of the importance of counter-ions in the control of crystallite growth. *Chem. Commun.* **2002**, 80–81.

[84] Vayssieres, L. Growth of arrayed nanorods and nanowires of ZnO from aqueous solutions. *Adv. Mater.* **2003**, *15*, 464–466.

[85] Ahuja, I. S.; Yadava, C. L.; Singh, R. Structural information on manganese(II), cobalt(II), nickel(II), zinc(II) and cadmium (II) sulphate complexes with hexamethylenetetramine (a potentially tetradentate ligand) from their magnetic moments, electronic and infrared spectra. *J. Mol. Struct.* **1982**, *81*, 229–234.

[86] Baruah, S.; Dutta, J. Hydrothermal growth of ZnO nanostructures. *Sci. Technol. Adv. Mat.* **2009**, *10*, 013001.

[87] Ashfold, M. N. R.; Doherty, R. P.; Ndifor-Angwafor, N. G.; Riley, D. J.; Sun, Y. The kinetics of the hydrothermal growth of ZnO nanostructures. *Thin Solid Films* **2007**, *515*, 8679–8683.

[88] Unalan, H. E.; Hiralal, P.; Rupesinghe, N.; Dalal, S.; Milne, W. I.; Amaratunga, G. A. J. Rapid synthesis of aligned zinc oxide nanowires. *Nanotechnology* **2008**, *19*, 255608.

[89] Jung, S. H.; Oh, E.; Lee, K. H.; Park, W.; Jeong, S. H. A sonochemical method for fabricating aligned ZnO nanorods. *Adv. Mater.* **2007**, *19*, 749–753.

[90] Shi, L.; Bao, K. Y.; Cao, J.; Qian, Y. T. Sunlight-assisted fabrication of a hierarchical ZnO nanorod array structure. *CrystEngComm* **2009**, *11*, 2009–2014.

[91] Xu, S.; Lao, C.; Weintraub, B.; Wang, Z. L. Density-controlled growth of aligned ZnO nanowire arrays by seedless chemical approach on smooth surfaces. *J. Mater. Res.* **2008**, *23*, 2072–2077.

[92] Cheng, C. W.; Yan, B.; Wong, S. M.; Li, X. L.; Zhou, W. W.; Yu, T.; Shen, Z. X.; Yu, H. Y.; Fan, H. J. Fabrication and SERS performance of silver-nanoparticle-decorated Si/ZnO nanotrees in ordered arrays. *ACS Appl. Mater. Inter.* **2010**, *2*, 1824–1828.

[93] Greene, L. E.; Law, M.; Goldberger, J.; Kim, F.; Johnson, J. C.; Zhang, Y. F.; Saykally, R. J.; Yang, P. D. Low-temperature wafer-scale production of ZnO nanowire arrays. *Angew. Chem. Int. Ed.* **2003**, *42*, 3031–3034.

[94] Liu, T. Y.; Liao, H. C.; Lin, C. C.; Hu, S. H.; Chen, S. Y. Biofunctional ZnO nanorod arrays grown on flexible substrates. *Langmuir* **2006**, *22*, 5804–5809.

[95] Manekkathodi, A.; Lu, M. Y.; Wang, C. W.; Chen, L. J. Direct growth of aligned zinc oxide nanorods on paper substrates for low-cost flexible electronics. *Adv. Mater.* **2010**, *22*, 4059–4063.

[96] Qin, Y.; Wang, X. D.; Wang, Z. L. Microfibre–nanowire hybrid structure for energy scavenging. *Nature* **2008**, *451*, 809–813.

[97] Bae, J.; Song, M. K.; Park, Y. J.; Kim, J. M.; Liu, M. L.; Wang, Z. L. Fiber supercapacitors made of nanowire-fiber hybrid structures for wearable/flexible energy storage. *Angew. Chem. Int. Ed.* **2011**, *50*, 1683–1687.

[98] Na, J. S.; Gong, B.; Scarel, G.; Parsons, G. N. Surface polarity shielding and hierarchical ZnO nano-architectures produced using sequential hydrothermal crystal synthesis and thin film atomic layer deposition. *ACS Nano* **2009**, *3*, 3191–3199.

[99] Kang, B. S.; Pearton, S. J.; Ren, F. Low temperature (< 100 degrees C) patterned growth of ZnO nanorod arrays on Si. *Appl. Phys. Lett.* **2007**, *90*, 083104.

[100] Xu, S.; Wei, Y. G.; Liu, J.; Yang, R.; Wang, Z. L. Integrated multilayer nanogenerator fabricated using paired nanotip-to-nanowire brushes. *Nano Lett.* **2008**, *8*, 4027–4032.

[101] Sun, H. K.; Luo, M.; Weng, W. J.; Cheng, K.; Du, P.; Shen, G.; Han, G. R. Position and density control in hydrothermal growth of ZnO nanorod arrays through pre-formed micro/nanodots. *Nanotechnology* **2008**, *19*, 395602.

[102] Ma, T.; Guo, M.; Zhang, M.; Zhang, Y. J.; Wang, X. D. Density-controlled hydrothermal growth of well-aligned ZnO nanorod arrays. *Nanotechnology* **2007**, *18*, 035605.

[103] Hsiao, C. S.; Peng, C. H.; Chen, S. Y.; Liou, S. C. Tunable growth of ZnO nanorods synthesized in aqueous solutions at low temperatures. *J. Vac. Sci. Technol. B* **2006**, *24*, 288–291.

[104] Qiu, J. J.; Li, X. M.; He, W. Z.; Park, S. J.; Kim, H. K.; Hwang, Y. H.; Lee, J. H.; Kim, Y. D. The growth mechanism and optical properties of ultralong ZnO nanorod arrays with a high aspect ratio by a preheating hydrothermal method. *Nanotechnology* **2009**, *20*, 155603.

[105] Cao, X. L.; Zeng, H. B.; Wang, M.; Xu, X. J.; Fang, M.; Ji, S. L.; Zhang, L. D. Large scale fabrication of quasi-aligned ZnO stacking nanoplates. *J. Phys. Chem. C* **2008**, *112*, 5267–5270.

[106] Greene, L. E.; Law, M.; Tan, D. H.; Montano, M.; Goldberger, J.; Somorjai, G.; Yang, P. D. General route to vertical ZnO nanowire arrays using textured ZnO seeds. *Nano Lett.* **2005**, *5*, 1231–1236.

[107] Yang, Y.; Chu, Y.; Zhang, Y. P.; Yang, F. Y.; Liu, J. L. Polystyrene–ZnO core–shell microspheres and hollow ZnO structures synthesized with the sulfonated polystyrene templates. *J. Solid State Chem.* **2006**, *179*, 470–475.

[108] Fang, Y. P.; Pang, Q.; Wen, X. G.; Wang, B. N.; Yang, S. H. Synthesis of ultrathin ZnO nanofibers aligned on a zinc substrate. *Small* **2006**, *2*, 612–615.

[109] Kar, S.; Dev, A.; Chaudhuri, S. Simple solvothermal route to synthesize ZnO nanosheets, nanonails, and well-aligned nanorod arrays. *J. Phys. Chem. B* **2006**, *110*, 17848–17853.

[110] Peterson, R. B.; Fields, C. L.; Gregg, B. A. Epitaxial chemical deposition of ZnO nanocolumns from NaOH solutions. *Langmuir* **2004**, *20*, 5114–5118.

[111] Zhou, Z. Z.; Deng, Y. L. Kinetics study of ZnO nanorod growth in solution. *J. Phys. Chem. C* **2009**, *113*, 19853–19858.

[112] Liu, J.; She, J. C.; Deng, S. Z.; Chen, J.; Xu, N. S. Ultrathin seed-layer for tuning density of ZnO nanowire arrays and their field emission characteristics. *J. Phys. Chem. C* **2008**, *112*, 11685–11690.

[113] Weintraub, B.; Chang, S.; Singamaneni, S.; Han, W. H.; Choi, Y. J.; Bae, J. H.; Kirkham, M.; Tsukruk, V. V.; Deng, Y. L. Density-controlled, solution-based growth of ZnO nanorod arrays via layer-by-layer polymer thin films for enhanced field emission. *Nanotechnology* **2008**, *19*, 435302.

[114] Gao, P. X.; Song, J. H.; Liu, J.; Wang, Z. L. Nanowire piezoelectric nanogenerators on plastic substrates as flexible power sources for nanodevices. *Adv. Mater.* **2007**, *19*, 67–72.

[115] Zeng, H. B.; Cui, J. B.; Cao, B. Q.; Gibson, U.; Bando, Y.; Golberg, D. Electrochemical deposition of ZnO nanowire arrays: Organization, doping, and properties. *Sci. Adv. Mater.* **2010**, *2*, 336–358.

[116] Izaki, M.; Watanabe, M.; Aritomo, H.; Yamaguchi, I.; Asahina, S.; Shinagawa, T.; Chigane, M.; Inaba, M.; Tasaka, A. Zinc oxide nano-cauliflower array with room temperature ultraviolet light emission. *Cryst. Growth Des.* **2008**, *8*, 1418–1421.

[117] Yu, L. G.; Zhang, G. M.; Li, S. Q.; Xi, Z. H.; Guo, D. Z. Fabrication of arrays of zinc oxide nanorods and nanotubes in aqueous solution under an external voltage. *J. Cryst. Growth* **2007**, *299*, 184–188.

[118] Konenkamp, R.; Boedecker, K.; Lux-Steiner, M. C.; Poschenrieder, M.; Zenia, F.; Levy-Clement, C.; Wagner, S. Thin film semiconductor deposition on free-standing ZnO columns. *Appl. Phys. Lett.* **2000**, *77*, 2575–2577.

[119] Cui, J. B.; Soo, Y. C.; Chen, T. P.; Gibson, U. J. Low-temperature growth and characterization of Cl-doped ZnO nanowire arrays. *J. Phys. Chem. C* **2008**, *112*, 4475–4479.

[120] Cui, J. B.; Gibson, U. J. Electrodeposition and room temperature ferromagnetic anisotropy of Co and Ni-doped ZnO nanowire arrays. *Appl. Phys. Lett.* **2005**, *87*, 133108.

[121] Elias, J.; Tena-Zaera, R.; Levy-Clement, C. Electrochemical deposition of ZnO nanowire arrays with tailored dimensions. *J. Electroanal. Chem.* **2008**, *621*, 171–177.

[122] Zhao, J.; Jin, Z. G.; Li, T.; Liu, X. X.; Liu, Z. F. Growth of ZnO nanorods by the chemical solution method with assisted electrical field. *J. Am. Ceram. Soc.* **2006**, *89*, 2654–2659.

[123] Elias, J.; Tena-Zaera, R.; Levy-Clement, C. Effect of the chemical nature of the anions on the electrodeposition of ZnO nanowire arrays. *J. Phys. Chem. C* **2008**, *112*, 5736–5741.

[124] Xu, L. F.; Guo, Y.; Liao, Q.; Zhang, J. P.; Xu, D. S. Morphological control of ZnO nanostructures by electrodeposition. *J. Phys. Chem. B* **2005**, *109*, 13519–13522.

[125] Tena-Zaera, R.; Elias, J.; Wang, G.; Levy-Clement, C. Role of chloride ions on electrochemical deposition of ZnO nanowire arrays from O-2 reduction. *J. Phys. Chem. C* **2007**, *111*, 16706–16711.

[126] Tena-Zaera, R.; Elias, J.; Levy-Clement, C.; Bekeny, C.; Voss, T.; Mora-Sero, I.; Bisquert, J. Influence of the potassium chloride concentration on the physical properties of electrodeposited ZnO nanowire arrays. *J. Phys. Chem. C* **2008**, *112*, 16318–16323.

[127] Anthony, S. P.; Lee, J. I.; Kim, J. K. Tuning optical band gap of vertically aligned ZnO nanowire arrays grown by homoepitaxial electrodeposition. *Appl. Phys. Lett.* **2007**, *90*, 103107.

[128] Zheng, M. J.; Zhang, L. D.; Li, G. H.; Shen, W. Z. Fabrication and optical properties of large-scale uniform zinc oxide nanowire arrays by one-step electrochemical deposition technique. *Chem. Phys. Lett.* **2002**, *363*, 123–128.

[129] Zhou, H. J.; Wong, S. S. A facile and mild synthesis of 1-D ZnO, CuO, and alpha-Fe_2O_3 nanostructures and nanostructured arrays. *ACS Nano* **2008**, *2*, 944–958.

[130] Liu, B.; Zeng, H. C. Fabrication of ZnO "dandelions" via a modified Kirkendall process. *J. Am. Chem. Soc.* **2004**, *126*, 16744–16746.

[131] Cong, H. P.; Yu, S. H. Hybrid ZnO-dye hollow spheres with new optical properties from a self-assembly process based on Evans blue dye and cetyltrimethylammonium bromide. *Adv. Funct. Mater.* **2007**, *17*, 1814–1820.

[132] Zhang, J.; Sun, L. D.; Pan, H. Y.; Liao, C. S.; Yan, C. H. ZnO nanowires fabricated by a convenient route. *New J. Chem.* **2002**, *26*, 33–34.

[133] Sun, X. M.; Chen, X.; Deng, Z. X.; Li, Y. D. A CTAB-assisted hydrothermal orientation growth of ZnO nanorods. *Mater. Chem. Phys.* **2003**, *78*, 99–104.

[134] Zhang, H.; Yang, D.; Ji, Y. J.; Ma, X. Y; Xu, J.; Que, D. L. Low temperature synthesis of flowerlike ZnO nanostructures by cetyltrimethylammonium bromide-assisted hydrothermal process. *J. Phys. Chem. B* **2004**, *108*, 3955–3958.

[135] Atanasova, P.; Weitz, R. T.; Gerstel, P.; Srot, V.; Kopold, P.; van Aken, P. A.; Burghard, M.; Bill, J. DNA-templated synthesis of ZnO thin layers and nanowires. *Nanotechnology* **2009**, *20*, 365302.

[136] Kim, J. H.; Kim, E. M.; Andeen, D.; Thomson, D.; DenBaars, S. P.; Lange, F. F. Growth of heteroepitaxial ZnO thin films on GaN-buffered Al_2O_3(0001) substrates by low-temperature hydrothermal synthesis at 90 °C. *Adv. Funct. Mater.* **2007**, *17*, 463–471.

[137] Shen, L. M.; Bao, N. Z.; Yanagisawa, K.; Zheng, Y. Q.; Domen, K.; Gupta, A.; Grimes, C. A. Direct growth of comet-like superstructures of Au-ZnO submicron rod arrays by solvothermal soft chemistry process. *J. Solid State Chem.* **2007**, *180*, 213–220.

[138] Gao, P. X.; Lee, J. L.; Wang, Z. L. Multicolored ZnO nanowire architectures on trenched silicon substrates. *J. Phys. Chem. C* **2007**, *111*, 13763–13769.

[139] Lee, J. Y.; Yin, D. H.; Horiuchi, S. Site and morphology controlled ZnO deposition on Pd catalyst prepared from Pd/PMMA thin film using UV lithography. *Chem. Mater.* **2005**, *17*, 5498–5503.

[140] Xu, C. X.; Wei, A.; Sun, X. W.; Dong, Z. L. Aligned ZnO nanorods synthesized by a simple hydrothermal reaction. *J. Phys. D: Appl. Phys.* **2006**, *39*, 1690–1693.

[141] Cao, B. Q.; Cai, W. P.; Duan, G. T.; Li, Y.; Zhao, Q.; Yu, D. P. A template-free electrochemical deposition route to ZnO nanoneedle arrays and their optical and field emission properties. *Nanotechnology* **2005**, *16*, 2567–2574.

[142] Liu, R.; Vertegel, A. A.; Bohannan, E. W.; Sorenson, T. A.; Switzer, J. A. Epitaxial electrodeposition of zinc oxide nanopillars on single-crystal gold. *Chem. Mater.* **2001**, *13*, 508–512.

[143] Niarchos, G.; Makarona, E.; Tsamis, C. Growth of ZnO nanorods on patterned templates for efficient, large-area energy scavengers. *Microsyst. Technol.* **2010**, *16*, 669–675.

[144] Ahsanulhaq, Q.; Umar, A.; Hahn, Y. B. Growth of aligned ZnO nanorods and nanopencils on ZnO/Si in aqueous solution: Growth mechanism and structural and optical properties. *Nanotechnology* **2007**, *18*, 115603.

[145] Nayak, J.; Sahu, S. N.; Kasuya, J.; Nozaki, S. Effect of substrate on the structure and optical properties of ZnO nanorods. *J. Phys. D: Appl. Phys.* **2008**, *41*, 115303.

[146] Zhou, H. L.; Chen, A.; Jian, L. K.; Ooi, K. F.; Goh, G. K. L.; Zang, K. Y.; Chua, S. J. Template-directed selective growth of ordered ZnO nanostructures on GaN by the hydrothermal method. *J. Cryst. Growth* **2008**, *310*, 3626–3629.

[147] Cole, J. J.; Wang, X.; Knuesel, R. J.; Jacobs, H. O. Integration of ZnO microcrystals with tailored dimensions forming light emitting diodes and UV photovoltaic cells. *Nano Lett.* **2008**, *8*, 1477–1481.

[148] Lee, S. D.; Kim, Y. S.; Yi, M. S.; Choi, J. Y.; Kim, S. W. Morphology control and electroluminescence of ZnO nanorod/GaN heterojunctions prepared using aqueous solution. *J. Phys. Chem. C* **2009**, *113*, 8954–8958.

[149] Cole, J. J.; Wang, X. Y.; Knuesel, R. J.; Jacobs, H. O. Patterned growth and transfer of ZnO micro- and nanocrystals with size and location control. *Adv. Mater.* **2008**, *20*, 1474–1478.

[150] Kim, J. H.; Andeen, D.; Lange, F. F. Hydrothermal growth of periodic, single-crystal ZnO microrods and microtunnels. *Adv. Mater.* **2006**, *18*, 2453–2457.

[151] Le, H. Q.; Chua, S. J.; Koh, Y. W.; Loh, K. P.; Chen, Z.; Thompson, C. V.; Fitzgerald, E. A. Growth of single crystal ZnO nanorods on GaN using an aqueous solution method. *Appl. Phys. Lett.* **2005**, *87*, 101908.

[152] Pauporte, T.; Lincot, D.; Viana, B.; Pelle, F. Toward laser emission of epitaxial nanorod arrays of ZnO grown by electrodeposition. *Appl. Phys. Lett.* **2006**, *89*, 233112.

[153] Le, H. Q.; Chua, S. J.; Loh, K. P.; Fitzgerald, E. A.; Koh, Y. W. Synthesis and optical properties of well aligned ZnO

nanorods on GaN by hydrothermal synthesis. *Nanotechnology* **2006**, *17*, 483–488.

[154] Zhang, H.; Yang, D. R.; Li, D. S.; Ma, X. Y.; Li, S. Z.; Que, D. L. Controllable growth of ZnO microcrystals by a capping-molecule-assisted hydrothermal process. *Cryst. Growth Des.* **2005**, *5*, 547–550.

[155] Wu, W. B.; Hu, G. D.; Cui, S. G.; Zhou, Y.; Wu, H. T. Epitaxy of vertical ZnO nanorod arrays on highly (001)-oriented ZnO seed monolayer by a hydrothermal route. *Cryst. Growth Des.* **2008**, *8*, 4014–4020.

[156] Zhou, Y.; Wu, W. B.; Hu, G. D.; Wu, H. T.; Cui, S. G. Hydrothermal synthesis of ZnO nanorod arrays with the addition of polyethyleneimine. *Mater. Res. Bull.* **2008**, *43*, 2113–2118.

[157] Tian, Z. R. R.; Voigt, J. A.; Liu, J.; McKenzie, B.; McDermott, M. J. Biomimetic arrays of oriented helical ZnO nanorods and columns. *J. Am. Chem. Soc.* **2002**, *124*, 12954–12955.

[158] Yang, Z.; Liu, Q. H.; Yu, H. C.; Zou, B. S.; Wang, Y. G.; Wang, T. H. Substrate-free growth, characterization and growth mechanism of ZnO nanorod close-packed arrays. *Nanotechnology* **2008**, *19*, 035704.

[159] Mclaren, A.; Valdes-Solis, T.; Li, G. Q.; Tsang, S. C. Shape and size effects of ZnO nanocrystals on photocatalytic activity. *J. Am. Chem. Soc.* **2009**, *131*, 12540–12541.

[160] Hidber, P. C.; Graule, T. J.; Gauckler, L. J. Citric acid—A dispersant for aqueous alumina suspensions. *J. Am. Ceram. Soc.* **1996**, *79*, 1857–1867.

[161] Tian, Z. R. R.; Voigt, J. A.; Liu, J.; McKenzie, B.; McDermott, M. J.; Rodriguez, M. A.; Konishi, H.; Xu, H. F. Complex and oriented ZnO nanostructures. *Nat. Mater.* **2003**, *2*, 821–826.

[162] Liang, L.; Liu, J.; Windisch, C. F.; Exarhos, G. J.; Lin, Y. H. Direct assembly of large arrays of oriented conducting polymer nanowires. *Angew. Chem. Int. Ed.* **2002**, *41*, 3665–3668.

[163] Tian, Z. R. R.; Voigt, J. A.; Liu, J.; McKenzie, B.; Xu, H. F. Large oriented arrays and continuous films of TiO_2-based nanotubes. *J. Am. Chem. Soc.* **2003**, *125*, 12384–12385.

[164] Yan, J.; Fang, X. S.; Zhang, L. D.; Bando, Y.; Gautam, U. K.; Dierre, B.; Sekiguchi, T.; Golberg, D. Structure and cathodoluminescence of individual ZnS/ZnO biaxial nanobelt heterostructures. *Nano Lett.* **2008**, *8*, 2794–2799.

[165] Choopun, S.; Hongsith, N.; Tanunchai, S.; Chairuangsri, T.; Krua-in, C.; Singkarat, S.; Vilaithonga, T.; Mangkorntong, P.; Mangkorntong, N. Single-crystalline ZnO nanobelts by RF sputtering. *J. Cryst. Growth* **2005**, *282*, 365–369.

[166] Wei, Y. G.; Ding, Y.; Li, C.; Xu, S.; Ryo, J. H.; Dupuis, R.; Sood, A. K.; Polla, D. L.; Wang, Z. L. Growth of vertically aligned ZnO nanobelt arrays on GaN substrate. *J. Phys. Chem. C* **2008**, *112*, 18935–18937.

[167] Xi, Y.; Hu, C. G.; Han, X. Y.; Xiong, Y. F.; Gao, P. X.; Liu, G. B. Hydrothermal synthesis of ZnO nanobelts and gas sensitivity property. *Solid State Commun.* **2007**, *141*, 506–509.

[168] Yang, J. H.; Liu, G. M.; Lu, J.; Qiu, Y. F.; Yang, S. H. Electrochemical route to the synthesis of ultrathin ZnO nanorod/nanobelt arrays on zinc substrate. *Appl. Phys. Lett.* **2007**, *90*, 103109.

[169] Song, R. Q.; Xu, A. W.; Deng, B.; Li, Q.; Chen, G. Y. From layered basic zinc acetate nanobelts to hierarchical zinc oxide nanostructures and porous zinc oxide nanobelts. *Adv. Funct. Mater.* **2007**, *17*, 296–306.

[170] Vayssieres, L.; Keis, K.; Hagfeldt, A.; Lindquist, S. E. Three-dimensional array of highly oriented crystalline ZnO microtubes. *Chem. Mater.* **2001**, *13*, 4395–4398.

[171] Zhang, J.; Sun, L. D.; Liao, C. S.; Yan, C. H. A simple route towards tubular ZnO. *Chem. Commun.* **2002**, 262–263.

[172] She, G. W.; Zhang, X. H.; Shi, W. S.; Fan, X.; Chang, J. C. Electrochemical/chemical synthesis of highly-oriented single-crystal ZnO nanotube arrays on transparent conductive substrates. *Electrochem. Commun.* **2007**, *9*, 2784–2788.

[173] Sun, Y.; Fuge, G. M.; Fox, N. A.; Riley, D. J.; Ashfold, M. N. R. Synthesis of aligned arrays of ultrathin ZnO nanotubes on a Si wafer coated with a thin ZnO film. *Adv. Mater.* **2005**, *17*, 2477–2481.

[174] Jiang, H.; Hu, J.; Gu, F.; Li, C. Self-assembly of solid or tubular ZnO rods into twinning microprisms via a hydrothermal route. *J. Alloys Compd.* **2009**, *478*, 550–553.

[175] Wang, Z.; Qian, X. F.; Yin, J.; Zhu, Z. K. Large-scale fabrication of tower-like, flower-like, and tube-like ZnO arrays by a simple chemical solution route. *Langmuir* **2004**, *20*, 3441–3448.

[176] Yu, K.; Jin, Z. G.; Liu, X. X.; Zhao, J.; Feng, J. Y. Shape alterations of ZnO nanocrystal arrays fabricated from $NH_3{\cdot}H_2O$ solutions. *Appl. Surf. Sci.* **2007**, *253*, 4072–4078.

[177] Xi, Y.; Song, J. H.; Xu, S.; Yang, R. S.; Gao, Z. Y.; Hu, C. G.; Wang, Z. L. Growth of ZnO nanotube arrays and nanotube based piezoelectric nanogenerators. *J. Mater. Chem.* **2009**, *19*, 9260–9264.

[178] Yang, A. L.; Cui, Z. L. ZnO layer and tubular structures synthesized by a simple chemical solution route. *Mater. Lett.* **2006**, *60*, 2403–2405.

[179] Elias, J.; Tena-Zaera, R.; Wang, G. Y.; Levy-Clement, C. Conversion of ZnO nanowires into nanotubes with tailored dimensions. *Chem. Mater.* **2008**, *20*, 6633–6637.

[180] Yu, H. D.; Zhang, Z. P.; Han, M. Y.; Hao, X. T.; Zhu, F. R. A general low-temperature route for large-scale fabrication

of highly oriented ZnO nanorod/nanotube arrays. *J. Am. Chem. Soc.* **2005**, *127*, 2378–2379.

[181] Israr, M. Q.; Sadaf, J. R.; Yang, L. L.; Nur, O.; Willander, M.; Palisaitis, J.; Persson, P. O. A. Trimming of aqueous chemically grown ZnO nanorods into ZnO nanotubes and their comparative optical properties. *Appl. Phys. Lett.* **2009**, *95*, 073114.

[182] Sun, Y.; Riley, D. J.; Ashfold, M. N. R. Mechanism of ZnO nanotube growth by hydrothermal methods on ZnO film-coated Si substrates. *J. Phys. Chem. B* **2006**, *110*, 15186–15192.

[183] Li, Q. C.; Kumar, V.; Li, Y.; Zhang, H. T.; Marks, T. J.; Chang, R. P. H. Fabrication of ZnO nanorods and nanotubes in aqueous solutions. *Chem. Mater.* **2005**, *17*, 1001–1006.

[184] Tong, Y. H.; Liu, Y. C.; Shao, C. L.; Liu, Y. X.; Xu, C. S.; Zhang, J. Y.; Lu, Y. M.; Shen, D. Z.; Fan, X. W. Growth and optical properties of faceted hexagonal ZnO nanotubes. *J. Phys. Chem. B* **2006**, *110*, 14714–14718.

[185] Tong, Y. H.; Liu, Y. C.; Dong, L.; Zhao, D. X.; Zhang, J. Y.; Lu, Y. M.; Shen, D. Z.; Fan, X. W. Growth of ZnO nanostructures with different morphologies by using hydrothermal technique. *J. Phys. Chem. B* **2006**, *110*, 20263–20267.

[186] She, G. W.; Zhang, X. H.; Shi, W. S.; Fan, X.; Chang, J. C.; Lee, C. S.; Lee, S. T.; Liu, C. H. Controlled synthesis of oriented single-crystal ZnO nanotube arrays on transparent conductive substrates. *Appl. Phys. Lett.* **2008**, *92*, 053111.

[187] Li, F.; Ding, Y.; Gao, P. X. X.; Xin, X. Q.; Wang, Z. L. Single-cystal hexagonal disks and rings of ZnO: Low-temperature, large-scale synthesis and growth mechanism. *Angew. Chem. Int. Ed.* **2004**, *43*, 5238–5242.

[188] Magalhaes, M.; Pusiol, D.; Ramia, M. E.; Neto, A. M. F. Phase diagram of a lyotropic mixture sodium bis (2-ethylhexyl) sulfosuccinate/dodecanol/water: Reverse micellar, cylindrical, lamellar, and sponge phases. *J. Chem. Phys.* **1998**, *108*, 3835–3843.

[189] Jung, S.; Cho, W.; Lee, H. J.; Oh, M. Self-template-directed formation of coordination-polymer hexagonal tubes and rings, and their calcination to ZnO rings. *Angew. Chem. Int. Ed.* **2009**, *48*, 1459–1462.

[190] Liu, X. G. Zinc oxide nano- and microfabrication from coordination-polymer templates. *Angew. Chem. Int. Ed.* **2009**, *48*, 3018–3021.

[191] Oner, M.; Norwig, J.; Meyer, W. H.; Wegner, G. Control of ZnO crystallization by a PEO-b-PMAA diblock copolymer. *Chem. Mater.* **1998**, *10*, 460–463.

[192] Taubert, A.; Kubel, C.; Martin, D. C. Polymer-induced microstructure variation in zinc oxide crystals precipitated from aqueous solution. *J. Phys. Chem. B* **2003**, *107*, 2660–2666.

[193] Zhang, S.; Shen, Y.; Fang, H.; Xu, S.; Song, J. H.; Wang, Z. L. Growth and replication of ordered ZnO nanowire arrays on general flexible substrates. *J. Mater. Chem.* **2010**, *20*, 10606–10610.

[194] Wang, B. G.; Shi, E. W.; Zhong, W. Z. Twinning morphologies and mechanisms of ZnO crystallites under hydrothermal conditions. *Cryst. Res. Techol.* **1998**, *33*, 937–941.

[195] Zhang, T. R.; Dong, W. J.; Keeter-Brewer, M.; Konar, S.; Njabon, R. N.; Tian, Z. R. Site-specific nucleation and growth kinetics in hierarchical nanosyntheses of branched ZnO crystallites. *J. Am. Chem. Soc.* **2006**, *128*, 10960–10968.

[196] Zhang, T. R.; Dong, W. J.; Njabon, R. N.; Varadan, V. K.; Tian, Z. R. Kinetically probing site-specific heterogeneous nucleation and hierarchical growth of nanobranches. *J. Phys. Chem. C* **2007**, *111*, 13691–13695.

[197] Sounart, T. L.; Liu, J.; Voigt, J. A.; Hsu, J. W. P.; Spoerke, E. D.; Tian, Z.; Jiang, Y. B. Sequential nucleation and growth of complex nanostructured films. *Adv. Funct. Mater.* **2006**, *16*, 335–344.

[198] Sounart, T. L.; Liu, J.; Voigt, J. A.; Huo, M.; Spoerke, E. D.; McKenzie, B. Secondary nucleation and growth of ZnO. *J. Am. Chem. Soc.* **2007**, *129*, 15786–15793.

[199] Ko, S. H.; Lee, D.; Kang, H. W.; Nam, K. H.; Yeo, J. Y.; Hong, S. J.; Grigoropoulos, C. P.; Sung, H. J. Nanoforest of hydrothermally grown hierarchical ZnO nanowires for a high efficiency dye-sensitized solar cell. *Nano Lett.* **2011**, *11*, 666–671.

[200] Mo, M.; Yu, J. C.; Zhang, L. Z.; Li, S. K. A. Self-assembly of ZnO nanorods and nanosheets into hollow microhemispheres and microspheres. *Adv. Mater.* **2005**, *17*, 756–760.

[201] Liu, B.; Zeng, H. C. Hollow ZnO microspheres with complex nanobuilding units. *Chem. Mater.* **2007**, *19*, 5824–5826.

[202] Penn, R. L.; Banfield, J. F. Imperfect oriented attachment: Dislocation generation in defect-free nanocrystals. *Science* **1998**, *281*, 969–971.

[203] Koh, Y. W.; Loh, K. P. Hexagonally packed zinc oxide nanorod bundles on hydrotalcite sheets. *J. Mater. Chem.* **2005**, *15*, 2508–2514.

[204] Chow, L.; Lupan, O.; Heinrich, H.; Chai, G. Self-assembly of densely packed and aligned bilayer ZnO nanorod arrays. *Appl. Phys. Lett.* **2009**, *94*, 163105.

[205] Thevenot, F.; Szymanski, R.; Chaumette, P. Preparation and characterization of Al-rich Zn-Al hydrotalcite-like compounds. *Clays Clay Miner.* **1989**, *37*, 396–402.

[206] Liu, J. P.; Huang, X. T.; Li, Y. Y.; Sulieman, K. M.; He, X.; Sun, F. L. Facile and large-scale production of ZnO/Zn-Al layered double hydroxide hierarchical heterostructures. *J.*

Phys. Chem. B **2006**, *110*, 21865–21872.

[207] Zhang, H.; Yang, D. R.; Ma, X. Y.; Que, D. L. Synthesis and field emission characteristics of bilayered ZnO nanorod array prepared by chemical reaction. *J. Phys. Chem. B* **2005**, *109*, 17055–17059.

[208] Li, H. X.; Xia, M. X.; Dai, G. Z.; Yu, H. C.; Zhang, Q. L.; Pan, A. L.; Wang, T. H.; Wang, Y. G.; Zou, B. S. Growth of oriented zinc oxide nanowire array into novel hierarchical structures in aqueous solutions. *J. Phys. Chem. C* **2008**, *112*, 17546–17553.

[209] Xu, C. K.; Wu, J. M.; Desai, U. V.; Gao, D. Multilayer assembly of nanowire arrays for dye-sensitized solar cells. *J. Am. Chem. Soc.* **2011**, *133*, 8122–8125.

[210] Liu, L.; Fu, L.; Liu, Y.; Liu, Y. L.; Jiang, P.; Liu, S. Q.; Gao, M. Y.; Tang, Z. Y. Bioinspired synthesis of vertically aligned ZnO nanorod arrays: Toward greener chemistry. *Cryst. Growth Des.* **2009**, *9*, 4793–4796.

[211] Tang, Y. W.; Hu, X. Y.; Chen, M. J.; Luo, L. J.; Li, B. H.; Zhang, L. Z. CdSe nanocrystal sensitized ZnO core–shell nanorod array films: Preparation and photovoltaic properties. *Electrochim. Acta* **2009**, *54*, 2742–2747.

[212] Hao, Y. Z.; Pei, J.; Wei, Y.; Cao, Y. H.; Jiao, S. H.; Zhu, F.; Li, J. J.; Xu, D. H. Efficient semiconductor-sensitized solar cells based on poly(3-hexylthiophene)@CdSe@ZnO core–shell nanorod arrays. *J. Phys. Chem. C* **2010**, *114*, 8622–8625.

[213] Wang, X. N.; Zhu, H. J.; Xu, Y. M.; Wang, H.; Tao, Y.; Hark, S.; Xiao, X. D.; Li, Q. A. Aligned ZnO/CdTe core–shell nanocable arrays on indium tin oxide: Synthesis and photoelectrochemical properties. *ACS Nano* **2010**, *4*, 3302–3308.

[214] Sounart, T. L.; Liu, J.; Voigt, J. A.; Hsu, J. W. P.; Spoerke, E. D.; Tian, Z.; Jiang, Y. B. Sequential nucleation and growth of complex nanostructured films. *Adv. Funct. Mater.* **2006**, *16*, 335–344.

[215] Shi, L.; Xu, Y. M.; Hark, S. K.; Liu, Y.; Wang, S.; Peng, L. M.; Wong, K. W.; Li, Q. Optical and electrical performance of SnO_2 capped ZnO nanowire arrays. *Nano Lett.* **2007**, *7*, 3559–3563.

[216] Plank, N. O. V.; Snaith, H. J.; Ducati, C.; Bendall, J. S.; Schmidt-Mende, L.; Welland, M. E. A simple low temperature synthesis route for ZnO–MgO core–shell nanowires. *Nanotechnology* **2008**, *19*, 465603.

[217] Plank, N. O. V.; Howard, I.; Rao, A.; Wilson, M. W. B.; Ducati, C.; Mane, R. S.; Bendall, J. S.; Louca, R. R. M.; Greenham, N. C.; Miura, H.; Friend, R. H.; Snaith, H. J.; Welland, M. E. Efficient ZnO nanowire solid-state dye-sensitized solar cells using organic dyes and core–shell nanostructures. *J. Phys. Chem. C* **2009**, *113*, 18515–18522.

[218] Tak, Y.; Yong, K. A novel heterostructure of Co_3O_4/ZnO nanowire array fabricated by photochemical coating method. *J. Phys. Chem. C* **2008**, *112*, 74–79.

[219] Wang, Z.; Qian, X. F.; Li, Y.; Yin, J.; Zhu, Z. K. Large-scale synthesis of tube-like ZnS and cable-like ZnS-ZnO arrays: Preparation through the sulfuration conversion from ZnO arrays via a simple chemical solution route. *J. Solid State Chem.* **2005**, *178*, 1589–1594.

[220] Panda, S. K.; Dev, A.; Chaudhuri, S. Fabrication and luminescent properties of c-axis oriented ZnO–ZnS core–shell and ZnS nanorod arrays by sulfidation of aligned ZnO nanorod arrays. *J. Phys. Chem. C* **2007**, *111*, 5039–5043.

[221] Chen, C. Y.; Lin, C. A.; Chen, M. J.; Lin, G. R.; He, J. H. ZnO/Al_2O_3 core–shell nanorod arrays: Growth, structural characterization, and luminescent properties. *Nanotechnology* **2009**, *20*, 185605.

[222] Law, M.; Greene, L. E.; Radenovic, A.; Kuykendall, T.; Liphardt, J.; Yang, P. D. ZnO–Al_2O_3 and ZnO–TiO_2 core–shell nanowire dye-sensitized solar cells. *J. Phys. Chem. B* **2006**, *110*, 22652–22663.

[223] Dergacheva, M. B.; Statsyuk, V. N.; Fogel, L. A. Electrodeposition of CdTe from ammonia-chloride buffer electrolytes. *J. Electroanal. Chem.* **2005**, *579*, 43–49.

[224] Kum, M. C.; Yoo, B. Y.; Rheem, Y.; Bozhilov, K. N.; Chen, W.; Mulchandani, A.; Myung, N. V. Synthesis and characterization of cadmium telluride nanowire. *Nanotechnology* **2008**, *19*, 325711.

[225] Xu, D. S.; Guo, Y. G.; Yu, D. P.; Guo, G. L.; Tang, Y. Q.; Yu, D. P. Highly ordered and well-oriented single-crystal CdTe nanowire arrays by direct-current electrodeposition. *J. Mater. Res.* **2002**, *17*, 1711–1714.

[226] Zhao, A. W.; Meng, G. W.; Zhang, L. D.; Gao, T.; Sun, S. H.; Pang, Y. T. Electrochemical synthesis of ordered CdTe nanowire arrays. *Appl. Phys. A* **2003**, *76*, 537–539.

[227] Cheng, C. W.; Liu, B.; Yang, H. Y.; Zhou, W. W.; Sun, L.; Chen, R.; Yu, S. F.; Zhang, J. X.; Gong, H.; Sun, H. D.; Fan, H. J. Hierarchical assembly of ZnO nanostructures on SnO_2 backbone nanowires: Low-temperature hydrothermal preparation and optical properties. *ACS Nano* **2009**, *3*, 3069–3076.

[228] Dloczik, L.; Engelhardt, R.; Ernst, K.; Lux-Steiner, M. C.; Konenkamp, R. Zinc sulfide columns by chemical conversion of zinc oxide. *Sens. Actuat. B-Chem.* **2002**, *84*, 33–36.

[229] Dloczik, L.; Engelhardt, R.; Ernst, K.; Fiechter, S.; Sieber, I.; Konenkamp, R. Hexagonal nanotubes of ZnS by chemical conversion of monocrystalline ZnO columns. *Appl. Phys. Lett.* **2001**, *78*, 3687–3689.

[230] Qiu, J. J.; Yu, W. D.; Gao, X. D.; Li, X. M. Sol-gel assisted ZnO nanorod array template to synthesize TiO_2 nanotube

arrays. *Nanotechnology* **2006**, *17*, 4695–4698.

[231] Qui, J. J.; Jin, Z. G.; Liu, Z. F.; Liu, X. X.; Liu, G. Q.; Wu, W. B.; Zhang, X.; Gao, X. D. Fabrication of TiO_2 nanotube film by well-aligned ZnO nanorod array film and sol–gel process. *Thin Solid Films* **2007**, *515*, 2897–2902.

[232] Dawood, F.; Schaak, R. E. ZnO-templated synthesis of wurtzite-type ZnS and ZnSe nanoparticles. *J. Am. Chem. Soc.* **2009**, *131*, 424–425.

[233] Alivisatos, A. P. Semiconductor clusters, nanocrystals, and quantum dots. *Science* **1996**, *271*, 933–937.

[234] Banholzer, M. J.; Millstone, J. E.; Qin, L. D.; Mirkin, C. A. Rationally designed nanostructures for surface-enhanced Raman spectroscopy. *Chem. Soc. Rev.* **2008**, *37*, 885–897.

[235] Sakano, T.; Tanaka, Y.; Nishimura, R.; Nedyalkov, N. N.; Atanasov, P. A.; Saiki, T.; Obara, M. Surface enhanced Raman scattering properties using Au-coated ZnO nanorods grown by two-step, off-axis pulsed laser deposition. *J. Phys. D: Appl. Phys.* **2008**, *41*, 235304.

[236] Wood, A.; Giersig, M.; Mulvaney, P. Fermi level equilibration in quantum dot–metal nanojunctions. *J. Phys. Chem. B* **2001**, *105*, 8810–8815.

[237] Fan, L. Y.; Yu, S. H. ZnO@Co hybrid nanotube arrays growth from electrochemical deposition: Structural, optical, photocatalytic and magnetic properties. *Phys. Chem. Chem. Phys.* **2009**, *11*, 3710–3717.

[238] Pacholski, C.; Kornowski, A.; Weller, H. Site-specific photodeposition of silver on ZnO nanorods. *Angew. Chem. Int. Ed.* **2004**, *43*, 4774–4777.

[239] Fan, F. R.; Ding, Y.; Liu, D. Y.; Tian, Z. Q.; Wang, Z. L. Facet-selective epitaxial growth of heterogeneous nanostructures of semiconductor and metal: ZnO nanorods on Ag nanocrystals. *J. Am. Chem. Soc.* **2009**, *131*, 12036–12037.

[240] Ko, H.; Singamaneni, S.; Tsukruk, V. V. Nanostructured surfaces and assemblies as SERS media. *Small* **2008**, *4*, 1576–1599.

[241] He, H.; Cai, W. P.; Lin, Y. X.; Chen, B. S. Surface decoration of ZnO nanorod arrays by electrophoresis in the Au colloidal solution prepared by laser ablation in water. *Langmuir* **2010**, *26*, 8925–8932.

[242] Yang, S. K.; Cai, W. P.; Liu, G. Q.; Zeng, H. B. From nanoparticles to nanoplates: Preferential oriented connection of Ag colloids during electrophoretic deposition. *J. Phys. Chem. C* **2009**, *113*, 7692–7696.

[243] Li, P.; Wei, Z.; Wu, T.; Peng, Q.; Li, Y. D. Au-ZnO hybrid nanopyramids and their photocatalytic properties. *J. Am. Chem. Soc.* **2011**, *133*, 5660–5663.

[244] Trejo, M.; Santiago, P.; Sobral, H.; Rendon, L.; Pal, U. Synthesis and growth mechanism of one-dimensional Zn/ZnO core–shell nanostructures in low-temperature hydrothermal process. *Cryst. Growth Des.* **2009**, *9*, 3024–3030.

[245] Zhang, W. D. Growth of ZnO nanowires on modified well-aligned carbon nanotube arrays. *Nanotechnology* **2006**, *17*, 1036–1040.

[246] Li, X. L.; Li, C.; Zhang, Y.; Chu, D. P.; Milne, W. I.; Fan, H. J. Atomic layer deposition of ZnO on multi-walled carbon nanotubes and its use for synthesis of CNT–ZnO heterostructures. *Nanoscale Res. Lett.* **2010**, *5*, 1836–1840.

[247] Zhang, W. D.; Jiang, L. C.; Ye, J. S. Photoelectrochemical study on charge transfer properties of ZnO nanowires promoted by carbon nanotubes. *J. Phys. Chem. C* **2009**, *113*, 16247–16253.

[248] Sernelius, B. E.; Berggren, K. F.; Jin, Z. C.; Hamberg, I.; Granqvist, C. G. Band-gap tailoring of ZnO by means of heavy Al doping. *Phys. Rev. B* **1988**, *37*, 10244–10248.

[249] Nadarajah, A.; Word, R. C.; Meiss, J.; Konenkamp, R. Flexible inorganic nanowire light-emitting diode. *Nano Lett.* **2008**, *8*, 534–537.

[250] Fang, T. H.; Kang, S. H. Electromechanical characteristics of ZnO:Al nanorods. *J. Nanosci. Nanotechnol.* **2010**, *10*, 405–412.

[251] Look, D. C.; Claflin, B.; Alivov, Y. I.; Park, S. J. The future of ZnO light emitters. *Phys. Status Solidi A* **2004**, *201*, 2203–2212.

[252] Xiang, B.; Wang, P. W.; Zhang, X. Z.; Dayeh, S. A.; Aplin, D. P. R.; Soci, C.; Yu, D. P.; Wang, D. L. Rational synthesis of *p*-type zinc oxide nanowire arrays using simple chemical vapor deposition. *Nano Lett.* **2007**, *7*, 323–328.

[253] Yuan, G. D.; Zhang, W. J.; Jie, J. S.; Fan, X.; Zapien, J. A.; Leung, Y. H.; Luo, L. B.; Wang, P. F.; Lee, C. S.; Lee, S. T. *p*-type ZnO nanowire arrays. *Nano Lett.* **2008**, *8*, 2591–2597.

[254] Hsu, Y. F.; Xi, Y. Y.; Tam, K. H.; Djurisic, A. B.; Luo, J. M.; Ling, C. C.; Cheung, C. K.; Ng, A. M. C.; Chan, W. K.; Deng, X.; Beling, C. D.; Fung, S.; Cheah, K. W.; Fong, P. W. K.; Surya, C. C. Undoped *p*-type ZnO nanorods synthesized by a hydrothermal method. *Adv. Funct. Mater.* **2008**, *18*, 1020–1030.

[255] Lin, C. C.; Chen, H. P.; Chen, S. Y. Synthesis and optoelectronic properties of arrayed *p*-type ZnO nanorods grown on ZnO film/Si wafer in aqueous solutions. *Chem. Phys. Lett.* **2005**, *404*, 30–34.

[256] Sun, M. H.; Zhang, Q. F.; Wu, J. L. Electrical and electroluminescence properties of As-doped *p*-type ZnO nanorod arrays. *J. Phys. D: Appl. Phys.* **2007**, *40*, 3798–3802.

[257] Thomas, M. A.; Cui, J. B. Electrochemical growth and characterization of Ag-doped ZnO nanostructures. *J. Vac. Sci. Technol. B* **2009**, *27*, 1673–1677.

[258] Yuhas, B. D.; Zitoun, D. O.; Pauzauskie, P. J.; Yang, P. Transition-metal doped zinc oxide nanowires. *Angew. Chem.*

Int. Ed. **2006**, *45*, 420–423.

[259] Cui, J.; Gibson, U. J. Enhanced nucleation, growth rate, and dopant incorporation in ZnO nanowires. *J. Phys. Chem. B* **2005**, *109*, 22074–22077.

[260] Cui, J. B.; Zeng, Q.; Gibson, U. J. Synthesis and magnetic properties of Co-doped ZnO nanowires. *J. Appl. Phys.* **2006**, *99*, 08M113.

[261] Yuhas, B. D.; Fakra, S.; Marcus, M. A.; Yang, P. D. Probing the local coordination environment for transition metal dopants in zinc oxide nanowires. *Nano Lett.* **2007**, *7*, 905–909.

[262] Liang, W. J.; Yuhas, B. D.; Yang, P. D. Magnetotransport in Co-doped ZnO nanowires. *Nano Lett.* **2009**, *9*, 892–896.

[263] Gayen, R. N.; Das, S. N.; Dalui, S.; Bhar, R.; Pal, A. K. Zinc magnesium oxide nanofibers on glass substrate by solution growth technique. *J. Cryst. Growth* **2008**, *310*, 4073–4080.

[264] Fang, T. H.; Kang, S. H. Preparation and characterization of Mg-doped ZnO nanorods. *J. Alloys Compd.* **2010**, *492*, 536–542.

[265] Shimpi, P.; Gao, P. X.; Goberman, D. G.; Ding, Y. Low temperature synthesis and characterization of MgO/ZnO composite nanowire arrays. *Nanotechnology* **2009**, *20*, 125608.

[266] Spanos, J. Photolithography applied to silicon transistor technology. *J. Electrochem. Soc.* **1961**, *108*, C176–C176.

[267] Boercker, J. E.; Schmidt, J. B.; Aydil, E. S. Transport limited growth of zinc oxide nanowires. *Cryst. Growth Des.* **2009**, *9*, 2783–2789.

[268] Coltrin, M. E.; Hsu, J. W. P.; Scrymgeour, D. A.; Creighton, J. R.; Simmons, N. C.; Matzke, C. M. Chemical kinetics and mass transport effects in solution-based selective-area growth of ZnO nanorods. *J. Cryst. Growth* **2008**, *310*, 584–593.

[269] Yi, S. H.; Choi, S. K.; Jang, J. M.; Kim, J. A.; Jung, W. G. Patterned growth of a vertically aligned zinc oxide rod array on a gallium nitride epitaxial layer by using a hydrothermal process. *J. Korean Phys. Soc.* **2008**, *53*, 227–231.

[270] Masuda, Y.; Kinoshita, N.; Sato, F.; Koumoto, K. Site-selective deposition and morphology control of UV- and visible-light-emitting ZnO crystals. *Cryst. Growth Des.* **2006**, *6*, 75–78.

[271] Morin, S. A.; Amos, F. F.; Jin, S. Biomimetic assembly of zinc oxide nanorods onto flexible polymers. *J. Am. Chem. Soc.* **2007**, *129*, 13776–13777.

[272] McCarley, R. L.; Vaidya, B.; Wei, S. Y.; Smith, A. F.; Patel, A. B.; Feng, J.; Murphy, M. C.; Soper, S. A. Resist-free patterning of surface architectures in polymer-based microanalytical devices. *J. Am. Chem. Soc.* **2005**, *127*, 842–843.

[273] Yang, P.; Zou, S. L.; Yang, W. T. Positive and negative ZnO micropatterning on functionatized polymer surfaces. *Small* **2008**, *4*, 1527–1536.

[274] Vieu, C.; Carcenac, F.; Pepin, A.; Chen, Y.; Mejias, M.; Lebib, A.; Manin-Ferlazzo, L.; Couraud, L.; Launois, H. Electron beam lithography: Resolution limits and applications. *Appl. Surf. Sci.* **2000**, *164*, 111–117.

[275] Kim, Y.; Lee, C.; Hong, Y. J.; Yi, G.; Kim, S. S.; Cheong, H. Controlled selective growth of ZnO nanorod and microrod arrays on Si substrates by a wet chemical method. *Appl. Phys. Lett.* **2006**, *89*, 163128.

[276] Lin, C. C.; Chen, S. Y.; Cheng, S. Y. Nucleation and growth behavior of well-aligned ZnO nanorods on organic substrates in aqueous solutions. *J. Cryst. Growth* **2005**, *283*, 141–146.

[277] Volk, J.; Nagata, T.; Erdelyi, R.; Barsony, I.; Toth, A. L.; Lukacs, I. E.; Czigany, Z.; Tomimoto, H.; Shingaya, Y.; Chikyow, T. Highly uniform epitaxial ZnO nanorod arrays for nanopiezotronics. *Nanoscale Res. Lett.* **2009**, *4*, 699–704.

[278] Liang, Y.; Zhen, C.; Zou, D.; Xu, D. Preparation of free-standing nanowire arrays on conductive substrates. *J. Am. Chem. Soc.* **2004**, *126*, 16338–16339.

[279] Dev, A.; Chaudhuri, S. Uniform large-scale growth of micropatterned arrays of ZnO nanowires synthesized by a surfactant assisted approach. *Nanotechnology* **2007**, *18*, 175607.

[280] Xu, S.; Ding, Y.; Wei, Y. G.; Fang, H.; Shen, Y.; Sood, A. K.; Polla, D. L.; Wang, Z. L. Patterned growth of horizontal ZnO nanowire arrays. *J. Am. Chem. Soc.* **2009**, *131*, 6670–6671.

[281] Wang, Z. L.; Yang, R. S.; Zhou, J.; Qin, Y.; Xu, C.; Hu, Y. F.; Xu, S. Lateral nanowire/nanobelt based nanogenerators, piezotronics and piezo-phototronics. *Mat. Sci. Eng. R* **2010**, *70*, 320–329.

[282] Qin, Y.; Yang, R. S.; Wang, Z. L. Growth of horizonatal ZnO nanowire arrays on any substrate. *J. Phys. Chem. C* **2008**, *112*, 18734–18736.

[283] Park, Y. K.; Choi, H. S.; Kim, J. H.; Kim, J. H.; Hahn, Y. B. High performance field-effect transistors fabricated with laterally grown ZnO nanorods in solution. *Nanotechnology* **2011**, *22*, 185310.

[284] Babak, N.; Chris, A. M.; Stephan, J. S.; Mark, D. V. Horizontal growth and *in situ* assembly of oriented zinc oxide nanowires. *Appl. Phys. Lett.* **2004**, *85*, 3244–3246.

[285] Harnack, O.; Pacholski, C.; Weller, H.; Yasuda, A.; Wessels, J. M. Rectifying behavior of electrically aligned ZnO nanorods. *Nano Lett.* **2003**, *3*, 1097–1101.

[286] Andeen, D. K. J. H.; Lang, F. F.; Goh, G. K. L.; Tripathy, S. Lateral epitaxial overgrowth of ZnO in water at 90 ˚C.

Adv. Funct. Mater. **2006**, *16*, 799–804.

[287] Saifullah, M. S. M.; Subramanian, K. R. V.; Kang, D. J.; Anderson, D.; Huck, W. T. S.; Jones, G. A. C.; Welland, M. E. Sub-10 nm high-aspect-ratio patterning of ZnO using an electron beam. *Adv. Mater.* **2005**, *17*, 1757–1761.

[288] Claeyssens, F.; Klini, A.; Mourka, A.; Fotakis, C. Laser patterning of Zn for ZnO nanostructure growth: Comparison between laser induced forward transfer in air and in vacuum. *Thin Solid Films* **2007**, *515*, 8529–8533.

[289] Guo, X. D.; Li, R. X.; Hang, Y.; Xu, Z. Z.; Yu, B. K.; Ma, H. L.; Lu, B.; Sun, X. W. Femtosecond laser-induced periodic surface structure on ZnO. *Mater. Lett.* **2008**, *62*, 1769–1771.

[290] Solak, H. H.; David, C.; Gobrecht, J.; Golovkina, V.; Cerrina, F.; Kim, S. O.; Nealey, P. F. Sub-50 nm period patterns with EUV interference lithography. *Microelectron. Eng.* **2003**, *67-68*, 56–62.

[291] Campbell, M.; Sharp, D. N.; Harrison, M. T.; Denning, R. G.; Turberfield, A. J. Fabrication of photonic crystals for the visible spectrum by holographic lithography. *Nature* **2000**, *404*, 53–56.

[292] Kim, K. S.; Jeong, H.; Jeong, M. S.; Jung, G. Y. Polymer-templated hydrothermal growth of vertically aligned single-crystal ZnO nanorods and morphological transformations using structural polarity. *Adv. Funct. Mater.* **2010**, *20*, 3055–3063.

[293] Wei, Y.; Wu, W.; Guo, R.; Yuan, D.; Das, S.; Wang, Z. L. Wafer-scale high-throughput ordered growth of vertically aligned ZnO nanowire arrays. *Nano Lett.* **2010**, *10*, 3414–3419.

[294] Yuan, D. J.; Guo, R.; Wei, Y. G.; Wu, W. Z.; Ding, Y.; Wang, Z. L.; Das, S. Heteroepitaxial patterned growth of vertically aligned and periodically distributed ZnO nanowires on GaN using laser interference ablation. *Adv. Funct. Mater.* **2010**, *20*, 3484–3489.

[295] Haynes, C. L.; Van Duyne, R. P. Nanosphere lithography: A versatile nanofabrication tool for studies of size-dependent nanoparticle optics. *J. Phys. Chem. B* **2001**, *105*, 5599–5611.

[296] Zeng, H. B.; Xu, X. J.; Bando, Y.; Gautam, U. K.; Zhai, T. Y.; Fang, X. S.; Liu, B. D.; Golberg, D. Template deformation-tailored ZnO nanorod/nanowire arrays: Full growth control and optimization of field-emission. *Adv. Funct. Mater.* **2009**, *19*, 3165–3172.

[297] Li, C.; Hong, G. S.; Wang, P. W.; Yu, D. P.; Qi, L. M. Wet chemical approaches to patterned arrays of well-aligned ZnO nanopillars assisted by monolayer colloidal crystals. *Chem. Mater.* **2009**, *21*, 891–897.

[298] Chou, S. Y.; Krauss, P. R.; Renstrom, P. J. Imprint of sub-25 nm vias and trenches in polymers. *Appl. Phys. Lett.* **1995**, *67*, 3114–3116.

[299] Wang, C. H.; Wong, A. S. W.; Ho, G. W. Facile solution route to vertically aligned, selective growth of ZnO nanostructure arrays. *Langmuir* **2007**, *23*, 11960–11963.

[300] Kwon, S. J.; Park, J. H.; Park, J. G. Patterned growth of ZnO nanorods by micromolding of sol–gel-derived seed layer. *Appl. Phys. Lett.* **2005**, *87*, 133112.

[301] Whitesides, G. M.; Ostuni, E.; Takayama, S.; Jiang, X. Y.; Ingber, D. E. Soft lithography in biology and biochemistry. *Annu. Rev. Biomed. Eng.* **2001**, *3*, 335–373.

[302] Hsu, J. W. P.; Tian, Z. R.; Simmons, N. C.; Matzke, C. M.; Voigt, J. A.; Liu, J. Directed spatial organization of zinc oxide nanorods. *Nano Lett.* **2005**, *5*, 83–86.

[303] Hsu, J. W. P.; Tian, Z. R.; Simmons, N. C.; Matzke, C. M.; Voigt, J. A.; Liu, J. Spatial organization of ZnO nanorods on surfaces via organic templating. *Proc. SPIE* **2005**, *5592*, 158–163.

[304] Lee, J. H.; Hon, M. H.; Chung, Y. W.; Leu, I. C. Microcontact printing of organic self-assembled monolayers for patterned growth of well-aligned ZnO nanorod arrays and their field-emission properties. *J. Am. Ceram. Soc.* **2009**, *92*, 2192–2196.

[305] Sirringhaus, H.; Kawase, T.; Friend, R. H.; Shimoda, T.; Inbasekaran, M.; Wu, W.; Woo, E. P. High-resolution inkjet printing of all-polymer transistor circuits. *Science* **2000**, *290*, 2123–2126.

[306] Kitsomboonloha, R.; Baruah, S.; Myint, M. T. Z.; Subramanian, V.; Dutta, J. Selective growth of zinc oxide nanorods on inkjet printed seed patterns. *J. Cryst. Growth* **2009**, *311*, 2352–2358.

[307] de Gans, B. J.; Duineveld, P. C.; Schubert, U. S. Inkjet printing of polymers: State of the art and future developments. *Adv. Mater.* **2004**, *16*, 203–213.

[308] Sekitani, T.; Noguchi, Y.; Zschieschang, U.; Klauk, H.; Someya, T. Organic transistors manufactured using inkjet technology with subfemtoliter accuracy. *Proc. Natl. Acad. Sci. USA* **2008**, *105*, 4976–4980.

[309] Rogers, J. A.; Someya, T.; Huang, Y. G. Materials and mechanics for stretchable electronics. *Science* **2010**, *327*, 1603–1607.

[310] Hariharan, C. Photocatalytic degradation of organic contaminants in water by ZnO nanoparticles: Revisited. *Appl. Catal. A* **2006**, *304*, 55–61.

[311] Yang, X.; Wolcottt, A.; Wang, G.; Sobo, A.; Fitzmorris, R. C.; Qian, F.; Zhang, J. Z.; Li, Y. Nitrogen-doped ZnO nanowire arrays for photoelectrochemical water splitting. *Nano Lett.* **2009**, *9*, 2331–2336.

[312] Jang, E. S.; Won, J. H.; Hwang, S. J.; Choy, J. H. Fine tuning of the face orientation of ZnO crystals to optimize

their photocatalytic activity. *Adv. Mater.* **2006**, *18*, 3309–3312.

[313] Akhavan, O. Graphene nanomesh by ZnO nanorod photocatalysts. *ACS Nano* **2010**, *4*, 4174–4180.

[314] Lu, F.; Cai, W. P.; Zhang, Y. G. ZnO hierarchical micro/nanoarchitectures: Solvothermal synthesis and structurally enhanced photocatalytic performance. *Adv. Funct. Mater.* **2008**, *18*, 1047–1056.

[315] Wu, Q.; Chen, X.; Zhang, P.; Han, Y.; Chen, X.; Yan, Y.; Li, S. Amino acid-assisted synthesis of ZnO hierarchical architectures and their novel photocatalytic activities. *Cryst. Growth Des.* **2008**, *8*, 3010–3018.

[316] Kurtz, M.; Strunk, J.; Hinrichsen, O.; Muhler, M.; Fink, K.; Meyer, B.; Woll, C. Active sites on oxide surfaces: ZnO-catalyzed synthesis of methanol from CO and H_2. *Angew. Chem. Int. Ed.* **2005**, *44*, 2790–2794.

[317] Lin, Y. G.; Hsu, Y. K.; Chen, S. Y.; Lin, Y. K.; Chen, L. C.; Chen, K. H. Nanostructured zinc oxide nanorods with copper nanoparticles as a microreformation catalyst. *Angew. Chem. Int. Ed.* **2009**, *48*, 7586–7590.

[318] Li, C. C.; Lin, R. J.; Lin, H. P.; Lin, Y. K.; Lin, Y. G.; Chang, C. C.; Chen, L. C.; Chen, K. H. Catalytic performance of plate-type Cu/Fe nanocomposites on ZnO nanorods for oxidative steam reforming of methanol. *Chem. Commun.* **2011**, *47*, 1473–1475.

[319] Lin, Y. G.; Hsu, Y. K.; Chen, S. Y.; Chen, L. C.; Chen, K. H. Microwave-activated CuO nanotip/ZnO nanorod nano-architectures for efficient hydrogen production. *J. Mater. Chem.* **2011**, *21*, 324–326.

[320] Boucher, M. B.; Yi, N.; Gittleson, F.; Zugic, B.; Saltsburg, H.; Flytzani-Stephanopoulos, M. Hydrogen production from methanol over gold supported on ZnO and CeO_2 nanoshapes. *J. Phys. Chem. C* **2011**, *115*, 1261–1268.

[321] Tak, Y.; Kim, H.; Lee, D.; Yong, K. Type-II CdS nanoparticle–ZnO nanowire heterostructure arrays fabricated by a solution process: Enhanced photocatalytic activity. *Chem. Commun.* **2008**, 4585–4587.

[322] Wang, W. W.; Zhu, Y. J.; Yang, L. X. ZnO–SnO_2 hollow spheres and hierarchical nanosheets: Hydrothermal preparation, formation mechanism, and photocatalytic properties. *Adv. Funct. Mater.* **2007**, *17*, 59–64.

[323] Tian, N.; Zhou, Z. Y.; Sun, S. G.; Ding, Y.; Wang, Z. L. Synthesis of tetrahexahedral platinum nanocrystals with high-index facets and high electro-oxidation activity. *Science* **2007**, *316*, 732–735.

[324] Li, G. R.; Hu, T.; Pan, G. L.; Yan, T. Y.; Gao, X. P.; Zhu, H. Y. Morphology–function relationship of ZnO: Polar planes, oxygen vacancies, and activity. *J. Phys. Chem. C* **2008**, *112*, 11859–11864.

[325] Feng, X.; Feng, L.; Jin, M.; Zhai, J.; Jiang, L.; Zhu, D. Reversible super-hydrophobicity to super-hydrophilicity transition of aligned ZnO nanorod films. *J. Am. Chem. Soc.* **2004**, *126*, 62–63.

[326] Onda, T.; Shibuichi, S.; Satoh, N.; Tsujii, K. Super-water-repellent fractal surfaces. *Langmuir* **1996**, *12*, 2125–2127.

[327] Sun, R. D.; Nakajima, A.; Fujishima, A.; Watanabe, T.; Hashimoto, K. Photoinduced surface wettability conversion of ZnO and TiO_2 thin films. *J. Phys. Chem. B* **2001**, *105*, 1984–1990.

[328] Ding, Y.; Xu, S.; Zhang, Y.; Wang, A. C.; Wang, M. H.; Xiu, Y. H.; Wong, C. P.; Wang, Z. L. Modifying the anti-wetting property of butterfly wings and water strider legs by atomic layer deposition coating: surface materials versus geometry. *Nanotechnology* **2008**, *19*, 355708.

[329] Soci, C.; Zhang, A.; Xiang, B.; Dayeh, S. A.; Aplin, D. P. R.; Park, J.; Bao, X. Y.; Lo, Y. H.; Wang, D. ZnO Nanowire UV photodetectors with high internal gain. *Nano Lett.* **2007**, *7*, 1003–1009.

[330] Badre, C.; Pauporté, T. Nanostructured ZnO-based surface with reversible electrochemically adjustable wettability. *Adv. Mater.* **2009**, *21*, 697–701.

[331] Guo, M.; Diao, P.; Cai, S. M. Highly hydrophilic and superhydrophobic ZnO nanorod array films. *Thin Solid Films* **2007**, *515*, 7162–7166.

[332] Xu, N. S.; Huq, S. E. Novel cold cathode materials and applications. *Mat. Sci. Eng. R* **2005**, *48*, 47–189.

[333] Dev, A.; Panda, S. K.; Kar, S.; Chakrabarti, S.; Chaudhuri, S. Surfactant-assisted route to synthesize well-aligned ZnO nanorod arrays on sol–gel-derived ZnO thin films. *J. Phys. Chem. B* **2006**, *110*, 14266–14272.

[334] Hung, C. H.; Whang, W. T. Low-temperature solution approach toward highly aligned ZnO nanotip arrays. *J. Cryst. Growth* **2004**, *268*, 242–248.

[335] Cui, J. B.; Daghlian, C. P.; Gibson, U. J.; Pusche, R.; Geithner, P.; Ley, L. Low-temperature growth and field emission of ZnO nanowire arrays. *J. Appl. Phys.* **2005**, *97*, 044315.

[336] Wei, A.; Sun, X. W.; Xu, C. X.; Dong, Z. L.; Yu, M. B.; Huang, W. Stable field emission from hydrothermally grown ZnO nanotubes. *Appl. Phys. Lett.* **2006**, *88*, 213102.

[337] Xu, C. X.; Sun, X. W. Field emission from zinc oxide nanopins. *Appl. Phys. Lett.* **2003**, *83*, 3806–3808.

[338] Cao, B. Q.; Teng, X. M.; Heo, S. H.; Li, Y.; Cho, S. O.; Li, G. H.; Cai, W. P. Different ZnO nanostructures fabricated by a seed-layer assisted electrochemical route and their photoluminescence and field emission properties. *J. Phys. Chem. C* **2007**, *111*, 2470–2476.

[339] Ahsanulhaq, Q.; Kim, J. H.; Hahn, Y. B. Controlled selective

growth of ZnO nanorod arrays and their field emission properties. *Nanotechnology* **2007**, *18*, 485307.

[340] Kee, C. S.; Ko, D. K.; Lee, J. Photonic band gaps of two-dimensional ZnO nanorod photonic crystals. *J. Phys. D: Appl. Phys.* **2005**, *38*, 3850–3853.

[341] Matsuu, M.; Shimada, S.; Masuya, K.; Hirano, S.; Kuwabara, M. Formation of periodically ordered zinc oxide nanopillars in aqueous solution: An approach to photonic crystals at visible wavelengths. *Adv. Mater.* **2006**, *18*, 1617–1621.

[342] Hirano, S. Oxide nanowire arrays and two-dimensional photonic crystals for control of light. *J. Ceram. Soc. Jpn.* **2007**, *115*, 92–100.

[343] Cui, J. B.; Gibson, U. Low-temperature fabrication of single-crystal ZnO nanopillar photonic bandgap structures. *Nanotechnology* **2007**, *18*, 155302.

[344] Cui, J. B. Structural and optical properties of periodically ordered ZnO nanowires. *Sci. China Ser. E* **2009**, *52*, 313–317.

[345] Volk, J.; Hakansson, A.; Miyazaki, H. T.; Nagata, T.; Shimizu, J.; Chikyow, T. Fully engineered homoepitaxial zinc oxide nanopillar array for near-surface light wave manipulation. *Appl. Phys. Lett.* **2008**, *92*, 183114.

[346] Alivov, Y. I.; Kalinina, E. V.; Cherenkov, A. E.; Look, D. C.; Ataev, B. M.; Omaev, A. K.; Chukichev, M. V.; Bagnall, D. M. Fabrication and characterization of *n*-ZnO/*p*-AlGaN heterojunction light-emitting diodes on 6H-SiC substrates. *Appl. Phys. Lett.* **2003**, *83*, 4719–4721.

[347] Lyu, S. C.; Zhang, Y.; Ruh, H.; Lee, H. J.; Shim, H. W.; Suh, E. K.; Lee, C. J. Low temperature growth and photoluminescence of well-aligned zinc oxide nanowires. *Chem. Phys. Lett.* **2002**, *363*, 134–138.

[348] Tam, K. H.; Cheung, C. K.; Leung, Y. H.; Djurisic, A. B.; Ling, C. C.; Beling, C. D.; Fung, S.; Kwok, W. M.; Chan, W. K.; Phillips, D. L.; Ding, L.; Ge, W. K. Defects in ZnO nanorods prepared by a hydrothermal method. *J. Phys. Chem. B* **2006**, *110*, 20865–20871.

[349] Lucas, M.; Wang, Z. L.; Riedo, E. Combined polarized Raman and atomic force microscopy: *In situ* study of point defects and mechanical properties in individual ZnO nanobelts. *Applied Physics Letts*. **2009**, *95*, 051904.

[350] Kim, Y. J.; Shang, H. M.; Cao, G. Z. Growth and characterization of [001] ZnO nanorod array on ITO substrate with electric field assisted nucleation. *J. Sol-Gel Sci. Technol.* **2006**, *38*, 79–84.

[351] Zhou, H.; Chen, X. M.; Wu, G. H.; Gao, F.; Qin, N.; Bao, D. H. Significantly enhanced red photoluminescence properties of nanocomposite films composed of a ferroelectric $Bi_{3.6}Eu_{0.4}Ti_3O_{12}$ matrix and highly *c*-axis-oriented ZnO nanorods on Si substrates prepared by a hybrid chemical solution method. *J. Am. Chem. Soc.* **2010**, *132*, 1790–1791.

[352] Xiang, S.; Wang, Z. L. Unpublished results.

[353] Mahalingam, T.; Lee, K. M.; Park, K. H.; Lee, S.; Ahn, Y.; Park, J. Y.; Koh, K. H. Low temperature wet chemical synthesis of good optical quality vertically aligned crystalline ZnO nanorods. *Nanotechnology* **2007**, *18*, 035606.

[354] Hu, Y. F.; Zhang, Y.; Xu, C.; Lin, L.; Snyder, R. L.; Wang, Z. L. Self-powered system with wireless data transmission. *Nano Letters* **2011**, *11*, 2572–2577.

[355] Ho, G. W.; Wong, A. S. W. One step solution synthesis towards ultra-thin and uniform single-crystalline ZnO nanowires. *Appl. Phys. A* **2007**, *86*, 457–462.

[356] Li, C. C.; Chen, H. P.; Liao, H. C.; Chen, S. Y. Enhanced luminescent and electrical properties of hydrogen-plasma ZnO nanorods grown on wafer-scale flexible substrates. *Appl. Phys. Lett.* **2005**, *86*, 183103.

[357] Lee, S. J.; Park, S. K.; Park, C. R.; Lee, J. Y.; Park, J.; Do, Y. R. Spatially separated ZnO nanopillar arrays on Pt/Si substrates prepared by electrochemical deposition. *J. Phys. Chem. C* **2007**, *111*, 11793–11801.

[358] Richters, J. P.; Voss, T.; Wischmeier, L.; Ruckmann, I.; Gutowski, J. Influence of polymer coating on the low-temperature photoluminescence properties of ZnO nanowires. *Appl. Phys. Lett.* **2008**, *92*, 011103.

[359] Varshni, Y. P. Temperature dependence of energy gap in semiconductors. *Physica* **1967**, *34*, 149–154.

[360] Sakai, K.; Noguchi, K.; Fukuyama, A.; Ikari, T.; Okada, T. Low-temperature photoluminescence of nanostructured ZnO crystal synthesized by pulsed-laser ablation. *Jpn. J. Appl. Phys.* **2009**, *48*, 085001.

[361] Su, F. H.; Wang, W. J.; Ding, K.; Li, G. H.; Liu, Y. F.; Joly, A. G.; Chen, W. Pressure dependence of the near-band-edge photoluminescence from ZnO microrods at low temperature. *J. Phys. Chem. Solids* **2006**, *67*, 2376–2381.

[362] Fang, F.; Zhao, D. X.; Li, B. H.; Zhang, Z. Z.; Shen, D. Z.; Wang, X. H. Bending-induced enhancement of longitudinal optical phonon scattering in ZnO nanowires. *J. Phys. Chem. C* **2010**, *114*, 12477–12480.

[363] Choy, J. H.; Jang, E. S.; Won, J. H.; Chung, J. H.; Jang, D. J.; Kim, Y. W. Soft solution route to directionally grown ZnO nanorod arrays on Si wafer; Room-temperature ultraviolet laser. *Adv. Mater.* **2003**, *15*, 1911–1914.

[364] Qiu, Z.; Wong, K. S.; Wu, M.; Lin, W.; Xu, H. Microcavity lasing behavior of oriented hexagonal ZnO nanowhiskers grown by hydrothermal oxidation. *Appl. Phys. Lett.* **2004**, *84*, 2739–2741.

[365] Voss, T.; Kudyk, I.; Wischmeier, L.; Gutowski, J. Nonlinear

optics with ZnO nanowires. *Phys. Status Solidi B* **2009**, *246*, 311–314.

[366] Johnson, J. C.; Yan, H. Q.; Schaller, R. D.; Petersen, P. B.; Yang, P. D.; Saykally, R. J. Near-field imaging of nonlinear optical mixing in single zinc oxide nanowires. *Nano Lett.* **2002**, *2*, 279–283.

[367] Jeong, M. C.; Oh, B. Y.; Ham, M. H.; Myoung, J. M. Electroluminescence from ZnO nanowires in *n*-ZnO film/ZnO nanowire array/*p*-GaN film heterojunction light-emitting diodes. *Appl. Phys. Lett.* **2006**, *88*, 202105.

[368] Jeong, M. C.; Oh, B. Y.; Ham, M. H.; Lee, S. W.; Myoung, J. M. ZnO-nanowire-inserted GaN/ZnO heterojunction light-emitting diodes. *Small* **2007**, *3*, 568–572.

[369] Reddy, N. K.; Ahsanulhaq, Q.; Hahn, Y. B. Fabrication of zinc oxide nanorods based heterojunction devices using simple and economic chemical solution method. *Appl. Phys. Lett.* **2008**, *93*, 083124.

[370] Chen, C. H.; Chang, S. J.; Chang, S. P.; Li, M. J.; Chen, I. C.; Hsueh, T. J.; Hsu, C. L. Electroluminescence from *n*-ZnO nanowires/*p*-GaN heterostructure light-emitting diodes. *Appl. Phys. Lett.* **2009**, *95*, 223101.

[371] Xu, S.; Xu, C.; Liu, Y.; Hu, Y.; Yang, R.; Yang, Q.; Ryou, J. H.; Kim, H. J.; Lochner, Z.; Choi, S.; Dupuis, R.; Wang, Z. L. Ordered nanowire array blue/near-UV light emitting diodes. *Adv. Mater.* **2010**, *22*, 4749–4753.

[372] Alivov, Y. I.; Van Nostrand, J. E.; Look, D. C.; Chukichev, M. V.; Ataev, B. M. Observation of 430 nm electro-luminescence from ZnO/GaN heterojunction light-emitting diodes. *Appl. Phys. Lett.* **2003**, *83*, 2943–2945.

[373] Bulashevich, K. A.; Evstratov, I. Y.; Karpov, S. Y. Hybrid ZnO/III-nitride light-emitting diodes: Modelling analysis of operation. *Phys. Status Solidi A* **2007**, *204*, 241–245.

[374] Titkov, I. E.; Zubrilov, A. S.; Delimova, L. A.; Mashovets, D. V.; Liniichuk, I. A.; Grekhov, I. V. White electro-luminescence from ZnO/GaN structures. *Semiconductors* **2007**, *41*, 564–569.

[375] Kishwar, S.; ul Hasan, K.; Tzamalis, G.; Nur, O.; Willander, M.; Kwack, H. S.; Dang, D. L. S. Electro-optical and cathodoluminescence properties of low temperature grown ZnO nanorods/*p*-GaN white light emitting diodes. *Phys. Status Solidi A* **2010**, *207*, 67–72.

[376] Guo, R.; Nishimura, J.; Matsumoto, M.; Higashihata, M.; Nakamura, D.; Okada, T. Electroluminescence from ZnO nanowire-based *p*-GaN/*n*-ZnO heterojunction light-emitting diodes. *Appl. Phys. B* **2009**, *94*, 33–38.

[377] Xu, H. Y.; Liu, Y. C.; Liu, Y. X.; Xu, C. S.; Shao, C. L.; Mu, R. Ultraviolet electroluminescence from *p*-GaN/*i*-ZnO/*n*-ZnO heterojunction light-emitting diodes. *Appl. Phys. B* **2005**, *80*, 871–874.

[378] Liu, H. F.; Hu, G. X.; Gong, H.; Zang, K. Y.; Chua, S. J. Effects of oxygen on low-temperature growth and band alignment of ZnO/GaN heterostructures. *J. Vac. Sci. Technol. A* **2008**, *26*, 1462–1468.

[379] Aguilar, C. A.; Haight, R.; Mavrokefalos, A.; Korgel, B. A.; Chen, S. C. Probing electronic properties of molecular engineered zinc oxide nanowires with photoelectron spectroscopy. *ACS Nano* **2009**, *3*, 3057–3062.

[380] Ng, A. M. C.; Xi, Y. Y.; Hsu, Y. F.; Djurisic, A. B.; Chan, W. K.; Gwo, S.; Tam, H. L.; Cheah, K. W.; Fong, P. W. K.; Lui, H. F.; Surya, C. GaN/ZnO nanorod light emitting diodes with different emission spectra. *Nanotechnology* **2009**, *20*, 445201.

[381] Alivov, Y. I.; Ozgur, U.; Dogan, S.; Liu, C.; Moon, Y.; Gu, X.; Avrutin, V.; Fu, Y.; Morkoc, H. Forward-current electroluminescence from GaN/ZnO double heterostructure diode. *Solid-State Electron.* **2005**, *49*, 1693–1696.

[382] Zhang, X. M.; Lu, M. Y.; Zhang, Y.; Chen, L. J.; Wang, Z. L. Fabrication of a high-brightness blue-light-emitting diode using a ZnO-nanowire array grown on *p*-GaN thin film. *Adv. Mater.* **2009**, *21*, 2767–2770.

[383] Bayram, C.; Teherani, F. H.; Rogers, D. J.; Razeghi, M. A hybrid green light-emitting diode comprised of *n*-ZnO/(InGaN/GaN) multi-quantum-wells/*p*-GaN. *Appl. Phys. Lett.* **2008**, *93*, 081111.

[384] Choi, H. W.; Jeon, C. W.; Dawson, M. D.; Edwards, P. R.; Martin, R. W.; Tripathy, S. Mechanism of enhanced light output efficiency in InGaN-based microlight emitting diodes. *J. Appl. Phys.* **2003**, *93*, 5978–5982.

[385] Konenkamp, R.; Word, R. C.; Schlegel, C. Vertical nanowire light-emitting diode. *Appl. Phys. Lett.* **2004**, *85*, 6004–6006.

[386] Konenkamp, R.; Word, R. C.; Godinez, M. Ultraviolet electroluminescence from ZnO/polymer heterojunction light-emitting diodes. *Nano Lett.* **2005**, *5*, 2005–2008.

[387] Bolink, H. J.; Coronado, E.; Repetto, D.; Sessolo, M. Air stable hybrid organic–inorganic light emitting diodes using ZnO as the cathode. *Appl. Phys. Lett.* **2007**, *91*, 223501.

[388] Konenkamp, R.; Nadarajah, A.; Word, R. C.; Meiss, J.; Engelhardt, R. ZnO nanowires for LED and field-emission displays. *J. Soc. Inf. Display* **2008**, *16*, 609–613.

[389] Willander, M.; Lozovik, Y. E.; Wadeasa, A.; Nur, O.; Semenov, A. G.; Vonorova, N. S. Light emission from different ZnO junctions and nanostructures. *Phys. Status Solidi A* **2009**, *206*, 853–859.

[390] Wadeasa, A.; Beegum, S. L.; Raja, S.; Nur, O.; Willander, M. The demonstration of hybrid *n*-ZnO nanorod/*p*-polymer heterojunction light emitting diodes on glass substrates. *Appl. Phys. A* **2009**, *95*, 807–812.

[391] Guo, H. G.; Zhou, J. Z.; Lin, Z. G. ZnO nanorod light-

emitting diodes fabricated by electrochemical approaches. *Electrochem. Commun.* **2008**, *10*, 146–150.

[392] Liu, J.; Ahn, Y. H.; Park, J. Y.; Koh, K. H.; Lee, S. Hybrid light-emitting diodes based on flexible sheets of mass-produced ZnO nanowires. *Nanotechnology* **2009**, *20*, 445203.

[393] Sun, X. W.; Huang, J. Z.; Wang, J. X.; Xu, Z. A ZnO nanorod inorganic/organic heterostructure light-emitting diode emitting at 342 nm. *Nano Lett.* **2008**, *8*, 1219–1223.

[394] Round, H. J. A note on carborundum. *Electrical World* **1907**, *49*, 309.

[395] Livingst. A. W.; Turvey, K.; Allen, J. W. Electroluminescence in forward-biased zinc selenide Schottky diodes. *Solid-State Electron.* **1973**, *16*, 351–356.

[396] Allen, J. W.; Livingstone, A. W.; Turvey, K. Electro-luminescence in reverse-biased zinc selenide Schottky diodes. *Solid-State Electron.* **1972**, *15*, 1363–1369.

[397] Lazarouk, S.; Jaguiro, P.; Katsouba, S.; Masini, G.; LaMonica, S.; Maiello, G.; Ferrari, A. Stable electroluminescence from reverse biased *n*-type porous silicon-aluminum Schottky junction device. *Appl. Phys. Lett.* **1996**, *68*, 2108–2110.

[398] Steckl, A. J.; Garter, M.; Birkhahn, R.; Scofield, J. Green electroluminescence from Er-doped GaN Schottky barrier diodes. *Appl. Phys. Lett.* **1998**, *73*, 2450–2452.

[399] Wang, Y. X.; Zhang, Q. F.; Sun, H.; Chang, Y. L.; Wu, J. L. Fabrication of ZnO nanowire-based diodes and their light-emitting properties. *Acta Phys. Sin.-Chin. Ed.* **2008**, *57*, 1141–1144.

[400] Guo, H. H.; Lin, Z. H.; Feng, Z. F.; Lin, L. L.; Zhou, J. Z. White-light-emitting diode based on ZnO nanotubes. *J. Phys. Chem. C* **2009**, *113*, 12546–12550.

[401] Bano, N.; Hussain, I.; Nur, O.; Willander, M.; Kwack, H. S.; Dang, D. L. S. Study of Au/ZnO nanorods Schottky light-emitting diodes grown by low-temperature aqueous chemical method. *Appl. Phys. A* **2010**, *100*, 467–472.

[402] Tan, S. T.; Sun, X. W.; Zhao, J. L.; Iwan, S.; Cen, Z. H.; Chen, T. P.; Ye, J. D.; Lo, G. Q.; Kwong, D. L.; Teo, K. L. Ultraviolet and visible electroluminescence from *n*-ZnO/SiO_x/(*n*,*p*)-Si heterostructured light-emitting diodes. *Appl. Phys. Lett.* **2008**, *93*, 013506.

[403] Benisty, H.; De Neve, H.; Weisbuch, C. Impact of planar microcavity effects on light extraction—Part I: Basic concepts and analytical trends. *IEEE J. Quantum. Elect.* **1998**, *34*, 1612–1631.

[404] Schnitzer, I.; Yablonovitch, E.; Caneau, C.; Gmitter, T. J.; Scherer, A. 30% external quantum efficiency from surface textured, thin-film light-emitting-diodes. *Appl. Phys. Lett.* **1993**, *63*, 2174–2176.

[405] Fujii, T.; Gao, Y.; Sharma, R.; Hu, E. L.; DenBaars, S. P.; Nakamura, S. Increase in the extraction efficiency of GaN-based light-emitting diodes via surface roughening. *Appl. Phys. Lett.* **2004**, *84*, 855–857.

[406] Kim, H.; Kim, K. K.; Choi, K. K.; Kim, H.; Song, J. O.; Cho, J.; Baik, K. H.; Sone, C.; Park, Y.; Seong, T. Y. Design of high-efficiency GaN-based light emitting diodes with vertical injection geometry. *Appl. Phys. Lett.* **2007**, *91*, 023510.

[407] Murai, A.; Thompson, D. B.; Masui, H.; Fellows, N.; Mishra, U. K.; Nakamura, S.; DenBaars, S. P. Hexagonal pyramid shaped light-emitting diodes based on ZnO and GaN direct wafer bonding. *Appl. Phys. Lett.* **2006**, *89*, 171116.

[408] Schubert, E. F.; Kim, J. K. Solid-state light sources getting smart. *Science* **2005**, *308*, 1274–1278.

[409] Barnes, W. L. Electromagnetic crystals for surface plasmon polaritons and the extraction of light from emissive devices. *J. Lightwave Technol.* **1999**, *17*, 2170–2182.

[410] Chen, L.; Nurmikko, A. V. Fabrication and performance of efficient blue light emitting III-nitride photonic crystals. *Appl. Phys. Lett.* **2004**, *85*, 3663–3665.

[411] Oder, T. N.; Kim, K. H.; Lin, J. Y.; Jiang, H. X. III-Nitride blue and ultraviolet photonic crystal light emitting diodes. *Appl. Phys. Lett.* **2004**, *84*, 466–468.

[412] Lu, Y.; Zhong, J.; Zhu, J.; Saraf, G.; Chen, H. H.; Duan, Z. Q.; Reyes, P.; Shen, H.; Mackie, D. M.; Wittkstruck, R. H.; Ballato, A. Novel devices using multifunctional ZnO and its nanostructures. http://dodreports.com/pdf/ada505710.pdf.

[413] Kim, K. K.; Lee, S. D.; Kim, H.; Park, J. C.; Lee, S. N.; Park, Y.; Park, S. J.; Kim, S. W. Enhanced light extraction efficiency of GaN-based light-emitting diodes with ZnO nanorod arrays grown using aqueous solution. *Appl. Phys. Lett.* **2009**, *94*, 071118.

[414] An, S. J.; Chae, J. H.; Yi, G. C.; Park, G. H. Enhanced light output of GaN-based light-emitting diodes with ZnO nanorod arrays. *Appl. Phys. Lett.* **2008**, *92*, 121108.

[415] Zhong, J.; Chen, H.; Saraf, G.; Lu, Y.; Choi, C. K.; Song, J. J.; Mackie, D. M.; Shen, H. Integrated ZnO nanotips on GaN light emitting diodes for enhanced emission efficiency. *Appl. Phys. Lett.* **2007**, *90*, 203515.

[416] Lai, E.; Kim, W.; Yang, P. Vertical nanowire array-based light emitting diodes. *Nano Res.* **2008**, *1*, 123–128.

[417] Bao, J. M.; Zimmler, M. A.; Capasso, F.; Wang, X. W.; Ren, Z. F. Broadband ZnO single-nanowire light-emitting diode. *Nano Lett.* **2006**, *6*, 1719–1722.

[418] Johnson, J. C.; Yan, H. Q.; Yang, P. D.; Saykally, R. J. Optical cavity effects in ZnO nanowire lasers and waveguides. *J. Phys. Chem. B* **2003**, *107*, 8816–8828.

[419] Kim, K. S.; Kim, S. M.; Jeong, H.; Jeong, M. S.; Jung, G. Y. Enhancement of light extraction through the wave-guiding effect of ZnO sub-microrods in InGaN blue light-emitting

diodes. *Adv. Funct. Mater.* **2010**, *20*, 1076–1082.

[420] Voss, T.; Svacha, G. T.; Mazur, E.; Muller, S.; Ronning, C.; Konjhodzic, D.; Marlow, F. High-order waveguide modes in ZnO nanowires. *Nano Letters*. **2007**, *7*, 3675–3680.

[421] Park, S. H.; Kim, S. H.; Han, S. W. Growth of homoepitaxial ZnO film on ZnO nanorods and light emitting diode applications. *Nanotechnology* **2007**, *18*, 055608.

[422] Sun, X. W.; Wang, J. X. Fast switching electrochromic display using a viologen-modified ZnO nanowire array electrode. *Nano Lett.* **2008**, *8*, 1884–1889.

[423] Granqvist, C. G. Electrochromic tungsten oxide films: Review of progress 1993–1998. *Sol. Energy Mater. Sol. Cells* **2000**, *60*, 201–262.

[424] Bonhote, P.; Gogniat, E.; Campus, F.; Walder, L.; Gratzel, M. Nanocrystalline electrochromic displays. *Displays* **1999**, *20*, 137–144.

[425] Hu, A. Z.; Wu, F.; Liu, J. P.; Jiang, J.; Ding, R. M.; Li, X.; Cheng, C. X.; Zhu, Z. H.; Huang, X. T. Density- and adhesion-controlled ZnO nanorod arrays on the ITO flexible substrates and their electrochromic performance. *J. Alloys Compd.* **2010**, *507*, 261–266.

[426] Li, M.; Zhang, H. Y.; Guo, C. X.; Xu, J. B.; Fu, X. J. The research on suspended ZnO nanowire field-effect transistor. *Chin. Phys. B* **2009**, *18*, 1594–1597.

[427] Sun, B. Q.; Sirringhaus, H. Surface tension and fluid flow driven self-assembly of ordered ZnO nanorod films for high-performance field effect transistors. *J. Am. Chem. Soc.* **2006**, *128*, 16231–16237.

[428] Ju, S. Y.; Facchetti, A.; Xuan, Y.; Liu, J.; Ishikawa, F.; Ye, P. D.; Zhou, C. W.; Marks, T. J.; Janes, D. B. Fabrication of fully transparent nanowire transistors for transparent and flexible electronics. *Nat. Nanotech.* **2007**, *2*, 378–384.

[429] Hsu, C. L.; Tsai, T. Y. Fabrication of fully transparent indium-doped ZnO nanowire field-effect transistors on ITO/glass substrates. *J. Electrochem. Soc.* **2011**, *158*, K20–K23.

[430] Ko, S. H.; Park, I.; Pan, H.; Misra, N.; Rogers, M. S.; Grigoropoulos, C. P.; Pisano, A. P. ZnO nanowire network transistor fabrication on a polymer substrate by low-temperature, all-inorganic nanoparticle solution process. *Appl. Phys. Lett.* **2008**, *92*, 154102.

[431] Gao, P. X.; Liu, J.; Buchine, B. A.; Weintraub, B.; Wang, Z. L.; Lee, J. L. Bridged ZnO nanowires across trenched electrodes. *Appl. Phys. Lett.* **2007**, *91*, 142108.

[432] Xu, S.; Qin, Y.; Xu, C.; Wei, Y. G.; Yang, R. S.; Wang, Z. L. Self-powered nanowire devices. *Nat. Nanotechnol.* **2010**, *5*, 366–373.

[433] Wang, J. X.; Sun, X. W.; Yang, Y.; Huang, H.; Lee, Y. C.; Tan, O. K.; Vayssieres, L. Hydrothermally grown oriented ZnO nanorod arrays for gas sensing applications. *Nanotechnology* **2006**, *17*, 4995–4998.

[434] Sun, K.; Jing, Y.; Park, N.; Li, C.; Bando, Y.; Wang, D. L. Solution synthesis of large-scale, high-sensitivity ZnO/Si hierarchical nanoheterostructure photodetectors. *J. Am. Chem. Soc.* **2010**, *132*, 15465–15467.

[435] Gao, P.; Wang, Z. Z.; Liu, K. H.; Xu, Z.; Wang, W. L.; Bai, X. D.; Wang, E. G. Photoconducting response on bending of individual ZnO nanowires. *J. Mater. Chem.* **2009**, *19*, 1002–1005.

[436] Wei, A.; Sun, X. W.; Wang, J. X.; Lei, Y.; Cai, X. P.; Li, C. M.; Dong, Z. L.; Huang, W. Enzymatic glucose biosensor based on ZnO nanorod array grown by hydrothermal decomposition. *Appl. Phys. Lett.* **2006**, *89*, 123902.

[437] Liu, N. S.; Fang, G. J.; Zeng, W.; Long, H.; Yuan, L. Y.; Zhao, X. Z. Novel ZnO nanorod flexible strain sensor and strain friving transistor with an ultrahigh 10^7 scale "On"–"Off" ratio fabricated by a single-step hydrothermal reaction. *J. Phys. Chem. C* **2011**, *115*, 570–575.

[438] Kwon, S. S.; Hong, W. K.; Jo, G.; Maeng, J.; Kim, T. W.; Song, S.; Lee, T. Piezoelectric effect on the electronic transport characteristics of ZnO nanowire field-effect transistors on bent flexible substrates. *Adv. Mater.* **2008**, *20*, 4557–4562.

[439] Wei, T. Y.; Huang, C. T.; Hansen, B. J.; Lin, Y. F.; Chen, L. J.; Lu, S. Y.; Wang, Z. L. Large enhancement in photon detection sensitivity via Schottky-gated CdS nanowire nanosensors. *Appl. Phys. Lett.* **2010**, *96*, 013508.

[440] Al-Hilli, S. M.; Willander, M.; Ost, A.; Stralfors, P. ZnO nanorods as an intracellular sensor for pH measurements. *J. Appl. Phys.* **2007**, *102*, 084304.

[441] Zhou, J.; Xu, N. S.; Wang, Z. L. Dissolving behavior and stability of ZnO wires in biofluids: A study on biode-gradability and biocompatibility of ZnO nanostructures. *Adv. Mater.* **2006**, *18*, 2432–2435.

[442] Li, Z.; Yang, R. S.; Yu, M.; Bai, F.; Li, C.; Wang, Z. L. Cellular level biocompatibility and biosafety of ZnO nanowires. *J. Phys. Chem. C* **2008**, *112*, 20114–20117.

[443] Gonzalez-Valls, I.; Lira-Cantu, M. Vertically-aligned nanostructures of ZnO for excitonic solar cells: A review. *Energy Environ. Sci.* **2009**, *2*, 19–34.

[444] Lee, Y. J.; Ruby, D. S.; Peters, D. W.; McKenzie, B. B.; Hsu, J. W. P. ZnO nanostructures as efficient antireflection layers in solar cells. *Nano Lett.* **2008**, *8*, 1501–1505.

[445] O'Regan, B.; Gratzel, M. A Low-cost, high-efficiency solar-cell based on dye-sensitized colloidal TiO_2 films. *Nature* **1991**, *353*, 737–740.

[446] Pradhan, B.; Batabyal, S. K.; Pal, A. J. Vertically aligned

ZnO nanowire arrays in Rose Bengal-based dye-sensitized solar cells. *Sol. Energy Mater. Sol. Cells* **2007**, *91*, 769–773.

[447] Baxter, J. B.; Aydil, E. S. Nanowire-based dye-sensitized solar cells. *Appl. Phys. Lett.* **2005**, *86*, 053114.

[448] Beermann, N.; Vayssieres, L.; Lindquist, S. E.; Hagfeldt, A. Photoelectrochemical studies of oriented nanorod thin films of hematite. *J. Electrochem. Soc.* **2000**, *147*, 2456–2461.

[449] Baxter, J. B.; Schmuttenmaer, C. A. Conductivity of ZnO nanowires, nanoparticles, and thin films using time-resolved terahertz spectroscopy. *J. Phys. Chem. B* **2006**, *110*, 25229–25239.

[450] Martinson, A. B. F.; McGarrah, J. E.; Parpia, M. O. K.; Hupp, J. T. Dynamics of charge transport and recombination in ZnO nanorod array dye-sensitized solar cells. *Phys. Chem. Chem. Phys.* **2006**, *8*, 4655–4659.

[451] Baxter, J. B.; Walker, A. M.; van Ommering, K.; Aydil, E. S. Synthesis and characterization of ZnO nanowires and their integration into dye-sensitized solar cells. *Nanotechnology* **2006**, *17*, S304–S312.

[452] Hsu, Y. F.; Xi, Y. Y.; Djurisic, A. B.; Chan, W. K. ZnO nanorods for solar cells: Hydrothermal growth versus vapor deposition. *Appl. Phys. Lett.* **2008**, *92*, 133507.

[453] Jiang, C. Y.; Sun, X. W.; Tan, K. W.; Lo, G. Q.; Kyaw, A. K. K.; Kwong, D. L. High-bendability flexible dye-sensitized solar cell with a nanoparticle-modified ZnO-nanowire electrode. *Appl. Phys. Lett.* **2008**, *92*, 143101.

[454] Leschkies, K. S.; Divakar, R.; Basu, J.; Enache-Pommer, E.; Boercker, J. E.; Carter, C. B.; Kortshagen, U. R.; Norris, D. J.; Aydil, E. S. Photosensitization of ZnO nanowires with CdSe quantum dots for photovoltaic devices. *Nano Lett.* **2007**, *7*, 1793–1798.

[455] Han, J. B.; Fan, F. R.; Xu, C.; Lin, S. S.; Wei, M.; Duan, X.; Wang, Z. L. ZnO nanotube-based dye-sensitized solar cell and its application in self-powered devices. *Nanotechnology* **2010**, *21*, 405203.

[456] Jensen, R. A.; Van Ryswyk, H.; She, C. X.; Szarko, J. M.; Chen, L. X.; Hupp, J. T. Dye-sensitized solar cells: Sensitizer-dependent injection into ZnO nanotube electrodes. *Langmuir* **2010**, *26*, 1401–1404.

[457] Yodyingyong, S.; Zhang, Q. F.; Park, K.; Dandeneau, C. S.; Zhou, X. Y.; Triampo, D.; Cao, G. Z. ZnO nanoparticles and nanowire array hybrid photoanodes for dye-sensitized solar cells. *Appl. Phys. Lett.* **2010**, *96*, 073115.

[458] Ku, C. H.; Wu, J. J. Chemical bath deposition of ZnO nanowire–nanoparticle composite electrodes for use in dye-sensitized solar cells. *Nanotechnology* **2007**, *18*, 505706.

[459] Cheng, K.; Cheng, G.; Wang, S. J.; Fu, D. W.; Zou, B. S.; Du, Z. L. Electron transport properties in ZnO nanowires/poly(3-hexylthiophene) hybrid nanostructure. *Mater. Chem. Phys.* **2010**, *124*, 1239–1242.

[460] Ku, C. H.; Wua, J. J. Electron transport properties in ZnO nanowire array/nanoparticle composite dye-sensitized solar cells. *Appl. Phys. Lett.* **2007**, *91*, 093117.

[461] Jiang, C. Y.; Sun, X. W.; Lo, G. Q.; Kwong, D. L.; Wang, J. X. Improved dye-sensitized solar cells with a ZnO-nanoflower photoanode. *Appl. Phys. Lett.* **2007**, *90*, 263501.

[462] Hosono, E.; Fujihara, S.; Honna, I.; Zhou, H. S. The fabrication of an upright-standing zinc oxide nanosheet for use in dye-sensitized solar cells. *Adv. Mater.* **2005**, *17*, 2091–2094.

[463] Xu, F.; Dai, M.; Lu, Y. N.; Sun, L. T. Hierarchical ZnO nanowire-nanosheet architectures for high power conversion efficiency in dye-sensitized solar cells. *J. Phys. Chem. C* **2010**, *114*, 2776–2782.

[464] Fu, Y. S.; Sun, J.; Xie, Y.; Liu, J.; Wang, H. L.; Du, X. W. ZnO hierarchical nanostructures and application on high-efficiency dye-sensitized solar cells. *Mater. Sci. Eng., B* **2010**, *166*, 196–202.

[465] Gao, Y. F.; Nagai, M. Morphology evolution of ZnO thin films from aqueous solutions and their application to solar cells. *Langmuir* **2006**, *22*, 3936–3940.

[466] Zou, D. C.; Wang, D.; Chu, Z. Z.; Lv, Z. B.; Fan, X. Fiber-shaped flexible solar cells. *Coord. Chem. Rev.* **2010**, *254*, 1169–1178.

[467] Wu, J. J.; Chen, G. R.; Yang, H. H.; Ku, C. H.; Lai, J. Y. Effects of dye adsorption on the electron transport properties in ZnO-nanowire dye-sensitized solar cells. *Appl. Phys. Lett.* **2007**, *90*, 213109.

[468] Zhang, Q. F.; Dandeneau, C. S.; Zhou, X. Y.; Cao, G. Z. ZnO nanostructures for dye-sensitized solar cells. *Adv. Mater.* **2009**, *21*, 4087–4108.

[469] Tak, Y.; Kim, H.; Lee, D.; Yong, K. Type-II CdS nanoparticle–ZnO nanowire heterostructure arrays fabricated by a solution process: Enhanced photocatalytic activity. *Chem. Commun.* **2008**, 4585–4587.

[470] Lee, M.; Yang, R.; Li, C.; Wang, Z. L. Nanowire–quantum dot hybridized cell for harvesting sound and solar energies. *J. Phys. Chem. Lett.* **2010**, *1*, 2929–2935.

[471] Tena-Zaera, R.; Katty, A.; Bastide, S.; Levy-Clement, C. Annealing effects on the physical properties of electrodeposited ZnO/CdSe core–shell nanowire arrays. *Chem. Mater.* **2007**, *19*, 1626–1632.

[472] Zhang, Y.; Xie, T. F.; Jiang, T. F.; Wei, X.; Pang, S.; Wang, X.; Wang, D. Surface photovoltage characterization of a ZnO nanowire array/CdS quantum dot heterogeneous film and its application for photovoltaic devices. *Nanotechnology* **2009**, *20*, 155707.

[473] Schaller, R. D.; Klimov, V. I. High efficiency carrier multiplication in PbSe nanocrystals: Implications for solar energy conversion. *Phys. Rev. Lett.* **2004**, *92*, 186601.

[474] Kongkanand, A.; Tvrdy, K.; Takechi, K.; Kuno, M.; Kamat, P. V. Quantum dot solar cells. Tuning photoresponse through size and shape control of CdSe–TiO_2 architecture. *J. Am. Chem. Soc.* **2008**, *130*, 4007–4015.

[475] Tak, Y.; Hong, S. J.; Lee, J. S.; Yong, K. Fabrication of ZnO/CdS core/shell nanowire arrays for efficient solar energy conversion. *J. Mater. Chem.* **2009**, *19*, 5945–5951.

[476] Consonni, V.; Rey, G.; Bonaime, J.; Karst, N.; Doisneau, B.; Roussel, H.; Renet, S.; Bellet, D. Synthesis and physical properties of ZnO/CdTe core shell nanowires grown by low-cost deposition methods. *Appl. Phys. Lett.* **2011**, *98*, 111906.

[477] Sun, X. W.; Chen, J.; Song, J. L.; Zhao, D. W.; Deng, W. Q.; Lei, W. Ligand capping effect for dye solar cells with a CdSe quantum dot sensitized ZnO nanorod photoanode. *Opt. Express* **2010**, *18*, 1296–1301.

[478] Cui, J.; Gibson, U. J. A simple two-step electrodeposition of Cu_2O/ZnO nanopillar solar cells. *J. Phys. Chem. C* **2010**, *114*, 6408–6412.

[479] Zhao, Q. D.; Xie, T. F.; Peng, L. L.; Lin, Y. H.; Wang, P.; Peng, L.; Wang, D. J. Size- and orientation-dependent photovoltaic properties of ZnO nanorods. *J. Phys. Chem. C* **2007**, *111*, 17136–17145.

[480] Tena-Zaera, R.; Ryan, M. A.; Katty, A.; Hodes, G.; Bastide, S.; Lévy-Clément, C. Fabrication and characterization of ZnO nanowires/CdSe/CuSCN *eta*-solar cell. *C.R. Chim.* **2006**, *9*, 717–729.

[481] Olson, D. C.; Piris, J.; Collins, R. T.; Shaheen, S. E.; Ginley, D. S. Hybrid photovoltaic devices of polymer and ZnO nanofiber composites. *Thin Solid Films* **2006**, *496*, 26–29.

[482] Takanezawa, K.; Tajima, K.; Hashimoto, K. Efficiency enhancement of polymer photovoltaic devices hybridized with ZnO nanorod arrays by the introduction of a vanadium oxide buffer layer. *Appl. Phys. Lett.* **2008**, *93*, 063308.

[483] Unalan, H. E.; Hiralal, P.; Kuo, D.; Parekh, B.; Amaratunga, G.; Chhowalla, M. Flexible organic photovoltaics from zinc oxide nanowires grown on transparent and conducting single walled carbon nanotube thin films. *J. Mater. Chem.* **2008**, *18*, 5909–5912.

[484] Liu, J.; Wang, S.; Bian, Z.; Shan, M.; Huang, C. Organic/inorganic hybrid solar cells with vertically oriented ZnO nanowires. *Appl. Phys. Lett.* **2009**, *94*, 173107.

[485] Takanezawa, K.; Hirota, K.; Wei, Q. S.; Tajima, K.; Hashimoto, K. Efficient charge collection with ZnO nanorod array in hybrid photovoltaic devices. *J. Phys. Chem. C* **2007**, *111*, 7218–7223.

[486] Briseno, A. L.; Holcombe, T. W.; Boukai, A. I.; Garnett, E. C.; Shelton, S. W.; Frechet, J. J. M.; Yang, P. D. Oligo- and polythiophene/ZnO hybrid nanowire solar cells. *Nano Lett.* **2010**, *10*, 334–340.

[487] Ravirajan, P.; Peiró, A. M.; Nazeeruddin, M. K.; Graetzel, M.; Bradley, D. D. C.; Durrant, J. R.; Nelson, J. Hybrid polymer/zinc oxide photovoltaic devices with vertically oriented ZnO nanorods and an amphiphilic molecular interface layer. *J. Phys. Chem. B* **2006**, *110*, 7635–7639.

[488] Bi, D. Q.; Wu, F.; Qu, Q. Y.; Yue, W. J.; Cui, Q.; Shen, W.; Chen, R. Q.; Liu, C. W.; Qiu, Z. L.; Wang, M. T. Device performance related to amphiphilic modification at charge separation interface in hybrid solar cells with vertically aligned ZnO nanorod arrays. *J. Phys. Chem. C* **2011**, *115*, 3745–3752.

[489] Olson, D. C.; Lee, Y. J.; White, M. S.; Kopidakis, N.; Shaheen, S. E.; Ginley, D. S.; Voigt, J. A.; Hsu, J. W. P. Effect of polymer processing on the performance of poly(3-hexylthiophene)/ZnO nanorod photovoltaic devices. *J. Phys. Chem. C* **2007**, *111*, 16640–16645.

[490] Olson, D. C.; Shaheen, S. E.; Collins, R. T.; Ginley, D. S. The effect of atmosphere and ZnO morphology on the performance of hybrid poly(3-hexylthiophene)/ZnO nanofiber photovoltaic devices. *J. Phys. Chem. C* **2007**, *111*, 16670–16678.

[491] Peiro, A. M.; Ravirajan, P.; Govender, K.; Boyle, D. S.; O'Brien, P.; Bradley, D. D. C.; Nelson, J.; Durrant, J. R. Hybrid polymer/metal oxide solar cells based on ZnO columnar structures. *J. Mater. Chem.* **2006**, *16*, 2088–2096.

[492] Lin, Y. Y.; Chen, C. W.; Chu, T. H.; Su, W. F.; Lin, C. C.; Ku, C. H.; Wu, J. J.; Chen, C. H. Nanostructured metal oxide/conjugated polymer hybrid solar cells by low temperature solution processes. *J. Mater. Chem.* **2007**, *17*, 4571–4576.

[493] Greene, L. E.; Law, M.; Yuhas, B. D.; Yang, P. D. ZnO-TiO_2 core-shell nanorod/P3HT solar cells. *J. Phys. Chem. C* **2007**, *111*, 18451–18456.

[494] Liu, J. P.; Qu, S. C.; Xu, Y.; Chen, Y. H.; Zeng, X. B.; Wang, Z. J.; Zhou, H. Y.; Wang, Z. G. Photovoltaic and electroluminescence characters in hybrid ZnO and conjugated polymer bulk heterojunction devices. *Chin. Phys. Lett.* **2007**, *24*, 1350–1353.

[495] Wang, Z. L. Self-powered nanotech—Nanosize machines need still tinier power plants. *Sci. Am.* **2008**, *298*, 82–87.

[496] Tian, B. Z.; Zheng, X. L.; Kempa, T. J.; Fang, Y.; Yu, N. F.; Yu, G. H.; Huang, J. L.; Lieber, C. M. Coaxial silicon nanowires as solar cells and nanoelectronic power sources. *Nature* **2007**, *449*, 885–890.

[497] Pan, C. F.; Wu, H.; Wang, C.; Wang, B.; Zhang, L.; Cheng,

Z. D.; Hu, P.; Pan, W.; Zhou, Z. Y.; Yang, X.; Zhu, J. Nanowire-based high performance "micro fuel cell": One nanowire, one fuel cell. *Adv. Mater.* **2008**, *20*, 1644–1648.

[498] Hudak, N. S.; Amatucci, G. G. Small-scale energy harvesting through thermoelectric, vibration, and radiofrequency power conversion. *J. Appl. Phys.* **2008**, *103*, 101301.

[499] Choi, M. Y.; Choi, D.; Jin, M. J.; Kim, I.; Kim, S. H.; Choi, J. Y.; Lee, S. Y.; Kim, J. M.; Kim, S. W. Mechanically powered transparent flexible charge-generating nanodevices with piezoelectric ZnO nanorods. *Adv. Mater.* **2009**, *21*, 2185–2189.

[500] Lei, Y.; Jiao, Z.; Wu, M. H.; Wilde, G. Ordered arrays of nanostructures and applications in high-efficient nano-generators. *Adv. Eng. Mater.* **2007**, *9*, 343–348.

[501] Su, W. S.; Chen, Y. F.; Hsiao, C. L.; Tu, L. W. Generation of electricity in GaN nanorods induced by piezoelectric effect. *Appl. Phys. Lett.* **2007**, *90*, 063110.

[502] Lu, M. T.; Song, J. H.; Lu, M. P.; Lee, C. Y.; Chen, L. J.; Wang, Z. L. ZnO-ZnS heterojunction and ZnS nanowire arrays for electricity generation. *ACS Nano* **2009**, *3*, 357–362.

[503] Huang, C. T.; Song, J. H.; Lee, W. F.; Ding, Y.; Gao, Z. Y.; Hao, Y.; Chen, L. J.; Wang, Z. L. GaN nanowire arrays for high-output nanogenerators. *J. Am. Chem. Soc.* **2010**, *132*, 4766–4771.

[504] Huang, C. T.; Song, J. H.; Tsai, C. M.; Lee, W. F.; Lien, D. H.; Gao, Z. Y.; Hao, Y.; Chen, L. J.; Wang, Z. L. Single-InN-nanowire nanogenerator with up to 1 V output voltage. *Adv. Mater.* **2010**, *22*, 4008–4013.

[505] Wang, X. B.; Song, J. H.; Zhang, F.; He, C. Y.; Hu, Z.; Wang, Z. L. Electricity generation based on one-dimensional group-III nitride nanomaterials. *Adv. Mater.* **2010**, *22*, 2155–2158.

[506] Lin, Y. F.; Song, J.; Ding, Y.; Lu, S. Y.; Wang, Z. L. Alternating the output of a CdS nanowire nanogenerator by a white-light-stimulated optoelectronic effect. *Adv. Mater.* **2008**, *20*, 3127–3130.

[507] Lu, M. Y.; Song, J. H.; Lu, M. P.; Lee, C. Y.; Chen, L. J.; Wang, Z. L. ZnO–ZnS heterojunction and ZnS nanowire arrays for electricity generation. *ACS Nano* **2009**, *3*, 357–362.

[508] Chen, X.; Xu, S.; Yao, N.; Shi, Y. 1.6 V Nanogenerator for mechanical energy harvesting using PZT nanofibers. *Nano Lett.* **2010**, *10*, 2133–2137.

[509] Qi, Y.; Jafferis, N. T.; Lyons, K.; Lee, C. M.; Ahmad, H.; McAlpine, M. C. Piezoelectric ribbons printed onto rubber for flexible energy conversion. *Nano Lett.* **2010**, *10*, 524–528.

[510] Qi, Y.; McAlpine, M. C. Nanotechnology-enabled flexible and biocompatible energy harvesting. *Energy Environ. Sci.* **2010**, *3*, 1275–1285.

[511] Feng, X.; Yang, B. D.; Liu, Y. M.; Wang, Y.; Dagdeviren, C.; Liu, Z. J.; Carlson, A.; Li, J. Y.; Huang, Y. G.; Rogers, J. A. Stretchable ferroelectric nanoribbons with wavy configurations on elastomeric substrates. *ACS Nano* **2011**, *5*, 3326–3332.

[512] Lee, M. H.; Javey, A. Power surfing on waves. *Nature* **2011**, *472*, 304–305.

[513] Qi, Y.; Kim, J.; Nguyen, T. D.; Lisko, B.; Purohit, P. K.; McAlpine, M. C. Enhanced piezoelectricity and stretchability in energy harvesting devices fabricated from buckled PZT ribbons. *Nano Lett.* **2011**, *11*, 1331–1336.

[514] Xu, S. Y.; Shi, Y. Power generation from piezoelectric lead zirconate titanate nanotubes. *J. Phys. D: Appl. Phys.* **2009**, *42*, 085301.

[515] Xu, S.; Hansen, B. J.; Wang, Z. L. Piezoelectric-nanowire-enabled power source for driving wireless microelectronics. *Nat. Commun.* **2010**, *1*, 93.

[516] Wang, Z. Y.; Hu, J.; Suryavanshi, A. P.; Yum, K.; Yu, M. F. Voltage generation from individual $BaTiO_3$ nanowires under periodic tensile mechanical load. *Nano Lett.* **2007**, *7*, 2966–2969.

[517] Ke, T. Y.; Chen, H. A.; Sheu, H. S.; Yeh, J. W.; Lin, H. N.; Lee, C. Y.; Chiu, H. T. Sodium niobate nanowire and its piezoelectricity. *J. Phys. Chem. C* **2008**, *112*, 8827–8831.

[518] Chang, C.; Tran, V. H.; Wang, J.; Fuh, Y. K.; Lin, L. Direct-write piezoelectric polymeric nanogenerator with high energy conversion efficiency. *Nano Lett.* **2010**, *10*, 726–731.

[519] Hansen, B. J.; Liu, Y.; Yang, R. S.; Wang, Z. L. Hybrid nanogenerator for concurrently harvesting biomechanical and biochemical energy. *ACS Nano* **2010**, *4*, 3647–3652.

[520] Service, R. F. Nanogenerators tap waste energy to power ultrasmall electronics. *Science* **2010**, *328*, 304–305.

[521] Wang, Z. L. Piezoelectric nanostructures: From growth phenomena to electric nanogenerators. *MRS Bull.* **2007**, *32*, 109–116.

[522] Zhao, M. H.; Wang, Z. L.; Mao, S. X. Piezoelectric characterization of individual zinc oxide nanobelt probed by piezoresponse force microscope. *Nano Lett.* **2004**, *4*, 587–590.

[523] Mitrushchenkov, A.; Linguerri, R.; Charnbaud, G. Piezoelectric properties of AlN, ZnO, and $Hg_xZn_{1-x}O$ nanowires by first-principles calculations. *J. Phys. Chem. C* **2009**, *113*, 6883–6886.

[524] Xiang, H. J.; Yang, J. L.; Hou, J. G.; Zhu, Q. S. Piezoelectricity in ZnO nanowires: A first-principles study. *Appl. Phys. Lett.* **2006**, *89*, 223111.

[525] Xin, J.; Zheng, Y.; Shi, E. Piezoelectricity of zinc-blende

and wurtzite structure binary compounds. *Appl. Phys. Lett.* **2007**, *91*, 112902.

[526] grawal, R.; Espinosa, H. D. Giant piezoelectric size effects in zinc oxide and gallium nitride nanowires. A first principles investigation. *Nano Lett.* **2011**, *11*, 786–790.

[527] Gao, Y.; Wang, Z. L. Electrostatic potential in a bent piezoelectric nanowire. The fundamental theory of nanogenerator and nanopiezotronics. *Nano Lett.* **2007**, *7*, 2499–2505.

[528] Scrymgeour, D. A.; Hsu, J. W. P. Correlated piezoelectric and electrical properties in individual ZnO nanorods. *Nano Lett.* **2008**, *8*, 2204–2209.

[529] Gao, Y.; Wang, Z. L. Equilibrium potential of free charge carriers in a bent piezoelectric semiconductive nanowire. *Nano Lett.* **2009**, *9*, 1103–1110.

[530] Mora-Sero, I.; Fabregat-Santiago, F.; Denier, B.; Bisquert, J.; Tena-Zaera, R.; Elias, J.; Levy-Clement, C. Determination of carrier density of ZnO nanowires by electrochemical techniques. *Appl. Phys. Lett.* **2006**, *89*, 203117.

[531] Tong, H.; Wang, B. L.; Ou-Yang, Z. C. Electric potential generated in ZnO nanowire due to piezoelectric effect. *Thin Solid Films* **2008**, *516*, 2708–2710.

[532] Allen, M. W.; Alkaisi, M. M.; Durbin, S. M. Metal Schottky diodes on Zn-polar and O-polar bulk ZnO. *Appl. Phys. Lett.* **2006**, *89*, 103520.

[533] Coppa, B. J.; Davis, R. F.; Nemanich, R. J. Gold Schottky contacts on oxygen plasma-treated, *n*-type ZnO(000$\bar{1}$). *Appl. Phys. Lett.* **2003**, *82*, 400–402.

[534] Wenckstern, H. V.; Kaidashev, E. M.; Lorenz, M.; Hochmuth, H.; Biehne, G.; Lenzner, J.; Gottschalch, V.; Pickenhain, R.; Grundmann, M. Lateral homogeneity of Schottky contacts on *n*-type ZnO. *Appl. Phys. Lett.* **2004**, *84*, 79–81.

[535] Kim, S. H.; Kim, H. K.; Seong, T. Y. Effect of hydrogen peroxide treatment on the characteristics of Pt Schottky contact on *n*-type ZnO. *Appl. Phys. Lett.* **2005**, *86*, 112101.

[536] Rakhshani, A. E. Schottky diodes on ZnO rods grown homoepitaxially by successive chemical solution deposition. *Semicond. Sci. Technol.* **2008**, *23*, 075037.

[537] Periasamy, C.; Chakrabarti, P. Time-dependent degradation of Pt/ZnO nanoneedle rectifying contact based piezoelectric nanogenerator. *J. Appl. Phys.* **2011**, *109*, 054306.

[538] Song, J. H.; Xie, H. Z.; Wu, W. Z.; Joseph, V. R.; Wu, C. F. J.; Wang, Z. L. Robust optimization of the output voltage of nanogenerators by statistical design of experiments. *Nano Res.* **2010**, *3*, 613–619.

[539] Shao, Z. Z.; Wen, L. Y.; Wu, D. M.; Zhang, X. A.; Chang, S. L.; Qin, S. Q. AFM analysis of piezoelectric nanogenerator based on n^+-diamond/*n*-ZnO heterojunction. *Appl. Surf. Sci.* **2011**, *257*, 4919–4922.

[540] Riaz, M.; Fulati, A.; Amin, G.; Alvi, N. H.; Nur, O.; Willander, M. Buckling and elastic stability of vertical ZnO nanotubes and nanorods. *J. Appl. Phys.* **2009**, *106*, 034309.

[541] Liu, J.; Fei, P.; Zhou, J.; Tummala, R.; Wang, Z. L. Toward high output-power nanogenerator. *Appl. Phys. Lett.* **2008**, *92*, 173105.

[542] Thundat, T. Flexible approach pays off. *Nat.Nanotechnol.* **2008**, *3*, 133–134.

[543] Zhang, J.; Li, M. K.; Yu, L. Y.; Liu, L. L.; Zhang, H.; Yang, Z. Synthesis and piezoelectric properties of well-aligned ZnO nanowire arrays via a simple solution-phase approach. *Appl. Phys. A* **2009**, *97*, 869–876.

[544] Park, H. K.; Lee, K. Y.; Seo, J. S.; Jeong, J. A.; Kim, H. K.; Choi, D.; Kim, S. W. Charge-generating mode control in high-performance transparent flexible piezoelectric nanogenerators. *Adv. Funct. Mater.* **2011**, *21*, 1187–1193.

[545] Choi, D.; Choi, M. Y.; Shin, H. J.; Yoon, S. M.; Seo, J. S.; Choi, J. Y.; Lee, S. Y.; Kim, J. M.; Kim, S. W. Nanoscale networked single-walled carbon-nanotube electrodes for transparent flexible nanogenerators. *J. Phys. Chem. C* **2010**, *114*, 1379–1384.

[546] Choi, D.; Choi, M. Y.; Choi, W. M.; Shin, H. J.; Park, H. K.; Seo, J. S.; Park, J.; Yoon, S. M.; Chae, S. J.; Lee, Y. H.; Kim, S. W.; Choi, J. Y.; Lee, S. Y.; Kim, J. M. Fully rollable transparent nanogenerators based on graphene electrodes. *Adv. Mater.* **2010**, *22*, 2187–2192.

[547] Shin, H. J.; Choi, W. M.; Choi, D.; Han, G. H.; Yoon, S. M.; Park, H. K.; Kim, S. W.; Jin, Y. W.; Lee, S. Y.; Kim, J. M.; Choi, J. Y.; Lee, Y. H. Control of electronic structure of graphene by various sopants and their effects on a nanogenerator. *J. Am. Chem. Soc.* **2010**, *132*, 15603–15609.

[548] Kumar, B.; Lee, K. Y.; Park, H. K.; Chae, S. J.; Lee, Y. H.; Kim, S. W. Controlled growth of semiconducting nanowire, nanowall, and hybrid nanostructures on graphene for piezoelectric nanogenerators. *ACS Nano* **2011**, *5*, 4197–4204.

[549] Yang, R. S.; Qin, Y.; Li, C.; Dai, L. M.; Wang, Z. L. Characteristics of output voltage and current of integrated nanogenerators. *Appl. Phys. Lett.* **2009**, *94*, 022905.

[550] Yang, R.; Qin, Y.; Li, C.; Zhu, G.; Wang, Z. L. Converting biomechanical energy into electricity by a muscle-movement-driven nanogenerator. *Nano Lett.* **2009**, *9*, 1201–1205.

[551] Li, Z.; Zhu, G.; Yang, R. S.; Wang, A. C.; Wang, Z. L. Muscle-driven *in vivo* nanogenerator. *Adv. Mater.* **2010**, *22*, 2534–2537.

[552] Zhu, G.; Yang, R. S.; Wang, S. H.; Wang, Z. L. Flexible high-output nanogenerator based on lateral ZnO nanowire array. *Nano Lett.* **2010**, *10*, 3151–3155.

[553] Agrawal, R.; Peng, B.; Espinosa, H. D. Experimental–computational investigation of ZnO nanowires strength and fracture. *Nano Lett.* **2009**, *9*, 4177–4183.

[554] Yu, A. F.; Li, H. Y.; Tang, H. Y.; Liu, T. J.; Jiang, P.; Wang, Z. L. Vertically integrated nanogenerator based on ZnO nanowire arrays. *Phys. Status Solidi R* **2011**, *5*, 162–164.

[555] van der Heyden, F. H. J.; Bonthuis, D. J.; Stein, D.; Meyer, C.; Dekker, C. Power generation by pressure-driven transport of ions in nanofluidic channels. *Nano Lett.* **2007**, *7*, 1022–1025.

[556] Hu, Y.; Zhang, Y.; Xu, C.; Lin, L.; Snyder, R. L.; Wang, Z. L. Self-powered system with wireless data transmission. *Nano Lett.* **2011**, *11*, 2572–2577.

[557] Khan, S. U. M.; Al-Shahry, M.; Ingler, W. B. Efficient photochemical water splitting by a chemically modified *n*-TiO_2 *Science* **2002**, *297*, 2243–2245.

[558] Chen, H.; Chen, C.; Chang, Y. C.; Tsai, C. W.; Liu, R. S.; Hu, S. F.; Chang, W. S.; Chen, K. H. Quantum dot monolayer sensitized ZnO nanowire-array photoelectrodes: True efficiency for water splitting. *Angew. Chem. Int. Ed.* **2010**, *49*, 5966–5969.

[559] Wang, G. M.; Yang, X. Y.; Qian, F.; Zhang, J. Z.; Li, Y. Double-sided CdS and CdSe quantum dot co-sensitized ZnO nanowire arrays for photoelectrochemical hydrogen generation. *Nano Lett.* **2010**, *10*, 1088–1092.

[560] Wang, X. W.; Liu, G.; Lu, G. Q.; Cheng, H. M. Stable photocatalytic hydrogen evolution from water over ZnO–CdS core–shell nanorods. *Int. J. Hydrogen Energy* **2010**, *35*, 8199–8205.

[561] Hong, K. S.; Xu, H. F.; Konishi, H.; Li, X. C. Direct water splitting through vibrating piezoelectric microfibers in water. *J. Phys. Chem. Lett.* **2010**, *1*, 997–1002.